A NOVEL MUSIC ALGORITHM BASED ELECTROMAGNETIC TARGET
RECOGNITION METHOD IN RESONANCE REGION FOR THE
CLASSIFICATION OF SINGLE AND MULTIPLE TARGETS

A THESIS SUBMITTED TO
THE GRADUATE SCHOOL OF NATURAL AND APPLIED SCIENCES
OF
MIDDLE EAST TECHNICAL UNIVERSITY

BY

MUSTAFA SEÇMEN

IN PARTIAL FULFILMENT OF THE REQUIREMENTS
FOR
THE DEGREE OF DOCTOR OF PHILOSOPHY
IN
ELECTRICAL AND ELECTRONICS ENGINEERING

FEBRUARY 2008

Approval of the thesis:

A NOVEL MUSIC ALGORITHM BASED ELECTROMAGNETIC TARGET RECOGNITION METHOD IN RESONANCE REGION FOR THE CLASSIFICATION OF SINGLE AND MULTIPLE TARGETS

submitted by **MUSTAFA SEÇMEN** in partial fulfillment of the requirements for the degree of **Doctor of Philosophy in Electrical and Electronics Engineering Department, Middle East Technical University** by,

Prof. Dr. Canan Özgen
Dean, Graduate School of **Natural and Applied Sciences**

Prof. Dr. İsmet Erkmen
Head of Department, **Electrical and Electronics Engineering**

Prof. Dr. Gönül Turhan Sayan
Supervisor, **Electrical and Electronics Eng. Dept., METU**

Prof. Dr. Altunkan Hızal
Co-Supervisor, **Electrical and Electronics Eng. Dept., METU**

Examining Committee Members:

Prof. Dr. Altunkan Hızal
Electrical and Electronics Engineering Dept., METU

Prof. Dr. Gönül Turhan Sayan
Electrical and Electronics Engineering Dept., METU

Prof. Dr. Mustafa Kuzuoğlu
Electrical and Electronics Engineering Dept., METU

Prof. Dr. Gülbin Dural
Electrical and Electronics Engineering Dept., METU

Prof. Dr. Adnan Köksal
Electrical and Electronics Engineering Dept., Hacettepe University

Date: 04.02.2008

I hereby declare that all information in this document has been obtained and presented in accordance with academic rules and ethical conduct. I also declare that, as required by these rules and conduct, I have fully cited and referenced all material and results that are not original to this work.

Name, Last Name: Mustafa, SEÇMEN

Signature:

ABSTRACT

A NOVEL MUSIC ALGORITHM BASED ELECTROMAGNETIC TARGET RECOGNITION METHOD IN RESONANCE REGION FOR THE CLASSIFICATION OF SINGLE AND MULTIPLE TARGETS

Seçmen, Mustafa

Ph. D., Department of Electrical and Electronics Engineering

Supervisor: Prof. Dr. Gönül Turhan Sayan

Co-Supervisor: Prof. Dr. Altunkan Hızal

February 2008, 246 pages

This thesis presents a novel aspect and polarization invariant electromagnetic target recognition technique in resonance region based on use of MUSIC algorithm for the extraction of natural-resonance related target features. In the suggested method, the feature patterns called "MUSIC Spectrum Matrices (MSMs)" are constructed for each candidate target at each reference aspect angle using targets' scattered data at

different late-time intervals. These individual MSMs correspond to maps of targets' natural-resonance related power distributions. All these patterns are first used to obtain optimal late-time interval for classifier design and a "Fused MUSIC Spectrum Matrix (FMSM)" is generated over this interval for each target by superposing MSMs. The resulting FMSMs include more complete information for target resonances and are almost insensitive to aspect and polarization. In case of multiple target recognition, the relative locations of a multi-target group and separation distance between targets are also important factors. Therefore, MSM features are computed for each multi-target group at each "reference aspect/topology" combination to determine the optimum late-time interval. The FMSM feature of a given multi-target group is obtained by the superposition of all these aspect and topology dependent MSMs. In both single and multiple target recognition cases, the resulting FMSM power patterns are main target features of the designed classifier to be used during real-time decisions. At decision phase, the unknown test target is classified either as one of the candidate targets or as an alien target by comparing correlation coefficients computed between MSM of test signal and FMSM of each candidate target.

Keywords: Electromagnetic target recognition, feature extraction, natural-resonance mechanism, target poles, MUSIC algorithm, isolated targets, multiple targets

ÖZ

TEK VE ÇOKLU HEDEFLERİN SINIFLANDIRILMASI İÇİN REZONANS BÖLGEDE MUSIC ALGORİTMASINA DAYALI YENİ BİR ELEKTROMANYETİK HEDEF TANIMA YÖNTEMİ

Seçmen, Mustafa

Doktora, Elektrik ve Elektronik Mühendisliği Bölümü

Tez Yöneticisi: Prof. Dr. Gönül Turhan Sayan

Ortak Tez Yöneticisi: Prof. Dr. Altunkan Hızal

Bu tez, doğal rezonansa bağlı hedef özniteliklerini çıkartmak için MUSIC algoritmasının kullanılmasına dayanan rezonans bölgesindeki görüş açısı ve polarizasyon bağımsız yeni bir elektromanyetik hedef tanıma tekniğini sunmaktadır. Önerilen yöntemde, her bir hedef için "MUSIC Tayf Matrisleri (MTMler)" adı verilen öznitelik matrisleri, farklı geç-zaman aralıklarındaki saçınım verileri kullanılarak önceden seçilmiş her bir referans açısı için hesaplanır. Bu MTMlerin her biri, hedefin doğal rezonanslara ilişkin güç dağılım haritalarına karşılık gelmektedir.

Bütün bu öznitelik matrisleri ilk olarak öznitelik çıkarımı için en uygun geç-zaman aralığının elde edilmesinde kullanılır. Sonra, hedefin "Kaynaştırılmış MUSIC Tayf Matrisi (KMTM)" bu en uygun geç zaman aralığı üzerinde o hedefe ait bütün MTMlerin bindirilmesi ile üretilir. Bu KMTMler hedeflerin rezonansları açısından daha fazla bilgi içermektedir ve görüş açısı/polarizasyon değişimlerine daha az duyarlıdırlar. Çoklu hedef tanınması durumunda ise, hedeflerin birbirlerine göre konumları ve hedefler arası ayrım mesafesi de önemli faktörlerdir. Bu yüzden, en uygun geç-zaman aralığının kestirimi için, MTM öznitelikleri her çoklu hedef grubunun her "referans görüş açısı/referans topoloji" kombinasyonunda hesaplanır. Çoklu hedef grubunun KMTM özniteliği, bütün bu görüş açısı ve topoloji şartlarına bağımlı MTM'lerin bindirilmesi ile elde edilir. Hem tek hem de çoklu hedef tanıma durumlarında, KMTM güç örüntüleri, tasarlanan sınıflandırıcının gerçek zamanlı karar evresinde kullanılan ana hedef öznitelikleridir. Karar evresinde, bilinmeyen test hedefine ait sinyalden hesaplanan MTM ile aday hedeflerin KMTMleri arasındaki ilinti katsayılarını karşılaştırılır. Bilinmeyen hedef ya aday hedeflerden biri ya da bunların dışında yabancı bir hedef olarak sınıflandırılır.

Anahtar Kelimeler: Elektromanyetik hedef tanıma, öznitelik çıkarımı, doğal rezonans mekanizması, hedef kutupları, MUSIC algoritması, yalıtık hedefler, çoklu hedefler

To My Family

ACKNOWLEDGMENTS

TABLE OF CONTENTS

LIST OF TABLES

xvi

LIST OF FIGURES

CHAPTER 1

INTRODUCTION

Electromagnetic target recognition is an ongoing field of exploration and development with critical applications in multi-disciplinary problems of both civilian and military use. In these problems, the main goal is to filter out characteristic properties (feature information) belonging to targets and identify the targets on the basis of comparison of these features. These features can be either direct or indirect information related to the targets' physical properties such as their size, shape or material structures or parameters related to their dynamical properties such as their position, speed or acceleration. In other words, target features can be any information which distinguish one target among the others as sensitively as possible.

It is possible to broadly categorize target recognition methods as cooperative and non-cooperative methods. The recognition of a target with a cooperative system where the target directly cooperates in some manner with the identification sensor is called Cooperative Target Recognition [1]-[3]. These cooperative systems can be some form of communication system, data link or transponder system, which allows the target to identify itself on a regular basis. A well-known example of Cooperative Target Recognition used in military cooperative identification systems is the Identification Friend or Foe (IFF) technique [4]-[7]. Another cooperative identification system example, which is used in air-traffic control, is the Air-Traffic Control Radar Beacon System (ATCRBS).

On the other hand, noncooperative target recognition methods, whose main interest areas are military applications, obtain target recognition information without any cooperation with the target. In these methods, recognition becomes possible by investigating the target features extracted from the scattered electromagnetic signals received from the target.

Target recognition from backscattered electromagnetic data has been a difficult problem to solve with complicated scattering mechanism even for geometrically simple targets. This is because the scattered signals are strongly dependent on aspect angle, polarization and operating frequency. In addition to these dependencies, presence of strong random additive noise brings further complications to this challenging problem. In noncooperative target recognition problems, each candidate target should be represented in the reference database by some characteristic features which should have minimum sensitivity to the variations in aspect angle and polarization to increase the accuracy rate of the method which is the most important design criterion. In addition to the accuracy, robustness under noisy conditions, high decision speed in real time, small memory requirements, modest need for diversity in the reference database, simplicity and repeatability of the design work and generality regarding the admissible types of candidate targets are all important classifier design criteria to meet.

In noncooperative target recognition, the suggested recognition method produces the identification decision automatically by the help of signal processing techniques, the pattern recognition methods, in particular. In the classifier design process, known or extracted target features for a set of library targets are stored in the classifier database. When a test signal from an unknown target is received, the feature corresponding to this unknown test target is extracted and compared with the features in the classifier's database to find the best match.

Different methods of noncooperative electromagnetic target recognition need to be used in different regions, which are mainly the Rayleigh region, the resonance region and the optical region. Common characteristics of electromagnetic scattered fields in each of these frequency regions are discussed in Appendix A together with a brief summary of target recognition methods used in the optical region.

The main purpose of this dissertation is to introduce a novel electromagnetic target recognition method, which is useful in the resonance region. As discussed in Appendix A, the wavelength (λ) of the electromagnetic signals must be comparable to the overall dimensions of the target in this frequency region. More specifically, if d is the largest dimension of the target in consideration, $\frac{d}{10} \leq \lambda \leq 10d$ condition needs to be met. It is well known that the scattered response of a target changes moderately in a resonative manner in the resonance region. In addition, the response is sensitive to the aspect and polarization conditions. As a result, the scattered response in resonance region carries valuable information regarding the size and overall geometry of the target.

In this chapter, Section 1.1 presents a brief overview about various electromagnetic target recognition methods, which are applicable in resonance region. More detailed information about these methods will be given in Chapter 2. Finally, Section 1.2 describes the target recognition method developed in this thesis and outlines the organization of the thesis.

1.1. Resonance Region Methods for Target Recognition

There have been several methods proposed for target recognition in the resonance region. One method makes use of the ramp response of a target and develops a feature space based on the amplitude, phase and polarization at each distinct

frequency over a bandwidth for a given target [8], [9]. Some other methods employ the complex natural resonances (CNRs) of targets (i.e. the system poles of the targets) to uniquely characterize the target [10]. The feature extraction approach used in these methods is conceptually based on the utilization of dominant natural resonance mechanisms in the scattered target response. The main idea behind this approach can be explained by the basic concepts of the linear system theory. The complex natural resonance mechanisms associated with the linear system models of electromagnetic targets were extensively studied and formalized as the Singularity Expansion Method (SEM) [11], [12] which is explained in detail in Chapter 2. Most of the target recognition methods suggested in resonance region depend on this SEM approach. These methods are based on the fact that shape, size and material properties of a target determine the values of complex natural resonance frequencies of that target in an aspect and polarization independent manner. All this feature information is provided by the late-time scattering signals, which are formed by the linear combination of natural response components oscillating at target's CNR frequencies [13]. Creeping waves traveling around a conducting target are directly related to the target's natural response, for example.

The earlier target recognition methods in resonance region attempted to estimate the target pole values directly from the scattered data by using methods such as Prony's Method, Matrix Pencil Method or Nonlinear Least Square Methods [14]-[16]. However, one of the major drawbacks of these methods is that the performance of such methods dramatically deteriorates as the signal-to-noise (SNR) of the scattered data gets lower. Another group of recognition methods based on the SEM theory is based on synthesizing a special time-limited input signal (an incident signal) as the main target feature, which leads to the annihilation of the target's transform domain poles and hence produced a time-limited target response. Kill pulse (K-pulse), extinction pulse (E-pulse) and single mode extraction pulse (S-pulse) techniques are the well known methods in this group [17]-[19] and they are all based on the work of Kennaugh published in 1981 [68]. In such methods if the target-specified signal

impinges on the correct target, the late-time energy of the scattered response will be very low (theoretically zero) due to the lack of natural modes; however, if it impinges on the other candidate targets of the database, the late-time response energies of these mismatched targets will be considerably higher. Although the methods like K-pulse, E-pulse are popular, they suffer from the difficulties of isolating late-time scattered data from the early-time scattered response especially for extremely low-Q targets such as a conducting sphere. In addition to these methods, there are other resonance region methods in the literature, which also use the late-time region of the scattered fields and give more successful results. These methods generally use advanced signal processing tools and algorithms such as neural networks, generalized likelihood ratio test (GLRT), matching pursuit method or time-frequency representations (TFRs) to form target features like late-time feature vector (LTFV) [20]-[23]. Furthermore, some other methods, which benefit from the full-time scattered response of the targets, also exist [24], [25]. Detailed information about the natural resonance mechanism as formulated by the SEM approach and the related resonance region methods will be given in Chapter 2.

1.2. Target Recognition Method Developed in This Thesis

The electromagnetic target recognition method developed in this thesis is a resonance region method, which is based on natural-resonance mechanism formulated by the SEM. As most of the other resonance region methods, the proposed method makes use of the late-time region of targets' scattered fields and it utilizes the Multiple Signal Classification (MUSIC) algorithm in the natural-resonance related feature extraction process. This method uses the MUSIC algorithm to construct feature maps in complex frequency domain, which give the targets' natural response related power distributions for late-time region. For this purpose, a matrix called MUSIC spectrum matrix (MSM) is generated from scattered field at each pre-selected reference aspect angle for each target. Then, each MSM is normalized to have normalized MUSIC

Spectrum Matrix. Afterwards, these normalized matrices are used to determine the optimal late-time interval to be used in the classifier design process. Details of this process will be explained in Section 3.2. Then, the MUSIC spectrum matrices of a given candidate target, which are computed at all reference aspect angles over the optimal late-time interval, are superposed and normalized to obtain the Fused MUSIC Spectrum Matrix (FMSM) for that specific target. The fused MUSIC spectrum matrix of a target has a substantially reduced dependency on aspect angle as it is constructed from multi-aspect scattered data. The FMSM features are used as the main target classifier features in the proposed target classification method. As an example, the MSM of a conducting sphere with 18 mm radius corresponding to optimal late-time interval at one reference aspect angle is shown in Figure 1.1(a). The FMSM of the same target, which is the superposition of three MSMs at three different reference aspect angles including the MSM in Figure 1.1(a), is shown in Figure 1.1(b) [26]. In these figures, the local peak points roughly show the pole locations. An FMSM contains the overall power distribution information of a given target due to the superposition of the power distribution information from all reference aspect angles. Hence, a resonance information missed at one aspect can be extracted at some other reference aspects, resulting in a more complete natural resonance information in the FMSM for that target of concern. For example, the resonance component seen in the fused MSM feature in Figure 1.1(b) (around α= -10 GNeper/s and f= 8 GHz location) is missing in the MSM in Figure 1.1(a)).
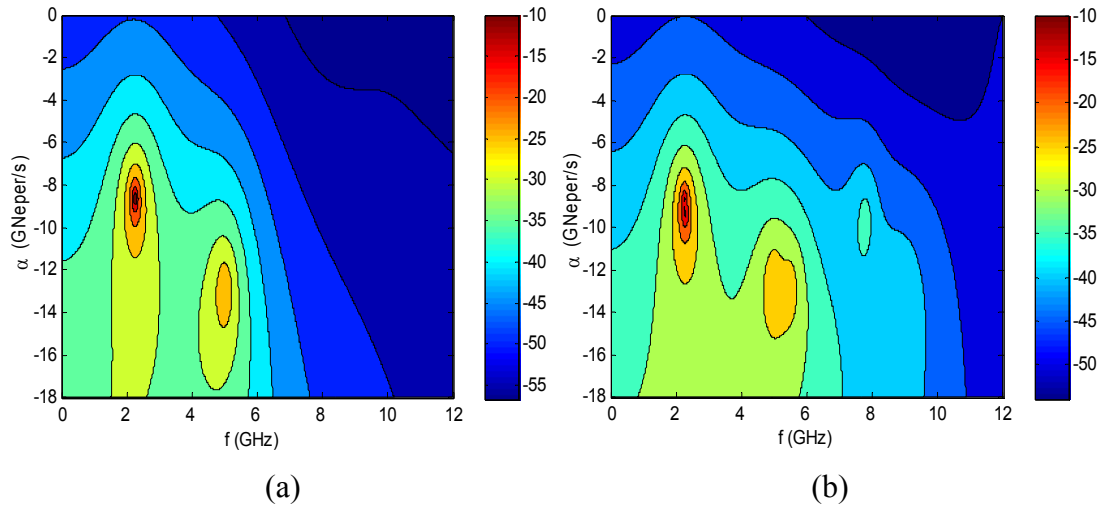
Figure 1.1   (a) The MSM of a conducting sphere with 18 mm radius obtained at one reference aspect angle (b) The FMSM of same sphere as the superposition of three different MSMs at one of which is the MSM in Figure 1.1(a).

Once the classifiers feature database is designed to include the fused MSM feature for each library target, an MSM is computed from the selected optimal late-time portion of the test scattered signal in the real-time classification phase and it is compared to the FMSM of each candidate target in the classifier database. The maximum correlation coefficient computed in this process indicates the classification label for the test target.

The aim of this thesis is to propose a novel target recognition method to design classifiers which can identify targets with high correct classification rates and also possess properties such as robustness to noise, minimum sensitivity to aspect angle and polarization changes and low memory requirements by using a small sized reference database.

This thesis introduces the theory and design steps for the suggested target recognition method together with the various classifier libraries with single and multiple targets. The organization of the thesis is as follows:

Chapter 2 gives the theory of natural-resonance mechanism of the target responses associated with the SEM. Details of familiar SEM based methods are also given in this chapter.

Chapter 3 presents the proposed method of classifier design and the feature extraction technique used to obtain fused MUSIC spectrum patterns for each target. Besides, the target recognition method developed in this thesis is compared to the other resonance region methods in this chapter.

Chapter 4 gives demonstrations of this novel method for single target libraries. Scattered target responses are used in this section obtained by using either analytical expressions or numerical simulations.

Chapter 5 presents the measurement set-up for scattered field measurements in Millimeter and Microwave (MMW) Laboratory at METU and demonstrates the usefulness of the proposed target classification method for single target libraries. Scattered fields used in these demonstrations are measured either at MMW of METU or at the ElectroScience Laboratory of the Ohio State University.

Chapter 6 explains the modifications made on the design method, which is suggested to classify single targets, so that it can be used to recognize multi-target groups as well. Simulation results obtained for this modified method is presented for target libraries including single targets as well as multi-target groups.

Finally, Chapter 7 gives an overall summary of the main contributions made in this thesis and also presents a brief discussion for future work.

Appendix A gives the characteristics of scattering regions as well as the target recognition methods in the optical region.

Appendix B gives the derivation of the singularity expansion method (SEM).

Appendix C presents the derivation of scattered far field expressions for perfectly conducting and dielectric spherical targets.

Appendix D contains a sample program code written in MATLAB for classifier design and target recognition simulations for small-scale aircraft targets modeled by perfectly conducting, straight, thin wires.

CHAPTER 2

NATURAL-RESONANCE MECHANISM AND ELECTROMAGNETIC TARGET RECOGNITION METHODS BASED ON NATURAL-RESONANCES

This chapter is initially focused on the theory of the natural-resonance mechanism of scattering phenomena. Then, the common resonance region methods using this mechanism are described.

2.1. Singularity Expansion Method (SEM)

The singularity expansion method (SEM) is a way to represent the solution of electromagnetic induction or scattering with linear system models. The analysis techniques of the linear system theory and the concept of impulse response were applied to electromagnetic scattering problems for the first time in 1958 [27]. Then, it is suggested that a linear time-invariant lumped parameter system model can be efficiently used for the electromagnetic targets at sufficiently low frequencies [28]. Besides, it has been observed that the frequency response in the range $\frac{\pi}{5} < k_o L < 10\pi$ (or $0.2L < \lambda_o < 10L$, where L is the maximum linear dimension of the target) can provide useful information on bulk dimensions, approximate shape and material composition of the scatterer [8], [29]. The higher frequencies, on the

other hand, characterize fine details. In the early 1970's, L. Marin showed that electromagnetic scattering from a perfectly conducting target is a meromorphic function of frequency under certain mathematical restrictions [30]. Finally, a more sophisticated identification method emerged after Marin's result and numerous observations had shown that the late-time scattered fields could be represented by a series of damped sinusoidal oscillations [31]. The basic concepts of this method stem from the observation of typical transient responses of complicated scatterers such as aircraft, missiles, etc. As an example, an experimentally observed current on one of the wire sections of the Boeing 707 aircraft, which is modeled by a few conducting sticks, is shown in Figure 2.1 [32].
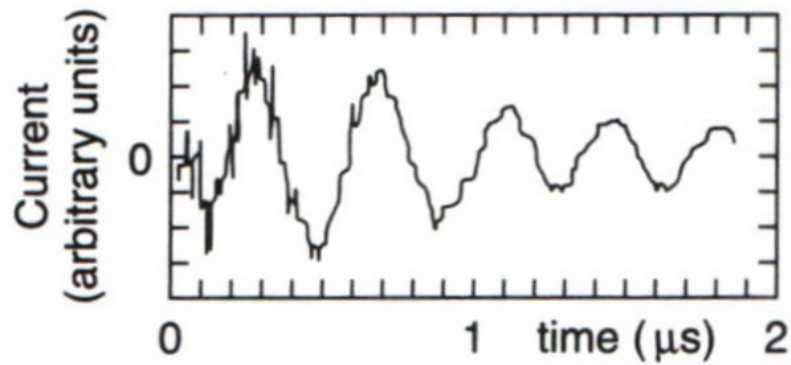
Figure 2.1   The experimental current response on a wire section of the Boeing 707 aircraft model, which is modeled by conducting wires [32].

This response reminds an oscillation of an R-L-C circuit. Response of such a circuit is in the form of $e^{-\alpha t}e^{\pm jwt}$ and it is associated with the presence of poles $(\alpha + j\omega)$ in the Laplace domain. It is shown that the complex frequencies associated with these oscillations depend only on the geometry and material parameters of the scatterer and not on the nature of the incident fields [31]. However, the representation of whole scattering phenomena in time-domain with a series of damped sinusoidal oscillations is inadequate especially when considering forced

response of the target due to specular scattered fields at early-times. By representing the early time scattering using a time-limited response, the total scattered field can be formally expressed with the Singularity Expansion Method (SEM) which formalizes the complex natural resonance mechanism observed in linear system models of targets [33], [34]. According to SEM, in the complex frequency (Laplace) domain, the aspect dependent system function of the target which is modeled as a distributed, linear, time-invariant system, can be given as

$$H(s,\theta_d,\phi_d) = E(s,\theta_d,\phi_d) + \underbrace{\sum_{n=1}^{\infty} \frac{R_n(s,\theta_d,\phi_d)}{(s-s_n)(s-s_n^*)}}_{L(s,\theta_d,\phi_d)} \quad where\ s = \alpha + j\omega \tag{2.1}$$

with θ_d and ϕ_d being the elevation and azimuth angles. The inverse Laplace transform of this expression, which is the aspect dependent impulse response of the target, can be obtained in the general form as

$$h(t,\theta_d,\phi_d) = e(t,\theta_d,\phi_d) + \sum_{n=1}^{\infty} b_n(\theta_d,\phi_d)e^{\alpha_n t}\cos(w_n t + \delta_n) \tag{2.2}$$

The derivation of the Singularity Expansion Method is given in Appendix B. In Equation (2.1), $E(s,\theta_d,\phi_d)$ is an entire function[a] in complex domain, $L(s,\theta_d,\phi_d)$ is a meromorphic function[b] in complex domain and $R_n(\theta_d,\phi_d)$ is an aspect and polarization dependent complex residue of the nth target pole.

---

[a] Functions, such as polynomials or convergent power series, which are differentiable everywhere are called entire functions [35].

[b] A function which is analytic in a domain except at isolated poles is called as a meromorphic function in this domain [35].

Therefore, the meromorphic function yields a damped sinusoidal signal in time domain which is the natural impulse response of the target, while the entire function yields a time-limited response in Equation (2.2) as $e(t,\theta_d,\phi_d)$, which comprises an important portion of the early-time scattered signature.

The complex natural frequencies in these equations, $s_n = \alpha_n + j\omega_n$ with $\alpha_n < 0$, are only the functions of the geometry and physical composition of scatterer, that they are independent of the aspect angle and polarization conditions. These complex natural resonance frequencies thus have the potential for use in aspect and polarization independent identification of scatterers. This beneficial property creates a distinguishable feature for a specific target. Some additional properties of these natural resonances are:

- The s_n's appear in complex conjugate pairs as a result of the real nature of source-free induced currents in physical problems.

- The real part of each s_n is less than zero to produce exponential decay of the magnitude of each mode, corresponding to power being radiated away from the scatterer (radiation loss).

- There are an infinite number of natural resonances, even for the targets of simplest shapes. In practice, however, only a finite number of resonances will be significantly excited by an incident signal of particular frequency bandwidth.

2.1.1. The Early-Time Response

Evolution of the scattered fields in time, under an impulse excitation, can be split into two time regions: the early-time and the late-time. Some qualitative statements can be made about these two zones, which may be separated by a transition time instant, which is approximately expressed as $t_{late} \cong 2L/v$, where L is the largest dimension of the target and v is the speed of propagation of the incident wave (equal to c in vacuum).

When an incident field first hits a smooth surfaced target, some of its electromagnetic energy is initially reflected according to the Snell's Law of reflection. The time duration needed for the wave to fully pass through the target is known as the early-time period. In the early-time, the forced response exists, by definition, as long as the target and the excitation wave directly interact. This forced response produces specular fields at the receiving point which correspond to the entire function in SEM expression (Equation (2.1)). This entire function is highly dependent on the polarization and aspect angle of the incident and reflected fields in addition to target parameters and geometry. Furthermore, this function has no standard form similar to $L(s,\theta_d,\phi_d)$ in Equation (2.1). The force fields have high frequency content that they are organized naturally according to the hierarchy of the reflected (surface reflections) and diffracted (edge diffractions) fields of the geometrical theory of diffraction. By its very nature, the early-time response conveys local information pertaining to the excited portions of the target.

As the incident field passes through a conducting target, for example, it induces currents on the target's conducting surface. The finite surface area of the target limits the current flow and causes it to flow back and forth on the body. When the excitation frequency coincides with the inverse of the period of oscillation of the induced currents, a strong resonance will occur. The contribution of these resonant modes could not be neglected in the early-time region because their fields have not

decayed significantly at early-times. Thus, these resonances create the natural resonance response component in addition to the forced response in early-time response [36]. Therefore, it is not possible to isolate forced and natural responses from each other perfectly in time domain as they overlap. This overlapping region is usually considered as a part of the early-time response. In early-time region, the surface reflected and diffracted field (due to the wavefront arrival) arrives first to the receiving point, followed by the creeping wave generated by the fields diffracted around the target. The SEM resonances have been attributed to these creeping waves, which, after one revolution, return in phase coherence with their initial values. This connection creates a complex hybrid approach, efficient at all early-times, in which specular returns and resonances both exist. However, the forced response of a target is dominant in the early-time where the resonances take over later on the late-time response [37]. The concept of the early-time and late-time responses of an incident wave on a conducting target is illustrated in Figure 2.2 [38].
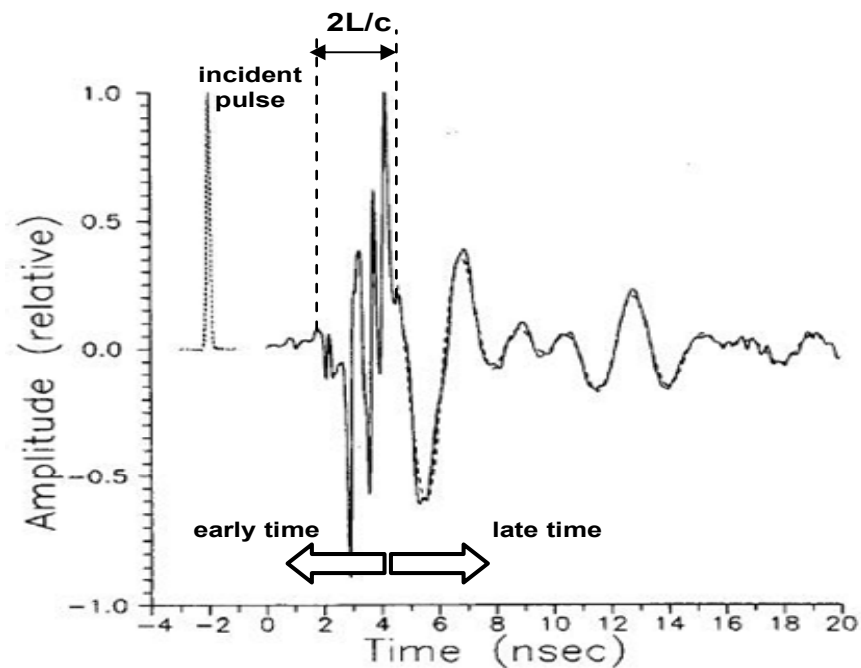
Figure 2.2   The concept of the early-time and late-time responses [38].

15

As indicated before, the early-time response has a very complex scattering mechanism due to having both forced and natural-resonance responses where the forced response highly depends on polarization and aspect angle of the incident and reflected fields. Therefore, the methods/techniques, which are based on the singularity expansion method, usually keep away from this early-time region. However, there exist some methods in the literature which also uses the early-time response information [24], [25], [38].

2.1.2. The Late-Time Response

The forced response, dominant at early-time, vanishes after a finite time duration when all specular fields reach the receiving point. The resonant signals (natural response), on the other hand, keep to exist in the response and they are exponentially attenuated as time progresses. The interval during which only the natural response (made of all natural resonances) exist is called the late-time period [39]. In this period, the time domain expression in Equation (2.2) reduces to a representation

$$h_{late}(t,\theta_d,\phi_d) = \sum_{n=1}^{\infty} b_n(\theta_d,\phi_d) e^{\alpha_n t} cos(w_n t + \delta_n), \quad t > t' \cong 2L/v \quad (2.3)$$

As mentioned earlier, the $s_n = \alpha_n + j\omega_n$ values characterize the target, in size, shape and material properties in a manner being independent of the nature of the incident wave and reflected wave (polarization, aspect angle, etc.). The oscillatory parts the target poles is more sensitive to size because of their dependence on path length. On the other hand, the attenuated part is more sensitive to shape because the radiation damping is influenced by curves, bends and edges [40].

The late-time resonance response, however, is weak as compared to the early-time values of the received signal beacuse the most dominant part of the overall response,

the forced response, does not exist in the late-time region. Besides, the resonances in the remaining natural response strongly attenuates with respect to their values at early-time while arriving late-time region. Even some of the target poles having relatively higher damping coefficients become negligibly small in amplitude and they may be easily suppressed in the presence of additive noise. The remaining poles, which have smaller damping coefficients, diminish slower and survive through the late-time region. These poles, which can be called as the dominant poles, are important for the natural-resonance based methods since they provide valuable signal information in the late-time region.

Although the values of complex natural resonance frequencies (target poles) depend only on target geometry and parameters, their residues (amplitudes in time domain) are strongly related with the aspect angle/polarization conditions of both incident and received fields which complicates the scattering mechanism even in the late-time region. Because the residue of a target pole is varying with respect to aspect angle/polarization conditions, a specific pole may be highly excited at one condition; while, it appears very weakly at another condition. Therefore, the aspect angle and polarization variance of pole residues is considered to be the major difficulty in target recognition based on natural-resonance mechanism [41]-[43].

2.2. Target Recognition Methods based on Late-Time SEM

2.2.1. Pole Extraction Methods

As mentioned in the previous section, target poles are independent from aspect and polarization conditions. Target poles could therefore give an initial rise to an aspect and polarization independent method of discriminating targets. After the SEM theory, the earlier target recognition methods have attempted to estimate the target pole values by using several methods/techniques since target poles constitute an

17

excellent feature set for target recognition purpose. One of the more popular pole extraction techniques is the Prony method.

Prony's method, which is also known as polynomial method, is a widely used method for modeling uniformly sampled data as a linear combination of complex exponential terms. This method attempts to fit a deterministic exponential model (target pole) to the sampled data that it requires N>2P data points to fit P exponentials containing in the exponents. In the Prony's method, the late-time scattered signal is modeled as [44]

$$x(t - t_0) = (\sum_{m=1}^{P} C_m e^{s_m(t-t_o)} + w(t - t_o))u(t - t_o) \qquad (2.4)$$

where P is the number of modes in the target response (system order), $w(t)$ is the noise signal, $s_m = \alpha_m + j\omega_m$ is m^{th} target pole and $c_m = b_m e^{j\theta_m}$ is the corresponding m^{th} complex residue. Unlike s_m, c_m is function of both target orientation and excitation source. It should be noted here that the poles and complex residues must be in complex conjugate pairs in order to ensure that $x(t)$ is real. $u(t)$ is a unit Heaviside function and t_o is assumed to be zero for convenience without any loss of generality. A discrete set of sampling points for this transient data of this signal can be written as

$$x(n) = \sum_{m=1}^{P} c_m e^{(s_m nT)} + w(n) = \sum_{m=1}^{P} c_m z_m^n + w(n), \quad 0 \le n \le N - 1 \qquad (2.5)$$

where T is the sampling period which should satisfy Nyquist sampling criteria to avoid higher mode aliasing and N>2P is the data length. The set of equations given in Equation (2.5) contains N nonlinear equations in 2P unknowns. Prony's method

can be applied to this set of equations to obtain an exact solution for N= 2P, or a least squares fit if more than 2P data points are used.

The complicated nonlinear curve fitting problem defined in Equation (2.5) was solved by Prony by realizing that $x(n)$ also satisfies the following forward difference and matrix equations:

$$x[k] = -\sum_{m=1}^{P} a_m x[k-m], \qquad P \leq k \leq N-1$$

$$\underbrace{\begin{bmatrix} x[P-1] & x[P-2] & \cdots & x[0] \\ x[P] & x[P-1] & \cdots & x[1] \\ \vdots & \vdots & \ddots & \vdots \\ x[N-2] & x[N-3] & \cdots & x[N-P-1] \end{bmatrix}}_{X} \underbrace{\begin{bmatrix} a_1 \\ a_2 \\ \vdots \\ a_P \end{bmatrix}}_{a} = -\underbrace{\begin{bmatrix} x[P] \\ x[P+1] \\ \vdots \\ x[N-1] \end{bmatrix}}_{x} \qquad (2.6)$$

The coefficients a_m in Equation (2.6) can be found by $a = -\left(X^{\#}x\right)$ where # is the pseudo inverse operation. By applying complex Z-transform to the above matrix equation, it can be shown that these coefficients are also the coefficients of the following Pth order polynomial:

$$\sum_{m=0}^{P} a_m z^{-m} = 0 \quad with \; a_o = 1 \qquad (2.7)$$

Then, the poles of the model are determined from the roots of the polynomial of Equation (2.7) as $s_m = \dfrac{\ln z_m}{T}, \quad m = 1,...,P$.

In the past, Prony's method has been a very popular technique for the extraction of target poles and used for target recognition purposes [14], [45]-[47]. Although this

technique is simple and efficient, it has serious drawbacks. Firstly, the method makes the assumption of using only the late-time portion of the signal. However, for many complicated targets, it is hard to isolate the late-time signal. Secondly, this method has been found to be overly sensitive to random noise and to the parameter P, which is the number of modes assumed to be present in the scattering response [48], [49]. Overestimating the number of poles generate both the correct poles and spurious poles. However, the actual number of significant target poles is usually unknown and is determined by the system bandwidth and target properties. In its basic form, Prony's method is inherently an ill-conditioned algorithm, but some improvements have made the scheme more robust [50]-[52]. However, in spite of these modifications, the accuracy of the Prony's method dramatically reduces as the SNR of the scattered data gets lower. This level appears to be in the 15 to 20 dB range for the individual signal components comprising the total signal. The signal-to-noise level for the total signal in some cases needs to be as good as 25 dB [48] which is assumed to be noise-free case in most applications. This fact causes Prony's method to be limited for use with clean data systems which are not always possible in practice.

Another popular pole extraction method is the Matrix Pencil method which is newer than the Prony's method. Similar to Prony's method, the mathematical derivation of the Matrix Pencil Method can be started from Equation (2.5) which models the late-time electromagnetic scattered response from a target. Different from Prony's method, the objective in this method is to find best estimates of P and s_m from the noisy data. Let's define the following set of information vector, $y(i)$ as

$$y(i) = [x(i)\ x(i+1)\ \cdots\ x(i+N-L-1)]^{T} \tag{2.8}$$

Based on this vector, two $(N-L) \times L$ matrices, Y_1 and Y_2, can be defined as follows:

$$Y_1 = \begin{bmatrix} y(0) & \cdots & y(L-1) \end{bmatrix} = \begin{bmatrix} x(0) & x(1) & \cdots & x(L-1) \\ x(1) & x(2) & \cdots & x(L) \\ \vdots & \vdots & \ddots & \vdots \\ x(N-L-1) & x(N-L) & \cdots & x(N-2) \end{bmatrix}_{(N-L) \times L}$$

$$Y_2 = \begin{bmatrix} y(1) & \cdots & y(L) \end{bmatrix} = \begin{bmatrix} x(1) & x(2) & \cdots & x(L) \\ x(2) & x(3) & \cdots & x(L+1) \\ \vdots & \vdots & \ddots & \vdots \\ x(N-L) & x(N-L+1) & \cdots & x(N-1) \end{bmatrix}_{(N-L) \times L}$$

(2.9)

where L is referred to as the pencil parameter [74]. This pencil parameter is very useful in eliminating some effects of noise in the data. For efficient noise filtering, the parameter L is chosen to be between N/3 to N/2 [53], [54]. For these values of L, the variance in the parameters z_m, due to noise, has found to be minimum. Based on the decomposition of Y_1 and Y_2, it can be shown that if $P \le L \le N - P$, the poles z_m with corresponding generalized eigenvectors p_m are the generalized eigenvalues of the Matrix Pencil $Y_2 - zY_1$. This means that if $P \le L \le N - P$, $z = z_m$ is a rank reducing number of $Y_2 - zY_1$. The matrix Y_1 can be approximated with best rank-P approximation by using the singular value decomposition (SVD) as follows:

$$Y_1 \cong \sum_{m=1}^{P} \sigma_m u_m v_m^H = UDV^H \tag{2.10}$$

where $U = [u_1, u_2, \cdots, u_P]$, $V = [v_1, v_2, \cdots, v_P]$, $D = diag[\sigma_1, \sigma_2, \cdots, \sigma_P]$. u_i and v_i are the left and right singular vectors for a singular value of σ_i, respectively. For noisy data $x(t)$, $\sigma_1 > \sigma_2 > \cdots > \sigma_P$ should be chosen to be the P largest values of Y_1 (i.e. $\sigma_P >> \sigma_{P+1}$). The choice of the number of poles, P, can be estimated from the singular values by looking at the raito of the various singular values to the largest one. By using Equation (2.10), it can be shown that

$$\left(D^{-1}U^H Y_2 V - z_m I\right)V^H p_m = (Z - z_m I)e_m = 0 \qquad (2.11)$$

Here, the steps of the derivation of this equation are omitted for simplicity. Note that the matrix Z is a $P \times P$ matrix, z_m and e_m are the eigenvalues and eigenvectors of Z respectively. Then, the values of the target poles, s_m, can be extracted from the eigenvalues of Z as $s_m = \dfrac{ln\, z_m}{T}$, $m = 1,...,P$.

When two methods (Prony and Matrix Pencil methods) are compared, it can be said that the Matrix Pencil Method has superiorities to Prony's method for pole extraction. First of all, it can be shown that the Matrix Pencil Method is more computationally efficient than the Prony's method [55], [56]. Besides, by using the dominant eigenvalues to estimate the modal number, the spurious poles due to noise can be distinguished from the target poles. Hence, the Matrix Pencil method estimates the number of target poles and reduces the number of spurious poles. The Matrix Pencil method is not only computationally more efficient and more successful in pole number estimation, but it has also better statistical properties as compared to the Prony's method. Under additive noise, the statistical variance of the poles for the Matrix Pencil method is less than those for the Prony's method [57]. Thus, it can be concluded that the Matrix Pencil method gives better results as compared to the Prony's method for noise corrupted data. The usage of Matrix pencil method has been considered in several studies for target pole estimation based on the SEM [15], [56], [58], [59]. However, in spite of having a few dB better noise performance than Prony's method, the method has still poor noise performance that only up to 20 dB of signal-to-noise ratio can be handled adequately by this technique and the performance of the pencil matrix method deteriorates below this ratio as stated in [56]. Besides, the difficulty of separating late-time region in Prony's method is still valid for the pencil method. The target recognition methods using Matrix pencil are

only demonstrated for simple targets such as thin wires and need to be validated for complex targets.

A variety of other techniques for target pole extraction have been also introduced including several nonlinear and combined linear-nonlinear approaches which require heavy computations [16], [60]-[62]. Additionally, the benefits of using multiple data sets are mentioned in some papers[63], [64], while Baum has stressed the importance of incorporating a priori information about the target [65]. Besides, alternative pole estimation techniques are suggested by Turhan-Sayan et al. in [66] and by Rothwell et al. in [67] requiring the synthesis of K-pulse and E-pulse signals, as to be explained in the following section. Not only in Prony's and Matrix pencil methods but also in the other pole extraction techniques, the main problem is the requirement of relatively low noise scattered data (around 15 dB of SNR value) for successful results. This dissertation research will propose an indirect pole estimation scheme as a side product of the suggested target classifier design technique, which is much more robust to noise than the previous pole estimation techniques discussed in literature so far.

2.2.2. K-pulse, E-pulse and S-pulse

Following the direct pole extraction techniques, the target recognition methods using the time-domain response of a target to design a specially synthesized incident waveform have generated considerable interest. Three well-known methods of this group are kill-pulse (K-pulse), extinction-pulse (E-pulse) and single-pulse (S-pulse) methods which are based on the same design principles. The oldest of these three methods is the "kill-pulse" technique which is first described by Kennaugh [68]. The common basic idea in this approach is to synthesize a discriminative excitation waveform in such a way that the transient scattered field response is minimized (ideally reduced tozero) at all aspects and polarizations in the late-time region. In a

formal definition, there exists a pulse $p(t)$ of minimal duration to match the scattered field in the following way:

$$c(t) = p(t) * h(t) = \int_0^{T_e} p(t')h(t-t')dt' = 0, \quad t \geq T_c \cong \frac{2L}{c} + T_e \qquad (2.12)$$

where $h(t)$ is the impulse response of the target as in Equation (2.2), T_e is the duration of the pulse $p(t)$ and T_c is the starting time of the late-time region of $c(t)$. Since the resulting convolution signal has finite duration theoretically, the pulse $p(t)$ should also be a time-limited signal. As considered in Laplace domain, this is achieved by annihilating the natural resonances of the target response by the zeros in the Laplace spectrum of the K-pulse signal. In other words, K-pulse can be defined as the inverse Laplace transform of the denominator of the transfer function (response) of the target. The K-pulse spectrum has only those zeros which coincide with the CNR's of the target but no additional zeros. The K-pulse is not unique in form unless its transform domain zeros coincides with all the target poles in one-to-one manner. This is to rule out the possibility that a linear combination of derivatives of the K-pulse as another possible K-pulse, as the differentiation process adds zeros which are not poles of targets. In K-pulse approach, the energy content outside the duration of the K-pulse response is minimized with respect to a set of unknowns. The assumed model of the K-pulse may be represented in terms of a set of N+1 equally-spaced continuous-time delta functions with unknown weights, a_n, as described in Equation (2.13).

$$p(t) = \delta(t) + \sum_{n=1}^{N} a_n \delta(t - n\tau) \qquad (2.13)$$

where $\tau = T_e / N$. Let's define the cost function, J, to be the energy outside the K-pulse response duration [69]:

$$J = \int\limits_{T_c}^{T_\infty} \left[p(t) * h(t) \right]^2 dt \qquad (2.14)$$

where T_∞ is the cutoff time representing an arbitrarily long duration. Impulsive functions, which are fairly general, are chosen as basis functions for $p(t)$ to simplify the evaluation of the convolution integral. Alternatively, the pulse $p(t)$ can be represented in terms of a set of time-limited, continuous basis functions such as Legendre polynomials [70]. The cost function in Equation (2.14) can be expressed in a quadratic form as

$$J = A^T \Phi A + 2 A^T S + \beta \qquad (2.15)$$

where

$$A = \begin{bmatrix} a_1 & a_2 & \cdots & a_N \end{bmatrix}^T, \ H = \begin{bmatrix} h(t-\tau) & h(t-2\tau) & \cdots & h(t-N\tau) \end{bmatrix}^T \quad (2.16)$$

$$\Phi = \int\limits_{T_c}^{T_\infty} H H^T dt, \ \ S = \int\limits_{T_c}^{T_\infty} h(t) H^T dt, \ \ \beta = \int\limits_{T_c}^{T_\infty} h^2(t) dt \qquad (2.17)$$

To find the extremum of a cost function, the gradient with respect to each a_n coefficient is equated to zero as given in Equation (2.18)

$$\nabla_a J = 2\Phi A + 2S = 0 \qquad (2.18)$$

25

Thus, the A vector can be evaluated via $A = -\Phi^{-1}S$. However, in most problems, $A = -\Phi^{-1}S$ cannot be used directly since Φ is ill-conditioned or singular. Therefore, the optimization schemes such as the steepest descent algorithm can be used to search for the minimum point of the cost function with respect to the unknowns. In Figure 2.3, the impulse response and the response to the K-pulse is given for a circular loop at $\theta = 0$ degree and ϕ polarization for noiseless case [69]. For this target, the K-pulse is obtained st a different aspect angle/polarization condition at $\theta = 45$ degree and θ polarization. It can be concluded from the figure that the K-pulse response has very little energy after $t = 2.4\pi r / c$.
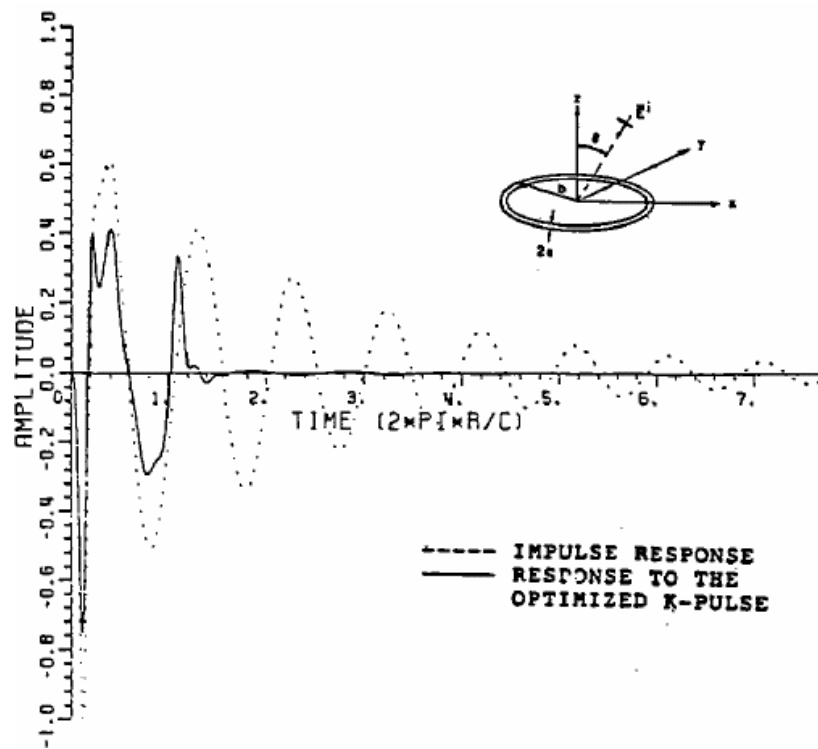
Figure 2.3   The impulse response and response to the K-pulse for the circular loop at $\theta = 0$ degree and ϕ polarization for noiseless case [69].

26

Another approach similar to the K-pulse method is the extinction-pulse (E-pulse) method which is almost the same as the K-pulse method under certain conditions [71]. An E-pulse is viewed as a transient, finite duration waveform which annihilates the contribution of only a selected number of natural resonances of a target as being different from the ideal K-pulse definition. In other words, an E-pulse eliminates the desired natural modal content of the late-time scattered field regardless of the orientation of the target with respect to transmitting and receiving antennas. Being another difference, a physical interpretation of the E-pulse can be facilitated by decomposing the waveform as

$$e(t) = e^f(t) + e^e(t) \qquad (2.19)$$

where $e^f(t)$ is a forcing component, nonvanishing during $0 \leq t < T_f$, and $e^e(t)$ is an extinction component during $T_f \leq t < T_e$ which extinguishes the response due to $e^f(t)$. Note that $e^f(t)$ is only a unit delta function in K-pulse. In Equation (2.19), while the forcing component is chosen freely, the extinction component is expanded in a set of basis functions

$$e^e(t) = \sum_{m=1}^{2N} a_m f_m(t) \qquad (2.20)$$

A variety of basis functions, $f_m(t)$, have been used in Equation (2.20) including delta functions, Fourier cosines, damped sinusoids, polynomials and subsectional basis functions [19], [72], [73]. It is important to mention that since the forcing component of E-pulse can be arbitrarily chosen, the duration of E-pulse and the E-pulse itself is not unique, which is the basic difference with K-pulse.

27

Let $h_k(t)$ represent the impulse scattered field response of a target to an interrogating waveform at aspect angle k. The convolution of the target's E-pulse with the impulse response is zero at all aspects in the late-time interval. Writing the convolution in time domain and using Equation (2.12), (2.19) and (2.20) gives

$$\sum_{m=1}^{2N} \alpha_m \int_0^{T_e} f_m(t')h_k(t_\ell - t')dt' = -\int_0^{T_e} e^f(t')h_k(t_\ell - t')dt'$$

$$k = 1,2,\ldots,K, \quad \ell = 1,2,\ldots,L \quad t_\ell > T_{Lk} + T_e \tag{2.21}$$

where T_{Lk} is the beginning of late-time region for the kth scattered response, K is the number of different aspect angles, L is the number of discrete times and N is the number of modes expected to be annihilated. The matrix form of Equation (2.21) is

$$\begin{bmatrix} f_{1,1}(t_1) & f_{1,2}(t_1) & \cdots & f_{1,2N}(t_1) \\ f_{2,1}(t_1) & \cdots & \cdots & f_{2,2N}(t_1) \\ \vdots & \cdots & \ddots & \vdots \\ f_{K,1}(t_1) & \cdots & \cdots & f_{K,2N}(t_1) \\ f_{1,1}(t_2) & f_{1,2}(t_2) & \cdots & f_{1,2N}(t_2) \\ \vdots & \cdots & \ddots & \vdots \\ f_{K,1}(t_\ell) & f_{K,2}(t_\ell) & \cdots & f_{K,2N}(t_\ell) \end{bmatrix} \begin{bmatrix} a_1 \\ a_2 \\ \vdots \\ a_{2N} \end{bmatrix} = - \begin{bmatrix} e_1^f(t_1) \\ e_2^f(t_1) \\ \vdots \\ e_K^f(t_1) \\ e_1^f(t_2) \\ \vdots \\ e_K^f(t_\ell) \end{bmatrix}, \tag{2.22}$$

where

$$f_{k,m}(t_\ell) = \int_0^{T_e} f_m(t')h_k(t_\ell - t')dt', \quad e_k^f(t_\ell) = \int_0^{T_e} e^f(t')h_k(t_\ell - t')dt' \tag{2.23}$$

Here, incorporating multiple aspect data is important as the modal amplitudes, a_m, are highly aspect dependent that some modes may not be excited at certain aspects.

Generally the product *KL* is chosen to be at least 2N, so that the matrix equation is not underdetermined, and a solution is obtained using least squares and singular value decomposition. The matrix equation (2.22) has a solution of the modal amplitudes for any choice of E-pulse duration. However, for some choice of T_e the determinant of the matrix vanishes, which correspond to discrete eigenvalues for the E-pulse duration T_e, and Equation (2.21) has a solution only if $e^f(t) = 0$. Since there is no excitatory component, this type of E-pulse is viewed as extinguishing its own excited field and is called a natural E-pulse. On the other hand, all other E-pulses, which have a nonzero excitatory component, are termed as forced E-pulse. The minimum natural E-pulse duration is determined as [74]

$$T_e = 2N \frac{\pi}{\omega_{max}}$$

(2.24)

where ω_{max} is the largest radian frequency among the target modes, if a priori knowledge of the target poles is available; otherwise, it is the largest radian frequency within operating frequency band. Figure 2.4 shows the impulse responses, E-pulse and the responses to E-pulse of a thin cylinder at θ = 30 and 60 degree, generated by using the first ten resonance frequencies [74].
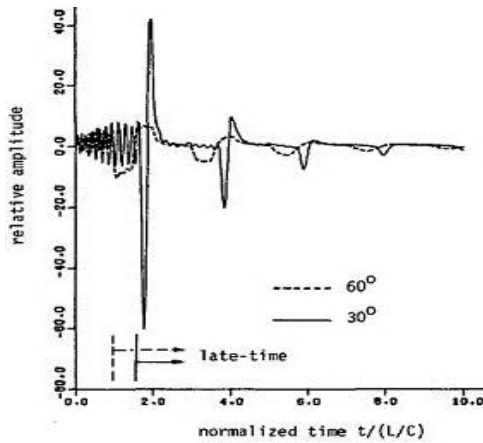
Figure 2.4(a)   Figure 2.4(b)

29
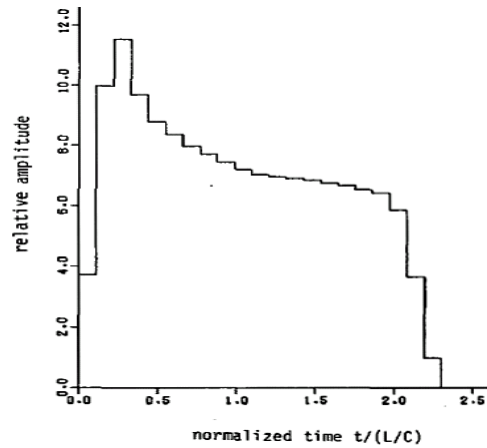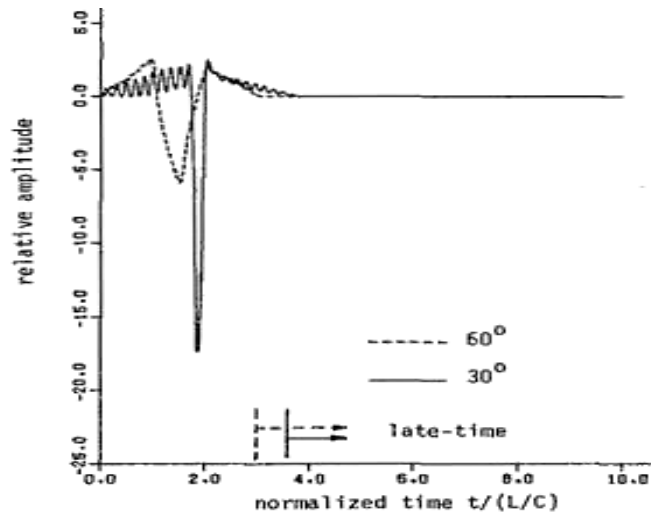
(c)

Figure 2.4   The responses and E-pulse of a thin cylinder for $\theta = 30$ and 60 degree generated using the first ten resonance frequencies [74]   (a) the impulse responses (b) E-pulse (same for both) (c) the responses to E-pulse.

In this specific noise-free case, 21 subsectional rectangular pulses, one of which constitutes the forced component, are used as basis functions in order to construct E-pulse and eliminate ten natural resonances. From the results in Figure 2.4(c), this E-pulse is quite successful in both aspect angles for noise-free case.

The other type of discriminative pulse is the single-pulse (S-pulse) which is strictly based on known natural frequencies [75]. Different from K and E pulses, the S-pulse's scheme consists of synthesizing the waveform of an incident signal which excites the target in such a way that the return signal from the target contains only a single natural resonance mode of the target in the late-time region. Equivalently, the S-pulse waveform for the ith mode of a particular target is defined as

30

$$s(t) * h(t) = \int_0^{T_e} s(t')h(t-t')dt' = b_i e^{\alpha_i t} \begin{Bmatrix} sin(\omega_i t + \theta_i) \\ cos(\omega_i t + \theta_i) \end{Bmatrix}, \quad t \geq T_c \cong \frac{2L}{c} + T_e \quad (2.25)$$

As seen from Equation (2.25) this pulse depends on the information of target pole values that at least, the value of the pole, which is desired to exist in the scattered field in the late-time region, should be known. By substituting Equation (2.3) into (2.25), it can be obtained

$$\sum_{n=1}^{N} b_n e^{\alpha_n t} [A_n \cos(\omega_n t + \theta_i) + B_n \sin(\omega_n t + \theta_i)] = b_i e^{\alpha_i t} \begin{Bmatrix} sin(\omega_i t + \theta_i) \\ cos(\omega_i t + \theta_i) \end{Bmatrix},$$

$$(2.26)$$

$$A_n = \int_0^{T_e} s(t')e^{-\alpha_n t'} \cos(\omega_n t')dt', \quad B_n = \int_0^{T_e} s(t')e^{-\alpha_n t'} \sin(\omega_n t')dt'$$

It should be noticed that A_n and B_n are numerically stable because they are finite integrals over a short period of time, even though there is a time growing factor of $e^{-\alpha_n t}$ in them. Hence, for instance, if a single pulse is synthesized in such way that $A_1 = 1$ and all other A_n and B_n vanish, then the output signal will be a cosine, a natural mode. By representing the single pulse with a set of basis functions as in Equation (2.20) and combining this with A_n and B_n in Equation (2.26), the matrix equation form for the S-pulse is obtained as

31

$$[M_{n,m}][a_m] = \begin{bmatrix} A_n \\ B_n \end{bmatrix} \Rightarrow \begin{bmatrix} M^c_{1,1} & M^c_{1,2} & \cdots & M^c_{1,2N} \\ \vdots & \cdots & \ddots & \vdots \\ M^c_{N,1} & M^c_{N,2} & \cdots & M^c_{N,2N} \\ M^s_{1,1} & \cdots & \cdots & M^s_{1,2N} \\ \vdots & \cdots & \ddots & \vdots \\ M^s_{N,1} & \cdots & \cdots & M^s_{N,2N} \end{bmatrix} \begin{bmatrix} a_1 \\ a_2 \\ \vdots \\ a_{2N} \end{bmatrix} = \begin{bmatrix} A_1 \\ \vdots \\ A_N \\ B_1 \\ \vdots \\ B_N \end{bmatrix} \quad (2.27)$$

$$where \quad M^{\{c\}}_{n,m}{}^{\{s\}} = \int_0^{T_e} f_m(t')e^{-\alpha_n t'} \begin{Bmatrix} cos(\omega_n t') \\ sin(\omega_n t') \end{Bmatrix} dt',$$

The coefficients a_m for constructing single pulse can be obtained from

$[a_m] = [M_{n,m}]^{-1} \begin{bmatrix} A_n \\ B_n \end{bmatrix}$. To synthesize $s(t)$ for the ith mode extraction, it is assigned

that $A_i = 1$ or $B_i = 1$ and all other A's and B's are set to zero. Using this approach,

an appropriate value for the single pulse duration T_e can be selected. As in the

E-pulse case, the signal duration T_e of S-pulse is not unique so does the pulse itself;

however, there exists an optimum value for which the single pulse possesses a

maximal sensitivity in discriminating the target [76]. In order to find this optimum

T_e, Equation (2.27) can be modified as

$$[A_1 \quad \cdots \quad A_{i-1} \quad A_{i+1} \quad \cdots \quad A_N \quad B_1 \quad \cdots \quad B_N]^T = [M_{n,m}]^{trunc}[a_m] \quad (2.28)$$

where $[M_{n,m}]^{trunc}$ is the truncated original $[M_{n,m}]$ matrix with its ith row and last

column removed. When all A_n and B_n are forced to be zero, the solution exists

when $det[M_{n,m}]^{trunc} = 0$. Then, Equation (2.28) can be solved numerically to

determine the optimum T_e value for the extraction of ith mode cosine signal.

These special discriminative pulses, especially K-pulse and E-pulse, were primarily constructed for target discrimination. However, they can be also used for pole estimation by computing the zeros of pulse spectrum in the literature [68], [69], [74]. The noise performance of these methods, on the other hand, is not so good as they can give successful target discrimination and pole value estimation up to SNR= 10 dB. As a remedy, the normalized instantaneous energy function of target response is defined in [77] in the context of K-pulse design and target discrimination, as

$$E_r^i(t) = \frac{\int_0^t \left| c^i(t) \right|^2 dt}{\int_0^{t_{max}} \left| c^i(t) \right|^2 dt},$$

$$with \quad c^i(t) = p(t) * h^i(t)$$

(2.29)

where $p(t)$ is the K-pulse of a specific target and t_{max} is a sufficiently late-time instant replacing infinity for practical purposes. The normalized energy curve of the target's matched K-pulse response should reach high energy levels earlier than those of the target's mismatched K-pulse responses. The discrimination parameter for E-pulse, E-pulse discrimination ratio (EDR), can be defined as [78]

$$EDR(dB) = 10 \log_{10} \left\{ \frac{EDN}{min(EDN)} \right\}$$

$$where \quad EDN = \left[\int_{T_c}^{t_{max}} c^2(t)dt \right] \left[\int_0^{T_e} (e^e(t))^2 dt \right]^{-1}$$

(2.30)

Therefore, the E-pulse yielding the smallest EDN has an EDR of 0 dB, while the EDR produced by the other E pulses is greater.

With the use of discrimination parameters defined in Equations (2.29) and (2.30), the K-pulse and E-pulse methods became more resistant to the additive noise for target recognition than the direct pole estimation methods. However, these methods contain crucial drawbacks and problems. First, these feature pulses are either synthesized from the known/extracted poles of the target where a good estimate for the number of target poles is needed, or they are optimized (without using target pole information) via conventional or global optimization techniques. Optimization itself is a tricky signal processing approach; results may not be repeatable especially when there are many local optimal solutions. Reaching the globally optimal solution may not be possible in complicated problems involving complex target geometries or non-conducting material compositions. Besides, all of these approaches require either noise-free synthesized data or very low noise measurement data recorded in specially controlled environments for classifier design purpose which may not be always possible. Additionally, in the K-pulse, a successful estimation for K-pulse duration is needed while it is not always easy to make a good guess of this duration, especially for complicated target geometries. This problem is also valid in the E-pulse and S-pulse methods for the choice of T_c. Even if the target dimensions are known, the forced response time may vary with respect to aspect angle which makes the estimation of T_c more difficult. Furthermore, estimation of T_c for dielectric or composite targets is much more difficult and needs the solution of a very complicated global optimization problem.

Modified and/or improved versions of all K-pulse, E-pulse and S-pulse methods have been published in late 90's and in 2000 and thereafter. The K-pulse estimation problem is solved by a genetic algorithm-based approach in 1998 by Turhan-Sayan et al. [79] to be used in complicated cases where the K-pulse duration can not be estimated beforehand. Later, this technique is applied to dielectric targets for the first time in [66]. An improved automated S-pulse scheme is analyzed by Gallego et al. [80] to show the superiority of using quadratic subsectional polynomials as basis functions in noise performance to classical rectangular S-pulses in [78]. According to

this study, although the scheme gives successful results even for SNR= 0 dB, the method is tested only for high-Q conducting thin wires at a fixed aspect angle and polarization and needs to be repeated for more complex targets and different aspect angle/polarization conditions. The performance of an automated E-pulse target identification scheme in white Gaussian noise is analytically evaluated by Mooney et al. in [81] to determine the probability of identification as a function of SNR. These probabilities are reported being less than 80 percent for small 4-target libraries when SNR values get lower than 30 dB. In this study, conducting wire model targets are used and simulation results are demonstrated at four different aspect angles. In 2004, an asymptotically unbiased E-pulse scheme is suggested by Blanco et al. in [82] to improve the noise performance of the conventional E-pulse technique. Up to 45 percent improvement in accuracy is demonstrated at low SNR levels when this method is applied to three conducting thin straight wires of different lengths. Although these results are promising, the method has been tested in a very simple case and at a single aspect angle of 60 degrees only. The usefulness of the method needs to be demonstrated in more complicated simulation problems involving low-Q targets, dielectric objects, targets with complex shapes, etc., together with the aspect/polarization invariance tests. Another modification to the E-pulse method is suggested in 2006 by the same group of researchers, Blanco et al., [83] where β-splines are used as the basis functions in E-pulse construction together with new E-pulse conditions. Better noise performance is demonstrated in this paper as compared to the classic E-pulse discrimination scheme but the proposed method is demonstrated for the same very simple target scenario used in [82] without any analysis for aspect/polarization invariance. Finally, in 2006, the feasibility of "banded" E-pulse technique is demonstrated by Lui and Shuley [84] using aircraft targets modeled by thin wires. Although an improvement in the discrimination performance with respect to the classic E-pulse scheme is demonstrated, the technique needs to be tested for low-Q and dielectric targets. Furthermore, the performance of the method is demonstrated at a single aspect angle and a fixed polarization only for the ideal noise free conditions. The important performance tests

showing the invariance of the target identification technique with respect to aspect angle (in both azimuth and elevation) and polarization as well as those showing robustness with respect to noise are not provided.

2.2.3. Other methods

In addition to the pole estimation methods and feature pulse techniques discussed so far, there are several other resonance region techniques suggested for target recognition, which are worth mentioning briefly in this section. Use of generalized likelihood ratio test (GLRT) in late-time target discrimination is suggested in [85] by Mooney et al. and the performance analysis of this method is given in [21]. The performance of the method is demonstrated for four wire targets with sufficiently complex geometries at four different azimuth aspect angles, for the SNR ranging from 20 to -20 dB. Although the performance tests for different elevation angles and different polarizations are not conducted, and the classifier shows a poor performance below 10 dB SNR, the authors present an interesting theoretical performance analysis and compare their analytical findings with the results of numerical demonstrations.

Another interesting target recognition work was published in 2000 by Kim et al. [86] where target's scattered responses at multi-aspect angles are processed both in the early and late-time regions using the adaptive Gaussian representation (in joint time-frequency domain), the principal component analysis (PCA) tool and a neural network technique, successively. The performance of the technique is demonstrated for five small-scale aircraft targets modeled by conducting thin wires, which are the same targets with the targets to be used in the classifier design example in Section 4.3. Despite the presence of too much complexity in the design process and extreme aspect-redundancy in the use of design data, aspect invariance (at least with respect to azimuth angle) and of noise performance are demonstrated. The target recognition method proposed in this thesis, however, is proven to show definitely

higher accuracy and better noise performance by using only 5 reference aspect angles for classifier design instead of 46 reference aspect angles under the same design conditions as discussed in detail in Section 4.3. In another recent paper published in 2006 by J. H. Lee and H. T. Kim [87], a closed-form expression for the normalized estimation error is presented for a late-time target recognition scheme which is based on the a priori knowledge of target pole values. The performance simulations are conducted for a very simple target set consisting of five conducting straight thin wires of different lengths, without any performance tests for aspect and polarization invariance. The noise analysis is given only for relatively high SNR values between 10 dB and 25 dB. Although, the paper presents an interesting analysis for the estimation error, the usefulness of the proposed study needs to be proven for challenging targets at arbitrary aspect and polarization conditions and at low SNR levels.

A considerable amount of target recognition applications are based on neural network (NN) techniques as seen in literature [20], [79], [88]-[90]. However, NN based feature extraction techniques have two main disadvantages. First of all, NN training needs a large set of scattering data at many different aspects for each target in the database. A large database for each target is not desirable; because generally it is neither feasible nor practical to use such kind of huge database especially in the real world applications. Furthermore, addition of a new target or even a new reference angle to a neural network type classifier requires the training of the whole classifier overall again with this new reference database which complicates the classifier design.

Finally, another late-time target classification technique is reported in [23] and [91] by Turhan-Sayan, which introduces a novel feature extraction technique using the Wigner distribution and the principal component analysis (PCA) based multi-aspect fusion. In this method, there exist late-time partitioned energy density vectors

constructed by computing the spectral distribution of scattered signal energy of some non-overlapping subsequent time bands which can be defined as

$$\overline{E}_q(f_m) = \begin{bmatrix} E_q(f_1) & E_q(f_2) & \dots & E_q(f_{N/2}) \end{bmatrix}, \quad q = 1,\dots,Q \qquad (2.31)$$

$$E_q(f_m) = \int_{(q-1)\frac{T_o}{Q}}^{q\frac{T_o}{Q}} W_x(t,f_m)dt, \quad m = 1,\dots,\frac{N}{2}, \quad f_m = \frac{m-1}{2T_o} \qquad (2.32)$$

where $W_x(t,f_m)$ is Wigner-Ville distribution of the scattered signal $x(t)$ as [92]

$$W_x(t,f) = \int_\tau x(t+\frac{\tau}{2})x^*(t-\frac{\tau}{2})e^{-j2\pi f\tau}d\tau \qquad (2.33)$$

The vectors corresponding to predetermined reference aspect angles for each target are obtained and a suitable late-time interval (optimum q value) is found by using these vectors after a detailed investigation [91]. Afterwards, late-time feature vectors (LTFVs) for each target are constructed and then combined to form one feature vector for each target, fused feature vector (FFV), by using PCA, which decreases aspect dependency and redundancy. In the last step, the decision is done by comparing FFV of candidate target in database and LTFV of test target.

The performance of this technique is demonstrated for four dielectric spheres of equal size but of different permittivities giving 100 percent accuracy rate at 20 dB SNR level, which drops to 90 percent at 10 dB SNR and to 75 percent at 5 dB SNR. The detailed aspect variance and noise analyses are provided in [91]. The method is also tested for dielectric coated conducting spheres resulting in similar noise performance results [93] and it gives successful accuracy rates for small-scale

aircraft targets modeled by thin, conducting wires for noise-free case [94]. However, the technique still needs a comprehensive noise analysis for low-Q and complex targets.

In the following chapter, a novel resonance region method proposed in this thesis will be introduced and explained by indicating the advantages with respect to the other resonance methods mentioned throughout Section 2.2.

CHAPTER 3

A NOVEL TARGET RECOGNITION METHOD WITH NATURAL-RESONANCE MECHANISM AND MUSIC ALGORITHM

As mentioned in Section 1.3, the electromagnetic target recognition method developed in this thesis is based on the utilization of natural resonance mechanism in the sufficiently late-time interval of the target's scattered response. While this method inspired by the singularity expansion method (SEM), the MUSIC (MUltiple SIgnal Classification) algorithm is employed as the main signal processing tool to extract natural resonance related target features which are not very sensitive to noise. The MUSIC algorithm is a well-known technique to extract the parameters of undamped/damped sinusoidal signal components of a composite signal such as the late-time scattered signal modeled in Equation (2.2) in the presence of Gaussian noise [95], [96]. This algorithm is widely used in biomedical, telecommunication, signal processing and electromagnetic areas especially for direction-of-arrival, multiple frequency, spectrum and signal parameter estimation applications due to its high resolution [97]-[99]. The MUSIC algorithm is quite successful in rather simple applications which contain at most a few sinusoidal signal components. However, the late-time scattered signal of a target may be composed of a large number of damped sinusoidal components due to target poles. Besides, as it happens with all the other pole estimation techniques mentioned in Section 2.2.1, the accuracy of pole extraction via the MUSIC algorithm also deteriorates by decreasing signal-to-noise

ratio (SNR) of the scattered signals. As an example, the true pole values and their estimation of the first four pole pairs of a perfectly conducting sphere with radii 1.8 cm are given in Table 3.1 for both noise free and SNR= 10 dB cases. In this table, the complex frequency values are normalized as $\bar{s} = (\alpha + j\omega)r/c$ with r being the sphere radius in meters and c is the speed of light while $s = (\alpha + j\omega)$ is being the unnormalized complex frequency. In addition, Table 3.2 shows the percentage error of real and imaginary parts of the estimated pole values with respect to true values for both noiseless and SNR= 10 dB cases.

Table 3.1   The true pole values and the estimated normalized pole values with MUSIC algorithm for perfectly conducting spheres of radii 1.8 cm for both noise free and SNR= 10 dB cases (in $\bar{s} = (\alpha + j\omega)r/c$ scale).

True pole values	Estimated pole values for conducting sphere of radius 1.8 cm using the MUSIC spectrum	
	Noise free case	SNR= 10 dB case
$-0.500 \pm j\, 0.866$	$-0.504 \pm j\, 0.867$	$-0.504 \pm j\, 0.848$
$-0.702 \pm j\, 1.807$	$-0.708 \pm j\, 1.827$	$-0.720 \pm j\, 1.884$
$-0.843 \pm j\, 2.758$	$-0.853 \pm j\, 2.762$	$-0.752 \pm j\, 2.698$
$-0.953 \pm j\, 3.718$	$-0.938 \pm j\, 3.742$	$-0.480 \pm j\, 3.624$

Table 3.2   The percentage error for the estimated pole values with MUSIC algorithm for perfectly conducting spheres of radii 1.8 cm for both noise free and SNR= 10 dB cases.

True pole values	(%) error for the estimated pole values for conducting sphere of radius 1.8 cm			
	Noise free case		SNR= 10 dB case	
	Real	Imaginary	Real	Imaginary
-0.500 ± j 0.866	0.8	0.11	0.8	2
-0.702 ± j 1.807	0.85	1	2.5	3.1
-0.843 ± j 2.758	1.2	0.14	10.8	2.17
-0.953 ± j 3.718	1.5	0.64	49	2.5

As to be reported in Table 3.2, the accuracy of extracted poles decreases, by a maximum of 3 percent error in imaginary parts and by almost 50 percent error in real parts at 10 dB SNR level, for instance. Therefore, the estimation and utilization of target poles in target feature extraction via MUSIC algorithm are strictly avoided in this method because of the susceptibility of pole extraction procedure to noise, as discussed above. Instead, the MUSIC algorithm is used to construct MUSIC Spectrum Matrices of the scattered signals as described in the next section.

3.1. The Definition of MUSIC Spectrum Matrix (MSM)

The MUSIC algorithm, which is the fundamental signal-processing tool used for the extraction of MUSIC Spectrum Matrices (MSMs), is a parametric method for line

spectra estimation manipulating the fact that the associated sinusoidal signal components and the Gaussian noise are uncorrelated. Let's assume that

$$z(n) = x(n) + w(n) = \sum_{i=1}^{L/2} b_i(\phi,\theta) e^{\alpha_i n} \cos(\omega_i n + \delta_i) + w(n)$$

$$= \sum_{i=1}^{L} c_i e^{s_i n} + w(n), \quad n = 1,\dots,N \qquad (3.1)$$

represents a late-time interval of the scattered signal of a given target recorded at a certain aspect angle/polarization condition and sampled at a total of N discrete time points in the presence of additive Gaussian noise $w(n)$. The noise-free (ideal) signal component $x(n)$ is expressed in Equation (3.1) in terms of the linear combination of L complex exponentials having the target poles s_i in the exponents. The c_i's are the related complex valued weight coefficients, which can be expressed as $c_i = b_i(\phi,\theta) e^{j\delta_i}$ in general. For an integer m that satisfies the condition of $L < m < N$, we can form the vector $\overline{y(n)}$ of length m as

$$\overline{y(n)} = \overline{x(n)} + \overline{w(n)} = \left[z(n) \quad z(n-1) \quad \dots \quad z(n-m+1)\right]^T \qquad (3.2)$$

By using basic assumption that the signal and noise components are uncorrelated, the correlation matrix IR can be expressed as

$$IR = E\left\{ \overline{y(n)}\,\overline{y(n)}^H \right\} = E\left\{ \overline{x(n)}\,\overline{x(n)}^H \right\} + E\left\{ \overline{w(n)}\,\overline{w(n)}^H \right\}$$

$$= AE\left\{cc^H\right\}A^H + \sigma^2 I_{MxM} = ACA^H + \sigma^2 I_{MxM} \qquad (3.3)$$

where E is the expected value operator, the superscript H denotes the complex conjugate transpose, σ^2 is the variance of Gaussian noise, I is the unit matrix. In

this expression, the matrix A, which is defined in Equation (3.4) is a Vandermonde matrix whose dimensions and rank are $m \times L$ and L respectively and the matrix C, which is defined in Equation (3.5), is an $L \times L$ matrix with rank L.

$$A = \begin{bmatrix} a(s_1) & a(s_2) & \dots & a(s_L) \end{bmatrix} \quad \text{with} \quad a(s) = \frac{\begin{bmatrix} 1 & e^{-s} & \dots & e^{-s(m-1)} \end{bmatrix}^T}{norm\begin{bmatrix} 1 & e^{-s} & \dots & e^{-s(m-1)} \end{bmatrix}^T} \quad (3.4)$$

$$C = E\{cc^H\} = E\left\{ \begin{bmatrix} c_1 e^{s_1 n} \\ c_2 e^{s_2 n} \\ \vdots \\ c_L e^{s_L n} \end{bmatrix} \begin{bmatrix} c_1^* e^{s_1 n} & c_2^* e^{s_2 n} & \dots & c_L^* e^{s_L n} \end{bmatrix} \right\} = \begin{bmatrix} m_1 & 0 & \dots & 0 \\ 0 & m_2 & \cdots & \vdots \\ \vdots & \vdots & \ddots & \vdots \\ 0 & \cdots & \cdots & m_L \end{bmatrix} \quad (3.5)$$

In Equation (3.5), the elements of matrix C are zero except the diagonal elements since

$$E\left\{ c_l e^{s_l n} c_k^* e^{s_k^* n} \right\} = E\left\{ b_l(\phi,\theta) e^{j\delta_l} e^{s_l n} b_k(\phi,\theta) e^{-j\delta_k} e^{s_k^* n} \right\}$$

$$= b_l(\phi,\theta) e^{s_l n} b_k(\phi,\theta) e^{s_k^* n} E\left\{ e^{j(\delta_l - \delta_k)} \right\} = \begin{cases} m_l & \text{if } k = l \\ 0 & \text{if } k \neq l \end{cases} \quad (3.6)$$

In Equation (3.5) and (3.6), the phases of c_i's are assumed to be random phases having uniform distribution in the interval [-π, π].

Equation (3.3) constitutes the covariance matrix model of the data and the eigenstructure of IR contains complete information on the complex frequencies. Let $\lambda_1 \geq \lambda_2 \geq \dots \geq \lambda_m$ denote the eigenvalues of the correlation matrix IR, arranged in nonincreasing order, $S = \begin{bmatrix} e_1 & e_2 & \dots & e_L \end{bmatrix}$ be the set of orthonormal eigenvector matrix associated with $\{\lambda_1 \ \lambda_2 \ \dots \ \lambda_L\}$ and $G = \begin{bmatrix} e_{L+1} & \dots & e_m \end{bmatrix}$ a set of orthonormal

eigenvector matrix associated with $\{\lambda_{L+1}......\lambda_m\}$. For $m > L$, the matrix ACA^H is singular; it has a rank equal to L [100]. So ACA^H has L strictly positive eigenvalues, the remaining $m-L$ eigenvalues all being equal to zero. Hence, the eigenvalues of IR for $i = L+1,...,m$ should be equal to σ^2. Then by using fundamental theorem such that $Ae = \lambda e$ where a scalar λ and a nonzero vector e are an eigenvalue and its associated eigenvector of a matrix A,

$$\left.\begin{array}{l} IRG = ACA^HG + \sigma^2 G \\ IRG = G(\sigma^2 I_{(m-L)\times(m-L)}) = \sigma^2 G \end{array}\right\} \Rightarrow ACA^HG = 0 \qquad (3.7)$$

In Equation (3.7), the matrix AC has full column rank since null space dimension of AC is equal to zero, so AC should be nonzero. Thus, the key result obtained from Equation (3.7) is that $A^HG = 0$. In other words, $\{e_i\}_{i=L+1}^{m}$ span both range space of G and null space of A^H. Then, the true complex frequency values, $\{s_i\}_{i=1}^{L}$, are the only solutions of the following equation

$$a^H(s)GG^H a(s) = 0 \quad (\text{for any } m > L) \qquad (3.8)$$

At this step, there are two submethods emerging that can be used for pole estimation within the framework of MUSIC algorithm. One of them is the root MUSIC method that can be used to estimate the poles by the roots of Equation (3.8). This method works well for undamped exponentials, aiming to find the roots nearest to the unit circle; but, it has a poor performance for damped exponentials where the locations of poles are far away from the unity circle. Therefore, complex poles with large real parts can not be estimated correctly by this submethod. Spectral MUSIC method, on the other hand, gives more accurate results for damped exponentials. Accordingly, the use of Spectral MUSIC method is preferred in the proposed target recognition

method. The Spectral MUSIC submethod can be used to search for the peaks of "MUSIC spectrum function" defined as

$$P_{unnorm}(s) = \frac{1}{a^H(s)\,GG^H a(s)}$$ (3.9)

where $s = \alpha + j\omega$ is the complex frequency. Obviously, the function $P(s)$ has peak values in the spectrum at $s = s_i$ values. The function $P_{unnorm}(s)$ in Equation (3.9) can be expressed in the form of a matrix by taking discrete values along the $\alpha = \text{Re}\{s\}$ and $\omega = \text{Im}\{s\}$ axes with indices u and v to compute the normalized MUSIC spectrum matrix (MSM) as

$$P(u,v) = \frac{P_{unnorm}(u,v)}{\left\| P_{unnorm}(u,v) \right\|}$$ (3.10)

$$P_{unnorm}(u,v) = \frac{1}{a^H(\alpha_u + j\omega_v)\,GG^H a(\alpha_u + j\omega_v)}$$ (3.11)

$$\left\| P_{unnorm}(u,v) \right\| = \sqrt{\sum_{v=1}^{k_2}\sum_{u=1}^{k_1}(P_{unnorm}(u,v))^2}$$ (3.12)

where $u = 1,\ldots,k_1$ and $v = 1,\ldots,k_2$ are the row and column indices of the MUSIC spectrum matrix. This matrix provides a natural-resonance related power distribution map for the target on the complex frequency plane. By using the expression of P_{unnorm}, in Equation (3.10) the matrix P should have peak values in the spectrum at $s_i = \alpha_i + j\omega_i$ values for low noise scattered data; however, the peak values can shift in the complex frequency plane with the increase in the noise level as indicated in Table 3.1.

In the proposed method, the MUSIC algorithm is used with the following steps to construct MUSIC spectrum matrices. First of all, for a noisy or noiseless scattered signal as given in Equation (3.1), the sampled correlation matrix is computed using

$$\tilde{IR} = \frac{1}{N} \sum_{n=m}^{N} \overline{y(n)} \; \overline{y(n)}^{H} \tag{3.13}$$

where $\overline{y(n)}$ is defined in Equation (3.2). While forming sampled correlation matrix, the modifications such as forward-backward approach are not used since they give inaccurate results for damped sinusoidal signals [101]. Afterwards, the eigendecomposition of the sampled correlation matrix is realized with singular value decomposition (SVD) and the matrix G is constructed. At the last step, the normalized MUSIC spectrum matrix (MSM) is computed using Equation (3.10).

The values of m and L are crucial parameters for MUSIC algorithm. Regarding the selection of a value for m, this parameter may be chosen as large as possible, but not too close to N, to still allow a reliable estimation of the covariance matrix. In some applications, the largest possible value that may be selected for m may also be limited by computational complexity considerations [101]. However, it is usually advised to choose $m = N/2$ to obtain best performance [102]. The value (L/2) gives the estimated number of damped sinusoids in the late-time scattered signals. For low noise cases, the selection of L has no significant importance. Even if the correct number of damped sinusoids is exceeded while choosing the value of L, the algorithm has the advantage of finding the correct number of damped sinusoids. However, for moderate and low SNR cases, the selection of L is important and it should not be chosen too small as to be demonstrated in Section 4.3.2. Based on experience, L can be chosen as $m/2$ or (N/4).

The MUSIC algorithm has some important advantages as compared to other signal processing techniques. First of all, MUSIC spectrum matrix has nonnegative values always as opposed to some quadratic Time-Frequency Representations such as the Wigner Distribution [103]. Besides, the MUSIC algorithm suffers from no undesired cross terms in its spectrum due to the fact that the damped sinusoidal signal and noise components are uncorrelated. As an example, even for moderate noise case, the MUSIC spectrum matrix gives one peak for the signal of one damped sinusoidal with noise and it gives only two peaks, without any other possible peaks due to cross-terms, for the signal of two damped sinusoidals with additive noise.

3.2. The Classifier Design Steps

In the proposed method, let's assume that a target classifier will be designed for K_T targets and scattered data are available for each target at K_A preselected aspect angle/polarization conditions called as reference aspect angle/polarization conditions. The scattered fields at these aspect angle/polarization conditions for each target are either synthesized or measured for each target. It should be indicated that for most of the classifier design examples presented in this thesis, the reference aspect angle/polarization conditions are chosen at different aspect angles at a fixed polarization. However, the whole procedure can be applied without any difficulty for arbitrary reference aspect angle/polarization conditions. The reference aspect angles should not be chosen too closely to each other to avoid redundancy. A minimum of 10-15 degrees of aspect angle separation would be proper for the initial choice of reference aspect angles when using scattered data for smooth conducting objects, for example, in the resonance region as discussed in Chapter 1. A simulation example investigating the effects of choosing the parameter K_A on classifier performance will be presented in Section 4.3.1.

As a distinct superiority of the suggested target classifier design method, it should be emphasized that scattered data used in this design process are not needed to be low noise or noise free. On the contrary, moderately noisy data are better to achieve higher accuracy rates within a wider SNR range.

DESIGN STEP 1:

The common time span of the scattered signals is divided into certain overlapping subintervals. Let's represent these subintervals with *index p (p=1,...,P)*. Without any priori information about the pole values, target dimensions, the initial time of late-time interval or any other quantity, the MUSIC spectrum matrices (MSMs) are constructed over each subinterval for each target at each reference aspect angle as explained in the previous section. It should be noted that these MSMs are aspect dependent. To get rid of the aspect variance in MSM features of a target, these non-negative valued individual MSMs belonging to different aspect angles are first superposed and then normalized to form the fused MUSIC spectrum matrix (FMSM) for this target. The same procedure is repeated for each candidate target and for each subinterval of the classifier given as

$$FMSM_i(u,v) = \frac{P_{sum,i}(u,v)}{\left\| P_{sum,i}(u,v) \right\|} \quad for \quad \forall\, i = 1,\dots,K_T$$

$$P_{sum,i}(u,v) = \sum_{j=1}^{K_A} P_{i,j}(u,v)$$

(3.14)

where $FMSM_i$ refers to the FMSM of the ith target and $P_{i,j}$ refers to the MSM of target i at the reference aspect j.

DESIGN STEP 2:

As a crucial step of the classifier design, an optimal late-time interval for feature extraction must be selected. In this step, the FMSMs for all candidate targets and the

individual MSMs computed for all targets at all reference aspects are used. As explained in Section 3.1, in the late-time region the scattered signal of a target can be modeled by the superposition of damped sinusoidals. Each sinusoidal signal is associated with a target pole pair which corresponds to a peak location in the MUSIC spectrum. Since these damped sinusoidal signals exist at all aspect angles in varying strengths, peak locations of aspect dependent MUSIC spectra remain roughly the same but with different excitation levels. Thus, for a given target, the superposition of the MUSIC spectrum matrices (FMSMs) over different aspects should contain all possible pole information observed at different reference aspects. This situation is not valid for earlier time intervals where the early-time non-resonant components are also effective. It is not valid also for too late time intervals where the additive noise becomes dominant over the natural resonances. Thus, every MSM constructed over the optimal (or near optimal) late-time interval should highly resemble the corresponding FMSM of this target with a high correlation coefficient. It should be also true that, over the optimal late-time interval, correlation between any MSM belonging to this target and the FMSMs of any other candidate target should be low since their pole distributions (peak locations of the MSMs) are quite different. Therefore, an optimal late-time interval can be chosen by searching for a specific time interval over which the sum of correlation coefficients between MSMs (computed at reference aspect angles only) and their corresponding FMSM is maximum while the sum of correlation coefficients between MSMs and the mismatched FMSMs is minimum. Mathematically speaking, an optimal late-time interval can be found by the following algorithm:

$$Index[Optimal\ late-time\ interval] = p^* \quad if\ r_{total}(p^*) \geq r_{total}(p) \quad \forall\ p = 1,..,P$$

where

$$r_{total}(p) = \frac{1}{K_T K_A} \sum_{i=1}^{K_T} r_{i,match} - \frac{1}{K_T(K_T-1)K_A} \sum_{i=1}^{K_T} r_{i,mismatch} \qquad (3.15)$$

with

$$r_{i,match} = \sum_{j=1}^{K_A} \sum_{v=1}^{k_2} \sum_{u=1}^{k_1} FMSM_i(u,v)P_{i,j}(u,v)$$ (3.16)

and

$$r_{i,mismatch} = \sum_{\substack{k=1 \\ k \neq i}}^{K_T} \sum_{j=1}^{K_A} \sum_{v=1}^{k_2} \sum_{u=1}^{k_1} FMSM_i(u,v)P_{k,j}(u,v)$$ (3.17)

It should be emphasized that in addition to m and L, the initial time for the late-time region and the time increment Δt of the discrete scattered signal (and hence the duration of the late-time signal subject to IR matrix computations) are also important design parameters. After the selection of an optimal late-time interval, FMSMs belonging to the determined late-time interval are used altogether to form the feature database of the classifier. As the scattered response of a target is strongly aspect dependent, the target's natural resonances may be excited at varying strengths at different aspect angles. Some of the resonances may be even too weak to make a detectable contribution under certain excitation conditions and additional noise as shown in Table 3.1. Consequently, the recognition ambiguity resulting from this sort of aspect dependency is minimized by superposing the individual MSM matrices of a target to obtain its fused MSM (FMSM) feature which incorporates the effects of more and more natural resonance components of the target. Characterization of each target by a single aspect invariant FMSM, instead of a bunch of aspect-sensitive MSMs, considerably improves the accuracy rate of the classifier in addition to reducing the dimensionality and redundancy of the classifier's reference database.

51

At the real-time target recognition phase, the recognition algorithm is diverged into two separate ways, which are quite similar, according to the description of test targets. For both ways, the test scattered signal received from an unknown target at an arbitrary and unknown aspect/polarization condition is first processed to obtain the associated testing MSM of the signal over the previously determined optimal late-time interval. Then, if all test targets belong to the candidate targets in database, in other words, if there is no test target out of the target library, the unknown test target is classified as one of the candidate targets based on the highest correlation coefficient computed between this testing MSM and candidate targets' FMSMs. The correlation coefficient between these matrices is defined as

$$r(i) = \sum_{v=1}^{k_2} \sum_{u=1}^{k_1} FMSM_i(u,v) P_{test}(u,v) \qquad (3.18)$$

If there exists a test target that does not belong to the classifier's target library, that target is called "alien target". To determine the presence of alien target, in addition to the FMSMs of candidate targets, the standard deviation, σ_i, and mean values, μ_i, of $r_{i,match}$ correlation coefficients for each library target are stored. Afterwards, the decision is made over the optimal late-time interval according to following algorithm:

$Test\ target = target\ i^*\quad if\ r(i^*) \geq r(i)\quad \forall i = 1,..,K_T\quad and\ (\mu_{i^*} - 3\sigma_{i^*}) \leq r(i^*)$

$Test\ target = alien\ target\ if\ r(i^*) \geq r(i)\quad \forall i = 1,..,K_T\ and\ r(i^*) < (\mu_{i^*} - 3\sigma_{i^*})$

where $r(i)$ is given in Equation (3.18). This algorithm is based on the fact that if the test target is one of the targets in database, the MSM of test target will be highly correlated with FMSM of the corresponding target in database since their power distribution maps are similar and the correlation coefficient evaluated will be close to

$r_{i,match}$ values of the decided target. However, if it is an alien target, the correlation coefficients between MSM of test target and FMSMs of all targets in database will be low since the power distributions are different and even the highest testing correlation coefficient among the correlation coefficients evaluated will be much smaller than all of the $r_{i,match}$ values computed for the candidate targets.

To clarify both ways in the proposed methods quantitatively, assume there are 5 targets with 3 reference aspect angles in the database. The correlation coefficients between MSM of test target and FMSMs of candidate targets through one to five are 0.2354, 0.5501, 0.1675, 0.0893 and 0.2907. If it is known that all test targets belong to targets in database, then the test target will be recognized as the second target in database. Accordingly, if it is known there may exist a test target out of database and $r_{2,match}$ coefficients of the second target at three aspect angles are found as 0.5223, 0.6887 and 0.6209 resulting in $\mu_2 = 0.6106$, $\sigma_2 = 0.0837$ and $\mu_2 - 3\sigma_2 = 0.3596$, then the test target will again be recognized as the second target in the database. However, if the correlation coefficient corresponding to the second target were 0.3501 instead of 0.5501 and all other correlation coefficients were also the same; this test target would be recognized as an alien target which does not belong to the target library. The schematic view of the overall procedure of the proposed method for both ways is demonstrated in Figure 3.1.
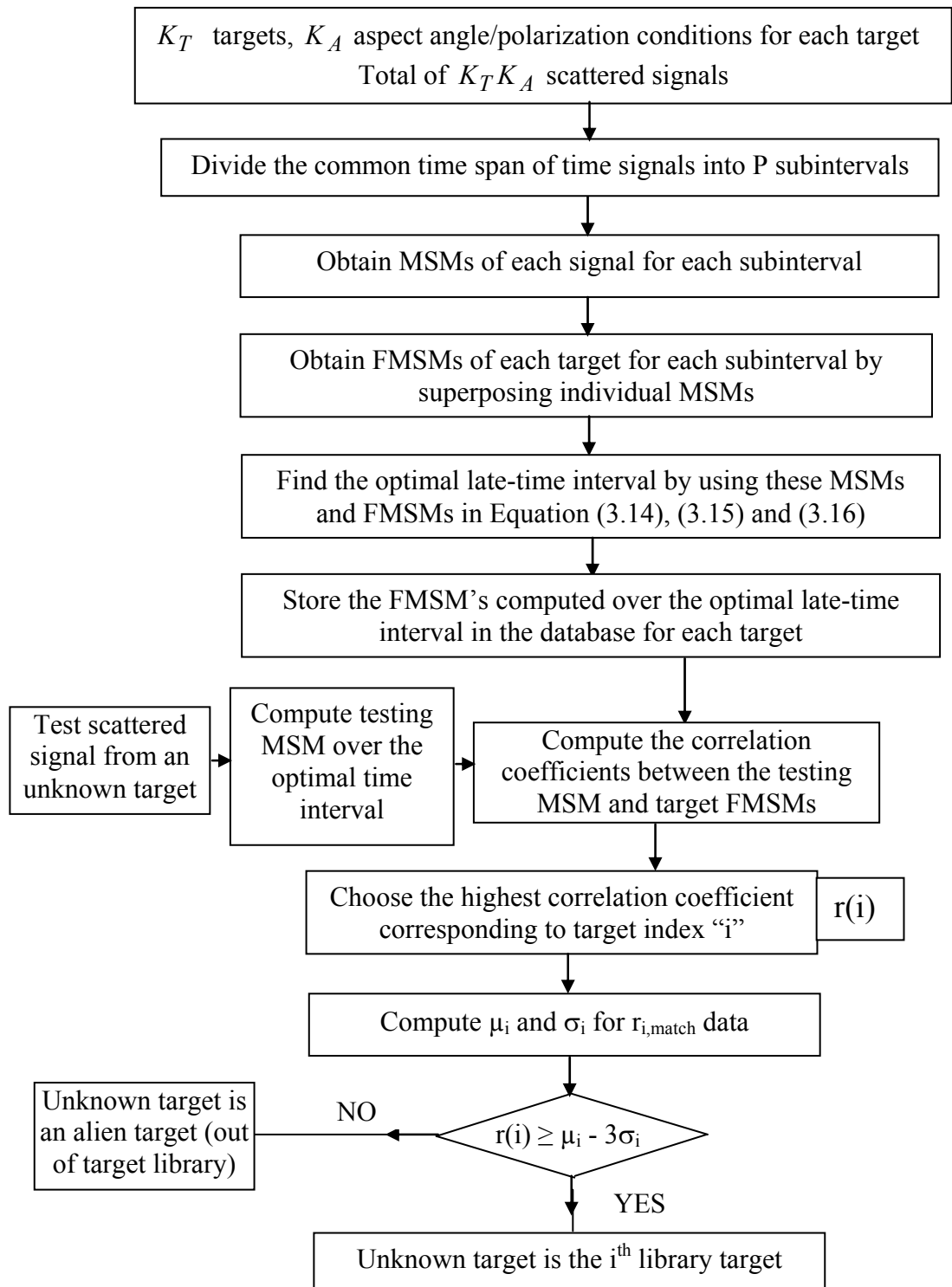
Figure 3.1   The flow chart of the design/decision algorithm for the proposed target recognition method.

3.3. Advantages of Using the Proposed Target Recognition Method

When compared to other resonance region methods mentioned in Section 2.2, the method suggested and explained throughout this chapter has many advantages both in the design and testing phases. First of all, this novel method needs no a priori information about the targets such as target geometry or target pole values as opposed to some other target recognition methods such as the E-pulse, S-pulse methods [104], [105]. This property is very important since a priori information may be available for some canonical targets such as spheres or infinitely long thin cylinders with analytical field expressions. However, it is not always possible to obtain this kind of information in real world target recognition problems. Secondly, almost all other resonance methods require reference scattered signals with no noise or very low noise in classifier design phase to construct classifier's feature in database. However, the classifier design method suggested in this dissertation is able to use noisy late-time scattered signals with moderate (or even low) SNR levels to design target classifiers with very high correct classification rates and with excellent testing noise performances. This property is demonstrated for the first time in literature for the resonance-region target recognition.

Another striking feature of the suggested target recognition method is the computational efficiency and theoretical simplicity of the signal processing approach used. The MUSIC algorithm is the only signal processing tool used for feature extraction and the computations are fast enough for real-time target recognition. Concerning the classifier performance, a high degree of aspect and polarization invariance can be provided by using reference scattered signals at only a few different design aspect angle/polarization conditions which also reduces the computational load and database memory requirements. The suggested classifier design method contains no complex signal processing tools/algorithms such as genetic algorithms or conventional optimization tools, which increase the complexity of these methods enormously. Furthermore, the feature database contains only one

matrix (FMSM) for each library target, which provides very small memory requirements in the database. These matrices are obtained with a simple superposition operation using MSMs of the targets to increase the accuracy of decisions while reducing the dimensionality of the problem. A similar task is achieved using a much more complex method involving the PCA method in [150] for example.

In addition to the advantages mentioned above, the method has also ability of being applied to all sorts of targets such as perfectly conducting or dielectric bodies, simple or complex geometries without any difficulty. Especially, the applications to dielectric targets are important since recognition of dielectric targets is not investigated in the literature except for a recent work reported in [91]. Furthermore, the proposed target recognition method is capable of discriminating an alien target from the targets in the classifier database. The other resonance region methods reported in literature labels the test target as one of the library targets and they give no indication or warning when the test target is out of the classifier library. This ability is important especially for the IFF (identification friend or foe) applications.

Finally, as it is going to be demonstrated in the following chapters, the suggested method has high accuracy rates with satisfactory noise performance when compared with the present resonance region methods. This result is achieved by the use of MUSIC algorithm in obtaining MSM and FMSM features of the targets, which are not significantly sensitive to noise. Therefore, the suggested target classifier method leads to sufficiently high accuracy rates even for the use of extremely noisy signals. Thus, in the present method, use of MUSIC algorithm for the indirect extraction of natural resonance related power distributions has the special advantage of leading to a very robust and aspect/polarization independent classification algorithm even at extremely low SNR levels as to be demonstrated later.

CHAPTER 4

APPLICATIONS AND RESULTS FOR SINGLE TARGET RECOGNITION USING NUMERICALLY SIMULATED SCATTERED FIELD DATA

In this chapter, validity and robustness of the proposed target recognition scheme are demonstrated by several simulation examples for highly challenging single target libraries where the scattered field database are constructed either analytically or numerically. The first demonstration example of Section 4.1 involves a set of three perfectly conducting spheres of different radii. Despite its simple geometry, a conducting sphere is known to be one of the most difficult targets for late-time target recognition studies, especially under noisy conditions, as it is an extremely low-Q target. In the second simulation example of Section 4.2, a classifier is designed for three lossless dielectric spheres with the same radius but different relative permittivity values. Again, despite its simple geometry, a dielectric sphere is a very challenging target as it has a very dense pole pattern resulting from the interior resonating modes [106]. Speaking from experience, a method displaying good performance for spherical targets usually works for the other targets. In other words, spherical targets can be thought as canonical reference targets for the target classifier design problems. Besides, considering the fact that almost all of the target recognition methods in literature have been demonstrated for only high-Q conducting targets such as conducting thin wires so far, this example is also particularly important to demonstrate the applicability of our target recognition technique to non-

conducting, penetrable targets. The scattered responses of these spherical targets are easily generated from the available analytical solutions at arbitrarily chosen aspect angles [107], [108] providing an easily accessible data set for design and verification tasks. The derivations and the resulting expressions of these scattered fields for both perfectly conducting spheres and dielectric spheres are given in Appendix C. Next, a target classifier is designed in Section 4.3 for a set of more realistic targets with complex but yet similar geometrical features. Five small-scale aircraft modeled by conducting thin wires are chosen to be the library targets for this challenging demonstration. The scattered responses of these aircraft targets are obtained with simulation programs FEKO and CST as explained in Section 4.3. The simulation examples presented in Section 4.3.1 and 4.3.2 demonstrate the importance of choosing the design parameters K_A and L properly. Finally, the aspect and polarization invariance of the suggested target recognition method will be further investigated in Section 4.3.3 and 4.3.4 using the aircraft-classifier designed in Section 4.3. Then, in Section 4.4, the suggested method will be demonstrated for the isolated target types from Section 4.1 to Section 4.3 using incomplete frequency domain data. The drawbacks of using such data in target recognition problems will be also investigated in this section. Moreover, the effect of frequency bandwidth on accuracy performance will be also examined. In the aircraft target simulations presented in this section, an alien aircraft target is also considered as a test target in order to test the performance of the classifier under such a special but important circumstance.

All the calculations including the generation of frequency domain and time domain responses of targets (except for the frequency domain responses of aircraft targets), the generation of MSMs and FMSMs, other intermediate design steps and test computations are done with MATLAB 7.1. As an example, the program code written in MATLAB for the design and testing of the classifier of Section 4.3 is given in Appendix D.

4.1. The Classifier Design for Low-Q Conducting Spheres

This first classifier is designed for a target library with three perfectly conducting spheres of radii 1.8 cm, 2.4 cm and 3 cm. As mentioned before, target responses are numerically synthesized with the expressions given in Appendix C for a plane wave excitation which is linearly polarized in x-direction and propagates in z-direction, as shown in Figure 4.1. The linear polarization in x-direction in this configuration can be also defined as ϕ polarization.
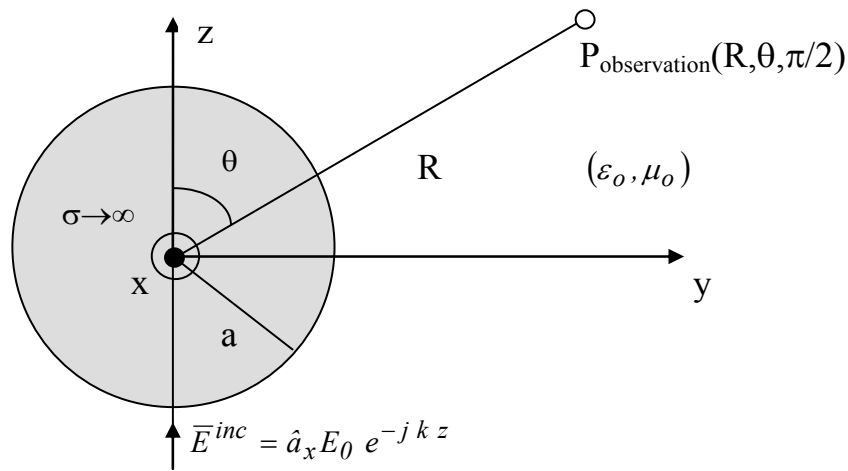
Figure 4.1   The problem geometry used to generate electromagnetic signals scattered from the spherical targets.

The far field scattered responses are computed using MATLAB 7.1 in frequency domain over a bandwidth from zero to 12 GHz at 873 frequency sample points with frequency resolution of 13.75 MHz which is deliberately chosen to be compatible with the resolution of measurements described in Chapter 5. With this frequency band, the targets are in the range of $[0, 2.4\lambda]$ which can be regarded in resonance region. These responses are also obtained at $\phi = \pi/2$ plane, with a radial distance of 72 cm from the sphere center, for twelve different bistatic aspect angles, $\theta_b = 5, 15,$

30, 45, 60, 75, 90, 105, 120, 135, 150 and 165 degrees which corresponds to 180-θ_b= θ= 175, 165, 150, 135, 120, 105, 90, 75, 60, 45, 30 and 15 degrees, respectively in Figure 4.1. It should be noted that studying with bistatic aspect angles in the recognition of spherical targets is compulsory since the monostatic (backscattered) response of a sphere is identical at every direction.

When considering the field expressions in Equation (B.13), this special case (ϕ= $\pi/2$) brings only ϕ component (-x direction) of electric field ($E_\theta = 0$) and no cross polarization ($\phi\theta$ polarization) in the observation point. This fact is also true for θ polarization that if the excitation is linearly polarized in y-direction (θ polarization), same geometry will bring only θ component of electric field ($E_\phi = 0$) without any $\theta\phi$ polarization component, in the observation point. Hence, only $\phi\phi$ polarization will be taken into account for this spherical target problem. The polarization invariance of the proposed recognition method will be investigated with different polarizations in Section 4.3 and 5.4. After getting frequency responses, time-domain scattered fields are computed by using Gaussian windowing, inverse fast Fourier transformation (IFFT) and zero padding to get a 5 picoseconds resolution, which is enough to observe the frequency range up to 12 GHz. The resulting time signals have 1024 sample points with a total time span of 5.115 nanoseconds. The noisy scattered time-domain signals at all the aspect angles stated above are synthesized at the signal-to-noise ratio (SNR) levels of 20, 15, 10, 5 and 0 dB to be used for classifier design and for performance testing. As an example, the scattered time domain signal for the perfectly conducting sphere of radius 1.8 cm is plotted in Figure 4.2 at the bistatic aspect angle of 30 degrees (θ=150 degrees) for 10 dB SNR level. Five of the bistatic aspect angles at θ= 45, 75, 105, 135 and 165 degrees are chosen as reference aspect angles to construct the FMSM features of the classifier design with noisy signals of 10 dB SNR level. It should be again emphasized that this is a very challenging classifier design example as the reference data used in design is highly noisy particularly over the late-time intervals for these low-Q conducting spheres.

60
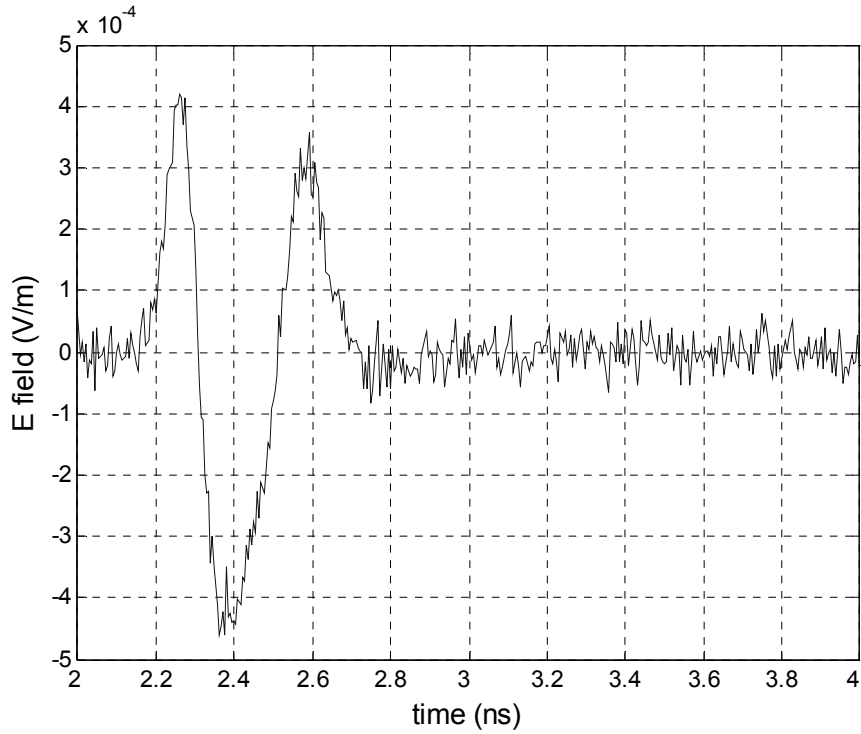
Figure 4.2   The time-domain signal scattered from the perfectly conducting sphere of radius 1.8 cm at 30 degree bistatic aspect angle with 10 dB SNR level.

As the first step of the design procedure, for each given target/reference aspect angle case, the scattered signal is divided into parts over the overlapping subintervals of time starting from 2.08 nanoseconds with a total length of N=128. For each subinterval and for every target/reference aspect angle, the normalized MUSIC spectrum matrices are constructed with L= 32 for two different values of m, $m = 64$ and $m = 96$, and two different values of time resolution, $\Delta t = 2.5$ psec and $\Delta t = 5$ psec where the signals with 2.5 psec resolution are obtained by the linear interpolation of signals with 5 psec resolution. Then, the MUSIC spectrum matrices computed at each different reference aspect angle over each subinterval are superposed for each given target to obtain the fused MUSIC spectrum matrices over individual subintervals. After obtaining these FMSMs, r_{total} values in

61

Equation (3.15) are computed for each subinterval to provide a measure of aspect invariance. Finally, the most suitable late-time interval is determined for optimum classifier performance choosing the highest r_{total} value. The computed r_{total} values for different late-time intervals and for two different m and Δt choices are shown in Figure 4.3 where

- indices 1 to 8 along the horizontal axis refers to a total of 8 subintervals in time established with $m = 64$, $\Delta t = 5$ psec, time duration= 128x5 psec= 0.64 nsec and shifting by 0.16 nsec (i.e. index 1 corresponds to 2.08 nsec-2.72 nsec interval; index 2 corresponds to 2.24 nsec-2.88 nsec interval, etc. and finally index 8 corresponds to 3.2 nsec-3.84 nsec interval).

- indices 9 to 24 along the horizontal axis refers to a total of 16 subintervals in time established with $m = 64$, $\Delta t = 2.5$ psec, time duration= 128x2.5 psec= 0.32 nsec and shifting by 0.08 nsec (i.e. index 9 corresponds to 2.08 nsec-2.40 nsec interval; index 10 corresponds to 2.16 nsec-2.48 nsec interval, etc. and finally index 24 corresponds to 3.28 nsec-3.6 nsec interval).

- indices 25 to 32 along the horizontal axis refers to a total of 8 subintervals in time established with $m = 96$, $\Delta t = 5$ psec, time duration= 128x5 psec= 0.64 nsec and shifting by 0.16 nsec (i.e. index 25 corresponds to 2.08 nsec-2.72 nsec interval; index 26 corresponds to 2.24 nsec-2.88 nsec interval, etc. and finally index 32 corresponds to 3.2 nsec-3.84 nsec interval).

- indices 33 to 48 along the horizontal axis refers to a total of 16 subintervals in time established with $m = 96$, $\Delta t = 2.5$ psec, time duration= 128x2.5 psec= 0.32 nsec and shifting by 0.08 nsec (i.e. index 33 corresponds to 2.08 nsec-2.40 nsec interval; index 34 corresponds to 2.16 nsec-2.48 nsec interval, etc. and finally index 48 corresponds to 3.28 nsec-3.6 nsec interval).
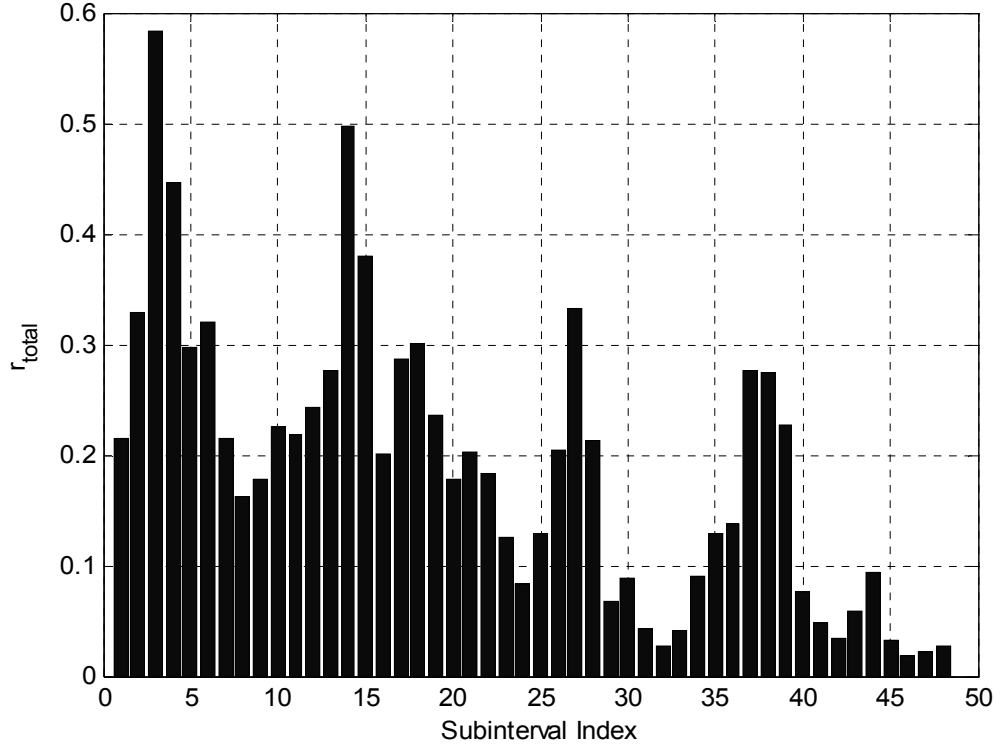
Figure 4.3   The r_{total} values computed for the classifier design for perfectly conducting spheres at SNR= 10 dB.

It can be concluded from Figure 4.3 that the intervals with $m = 96$ (index 25-48) have lower r_{total} values compared to intervals with $m = 64$ (index 1-24). Consequently, the intervals with $m = N / 2 = 64$ give better results [109] and hence the parameter m is chosen to be N/2 for classifier design to follow. Besides, from Figure 4.3, it can be seen that r_{total} values in the earlier time intervals are smaller since these intervals contain forced scattered response components in addition to the superposition of damped sinusoidal signals. The presence of highly aspect dependent early-time scattered response components in data obviously causes deterioration in the aspect invariance and hence in the correct classification capacity of the classifier. As it is moved into later time intervals, these forced response components vanish

leading to higher r_{total} values. However, at very late-time intervals, the effective SNR becomes very low as the amplitudes of damped sinusoidal signals attenuate to very small values. So, staying away from the low SNR zone and keeping as much of the useful resonance information as possible, the optimal subinterval index is selected to be 3 (interval from 2.4 to 3.04 nsec) for which the highest r_{total} value is observed. It should be noted that although SNR levels of reference signals are 10 dB, SNR levels belonging to only this subinterval, which can be called as effective SNR, are much lower than 10 dB since the selected time interval is in late-time region which is much weaker than the early time intervals. Then, the feature database of the classifier design is constructed by using the FMSM features computed over this optimal subinterval. The resulting FMSM features for the conducting spheres with 1.8 cm, 2.4 cm and 3 cm radii are given in Figure 4.4(a), 4.4(b) and 4.4(c), respectively. After completing the design procedure as described above, the resulting classifier is extensively tested for aspect invariance and noise performance. While preparing the noisy scattered data set for testing, addition of the random Gaussian noise to the ideal noise free scattered signals is repeated in 50 independent trials at each SNR level to obtain reliable results for noise analysis. A total of (3 targets) x (12 bistatic aspect angles) x (5 SNR levels) x (50 trials at each SNR level) = 9000 noisy scattered test signals are generated for performance tests. As an example, the MSM feature for the conducting sphere of radius 1.8 cm at 30 degree bistatic aspect with 10 dB SNR level (see the associated scattered test signal in Figure 4.2) is constructed over the optimal time interval [2.4, 3.04] nsec as shown in Figure 4.4(d). The matched correlation coefficient computed between the FMSM of Figure 4.4(a) and the MSM of Figure 4.4(d) is 0.8194 while the mismatched correlation coefficients computed between the MSM of Figure 4.4(d) and the FMSMs of Figure 4.4(b) and 4.4(c) turn out to be 0.3462 and 0.1371, respectively, leading to a correct classification result in favor of the conducting sphere of radius 1.8 cm by a very large safety margin.
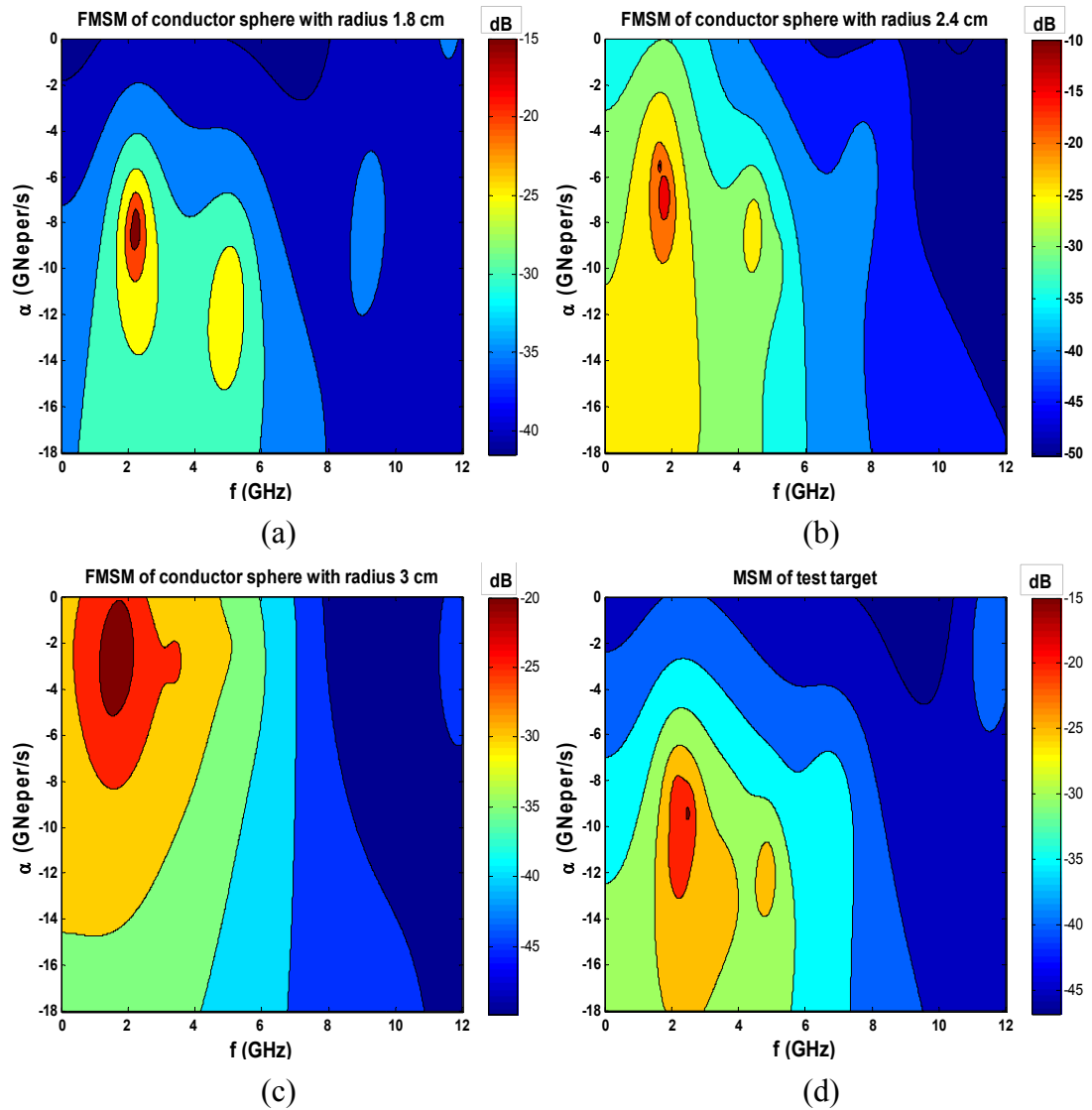
Figure 4.4 (a)-(c) The FMSM features of the perfectly conducting spheres with 1.8 cm, 2.4 cm and 3 cm radii (d) the MSM feature of the test target (the conducting sphere with radius of 1.8 cm at 30 degree bistatic aspect angle) at SNR= 10 dB.

The correct classification rates obtained as a result of all those 9000 tests are presented in Table 4.1 for various SNR levels not only for the optimum late-time interval labeled by the index 3 but also for two other suboptimal but promising intervals with indices 4 and 14 to show the importance of choosing the proper design

interval in time. In this table, while the decision criterion of "0% margin" looks for the condition that the matched correlation coefficient is simply higher than all mismatched correlation coefficients, the more demanding decision criterion of "5% margin" looks for the case that the highest mismatched correlation coefficient is at least 5 percent lower than matched correlation coefficient [91].

Table 4.1   The correct classification rates (in percentage) of optimal and suboptimal perfectly conducting sphere classifiers which are designed over three different late-time interval with 10 dB SNR.

SNR Levels	20 dB SNR		15 dB SNR		10 dB SNR		5 dB SNR		0 dB SNR	
Safety margin for decisions	0%	5%	0%	5%	0%	5%	0%	5%	0%	5%
Late-time Index 3 (Optimal) [2.4, 3.04] nsec	100	100	98	97	94	91	89	85	83	80
Late-time Index 14 [2.48, 2.80] nsec	100	99	97	94	91	87	84	79	77	73
Late-time Index 4 [2.72, 3.36] nsec	99	98	96	92	88	85	81	76	74	70

According to the results displayed in Table 4.1, the late-time interval [2.4, 3.04] nsec corresponding to the index 3 gives the highest accuracy, as expected. For this optimal late-time interval, it is verified that the resulting classifier reaches a correct decision rate of 97 percent for low noise test signals with SNR levels of 15 dB and higher. This rate drops to 80 percent at 0 dB overall SNR level with 5% margin decision criterion. However, it can be concluded that the proposed method performs quite effectively in this conducting sphere classifier with still high accuracy rates even in the case of highly contaminated test signals.

The performance analysis of the method with respect to the construction of FMSMs at different SNR levels is also important and an optimal SNR level required for constructing the optimal FMSMs, which gives the highest accuracy rates at wider SNR ranges, should be determined. In the conducting sphere simulation of this section, the reference signals with 10 dB SNR are used for constructing the FMSMs. However, in addition to 10 dB SNR, the simulation is repeated with the reference signals with lowest and highest SNR levels in SNR range, 0 dB SNR and 20 dB SNR. The correct decision rates of the classifiers designed by using reference signals at 0 dB, 10 dB and 20 dB SNR levels are given in Table 4.2.

Table 4.2   The correct classification rates (in percentage) of perfectly conducting sphere classifiers, which are designed with reference signals at 0, 10 and 20 dB SNR levels.

SNR Levels	20 dB SNR		15 dB SNR		10 dB SNR		5 dB SNR		0 dB SNR	
Safety margin for decisions	0%	5%	0%	5%	0%	5%	0%	5%	0%	5%
Classifier design with 0 dB SNR reference signals	97	95	95	93	91	88	87	84	82	79
Classifier design with 10 dB SNR reference signals	100	100	98	97	94	91	89	85	83	80
Classifier design with 20 dB SNR reference signals	100	100	99	97	94	90	86	81	80	77

According to the results in Table 4.2, the classifier design having reference signals with 10 dB SNR gives highest accuracy rates and hence 10 dB is the optimum SNR level for this classifier design example. The classifier with 0 dB SNR gives successful rates for low SNR values (at 0 dB and 5 dB); however, it gives lower

accuracy rates for high SNR values (at 20 dB) when compared to the classifier designed with 10 dB SNR data. On the other hand, the classifier designed with 20 dB data SNR gives successful rates for high SNR values (at 15 dB and 20 dB); however, it gives lower accuracy rates for low SNR values such as 0 dB.

4.2. The Classifier Design for Dielectric Spheres

In this second classifier design, the performance of the proposed MUSIC-based classification method is tested for a non-conducting target set containing three lossless dielectric spheres with the same radius of 1.8 cm but with different relative permittivity values of $\varepsilon_r = 2$, 3 and 4. The problem geometry, generation scheme of scattered time-domain signals, choice of testing and reference aspect angles of this classifier design are exactly the same as those used in the first classifier design example of Section 4.1. The only difference is that the noisy scattered time-domain signals are synthesized at the signal-to-noise ratio (SNR) levels of 15, 10, 5, 0 and -5 dB to be used for classifier design and for performance testing. As an example, the scattered time domain signal for lossless dielectric sphere of $\varepsilon_r = 3$ is plotted in Figure 4.5 at the bistatic aspect angle of 15 degrees for 5 dB SNR level. The same five bistatic aspect angles, 45, 75, 105, 135 and 165 degrees, are chosen as reference aspect angles to construct the FMSM features with noisy signals of 5 dB SNR level for this classifier design. The normalized MUSIC spectrum matrices are constructed with $m = 64$ (only), L= 32 for two different values of time resolution, $\Delta t = 2.5$ psec and $\Delta t = 5$ psec. The results of r_{total} calculations for various subintervals are displayed in Figure 4.6 where the definitions of subintervals from index 1 to index 24 are the same as those given in the previous classifier design. The late-time interval [2.56, 2.88] nsec corresponding to index 15 is the optimal choice for this classifier.
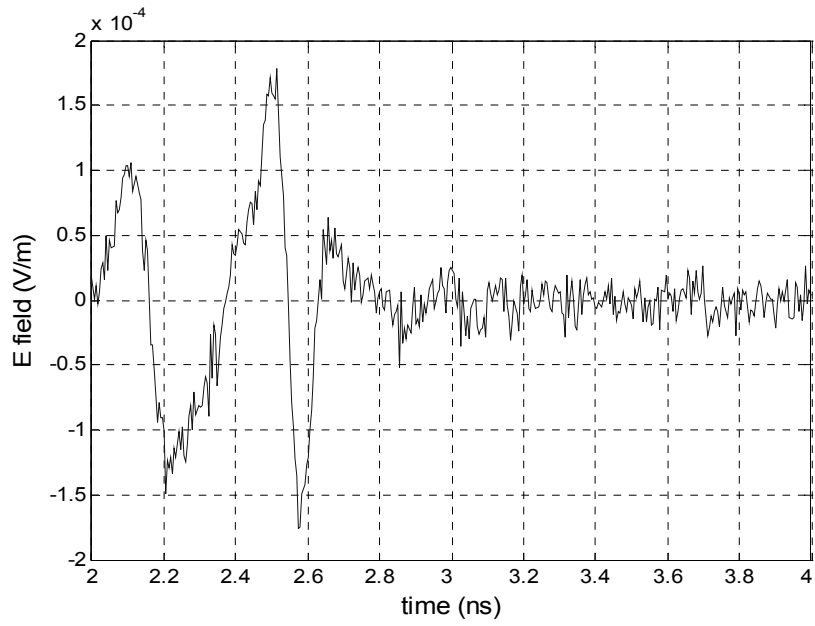
Figure 4.5   The time-domain signal scattered from lossless dielectric sphere of $\varepsilon_r = 3$ at 15 degree bistatic aspect angle with 5 dB SNR level.
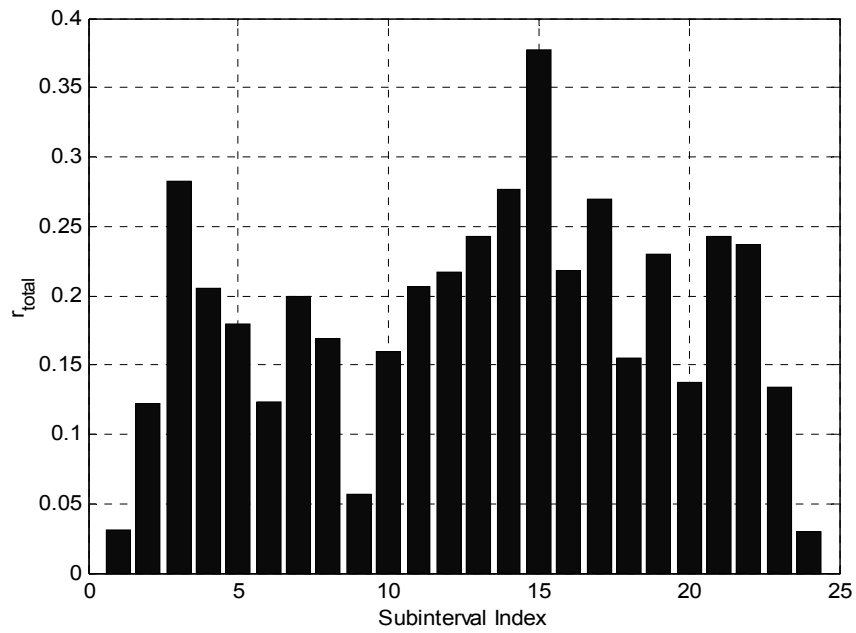
Figure 4.6   The r_{total} values computed for the classifier design for dielectric spheres at SNR= 5 dB.

The FMSM features of the dielectric spheres extracted over this optimal time interval for SNR= 5 dB case are shown in Figure 4.7(a)-(c). A total of (3 targets) x (12 aspect angles) x (5 SNR levels) x (50 trials at each level)= 9000 noisy test signals are used altogether to test the performance of this dielectric sphere-classifier. Again, it is important to notice that, for the first time in literature, a classifier design is accomplished by such highly contaminated data with 5 dB SNR level.

(a)

(b)

(c)
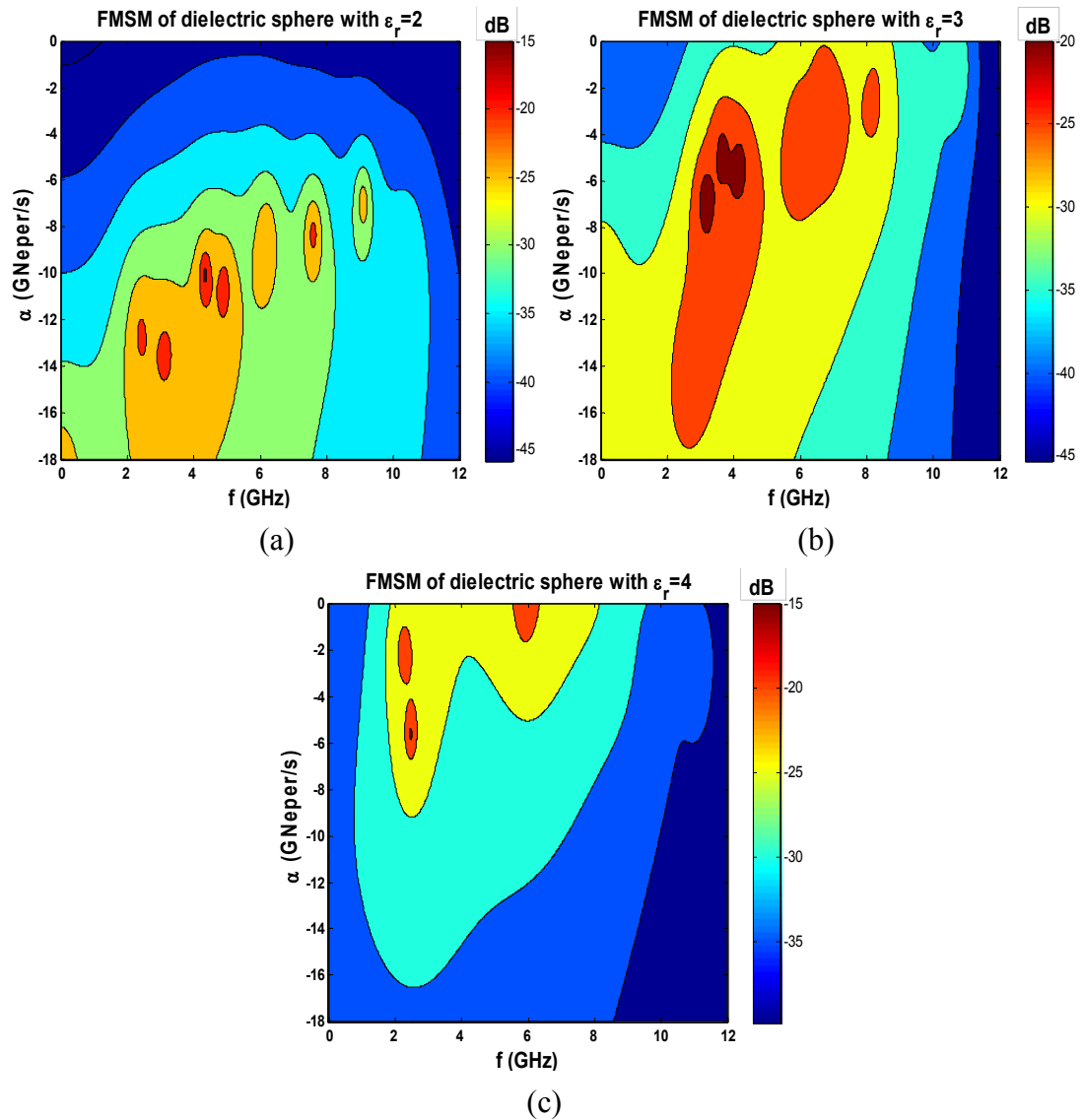
Figure 4.7   The FMSM features of the lossless dielectric spheres with a common radius r= 1.8 cm with relative permittivity values ε_r= 2, 3 and 4 at SNR= 5 dB.

As an example to the decision tests, the MSM computed using an arbitrarily selected test signal in Figure 4.5 (belonging to the dielectric sphere of ε_r= 3 at 15 degree bistatic aspect angle with 5 dB SNR) over the optimal time interval is shown in Figure 4.8(a). The matched correlation coefficient between this testing MSM and the FMSM of the sphere with ε_r= 3 is found to be 0.7963 while the mismatched correlation coefficients are 0.3264 and 0.3571 for the sphere with ε_r= 2 and 4, respectively. The MSM computed using another test signal belonging to the dielectric sphere of ε_r= 2 at 60 degree bistatic aspect angle with 0 dB SNR, where the SNR levels of the reference signals in database (5 dB) and the test signal (0 dB) are different, is shown in Figure 4.8(b). For this challenging test case, the matched correlation coefficient between this testing MSM and the FMSM of the sphere with ε_r= 2 is found to be 0.6067 while the mismatched correlation coefficients are 0.4792 and 0.2810 for the sphere with ε_r= 3 and 4, respectively, which satisfies both decision criteria of 0% and 5% safety margin.

(a)   (b)
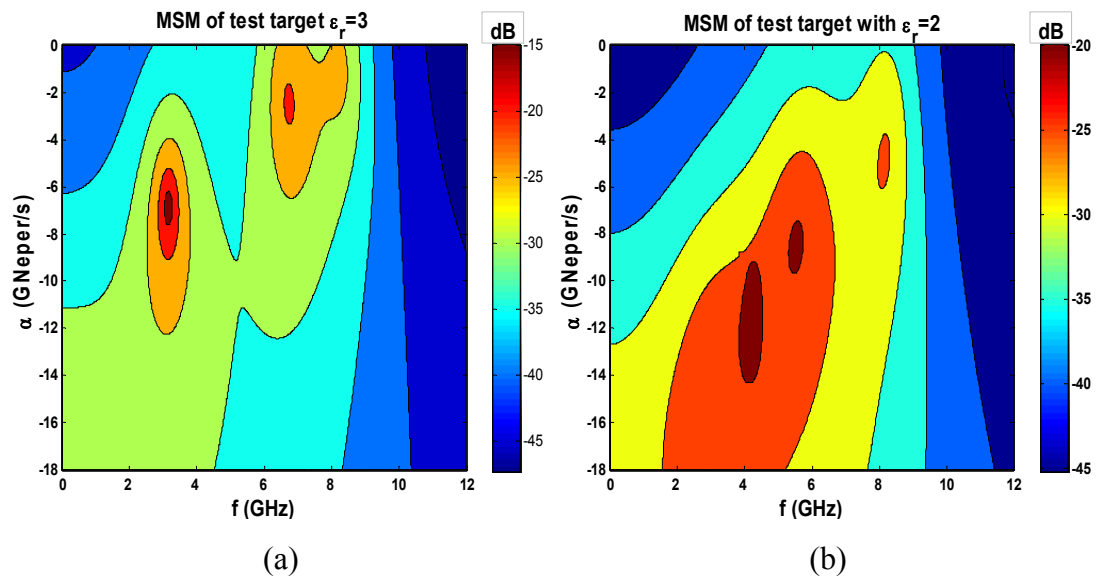
Figure 4.8   (a) The MSM feature of the test target (dielectric sphere with ε_r= 3 at 15 degree bistatic angle) at SNR= 5 dB   (b) The MSM feature of the test target (dielectric sphere with ε_r= 2 at 60 degree bistatic angle) at SNR= 0 dB.

The accuracy rates computed for the dielectric sphere classifier for three different late-time subintervals (the next-to-optimal intervals with indices 5 and 14 in addition to the optimal interval with index 15) are displayed in Table 4.3 for various SNR values and for two different decision criteria.

Table 4.3   The correct classification rates (in percentage) of optimal and suboptimal lossless dielectric sphere classifiers which are designed over three different late-time interval with 5 dB SNR.

SNR Levels	15 dB SNR		10 dB SNR		5 dB SNR		0 dB SNR		-5 dB SNR	
Safety margin for decisions	0%	5%	0%	5%	0%	5%	0%	5%	0%	5%
Late-time Index 15 (Optimal) [2.56, 2.88] nsec	100	100	97	95	92	88	86	82	80	77
Late-time Index 3 [2.40, 3.04] nsec	98	95	95	91	89	84	82	77	75	71
Late-time Index 14 [2.48, 2.80] nsec	96	92	93	88	87	82	80	74	72	66

According to these results, the optimal classifier designed over the time interval with index 15 gives the highest accuracy rates at all SNR levels. From the results in Table 4.1 and 4.3, it can be concluded that the highest accuracy rates are obtained from the subinterval having highest r_{total} value as expected. Therefore, the correct decision rates only belonging to the subinterval with highest r_{total} value are given for the classifier design examples to follow. The proposed method has 95 percent accuracy at 10 dB SNR with the more stringent 5% decision criterion for this dielectric sphere set. This rate drops to only 76 percent at a very low SNR value of -5 dB under the same 5% margin criterion. In other words, the proposed classifier

design method works out very satisfactorily not only for conducting targets but also for dielectric targets, which are characterized by much more complicated internal natural resonance mechanisms.

The performance analysis of the method with respect to the construction of FMSMs at different SNR levels is also done for this dielectric sphere classifier. In this simulation, classifier design is repeated with the reference signals having 15 dB SNR levels. Comparison of correct decision rates of the resulting classifiers are given in Table 4.4.

Table 4.4   The correct classification rates (in percentage) of dielectric sphere classifiers which are designed with 5 and 15 dB SNR reference signals.

SNR Levels	15 dB SNR		10 dB SNR		5 dB SNR		0 dB SNR		-5 dB SNR	
Safety margin for decisions	0%	5%	0%	5%	0%	5%	0%	5%	0%	5%
Classifier design with 5 dB SNR reference signals	100	100	97	94	91	88	86	82	79	76
Classifier design with 15 dB SNR reference signals	100	100	96	93	90	87	84	79	75	71

As being similar to the results in Table 4.2, the classifier design with 5 dB SNR, the middle SNR value of the considered SNR test range, gives highest accuracy rates. Besides, the other classifiers have higher accuracy rates for SNR levels close to SNR value of the classifier; however, they give lower accuracy rates for SNR levels far away from SNR value of the classifier when compared to the classifier with 5 dB SNR.

4.3. A Classifier Design for Small-Scale Aircraft Targets Modeled by Perfectly Conducting, Straight, Thin Wires

In this simulation example, the performance of the proposed MUSIC-based classifier design technique is demonstrated for a target set of five small-scale aircraft; Airbus, Boeing 747, Caravelle, P-7 and Tu 154, which are modeled by perfectly conducting, straight, thin wires (with length to radius ratio of 2000 for all wire structures). The design code written in MATLAB for this simulation example is given in Appendix D. It should be indicated that the target set includes all five aircraft targets in the database and there exists no alien aircraft target throughout the simulations in Section 4.3. The actual aircraft dimensions are scaled down by a factor of 100 to obtain the small-scale target dimensions. The resulting wire lengths for body, wing and tail of each target are given in Table 4.5.

Table 4.5   The dimensions of the small-scale aircraft targets used in the simulations in Section 4.3.

Substructures	Target 1 (Airbus)	Target 2 (Boeing 747)	Target 3 (Caravelle)	Target 4 (P-7)	Target 5 (Tu 154)
Body length (m)	0.5408	0.7066	0.3200	0.3435	0.4790
Wing length (m)	0.4484	0.5964	0.3440	0.3250	0.3755
Tail length (m)	0.1626	0.2217	0.1092	0.1573	0.1340

As seen in this table, the dimensions of target 3 and target 4 are especially close which makes the classification problem in hand quite difficult. It should be noted that the same target set is used in [86] where a different target classifier design method is

used based on the combination of Adaptive Gaussian Distribution, Principal Component Analysis (PCA) and neural networks. In the classifier design given in [86], 46 reference aspect angles are used for each target in the range of 0-90 degrees azimuth angle to train the classifier. It is decided to use the same target set with the similar problem definition so that the results obtained from the proposed method could be easily compared with the results reported in [86]. The same target is also used in [94] with a classification method using late-time feature vector (LTFV) and PCA; however, since there is no noise analysis results presented in [94], results of that work are not taken into account for comparisons.

Geometrically, the aircraft models lie in the x-y plane with nose pointing +y direction as described in Figure 4.9.
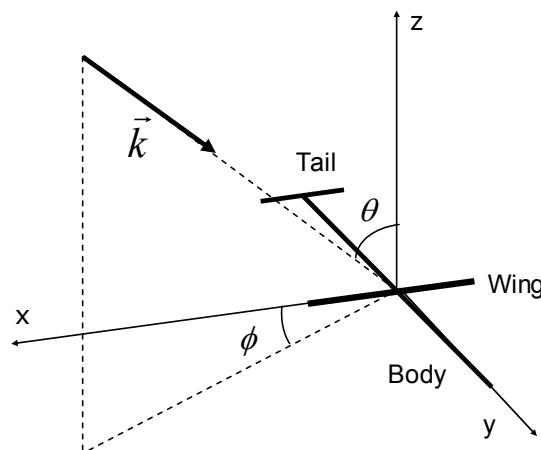
Figure 4.9   Target geometry for aircraft-classifier simulations where the vector $\vec{k}$ denotes the propagation direction of incident plane wave with θ and ϕ are being the elevation and azimuth aspect angles, respectively.

The scattered responses of aircraft targets are obtained by using a simulation program FEKO, an abbreviation derived from the German phrase **FE**ldberechnung

bei **K**örpern mit beliebiger **O**berfläche (field computations involving bodies of arbitrary shape), in [94] by Mehmet Okan Ersoy. The program FEKO, whose details can be found in [94] and [110], is based on the Method of Moments (MoM). In this program, the electromagnetic fields are obtained by first calculating the electric surface currents on conducting surfaces (which is the case in this section because targets modeled by perfectly conducting, thin wire structures are used throughout this section) and equivalent electric and magnetic surface currents on the surface of a dielectric solid. FEKO implements the frequency-domain MoM solution of the Electric Field Integral Equation (EFIE) for low frequency problems, and the Physical Optics (PO), Geometrical Theory of Diffraction (GTD) and Uniform Theory of Diffraction (UTD) for high frequency problems. The currents are calculated using a linear combination of basis functions, where the coefficients are obtained by solving a system of linear equations. Once the current distribution is known, further parameters can be obtained e.g. the near field, the far field, radar cross sections, directivity or the input impedance of antennas.

The backscattered (monostatic) responses of aircraft are numerically generated by using FEKO for $\phi\phi$ polarization (ϕ-polarized) over the frequency band from 4 MHz to 1024 MHz (with frequency steps of 4 MHz) using ϕ-polarized uniform plane wave illumination at a fixed elevation of $\theta = 60$ degrees and at the azimuth angles of $\phi = 5$, 10, 15, 22.5, 30, 37.5, 45, 52.5, 60, 67.5, 75 and 82.5 degrees [111]. The targets' noise-free time domain responses are produced using the IFFT technique at all these aspects and then the noisy backscattered responses are synthesized at the SNR levels of 20, 15, 10, 5, 0 and -5 dB with 50 independent trials at each SNR level. The common time span of all scattered responses is 250 nanoseconds with 512 time samples. As an example, the backscattered time domain signal for Airbus at 5 degrees aspect angle for 10 dB SNR level is plotted in Figure 4.10.
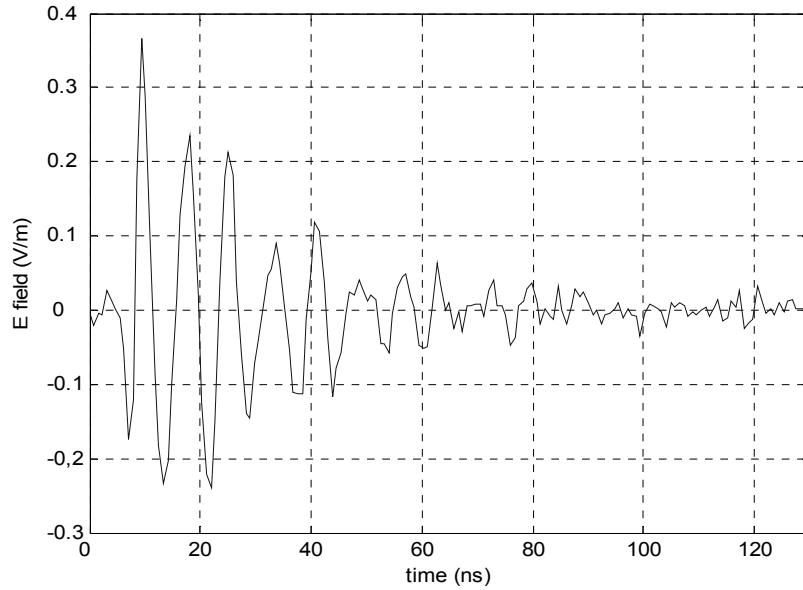
Figure 4.10   The time-domain signal backscattered from Airbus at ϕ= 5 degree aspect angle with 10 dB SNR level.

Out of 12 different aspect angles listed above, five of them (ϕ= 5, 15, 30, 45 and 75 degrees) are chosen as the reference aspect angles to construct the feature database of the classifier at 10 dB SNR level. The design parameters of the MUSIC algorithm are chosen to be N= 64, m = 32 and L= 16 with two alternatives, approximately 250 psec and 500 psec, for the time resolution Δt. The computed r_{total} values for different late-time intervals and for two different Δt choices are shown in Figure 4.11 where

- indices 1 to 8 along the horizontal axis refers to a total of 8 subintervals in time established with m = 32, $\Delta t \approx$ 500 psec, time duration= 64x500 psec= 32 nsec and shifting by 8 nsec (i.e. index 1 corresponds to 0 nsec-32 nsec interval; index 2 corresponds to 8 nsec-40 nsec interval, etc. and finally index 8 corresponds to 56 nsec-88 nsec interval).

77

- indices 9 to 24 along the horizontal axis refers to a total of 16 subintervals in time established with $m = 32$, $\Delta t \approx 250$ psec, time duration= 64x250 psec= 16 nsec and shifting by 4 nsec (i.e. index 9 corresponds to 0 nsec-16 nsec interval; index 10 corresponds to 4 nsec-20 nsec interval, etc. and finally index 24 corresponds to 60 nsec-76 nsec interval).
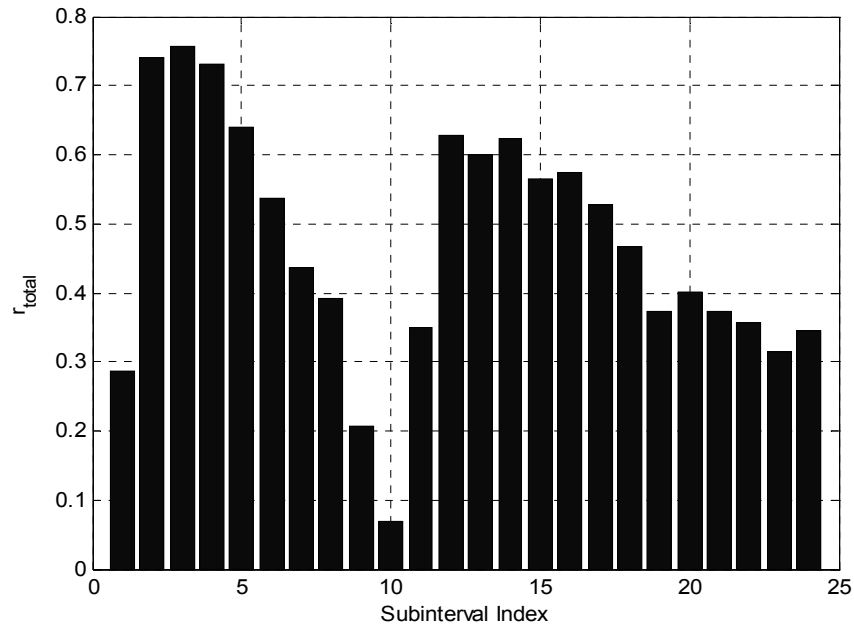
Figure 4.11   The r_{total} values computed for the classifier design for small-scale aircraft targets at SNR= 10 dB.

The optimal late-time interval for this design problem is found to be [16, 48] nsec (index 3). The resulting FMSM features characterizing five aircraft targets in the classifier database are shown in Figure 4.12(a)-(e). Although the extraction of target poles is not necessary in the proposed method, the most dominant pole values of library targets can be easily estimated from these figures, if needed, simply reading the coordinates of the spectrum peaks. From these figures, the peak locations of power distributions are found at the frequencies about 200 and 300 MHz for

aircraft 1, 155 and 230 MHz for aircraft 2, 330 and 450 MHz for aircraft 3, 290 and 430 MHz for aircraft 4, 235 and 345 MHz for aircraft 5 [112]. Even for the geometrically similar targets, aircraft 3 and aircraft 4, the peak values of the computed MUSIC spectra occur at quite distinct locations on the complex frequency plane.
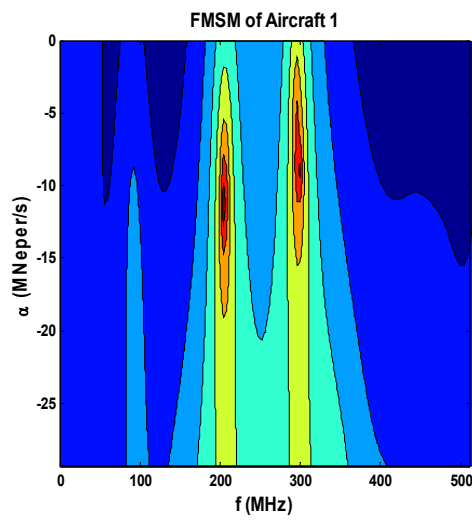
Figure 4.12(a)
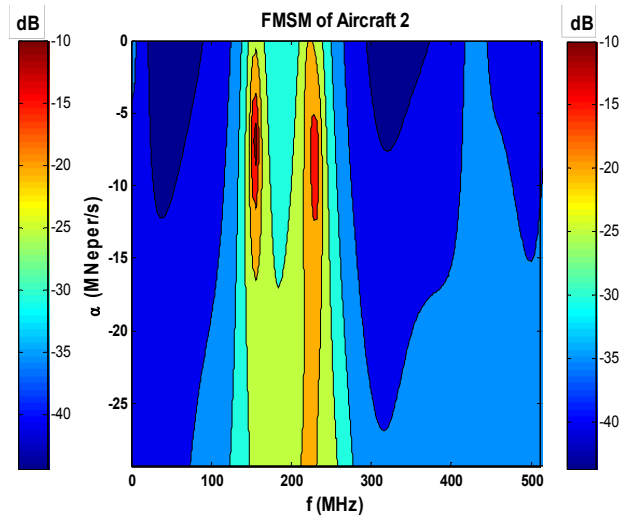
Figure 4.12(b)
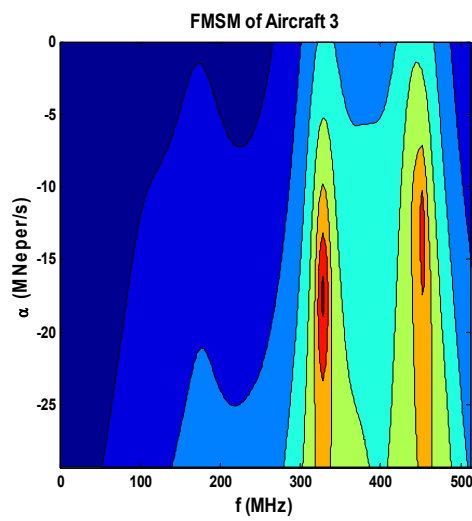
Figure 4.12(c)
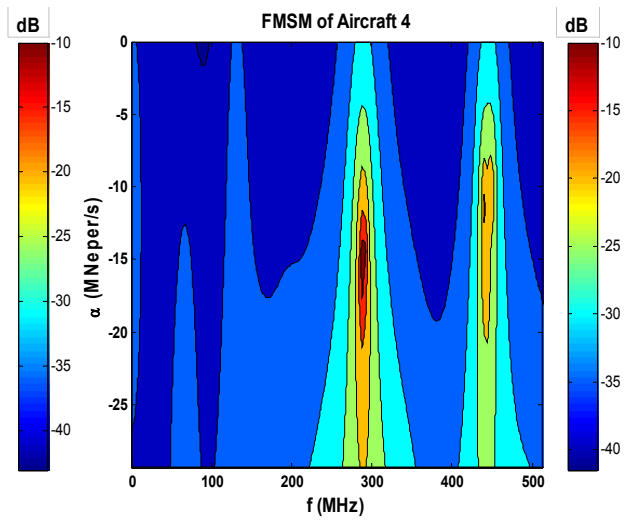
Figure 4.12(d)
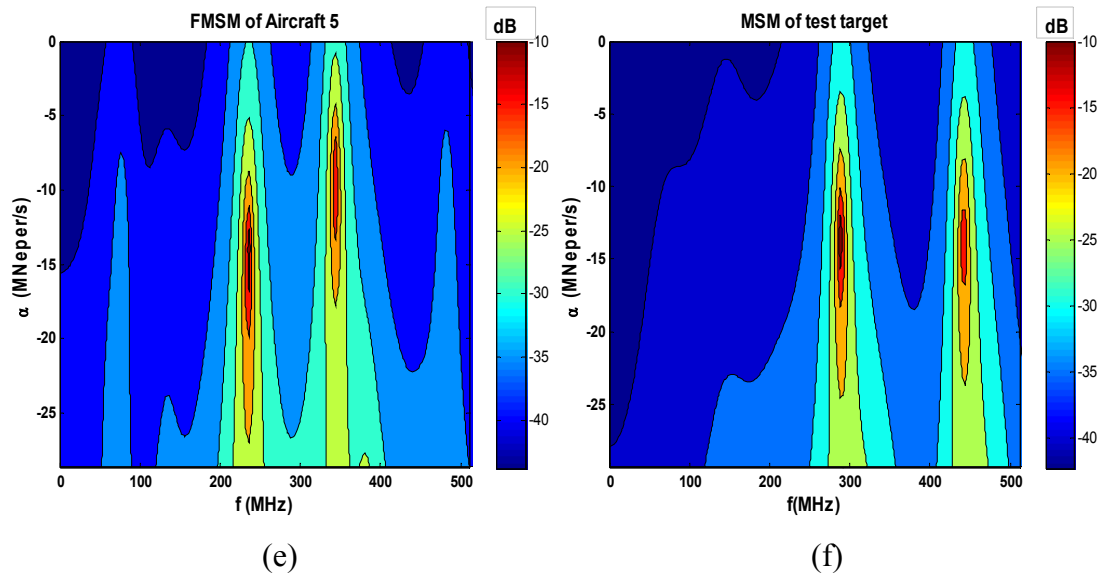
Figure 4.12   (a)-(e) The FMSM features of the small-scale aircraft targets for the classifier designed at 5-azimuth aspects using the ϕ-polarized data at θ= 60 degree elevation angle with SNR= 10 dB (f) the MSM of the test target (arbitrarily chosen as the aircraft 4) for ϕ-polarized data at θ= 60 degrees elevation and ϕ= 22.5 degrees azimuth angles with SNR= 10 dB.

The resulting aircraft-classifier is tested by a total of (5 targets) x (12 azimuth aspect angles) x (6 SNR levels) x (50 trials per SNR level)= 18000 noisy ϕ-polarized backscattered signals to begin with. As an example, the MSM for the aircraft 4 (P-7) at 22.5 degree computed over the optimal late-time interval of the classifier is shown in Figure 4.12(f). The matched correlation coefficient for this test target/aspect angle is computed as 0.8221 (between spectra of Figure 4.12(d) and Figure 4.12(f)) while the mismatched correlation coefficients are computed as 0.0994, 0.0232, 0.1668 and 0.0325 for Airbus, Boeing 747, Caravelle and Tu 154, respectively. In these initial tests, the elevation aspect angle of the test signals is intentionally kept constant at 60 degrees so that the results could be directly compared to the results in [86] closely mimicking the same classifier design/test conditions. (The effects of changing

elevation aspect and polarization of the test signals on the classifier performance will be investigated later in Section 4.3.3 and 4.3.4) The correct classification rates of this aircraft classifier are plotted in Figure 4.13 against various SNR values for two different decision criteria of the proposed method and the method in [86].
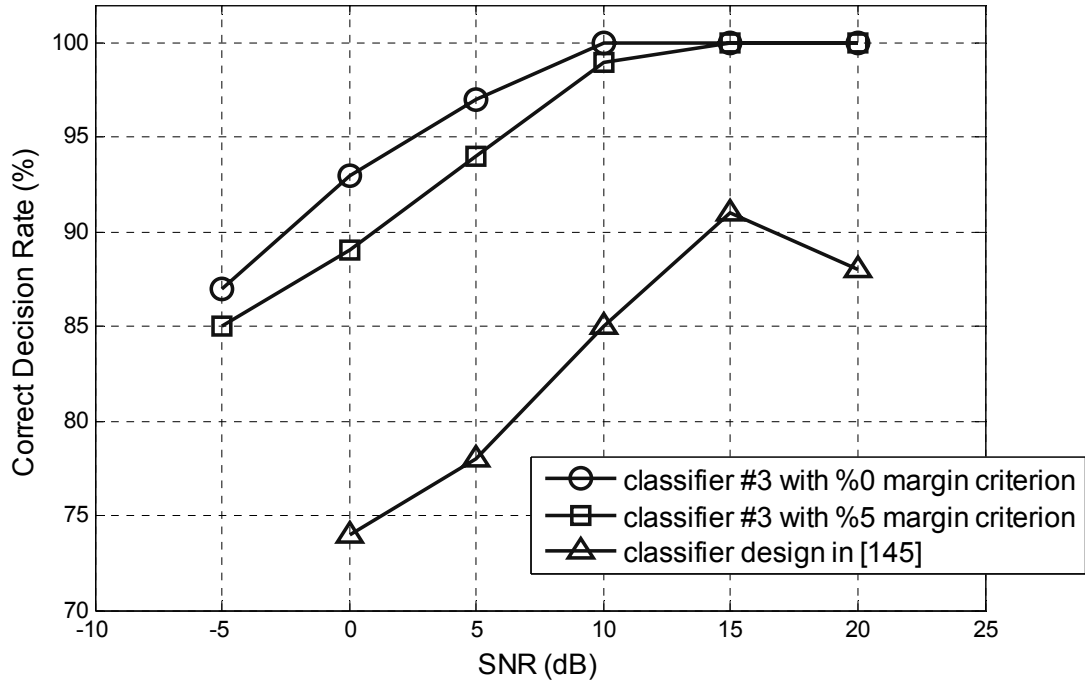
Figure 4.13   Correct decision rates demonstrated by the aircraft-classifier designed at 5-azimuth aspect angles using ϕ-polarized data at $\theta=60$ degree elevation angle with SNR= 10 dB for 0% margin and 5% margin decision criteria. These results are compared to the correct decision rates in [86] for the same set of aircraft targets.

In this figure, the accuracy rate is observed to be 100 percent for SNR levels as low as 10 dB. Accuracy rate gradually decreases to 93 percent at 0 dB SNR and drops to 87 percent at the worst case of -5 dB SNR with 0% margin criterion. These rates become 89 percent and 85 percent, respectively, by using the more demanding 5% margin decision criterion. Assuming that the correct classification rates of at least 90

percent are acceptable, from the results in Figure 4.13, it can be seen that the resulting aircraft classifier has successful classification performance even at SNR levels as low as 0 dB. Besides, from the results displayed in Table 4.1 and Figure 4.13, it can be concluded that the classifier designed for the conducting aircraft target set has higher accuracy rates as compared to the classifier designed for the conducting spheres because the conducting aircraft targets are higher-Q targets with more signal energy to be processed at later times. These results are also compared to the performance test results of the classifier designed in [86] revealing the fact that the accuracy rate of our technique is higher by about 15 percent accuracy at all SNR levels although our classifier design approach is much simpler and needs only 5 reference aspect angles (instead of 46 as used in [86]) during the design phase.

4.3.1. The Effect of the Design Parameter K_A on Classifier Performance

The number of reference aspect angles, K_A, is an important design parameter that should be chosen as small as possible for practical reasons but yet, it must be large enough to characterize the target properly. It is well known that a target's electromagnetic scattered response is highly aspect dependent but it does not change much within a few degrees of aspect angle in the resonance region. As previous experience has shown [23], 10-15 degrees of separation between the reference aspects would be adequate for a classifier design realized in the resonance region. Besides, especially when realistic targets of complex structures are considered, scattered data (directly measured or synthesized with high accuracy) may not be easily available at many different reference aspect angles. After choosing the value for the K_A parameter, specific determination of the reference aspect angle values may require some trial-and-error phase during the design procedure but they can be chosen usually in at most several trials without much trouble.

In this simulation example, the accuracy rates and noise behaviors of three different aircraft classifier desings are compared in Table 4.6 to show the effect of the design parameter K_A on classifier performance. The first classifier listed in Table 4.4 is the one already designed in the previous section by using ϕ-polarized data with 10 dB SNR at 5 reference aspects, (ϕ=5, 15, 30, 45 and 75 degrees) by about 15 degrees separation, where the elevation angle θ is kept constant at 60 degrees. The second and third aircraft-classifiers are newly designed for this example by using three reference aspects (ϕ= 15, 45 and 75 degrees) by about 30 degrees separation and four reference aspects (ϕ=5, 22.5, 45 and 67.5 degrees) by about 20 degrees separation, respectively, keeping all the other design parameters the same. All three classifiers are tested at various SNR levels using exactly the same test signal database of 18000 noisy signals as described in the previous section.

Table 4.6   The correct classification rates of the aircraft-classifiers designed in Section 4.3 by ϕ-polarized data with 10 dB SNR at θ=60^0 elevation with K_A= 3, 4 and 5 reference aspect angles in the azimuth. The classifiers are tested by ϕ-polarized data at θ=60^0; ϕ= 5, 10, 15, 22.5, 30, 37.5, 45, 52.5, 60, 67.5, 75, 82.5 degrees.

SNR Levels	20 dB		15 dB		10 dB		5 dB		0 dB		-5 dB	
Safety margin for decisions	0%	5%	0%	5%	0%	5%	0%	5%	0%	5%	0%	5%
K_A= 5, ϕ= 5, 15, 30, 45, 75	100	100	100	100	100	99	97	94	93	89	87	85
K_A= 4, ϕ= 5, 22.5, 45, 67.5	100	100	100	99	99	97	95	92	92	87	86	83
K_A= 3, ϕ= 15, 45, 75	99	98	97	94	93	91	89	86	85	82	80	77

As revealed by the results in Table 4.6, the performance of the four-aspect design is very close to that of the five-aspect design. Both classifiers have 100 percent accuracy rate at 20 dB SNR and a relative drop of 2 percent in maximum is observed in the accuracy rate of the four-aspect classifier at very low SNR levels. The three-aspect design, on the other hand, produces poor results especially at very low SNR levels with almost 8 percent decrease (as compared to five-aspect classifier) at the accuracy rate. This deterioration in classifier performance is pronounced especially for SNR levels of 10 dB and lower. Based upon these results, it can be concluded that, for the aircraft-classifier, choice of three aspects is insufficient, four aspects may be used but the five-aspect design gives slightly better results especially for highly contaminated test signals.

4.3.2. The Effect of the Design Parameter L on Classifier Performance

Another important design parameter is L, half of which denotes the estimated number of damped sinusoidal signals in the design data. Based on our experience with the MUSIC algorithm [26], an optimal value for the parameter L is around $m/2$. While the overestimation of L does not cause a serious problem but reduces the accuracy rate of the classifier very slightly (within tolerable limits), the underestimation of this parameter may cause serious deterioration in the classifier performance. To demonstrate this argument, in addition to the aircraft-classifier designed in Section 4.3 with L =16, three more classifiers are designed with L = 4, 8, and 24, keeping all the other design parameters the same. All these four classifiers are tested by the same test signal database of 18000 signals and their performance results are reported in Table 4.7.

Table 4.7   The correct classification rates of the aircraft-classifiers designed in Section 4.3 using ϕ-polarized data with 10 dB SNR at five aspect angles ($\theta=60^0$; $\phi=$ 5, 15, 30, 45 and 75 degrees) for various L values. The classifiers are tested by ϕ-polarized data at $\theta=60^0$ and $\phi=$ 5, 10, 15, 22.5, 30, 37.5, 45, 52.5, 60, 67.5, 75 and 82.5 degrees.

SNR Levels	20 dB		15 dB		10 dB		5 dB		0 dB		-5 dB	
Safety margin for decisions	0%	5%	0%	5%	0%	5%	0%	5%	0%	5%	0%	5%
L=24	100	100	100	100	99	98	95	94	92	88	86	84
L=16	100	100	100	100	100	99	97	94	93	89	87	85
L=8	100	100	99	98	98	96	94	92	91	88	85	82
L=4	98	97	94	91	89	88	86	84	82	79	77	74

It is seen that the performances of the classifier designs with L= 16 and L= 24 are very close to each other while a relative drop of 3 percent in accuracy is observed in the L= 8 classifier. The L= 4 classifier, on the other hand, turns out to be the worst case with 2-3 percent drop in accuracy at 20 dB SNR level and almost 11 percent drop in accuracy at -5 dB SNR level, as compared to the classifier with L= 16. In conclusion, choosing L very small may seriously deteriorate the classifier performance but this problem can be easily handled by increasing L to a value around $m/2$. The extra computational load due to choosing L larger is a negligible factor within the context of the whole design procedure.

4.3.3. The Aspect Invariance of Classifier Performance: Additional Tests for Elevation Aspect Angles

As indicated in previous chapters, the aspect invariance is a critical performance criterion for a target classifier. The aircraft classifier designed in Section 4.3 has been tested intensively for the aspect invariance with respect to azimuth angle but keeping the elevation angle fixed at 60 degrees which is already used for design. Now, in this example, that previously designed classifier will be tested at two different elevation angles, (θ= 30 and 45 degrees), which are not used in design procedure earlier. In this simulation, all reference aspect angles (θ= 60 degrees; ϕ= 5, 15, 30, 45 and 75 degrees), optimal late-time subinterval and FMSMs in feature database are the same with the classifier design of Section 4.3. Using two different elevation angles (θ= 30 and 45 degrees) and three azimuth angles (ϕ= 22.5, 37.5 and 60 degrees) at the SNR levels of 20, 15, 10, 5, 0 and -5 dB, a total of (5 targets) x (2 new elevation angles) x (3 azimuth angles) x (6 SNR levels) x (50 trials per SNR level)= 9000 additional noisy test signals are synthesized for this simulation. While the noiseless backscattered frequency responses corresponding to all (reference and test) aspect angles at θ= 60 degrees are generated by simulation program FEKO, the noiseless backscattered frequency responses corresponding to test aspect angles in this section (θ= 30 and 45 degrees; ϕ= 22.5, 37.5 and 60 degrees) are generated by simulation program Computer Science Technology (CST) Microwave Studio.

CST Microwave Studio is a general-purpose electromagnetic simulator dedicated to fast and accurate 3D EM Simulation of high frequency problems. This simulation program is based on Finite Integration Technique [113] which provides a universal spatial discretization scheme applicable to various electromagnetic problems ranging from static field calculations to high frequency applications in time and frequency domains. CST embeds a variety of different solvers operating in time and frequency domains. A key feature of CST Microwave Studio is the method on demand approach which allows using the simulator or mesh type that is best suited to a

particular problem. All simulators support hexahedral grids in combination with Perfect Boundary Approximation (PBA) Method. Since no method works equally well in all application domains, the software contains three different simulation techniques (transient solver, frequency domain solver, eigenmode solver) to best fit their particular applications. The most flexible tool is the transient (time domain) solver, which is based on the solution of the discretized set of Maxwell's Grid Equations. Transient solver allows the simulation of a structure's behavior in a wide frequency range in just a single computation run. Consequently, this solver is remarkably efficient for most kinds of high frequency applications such as scattered fields from a target. The field results for many frequencies can be obtained from a single simulation run [114].

The performance of the aircraft classifier regarding the attained correct classification rates for this new set of test signals is given in Table 4.8.

Table 4.8   Aspect invariance of the aircraft-classifier demonstrated via accuracy rates (in percentage): classifier is designed by ϕ-polarized data with 10 dB SNR at 5 aspect angles ($\theta=60^0$; $\phi= 5^0$, 15^0, 30^0, 45^0, 75^0) and tested using ϕ-polarized data at aspect angles $\theta=30^0$, 45^0, 60^0; $\phi= 22.5^0$, 37.5^0, 60^0.

SNR Levels	20 dB		15 dB		10 dB		5 dB		0 dB		-5 dB	
Safety margin for decisions	0%	5%	0%	5%	0%	5%	0%	5%	0%	5%	0%	5%
$\theta= 60^0$ elevation tests only	100	100	100	100	100	99	98	94	93	89	87	85
$\theta= 30^0$ and 45^0 elevation tests only	100	100	100	100	99	98	98	93	92	88	86	84

In this table, to make a fair comparison, the correct classification rates obtained for θ= 30 and 45 degrees are compared to those obtained for θ= 60 degree at the same azimuth angles of 22.5, 37.5 and 60 degrees. As revealed with strong confidence by the content of Table 4.6, the performance of the classifier (designed with data at θ= 60 degrees) remains almost the same at all SNR levels when it is tested at completely new elevation aspects of 30 and 45 degrees.

4.3.4. The Polarization Invariance of Classifier Performance

In this simulation example, the aircraft-classifier designed in Section 4.3 will be tested for polarization invariance that is also a very important performance criterion. This classifier, which is designed by ϕ-polarized backscattered data at 10 dB SNR, will be tested in this example by a total of 13500 newly generated θ-polarized ($\theta\theta$ polarization) noisy backscattered signal at various SNR levels (with 50 independent trials at each level) using the elevation/azimuth aspect angles (θ= 30, 45 and 60 degrees; ϕ= 22.5, 37.5, 60 degrees), which are not used in the design procedure at all. All these newly generated test signals are again obtained with CST Microwave Studio. The performance test results obtained under these different polarization conditions are presented in Table 4.9. Comparing the classifier's accuracy rates in Table 4.8 and Table 4.9, it is observed that the accuracy rate of the classifier remains to be 100 percent at the SNR level of 20 dB. As the noise level of test signals gets higher, i.e. as the SNR gets lower, accuracy of the classifier drops slightly. It becomes 96 percent on the average at 10 dB SNR level with a 2 percent drop due to polarization change. Even with the 5% margin criterion, the classifier's accuracy rate becomes 85 percent (after a 3 percent drop due to polarization change only) at 0 dB when the noise power is equal to the signal power at this extremely noisy case.

Table 4.9   Polarization invariance of the aircraft-classifier demonstrated via accuracy rates (in percentage): classifier is designed by ϕ-polarized data with 10 dB SNR at 5 aspect angles ($\theta=60^0$; $\phi= 5^0, 15^0, 30^0, 45^0, 75^0$) and tested using θ-polarized data at aspect angles ($\theta=30^0, 45^0, 60^0$; $\phi= 22.5^0, 37.5^0, 60^0$).

SNR Levels	20 dB		15 dB		10 dB		5 dB		0 dB		-5 dB	
Safety margin for decisions	0%	5%	0%	5%	0%	5%	0%	5%	0%	5%	0%	5%
Accuracy rates for θ-Polarization tests	100	100	99	98	98	96	95	90	89	85	84	81

As a worst-case testing example, the MSM feature computed over the optimal late-time interval [32, 96] nsec for an arbitrarily selected test signal (which happens to be the θ-polarized scattered signal belonging to the Aircraft (P-7), i.e. target 4, at $\theta=30$ degrees elevation and $\phi=22.5$ degrees azimuth angles with 5 dB SNR level) is shown in Figure 4.14. The matched correlation coefficient for this test scenario is computed to be 0.6411 (between the FMSM of Figure 4.12(d) and the MSM of Figure 4.14) while the mismatched correlation coefficients turn out to be 0.1212, 0.0575, 0.2038 and 0.0568 for Airbus, Boeing 747, Caravelle and Tu 154, respectively. In other words, the classifier correctly identifies the test target with a very large safety margin at this very low SNR level, although the classifier is tested at the worst condition where not only the polarization type but also the elevation, azimuth aspect angles and SNR level of the test data are totally different from the reference data used to design this aircraft classifier.
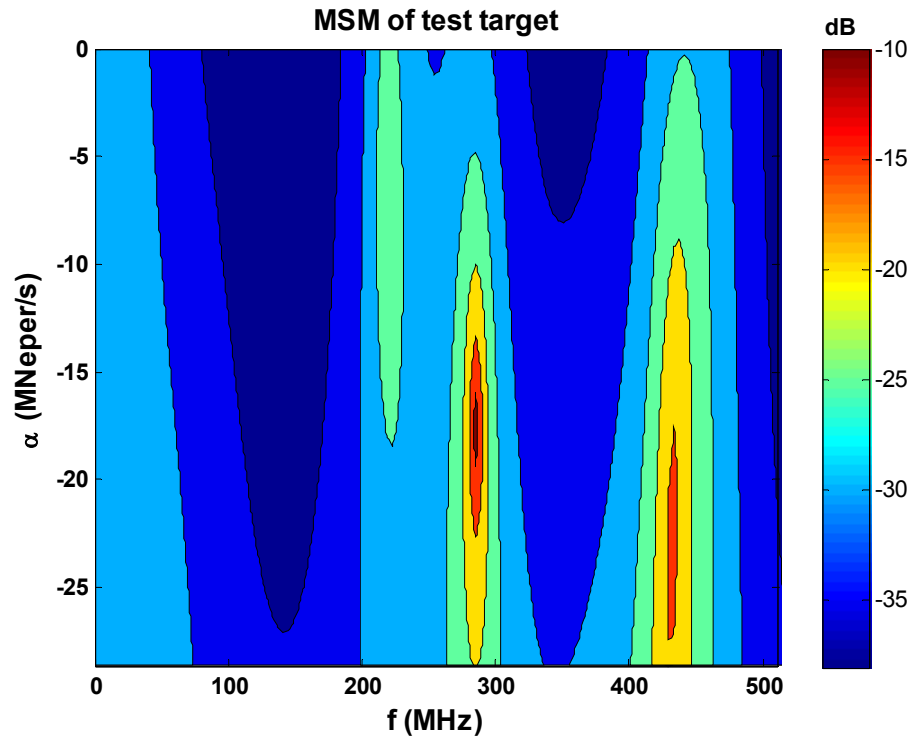
Figure 4.14 The MSM of the test target (arbitrarily chosen as the aircraft 4) for θ-polarized data at θ= 30 degrees elevation and ϕ= 22.5 degrees azimuth angles with SNR= 5 dB.

According to the results obtained from the simulations throughout Section 4.3, the designed aircraft-classifier displays a perfect aspect invariance (both in elevation and azimuth) and an almost perfect polarization invariance at all SNR levels (based on the results of more than 40,000 performance tests) although this 5 target-classifier is designed by reference data at only 5 different azimuth angles (at a fixed elevation and fixed polarization with 10 dB SNR level) using 25 scattered signals altogether.

4.4. The Classifier Design Simulations for Single Targets with Incomplete Frequency Domain Data

The resonance region target recognition methods, including the proposed method, are ultrawideband methods covering the effects of sufficiently large numbers of target poles. However, ensuring ultrawide frequency bandwidth while covering very low frequencies is difficult for the real-world target recognition applications since the practical antennas do not have this order of wide operating frequency bands. The ultrawide operating frequency bandwidth of a target recognition method should be reduced in order to be more compatible with the bandwidth of the practical antennas in radar systems. Therefore, the effect of frequency bandwidth (incomplete frequency domain data) on the accuracy performance of the target recognition method should be investigated and an optimum frequency bandwidth satisfying sufficient accuracy rate should be determined. This frequency bandwidth effect is mentioned in only a few studies in the literature [84], [115]-[117] and in these studies either this effect is only investigated for noiseless or low noise data [84], [115] or the method simply gives poor noise performance for all frequency bandwidths considered [116], [117].

The scattered frequency response containing frequency data starting from DC region (for 0-12 GHz bandwidth, for example) can be called as complete data. Studying with incomplete data, which do not include some portion of low frequencies (such as 1-12 GHz or 2-12 GHz bandwidths), is more realistic since the operating frequency bands of practical antennas do not include very low frequencies around DC region. However, dealing with incomplete data brings additional difficulties compared to using complete data in target classification due to the following reasons: The dominant target poles with small real parts are important in natural-resonance based target classification and they may be located in low frequency region for certain targets such as conducting spheres and thin wires By excluding the frequency response data at low frequencies, important contributions of these dominant poles

91

(falling into the excluded frequency region) are totally lost. Besides, bandpass Gaussian windowing used prior to IFFT operations in the case of incomplete (i.e. bandpass) data further attenuates the frequency information around the lower edge of the available frequency band. Therefore, contributions of the dominant poles close to lowest frequency of the operating band are dramatically reduced due to windowing. Then, only the effects of the poles placed comparably in the middle region of the frequency band are dominantly observed in the time domain response. Information loss caused by the incomplete data conditions may become very serious if most of the dominant target poles fall in the missing data region depending on the geometry and material composition of the targets. In this section, the performance results of the classifier designs in Section 4.1, 4.2 and 4.3 with respect to different frequency bandwidths will be reported.

4.4.1. Classifier Designs for Perfectly Conducting Spheres and Lossless Dielectric Spheres with Incomplete Frequency Data

In this simulation, effects of frequency bandwidth on classifier performance are examined for two different target library; first for the set of three perfectly conducting spheres (r= 1.8, 2.4 and 3 cm) in Section 4.1 and then, for the set of three lossless dielectric spheres (r= 1.8 cm, ε_r=2, 3, 4) used in Section 4.2. Not only the problem geometries but also the choice of testing and reference aspect angles used for these two new classifier designs are exactly the same as those used in Section 4.1 and 4.2. The far field scattered responses of the library targets are computed in frequency domain over the frequency bands of (1-12 GHz), (2-12 GHz) and (3-10 GHz) with frequency resolution of 13.75 MHz by truncating frequency responses for (0-12 GHz). The incomplete frequency band (1-12 GHz) is the same as the band of measurements to be used in Chapter 5. The noisy scattered time-domain signals at all aspect angles for each bandwidth are again synthesized at the same SNR levels for both conducting and dielectric spheres. By using the same MUSIC parameters and subintervals as those used in Section 4.1, the optimal late-time subintervals for

92

conducting spheres are found as [2.4, 3.04 nsec] for the frequency bands of (1-12 GHz) and (2-12 GHz), and [2.56, 2.88] nsec for the band (3-10 GHz). The FMSM features of the conducting sphere with 1.8 cm radius are given in Figure 4.15(a)-(d) for frequency bands (0-12 GHz), (1-12 GHz), (2-12 GHz), (3-10 GHz), respectively.

(a)   (b)

(c)   (d)
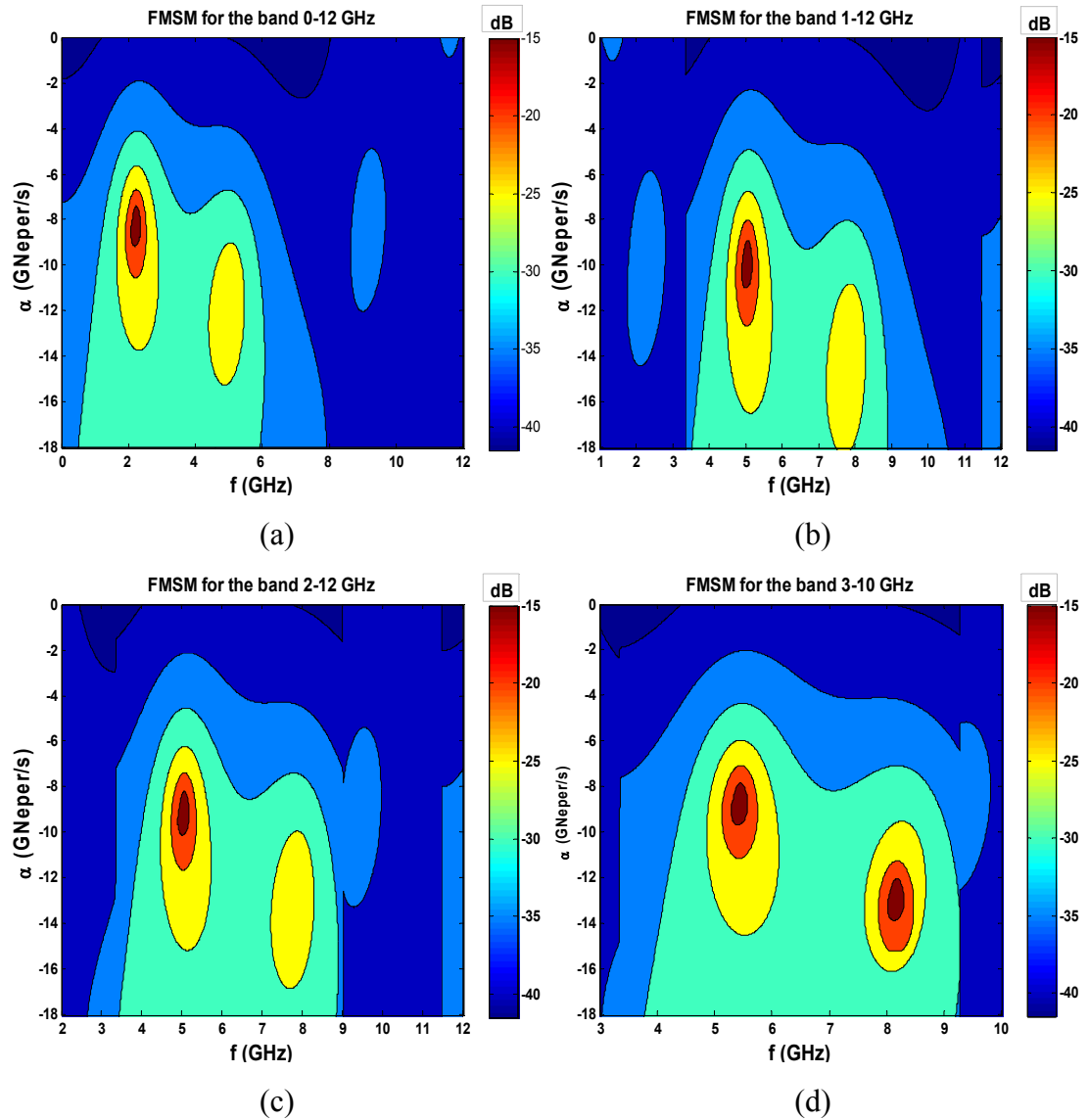
Figure 4.15   (a)-(d) The FMSM features of the conducting sphere with 1.8 cm radii for the frequency bands 0-12 GHz, 1-12 GHz, 2-12 GHz and 3-10 GHz.

It should be noted that the FMSMs for conducting and dielectric sphere targets are again constructed with SNR levels of 10 dB and 5 dB, respectively. From the FMSMs in Figure 4.15, it can be observed that the most dominant pole for the complete data (0-12 GHz) appears around 2 GHz but the resonance associated with this pole attenuates and further vanishes as the frequency band becomes narrower. In the meantime, poles in the middle of the frequency band (around 5 GHz and 8 GHz) start showing their effects more strongly. With the same approach, the optimal late-time subintervals for dielectric spheres are found as [2.56, 2.88] nsec for the bands of (1-12 GHz) and (3-10 GHz) and as [2.56, 3.20] nsec for the band of (2-12 GHz). A total of (3 targets) x (12 bistatic aspect angles) x (5 SNR levels) x (10 trials at each SNR level)= 1800 noisy scattered test signals for each frequency band are generated for performance tests of each of these libraries. The correct decision rates of conducting and dielectric sphere sets for each frequency band, including the complete data band (0-12 GHz) with 10 trials at each SNR levels are given in Table 4.10 and Table 4.11, respectively.

Table 4.10   The correct classification rates (in percentage) of perfectly conducting sphere classifiers designed at 10 dB SNR for different frequency bands.

SNR Levels	20 dB SNR		15 dB SNR		10 dB SNR		5 dB SNR		0 dB SNR	
Safety margin for decisions	0%	5%	0%	5%	0%	5%	0%	5%	0%	5%
Frequency Band 0-12 GHz	100	100	98	97	94	91	89	85	83	80
Frequency Band 1-12 GHz	100	100	97	96	92	90	86	84	80	78
Frequency Band 2-12 GHz	100	99	95	93	89	87	84	81	79	77
Frequency Band 3-10 GHz	99	97	92	91	86	83	82	79	75	72

Table 4.11   The correct classification rates (in percentage) of dielectric sphere classifiers designed at 5 dB SNR for different frequency bands.

SNR Levels	15 dB SNR		10 dB SNR		5 dB SNR		0 dB SNR	
Safety margin for decisions	0%	5%	0%	5%	0%	5%	0%	5%
Frequency Band 0-12 GHz	100	100	97	94	91	88	86	82
Frequency Band 1-12 GHz	100	100	96	93	91	87	86	81
Frequency Band 2-12 GHz	100	99	95	93	89	85	84	79
Frequency Band 3-10 GHz	100	98	95	92	90	85	82	78

From the results displayed in Table 4.10 and Table 4.11, it can be concluded that as the frequency data gets more incomplete, the classification problem becomes more difficult and the correct classification rate degrades. However, the decrease in accuracy rates is faster for the conducting sphere classifier as compared to the dielectric sphere classifier. While the accuracy rates of dielectric sphere classifiers designed for (0-12 GHz) and (1-12 GHz) bands are almost the same, there are 2 or 3 percent differences in the accuracy rates of the conducting sphere classifiers over these designed bands. This is due to fact that the dominant poles of conducting spheres appear at the lower frequencies covered by the complete frequency band of (0-12 GHz) (i.e. the pole at 2 GHz). The same argument does not hold for the dielectric spheres, as their dominant poles are not located only at lower frequencies. Therefore, the accuracy rates of the dielectric sphere classifiers are not affected much by the incomplete frequency band conditions. However, there exists no dramatic decrease in accuracy rates for both target sets under these incomplete data tests and it

is concluded that the performance of the method is not so sensitive to frequency bandwidth for these spherical target sets.

4.4.2. The Classifier Designs for Small-Scale Aircraft Targets with Incomplete Frequency Data

In this experiment, performance of the proposed classifier design method is demonstrated for a target set of five small-scale aircraft described in Section 4.3. An alien aircraft (DC-10), which is not one of the targets in the training set of the training set of the classifier, is also used as a test target in the following simulations. The aim of these simulations is to classify all five aircraft in the target set while discriminating DC-10 as an outsider test target. The dimensions for the wire models (i.e. the body, wing and tail lengths) of six aircraft targets are given in Table 4.12.

Table 4.12   The dimensions of the small-scale aircraft targets used in the simulations in Section 4.4.2.

Substructure	Target 1 Airbus	Target 2 Boeing-747	Target 3 Caravelle	Target 4 P-7	Target 5 Tu 154	Target 6 DC-10
Body length (m)	0.5408	0.7066	0.3200	0.3435	0.4790	0.6342
Wing length (m)	0.4484	0.5964	0.3440	0.3250	0.3755	0.5348
Tail length (m)	0.1626	0.2217	0.1092	0.1573	0.1340	0.2437

As seen in this table, dimensions of the alien target (target 6) and the library target 2 are so similar that the presence of alien target in the test bench may seriously affect the decision accuracy of the classifier. The ϕ-polarized ($\phi\phi$ polarization)

backscattered responses of targets are again numerically generated at the aspect angles of ϕ= 5, 10, 15, 22.5, 30, 37.5, 45, 52.5, 60, 67.5, 75 and 82.5 degrees and at θ= 60 degree for complete and incomplete data of (0-1024 MHz), (100-1024 MHz), (200-1024) MHz and (300-800 MHz) frequency bands with Δf = 4 MHz for all cases. For the sake of noise analysis, the targets' time-domain scattered data are again synthesized at the SNR values of 20, 15, 10, 5, 0 and -5 dB. The feature database of the classifier is constructed at 10 dB SNR level for only the first five aircraft at five aspect angles (ϕ= 5, 15, 30, 45 and 75 degrees) out of 12 different aspect angles. In the design step of determining the optimal late-time intervals, the same MUSIC parameters and subintervals used previously in Section 4.3 are chosen. The optimal late-time interval is obtained for each frequency band by searching for r_{total} value. As an example, r_{total} values of subintervals for (300-800 MHz) band at SNR= 10 dB are given in Figure 4.16.
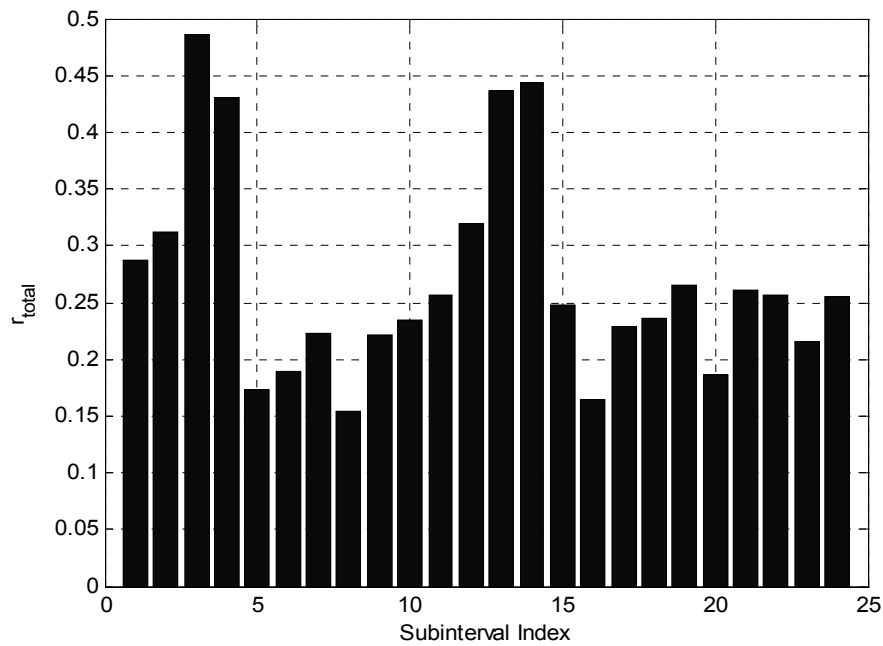
Figure 4.16   The r_{total} values of the classifier design for small-scale aircraft targets at the frequency band (300-800 MHz) and at SNR= 10 dB.

The optimal late-time interval is found to be [16-48 nsec] (corresponding to index 3 in Figure 4.16) for the (300-800 MHz) band as well as the (100-1024 MHz) band. For the (200-1024 MHz) band, on the other hand, the optimal late-time interval is found to be [8-40 nsec] for band. The FMSM target features computed for the (300-800 MHz) frequency band and optimal late-time interval [16-48 nsec] are shown in Figure 4.17(a)-(e).
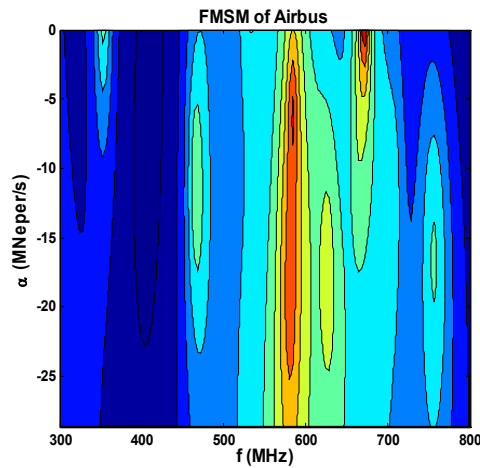
Figure 4.17(a)
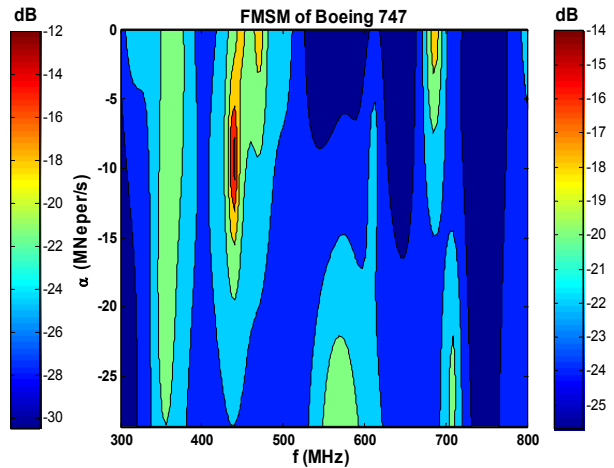
Figure 4.17(b)
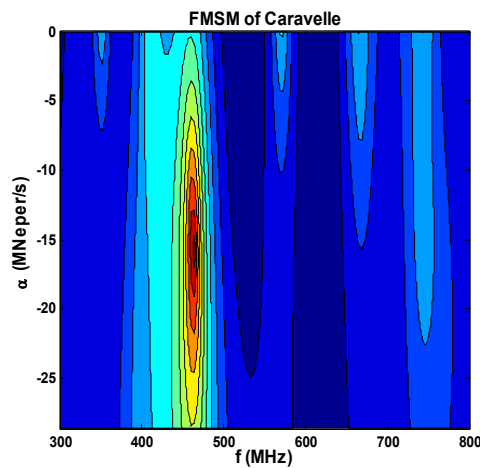
Figure 4.17(c)
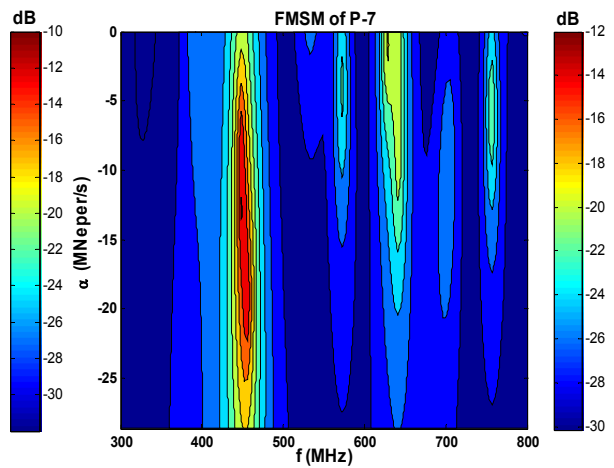
Figure 4.17(d)
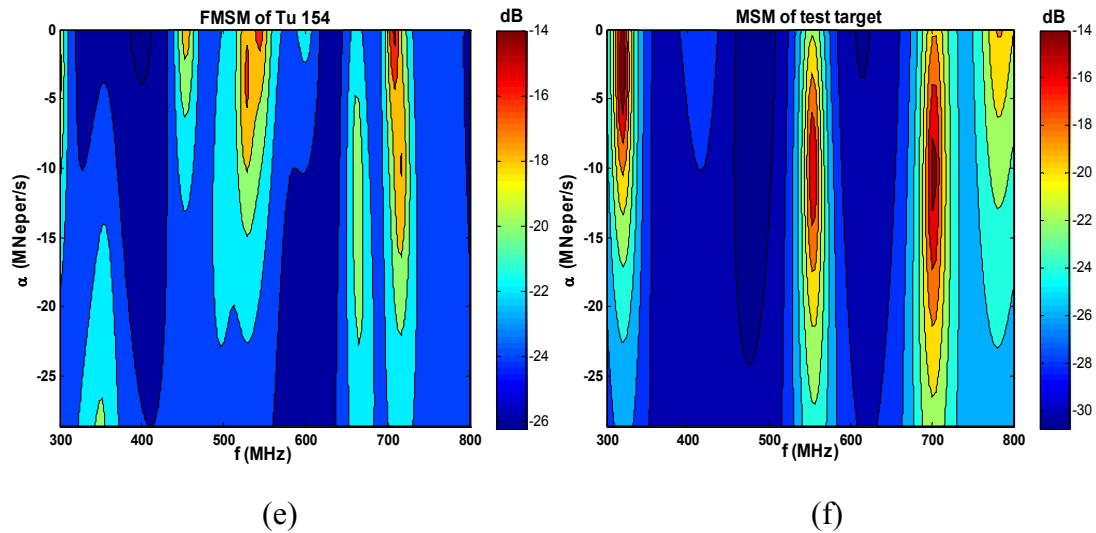
Figure 4.17   (a)-(e) The FMSM features of the small-scale aircraft targets for the frequency band (300-800 MHz) and at SNR= 10 dB (f) the MSM of the test target (arbitrarily chosen as Tu 154) for ϕ= 52.5 degrees azimuth angle with SNR= 5 dB.

The approximate peak locations of the power distributions of candidate targets for the (300-800 MHz) frequency band can be easily distinguishable in these figures. As indicated in Section 4.3, the peak locations of power distributions for complete data of (0-1024 MHz) are found at the frequencies about 200 and 300 MHz for Airbus, 155 and 230 MHz for Boeing 747, 330 and 450 MHz for Caravelle, 290 and 430 MHz for P-7, 235 and 345 MHz for Tu 154. However, when the frequency band is reduced to 300-800 MHz, as seen in Figure 4.17(a)-(e), the contributions of poles located lower than 300 MHz are lost and the effects of poles around 300 MHz are fairly reduced. Thus, only, the contributions of poles sufficiently far away from 300 MHz (450 MHz in Caravelle and 470 MHz in P-7) are preserved and new resonance contributions become dominant in the FMSMs patterns. After completing the classifier design, the resulting classifier is tested for a total of (6 targets) x (12 aspect angles) x (10 trials)= 720 signals at each SNR level. As an example, the MSM for Tu 154 at 52.5 degree and SNR= 5 dB computed over the optimal late-time interval is

shown in Figure 4.17(f). The matched correlation coefficient for this test target/aspect is computed as 0.5701 (between spectra in Figure 4.17(e) and Figure 4.17(f)) while the mismatched correlation coefficients are computed as 0.3672, 0.4199, 0.1422 and 0.1889 for Airbus, Boeing 747, Caravelle and P-7, respectively. The overall correct classification rate of the aircraft classifiers designed for four frequency bands and tested for various SNR levels using two different decision criteria are given in Table 4.13. The confusion matrices[a] obtained for (100-1024 MHz), (200-1024 MHz) and (300-800 MHz) frequency bands (with SNR= 5 dB and for the 0% margin case are) given in Table 4.14, Table 4.15 and Table 4.16, respectively.

Table 4.13   The   correct   classification   rates   (in   percentage)   of   the aircraft-classifiers designed with 10 dB SNR for different frequency bands.

SNR Levels	20 dB		15 dB		10 dB		5 dB		0 dB	
Safety margin for decisions	0%	5%	0%	5%	0%	5%	0%	5%	0%	5%
Frequency Band 0-1024 MHz	100	100	100	100	100	99	97	94	93	89
Frequency Band 100-1024 MHz	100	100	98	97	97	95	94	91	90	87
Frequency Band 200-1024 MHz	100	99	97	95	93	91	91	88	87	84
Frequency Band 300-800 MHz	99	98	95	92	89	87	85	82	83	80

[a] The confusion matrix is simply a square matrix that shows the number of accurate classifications and the number and type of misclassifications of the classifier given the test targets and the classifier decisions [118].

Table 4.14   The confusion matrix of the aircraft-classifier designed for the (100-1024 MHz) frequency band and tested at SNR= 5 dB with the decision criterion of 0% margin (the overall decision rate of the classifier is 94.02 percent).

Test Targets ⇓	Decision					
	Airbus	Boeing 747	Caravelle	P-7	Tu 154	DC-10 (Alien target)
Airbus	114	4	0	0	2	0
Boeing 747	3	113	0	0	3	1
Caravelle	0	0	112	7	1	0
P-7	0	0	7	112	0	1
Tu 154	3	2	1	2	112	0
DC-10 (Alien target)	2	3	0	0	1	114

Table 4.15   The confusion matrix of the aircraft-classifier designed for the (200-1024 MHz) frequency band and tested at SNR= 5 dB with the decision criterion of 0% margin (the overall decision rate of the classifier is 90.97 percent).

Test Targets ⇓	Decision					
	Airbus	Boeing 747	Caravelle	P-7	Tu 154	DC-10 (Alien target)
Airbus	109	6	0	0	4	1
Boeing 747	5	110	1	0	3	1
Caravelle	1	0	109	9	1	0
P-7	0	0	9	108	2	1
Tu 154	3	4	1	2	109	1
DC-10 (Alien target)	3	5	0	0	2	110

Table 4.16   The confusion matrix of the aircraft-classifier designed for the (300-800 MHz) frequency band and tested at SNR= 5 dB with the decision criterion of 0% margin (the overall decision rate of the classifier is 85.27 percent).

Test Targets ⇓	Decision					
	Airbus	Boeing 747	Caravelle	P-7	Tu 154	DC-10 (Alien target)
Airbus	103	9	0	0	6	2
Boeing 747	9	104	1	0	4	2
Caravelle	1	0	100	16	3	0
P-7	0	0	15	101	3	1
Tu 154	5	8	2	2	102	1
DC-10 (Alien target)	5	7	0	1	3	104

From the results displayed in Table 4.13, it can be concluded that as the frequency data gets more incomplete, the classification problem becomes more difficult and the correct classification rate degrades. However, even in the case of most challenging frequency band (300-800 MHz), for which the bandwidth is shrinked to almost fifty percent of the complete bandwidth of (0-1024 MHz), the accuracy rate is above 80 percent for SNR levels exceeding 0 dB. This superior noise performance is the result of using noisy reference data in classifier design. Besides, the accuracy rates for the identification of DC-10 aircraft as an alien target is also similar to the overall accuracy rates in Table 4.13 (i.e. while the overall accuracy rate in Table 4.16 is 85.27 percent (614/720), it is 86.66 percent (104/120) for the DC-10 aircraft) that shows the capability of the classifier to discriminate an alien target successfully.

CHAPTER 5

APPLICATIONS AND RESULTS FOR SINGLE TARGET RECOGNITION USING MEASURED SCATTERED FIELD DATA

In order to be suitable for real-time applications, a target recognition method should be proven to give satisfactory results in classifying realistic targets under real world sensing conditions. Thus, in this chapter, the performance of the proposed target recognition method is demonstrated by several classifier designs for realistic single target types whose scattered fields are obtained by measurements. The measurement setup constructed in METU Millimeter and Microwave (MMW) Laboratory for obtaining measured scattered fields of the targets is described in detail in Section 5.1. The properties of the vector network analyzer (VNA) and the wideband double ridge horn antennas used in the measurement setup are also mentioned in this section. In Section 5.2, a classifier design example involving four thick dielectric rods with the same dimensions but different permittivities is demonstrated. The scattered fields of these targets are measured for a constant polarization with the setup described in Section 5.1. The performance analysis for different frequency bands of this classifier design is also presented in this section. Another design example, which also uses the same measurement setup for scattered fields, is provided for three small-scale aircraft targets in Section 5.3. The targets in this section are not simple models constructed by thin wires as the targets used in Section 4.3 but they are small-scale models of actual aircraft targets. In the last section, another target classifier is designed for two

small-scale aircraft targets (again small-scale models of real aircraft targets) whose scattered fields are obtained by using the measurement setup at the ElectroScience Laboratory of the Ohio State University. In this section, since the measured scattered fields of the targets for different polarizations are available, the polarization invariance of the proposed method is also investigated for a target set using measurement data.

5.1. The Measurement Setup at METU Millimeter and Microwave (MMW) Laboratory

In order to measure the scattered signals of library targets, a measurement setup is constructed in Millimeter and Microwave Laboratory. The measurement setup contains a vector network analyzer (HP 8720D), two wideband ridge horn antennas and a foam structure on which the target is placed. The target lies on H-planes of the antennas (xz plane in Figure 5.1) and the center of target is 95 cm away from the centers of both antennas. The reason of choosing this distance will be explained in Section 5.1.3. The antennas are placed as to form 10 degree bistatic angle with the center of target. The antennas' positions are kept fixed during the measurements and the target on the foam structure can be rotated with respect to its center by changing the azimuth angle. The vector network analyzer (VNA) is behind the antennas and its both ports are attached to both antennas (port 1 is attached to transmitter antenna and port 2 is attached to receiver antenna). The scattered fields are measured with the transmission coefficient (S_{21}) parameter of the vector network analyzer. The schematic view of the measurement setup and the photographs of antennas-target configuration and antennas-network analyzer configuration of the setup are given in Figure 5.1, Figure 5.2(a) and Figure 5.2(b), respectively.
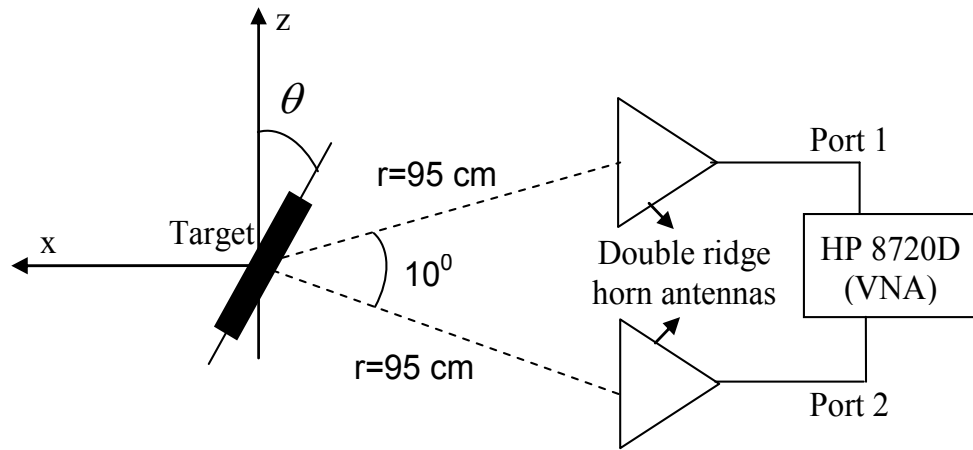
Figure 5.1   The schematic top view of the measurement setup.
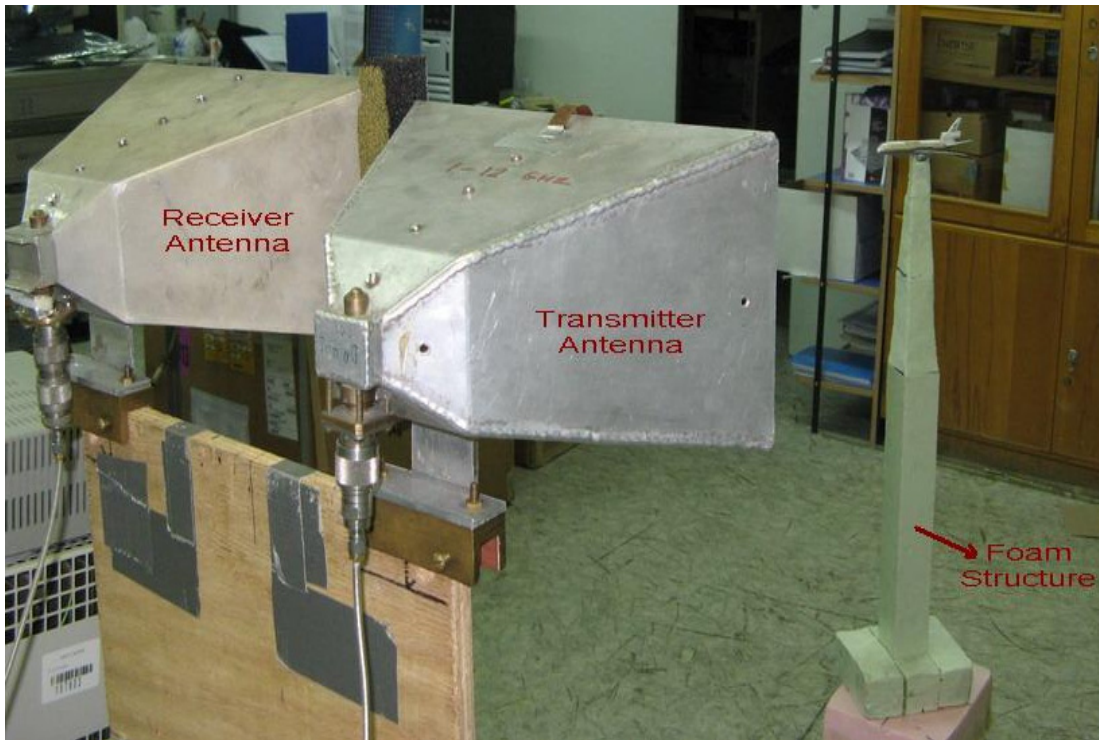
Figure 5.2(a)
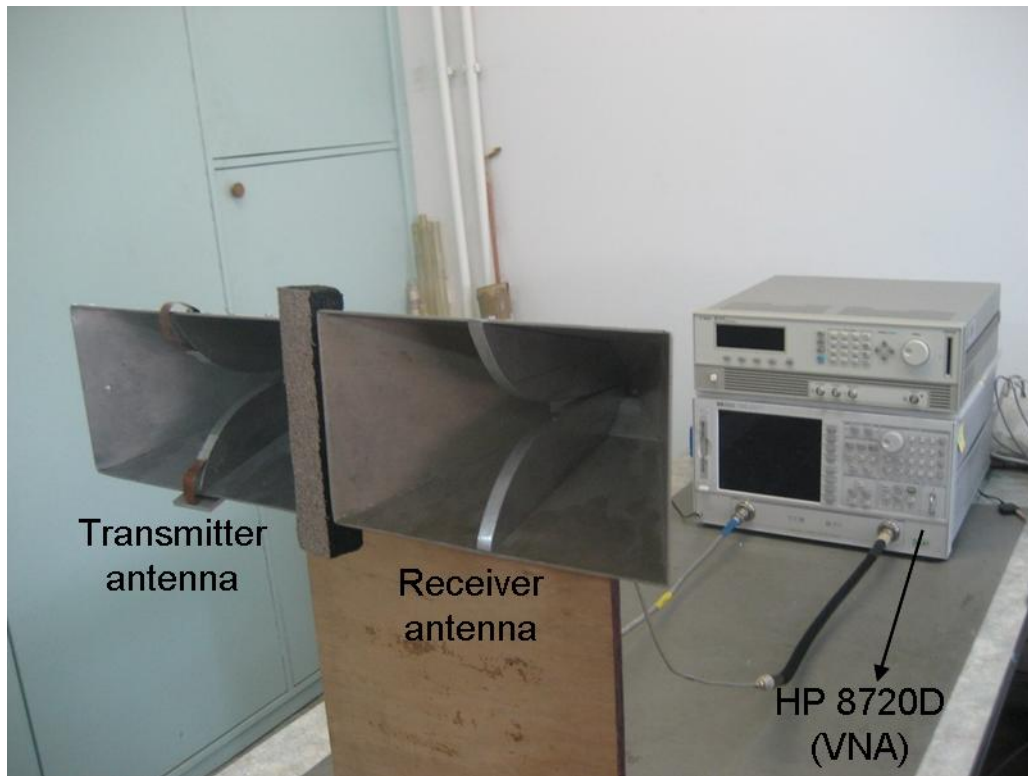
(b)

Figure 5.2   The photographic views of the measurement setup (a) the antennas and target configuration (b) the antennas and vector network analyzer configuration.

Since there are two separate antennas (one transmitter and one receiver) in the setup, only the bistatic scattered responses of the targets can be measured. Initially, a different measurement setup for monostatic scattered field measurements was considered using a single antenna and a circulator to separate the incident and reflected fields. The responses were again measured with the transmission coefficient (S_{21}) parameter of the vector network analyzer. However, due to high noise and high circulator leakage level, this setup was abandoned. Although the current setup in Figure 5.1 has a configuration for bistatic response measurements with fix antenna positions, it can be thought as measuring almost monostatic (backscattered) responses of the targets since the bistatic angle between the antennas is as small as 10

degrees. In this setup, in addition to keeping the antennas' positions fixed, the antennas can not be rotated with respect to its center. Therefore, both antennas have constant polarizations (V polarization) that the measurement setup can only measure VV polarization responses of the targets. Two main components of this measurement setup, which are horn antennas and HP 8720D vector network analyzer, and the process of obtaining measured signals are explained in the following sections.

5.1.1. The Double Ridge Horn Antennas

The antennas used in this setup are double ridged horn antennas which is shown in Figure 5.3 where antenna on the left is the transmitting antenna and antenna on the right is the receiving antenna.

Figure 5.3   The double ridge horn antennas used in the measurement setup (left hand side antenna is the transmitting antenna; right hand side antenna is the receiving antenna).

The antennas were previously designed by Prof. Dr. Altunkan Hızal to operate within the frequency band 1-12 GHz. Indeed, at the frequencies higher than 12 GHz and lower than 1 GHz, the input return losses are higher and the gains of both antennas are lower as compared to the band 1-12 GHz. As shown in Figure 5.4, the input return losses of the antennas within 1-12 GHz are below -10 dB which means that a minimum of 90 percent of the transmitted power is transferred to the antennas.
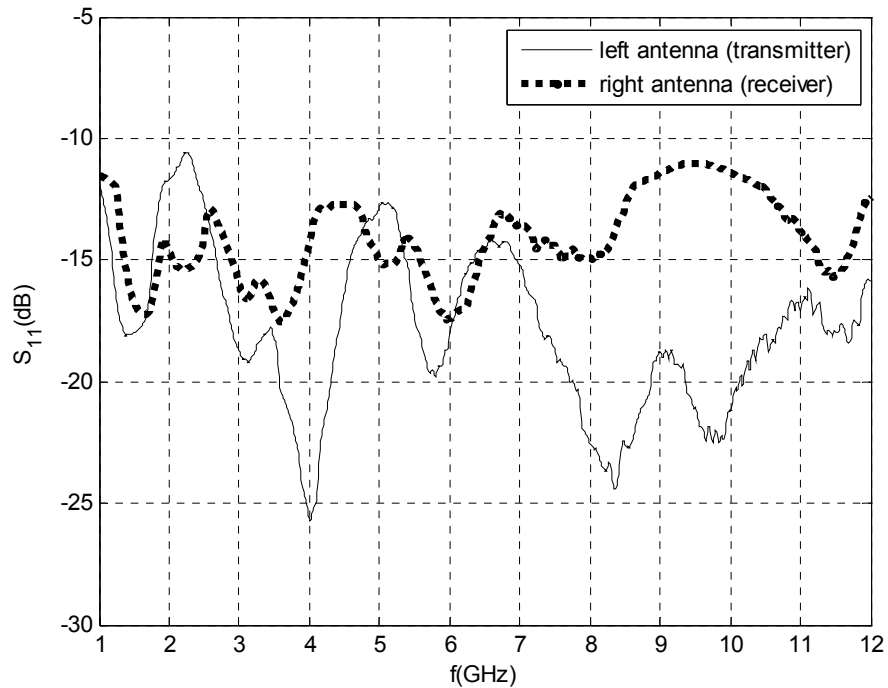
Figure 5.4   The input return loss graphs of the horn antennas in the setup.

As a result, the operating frequency band of the measurement setup is assigned to be (1-12 GHz). The horn antennas shown in Figure 5.3 have 27 cm maximum linear dimensions and there is an absorber placed between them in order to decrease mutual coupling which also causes interference like noise. The thickness of the absorber is arranged to minimize the mutual coupling and the distance between horn antennas is arranged to obtain minimum distance between the antennas for minimum bistatic

angle of the setup. However, since there is a trade-off between mutual coupling and the distance between the horn antennas, the thickness of the absorber and the distance between the horn antennas are optimized that the absorber thickness is 3 cm and the distance between antennas is 26 cm. For these values, the mutual coupling between antennas is below -60 dB within most of the frequency band (1-12 GHz) as shown in Figure 5.5.
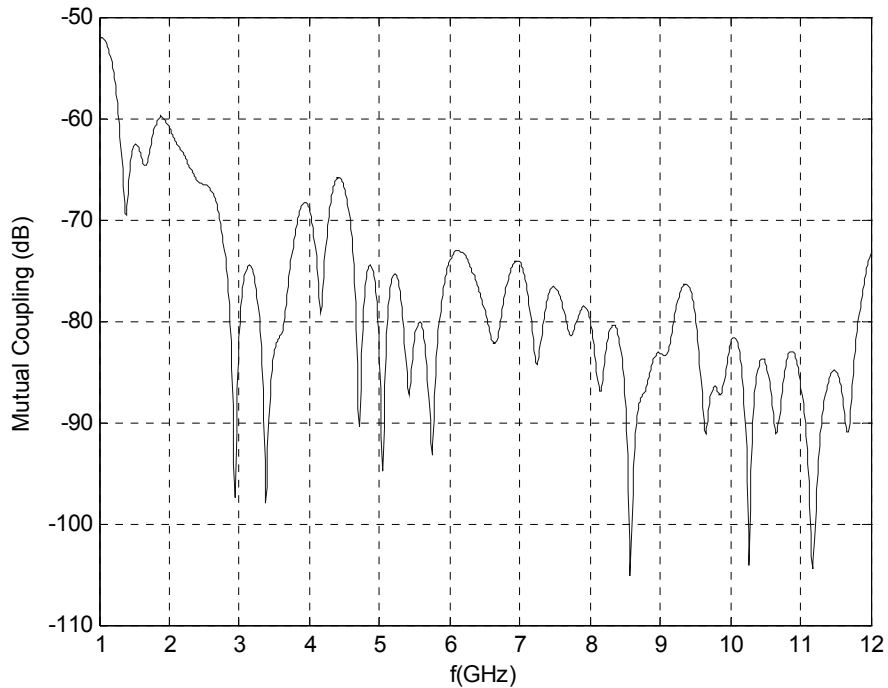
Figure 5.5   The mutual coupling between the horn antennas.

5.1.2.   HP 8720D Vector Network Analyzer (VNA)

The HP8720D vector network analyzer, which is shown in Figure 5.6, is a high performance vector network analyzer for laboratory or production line measurements of reflection (S_{11} and S_{22}) or transmission (S_{21} and S_{12}) parameters [119].

Figure 5.6   HP 8720D Vector Network Analyzer.

It integrates a high resolution synthesized RF source, an S parameter test set and a dual channel three-input receiver to measure and display magnitude, phase and group delay responses of active and passive RF networks in frequency and time domains. Two independent display channels and a large screen color display show the measured results of one or both channels, in rectangular or polar/Smith chart formats. In measurements, the vector network analyzer mainly measures the frequency domain response of the test setup paramaters between 50 MHz and 20.05 GHz with 201, 401, 801 or 1601 sample points (i.e. it is 1-12 GHz with 801 points in the measurement setup used in this thesis). Then, if desired, the frequency response of a certain parameter is converted to time domain with a software in the analyzer's internal computer described in Section 5.1.2.1.

The accuracy of network analysis is greatly influenced by factors external to the network analyzer. Components of the measurement setup, such as interconnecting cables, probes and adapters, introduce variations in magnitude and phase that can mask the actual response of the device under test, so calibration (error-correction) is required during the testing.

Making calibration (error-correction) is just trying to calculate the errors inserted by the measurement device parts or discontinuities at the connection of those parts. For this purpose, some devices with well-known characteristics such as short circuit are measured first and their responses are compared with the ideal expected characteristics. From the difference between the ideal and the measured results of these known devices, the errors inserted by the whole measurement system is calculated, and in a sense "subtracted" from the response of the real device to be measured.

In measurements with VNA, the following system characteristics may be affected by the amplitude at device input: frequency response accuracy, directivity, crosstalk (isolation), source match, load match errors. There are several different calibration techniques in the literature [120] which all use different models and require different calibration standards (known devices) to calculate and remove some or all (six errors with two ports) of the systematic errors. The standard short-open-load-thru (SOLT) full 2-port correction, where the names short-open-load-thru are the names of the calibration standards utilized during the calibration method, used in the measurement of the scattered fields to effectively remove all twelve correctable systematic errors.

5.1.2.1. Transformation of Measurements from Frequency to Time Domain

As indicated previously, the network analyzer first measures the response of a test device as a function of frequency and then transforms these measurements to time domain synthetically to obtain the time domain response. The transformations used

by the analyzer resemble those used in time domain reflectometry (TDR) measurements. TDR measurements, however, are made by launching an impulse or step signal into the test device and observing the response in time with a receiver similar to an oscilloscope. In contrast, the analyzer makes swept frequency response measurements, and mathematically transforms the data into a TDR-like display. The signal processing tool used for this transformation is the inverse chirp Z-transform [121] which is more flexible than classical IFFT such that while the time resolution of classical IFFT is fixed, it is variable for inverse chirp Z-transform. In time domain, the analyzer displays the response with a constant number of sample points which is the same as the number of sample points used in frequency domain, i.e. 801 in our measurements, over the selected time interval. Thus, the time resolution changes with the selected time interval which reveals the necessity of using a signal processing tool with variable time resolution. For the network analyzer we used, the time domain response of a test setup is equal to IFFT of frequency response only

when the time interval is selected as [0, $\dfrac{1}{2\Delta f}$] sec where $\Delta f = \dfrac{Frequency\,span}{\#\,of\,point}$ is

the frequency resolution of the system. By using the inverse chirp Z-transform, the analyzer obtains received time signals as if it generates and sends a pulse signal and then measures the received time signal. However, while transforming into time domain, the analyzer takes one sided inverse chirp Z-transform that the resulting time signal displayed in the analyzer is complex. The artificial transmitted pulse has the

form of $e^{j2\pi f_m t} p(t)$, where f_m is the center of operating frequency band and $p(t)$

is a purely real synthesized pulse. The received time signal has the form of $e^{j2\pi f_m t} h(t)$ where $h(t)$ can be complex or real. The genuine time response can be

found by $2\,Re\{e^{j2\pi f_m t} h(t)\}$ which can be thought as the time response of the system

to a real transmitted pulse of $2\,Re\{e^{j2\pi f_m t} p(t)\} = 2\cos(2\pi f_m t)p(t)$. Without any

windowing in frequency domain the network analyzer produces rectangular shape pulse in frequency domain (it produces signals having the same power level for all

frequencies) and the artificially synthesized pulse $p(t)$ has a $\frac{sin(kt)}{(kt)}$ shape. However, although this form of the synthesized pulse has narrowest beamwidth, it causes overshoot and ringing in the time domain response because of the abrupt transitions in the frequency domain measurements at the start and stop frequencies which is known as the Gibbs phenomenon. This has two effects limiting the usefulness of time domain measurements:

- Finite impulse width: Finite impulse width limits the ability to resolve between two closely spaced responses. The effects of the finite impulse width cannot be improved without increasing the frequency span of the measurement.

- Sidelobes: The impulse sidelobes limit the dynamic range of the time domain measurement by hiding low level responses within the sidelobes of higher level responses. The effects of sidelobes can be improved by windowing.

In order to balance these effects, the network analyzer has the windowing option. In windowing, the network analyzer rearranges the frequency response of the measured frequency response data by multiplying the frequency response of window by the measured frequency response data then taking its inverse chirp Z-transform (ICZT) to find the time domain response of the system, which is equivalent to $H(w).W(w) = G(w) \xrightarrow{ICZT} g(t)$ where $H(w)$ is the measured frequency response and $W(w)$ is the window frequency response. Windowing improves the dynamic range of a time domain measurement by altering the frequency domain data prior to converting it to the time domain, producing an impulse stimulus that has lower sidelobes. This makes it much easier to measure time domain responses having very different magnitudes. The sidelobe reduction is achieved, however, at the expense of increased impulse width. The network analyzer has three standard windows (minimum, normal and maximum) and a user-specified window. While the

artificial pulses for standard windows are fixed and only depend on the frequency span, user can arrange the shape of the pulse in the user-specified window. The sidelobe level and 6-dB beamwidth values of pulses ($p(t)$) for minimum, normal and maximum windows and pulse beamwidths for the operating frequency band of the setup (1-12 GHz) are given in Table 5.1.

Table 5.1   The sidelobe levels and 6-dB beamwidths for minimum, normal and maximum windows.

Window Type	Sidelobe Level	6-dB Beamwidth	Beamwidth for the setup
Minimum	-13 dB	1.2/Frequency Span	109.1 ps
Normal	-44 dB	1.96/Frequency Span	178.2 ps
Maximum	-75 dB	2.78/Frequency Span	252.7 ps

In Table 5.1, the minimum window essentially corresponds to no window or rectangular window and as indicated above the pulse has sinc form resulting in highest sidelobe level. The normal window, which is also the preset mode, gives reduced sidelobes by increasing beamwidth and is the mode most often used. The maximum window gives the minimum sidelobes, providing the greatest dynamic range. In user-specified window, a pulse beamwidth can be assigned being different from the beamwidths of the standard windows in the range from 1.2/Frequency Span (109.1 ps) to 2.78/Frequency Span (252.7 ps). However, there is again a trade-off between sidelobe level and impulse width that as the beamwidth decreases, the sidelobe increases. A window is activated only for viewing a time domain response, and does not affect a displayed frequency domain response. In other words, the frequency response of a system is fixed for all windows; however, the time response changes with respect to selected window since the artificially synthesized pulse

114

changes. In the measurements of scattered time signals from single targets in this thesis, the effects of sidelobe level is much more important than the effects of impulse width. Since there exists only one target to be sensed in the test setup, there is only one time response measured at a given attempt. Therefore, having narrow beamwidth for the pulse has no practical importance. On the other hand, a pulse with high sidelobe level can create problems that the high sidelobe of early-time response can mask the late-time response. Thus, the pulse in the setup should have low sidelobe levels rather than having narrow beamwidths. For these reasons, the normal window is selected in time domain calculations to construct the classifier's database in this chapter due to the requirements of low sidelobe level and moderate beamwidth. The artificially synthesized pulse in time domain and the window response in frequency domain for the normal window option are given in Figure 5.7(a) and Figure 5.7(b), respectively. In order to obtain these responses, first thru connection (connecting two ports from the calibrated points with a thru used in calibration) is done between two ports which gives $H(w) = 1$ and $W(w) = G(w)$ as the transmission coefficient (S_{21} parameter) for all frequencies in (1-12 GHz) band in the frequency domain. Then, by using normal window, the time response of the transmission coefficient is measured in network analyzer which is equal to $g(t) = e^{j2\pi 6.5 \times 10^9 t} p(t)$ where $p(t)$ is given in Figure 5.7. Afterwards, by selecting time interval as $[0, \dfrac{1}{2\Delta f}]$ and taking FFT of $g(t)$ synthetically, the window frequency response of the normal window is gathered as shown in Figure 5.7(b).
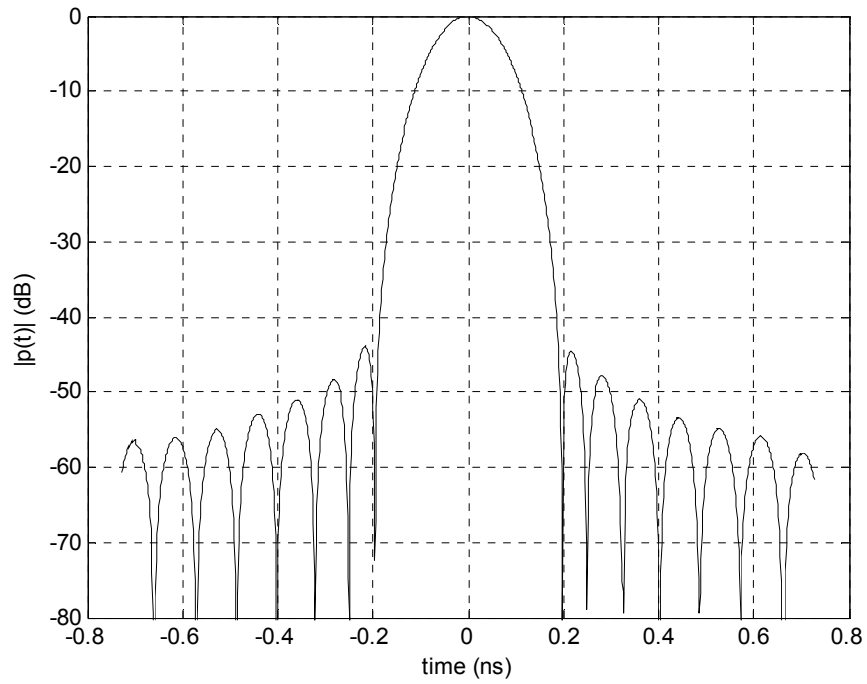
(a)
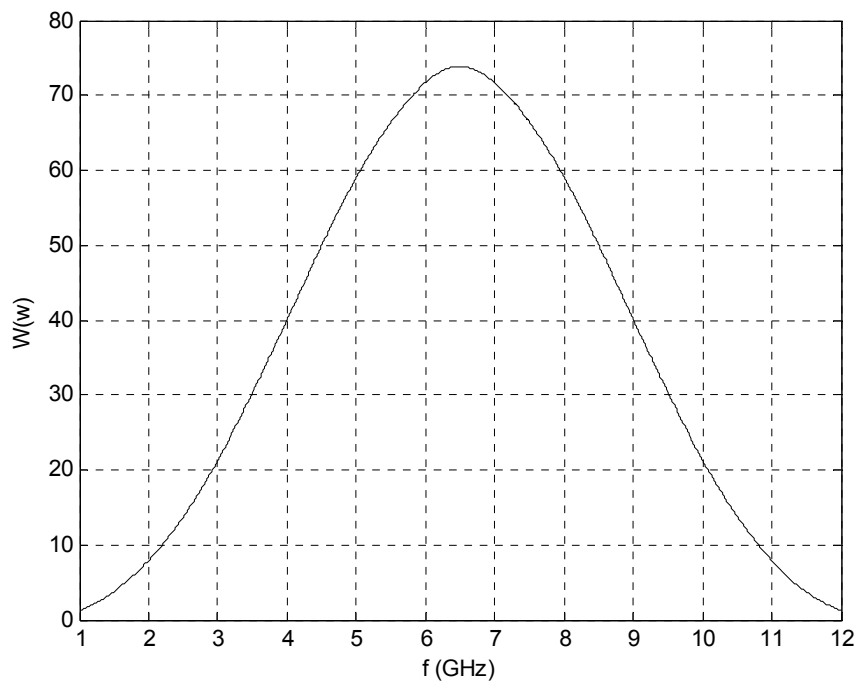
(b)

Figure 5.7 The time and frequency domain responses of normal window (a) time domain response (b) frequency domain response.

5.1.2.2.   Gating Option

In network analyzer, gating option provides the flexibility of selectively removing time domain responses or focusing on a specific region of time response. The remaining region of the time domain response can then be transformed back to the frequency domain by using chirp Z-transform. This gate option is usually used in the reflection (or fault location) measurements in order to remove the effects of unwanted discontinuities in the time domain or in the transmission measurements in order to remove the effects of multiple transmission paths. The gate can be thought as a bandpass filter in the time domain which can be seen in Figure 5.8 [119].
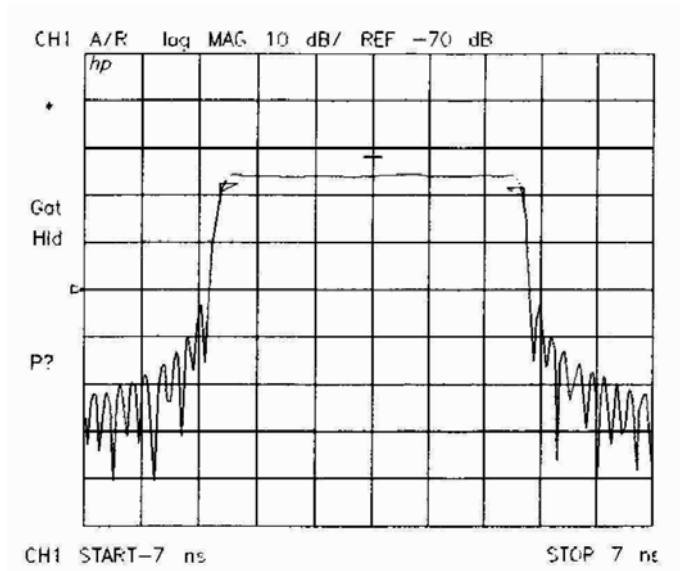
Figure 5.8   A sample gate shape of the network analyzer [119].

When the gate is on, the responses outside the gate are mathematically removed from the time domain trace. The gate position can be entered as a start and stop time (not frequency) or as a center and span time. The start and stop times are the -6 dB cutoff times of the bandpass filter. Four gate shapes are available in this netwok analyzer

and they are listed in Table 5.2. Each gate has a different passband flatness, cutoff rate and sidelobe levels.

Table 5.2　　　The characteristics of the gates available in network analyzer.

Gate Shape	Passband Ripple	Sidelobe Levels	Cutoff time
Minimum	± 0.10 dB	-48 dB	1.4/Frequency Span
Normal	± 0.01 dB	-68 dB	2.8/Frequency Span
Wide	± 0.01 dB	-67 dB	4.4/Frequency Span
Maximum	± 0.01 dB	-70 dB	12.7/Frequency Span

The passband ripple and sidelobe levels are descriptive of the gate shape. The cutoff time is the time between the stop time (-6 dB on the filter skirt) and the peak of the first sidelobe, and is equal on the left and right side skirts of the gate. In a gate option, it is common to choose a gate span wider than the minimum, and for most applications, simply the knob is used to position the gate markers around the desired portion of the time domain trace. Normal gate shape is again the preset mode and the most commonly used one so that it is also used in the measurements of scattered signals used in this chapter.

Since the measurements of the scattered time signals from a target can be considered as a transmission measurement, it is useful to use gate option of network analyzer for removing unwanted signals in time response. The main time interval to be processed for the proposed target recognition method starts from the time instant when the first return from the target is recorded at the receiving point (starting point of early-time signal). Therefore, the time intervals before this time instant (which contain the effects of mutual coupling, multiple transmission paths of the cables and adapters

and thermal noise) are not needed and even they should be removed due to being strong interferences to the frequency domain response. Besides, further late-time intervals where thermal noise is dominant may also be removed. Thus, gate option is compulsory in the measurement setup in order to obtain the frequency response of the system only coming from the target itself. The usage of gate option in the measurement setup will also be explained illustratively in Section 5.1.3.

5.1.3.   The Extraction of Scattered Time Signals from Measurements

After determining the antenna positions and absorber thickness as indicated in Section 5.1.1, an SOLT calibration in network analyzer is done with respect to feed adapter points of the horn antennas before attaching the port cables to the antennas. The calibration parameters are f_{start}= 1 GHz, f_{stop}= 12 GHz, # of points= 801, Δf= 13.75 MHz, Power level= 0 dBm, Averaging= ON, Averaging Number= 16 and Smoothing= OFF. After attaching the port cables, a suitable and clear time interval in the time domain response to be used for the process in the method, in other words, a suitable position for the foam structure and the target is investigated. For this purpose, without putting any target to the system, the overall time domain response, which contains the effects of all interferences such as mutual coupling, multipath and thermal noise, is measured. This response, which can be also called as noise time response, is shown in Figure 5.9(a). By examining the response in Figure 5.9(a), the suitable (clear) time interval in this response is decided as the interval [5.635, 10.152] nsec and a time gate is put in this interval. In Figure 5.9(b), the noise time response is given when a time gate with normal shape is put between [5.635, 10.152] nsec. Thus, by using the gate option and removing unwanted signals, the noise level is decreased and the overall SNR values of the signals are also improved.
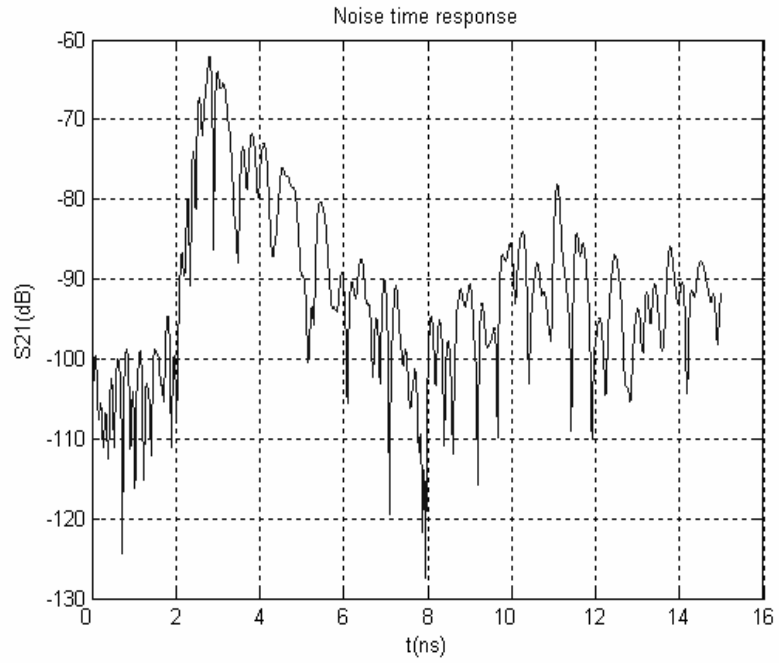
(a)
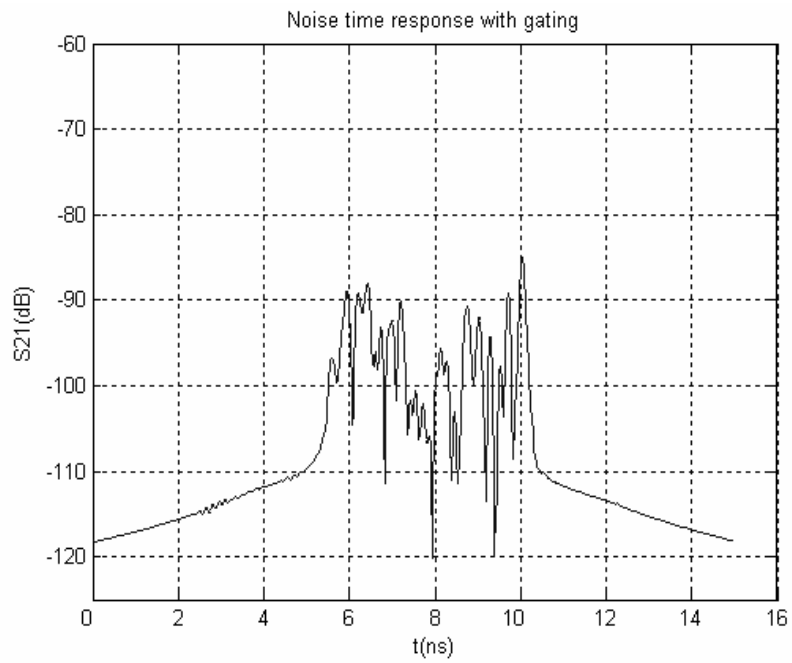
(b)

Figure 5.9   The noise time response of the setup with and without gate   (a) the
noise response when the gate in the interval [5.635, 10.152] nsec is off (b) the noise
response when the gate in the interval [5.635, 10.152] nsec is on.

After the selection of time interval [5.635, 10.152] nsec, the foam structure, consequently, the center of the test target is decided to place 95 cm away from both horn antennas which corresponds to 6.82 nsec in time domain response. Therefore, there exists a clear time interval about 3.3 nsec after the time instant of the target center and about 1.2 nsec before the time instant of the target center to observe the time response of the target. When it is considered that the largest dimension of the targets in the classifier designs mentioned in the following sections is about 15 cm which corresponds to 0.5 nsec in time domain, 3.3 nsec time interval is sufficiently wide to observe both early and late-time responses of the targets. Besides, to preserve a time interval before the target center is needed since the incident field can first hit the test target before its center, which is equivalent to a time instant earlier than 6.82 nsec in time domain, by rotating the test target and positioning some parts of the target closer to the transmitter antenna than the target center point.

Before putting a test target on the foam structure and measuring its frequency response, to improve the accuracy of the measurements a calibration method using conducting spheres, which is common calibration method [122], [123], is applied. In this method, the conducting spheres with known dimensions are used. Since these spheres' frequency responses at all frequencies can be evaluated theoretically, when these spheres' frequency responses are measured with a measurement setup, the ratio of this measurement to the theoretical response gives the overall response effects of the measurement system (antenna effects, cable effects etc.) except frequency response effect of the target. So dividing the measured frequency response of any target into this ratio gives almost true frequency response of this target. Briefly this calibration method can be explained as:

$$\frac{Y_{measuredsphere}(w)}{X_{theoricsphere}(w)} = H(w) \Rightarrow \frac{Y_{measured}(w)}{H(w)} = Y_{true}(w) \qquad (5.1)$$

For this calibration, two conducting spheres of radii 1.8 cm and 3 cm are used in the proposed setup and average of $H(w)$ of these two spheres are taken as the overall response effect of the measurement system and stored as $H_{overall}(w)$. Since this $H_{overall}(w)$ has no zeros in the frequency band 1-12 GHz, dividing the measured data by $H_{overall}(w)$ does not add any additional pole to the system.

The network analyzer can be able to divide two responses with DATA/MEM option. However, it can only divide the displayed data in the screen by memory trace previously stored. Due to the fact that the implementation or store of an exterior data (function) such as $H_{overall}(w)$ to the memory trace is not possible in this network analyzer, the calculations in order to obtain $Y_{true}(w)$ in Equation (5.1) are done with Matlab simulator. Thus, after the construction of the measurement setup described above, a target with specific allocation (specific θ in Figure 5.1) is placed on the foam structure in order to obtain its scattered signal. Then, only the frequency response of the target within the frequency band 1-12 GHz by putting a time gate in the interval [5.635, 10.152] nsec is measured with the network analyzer and stored. The network analyzer is not used hereafter that the calculations and operations after this step are done synthetically with Matlab codes up to the extraction of time signals. After obtaining the measured frequency response, it is divided by $H_{overall}(w)$ to get the true frequency response $Y_{true}(w)$ cleaning from the antenna and cable effects. Afterwards, in the transformation to time domain, the normal window given in Figure 5.7(b) is used that $Y_{true}(w)$ is multiplied with this window and the scattered time signal of a target is obtained by using classical IFFT and zero padding if necessary. Thus, with these operations, the time response of a test target, whose frequency response is $Y_{true}(w)$, to an illuminated pulse given in Figure 5.7(a) is obtained as if it is measured by the network analyzer.

5.2. The Classifier Design for Thick Dielectric Rods with Scattered Data Measured at METU MMW Laboratory

In this classifier design, the target library includes four dielectric rods with the same length and the same radius but different permittivity values. No alien target is used in the testing phases of the resulting classifier. The controlled dielectric rods manufactured by Custom Materials Inc. [124] have 15 cm length, 1.25 cm radii and different permittivities of ε_r= 3, 4, 5 and 5.5 that the material and physical characteristics of the targets are highly close to each other. The target dimensions, between 0.5λ and 6λ, are again in the resonance region. The VV-polarized frequency responses of targets are measured at the aspect angles of θ= 0 to 170 degrees with 10 degree steps, where at 0 degree the rod lies along z axis as shown in Figure 5.1, over incomplete frequency band of (1-12 GHz) with $\varDelta f$ = 13.75 MHz. Then, the scattered time domain signals at each target/aspect angle case (with 5 psec time resolution) are obtained with the process explained in Section 5.1.3. The resulting time signals have 1024 sample points with a total time span of 5.115 nanoseconds. As an example, the scattered time domain signals corresponding to the dielectric rods with ε_r= 3 and 4 at the aspect angle of θ= 90 degree over the frequency band of (1-12 GHz) are given in Figure 5.10. In order to observe the effect of frequency bandwidth on classifier performance, the scattered responses are also obtained at the other incomplete frequency bands of (2-12 GHz) and (3-10 GHz) with the same frequency resolution by truncating the frequency responses measured over the (1-12 GHz) band. Then, these responses are transformed into the time domain with the procedure explained earlier. By assuming that the overall noise level of the system is constant and has the time response given in Figure 5.9(b), the SNR values of scattered signals calculated over the time interval [5.635, 10.152] nsec are found as 16 dB on the average.
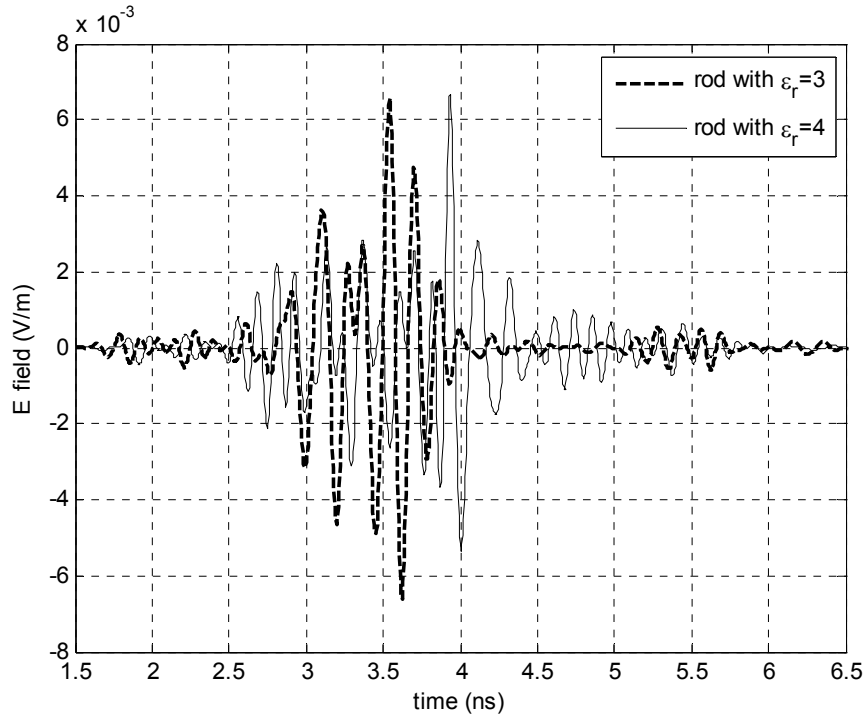
Figure 5.10   Scattered time signals of the dielectric rods with ε_r= 3 and 4 at the aspect angle of θ= 90 degree for the frequency band 1-12 GHz.

Six of the aspect angles, θ= 0, 30, 60, 90, 120 and 150 degrees, out of eighteen aspect angles are chosen as reference aspect angles to construct the FMSM features of the classifiers designed for each frequency band. As the first step of the design procedure, for a given target/reference aspect angle case, the scattered time signal is divided into some overlapping subintervals starting from 2.5 nanoseconds with a total length of N= 128. For each subinterval and for every target/reference aspect angle, the parameters of normalized MUSIC spectrum matrices are chosen as m = 64, L= 32 with two different values of time resolution, $\varDelta t$ = 2.5 psec and $\varDelta t$ = 5 psec. The subinterval having the highest r_{total} value is again selected as the optimal late-time interval. These design steps are repeated for each frequency band to design

alternative classifiers. As an example, r_{total} values of subintervals for the (1-12 GHz) band are given in Figure 5.11 where

- indices 1 to 10 along the horizontal axis refers to a total of 10 subintervals in time established with $m = 64$, $\Delta t = 5$ psec, time duration= 128x5 psec= 0.64 nsec and shifting by 0.32 nsec (i.e. index 1 corresponds to 2.5 nsec-3.14 nsec interval; index 2 corresponds to 2.82 nsec-3.46 nsec interval, etc. and finally index 10 corresponds to 5.38 nsec-6.02 nsec interval).

- indices 11 to 31 along the horizontal axis refers to a total of 23 subintervals in time established with $m = 64$, $\Delta t = 2.5$ psec, time duration= 128x2.5 psec= 0.32 nsec and shifting by 0.16 nsec (i.e. index 11 corresponds to 2.5 nsec-2.82 nsec interval; index 12 corresponds to 2.66 nsec-2.98 nsec interval, etc. and finally index 31 corresponds to 5.7 nsec-6.02 nsec interval).
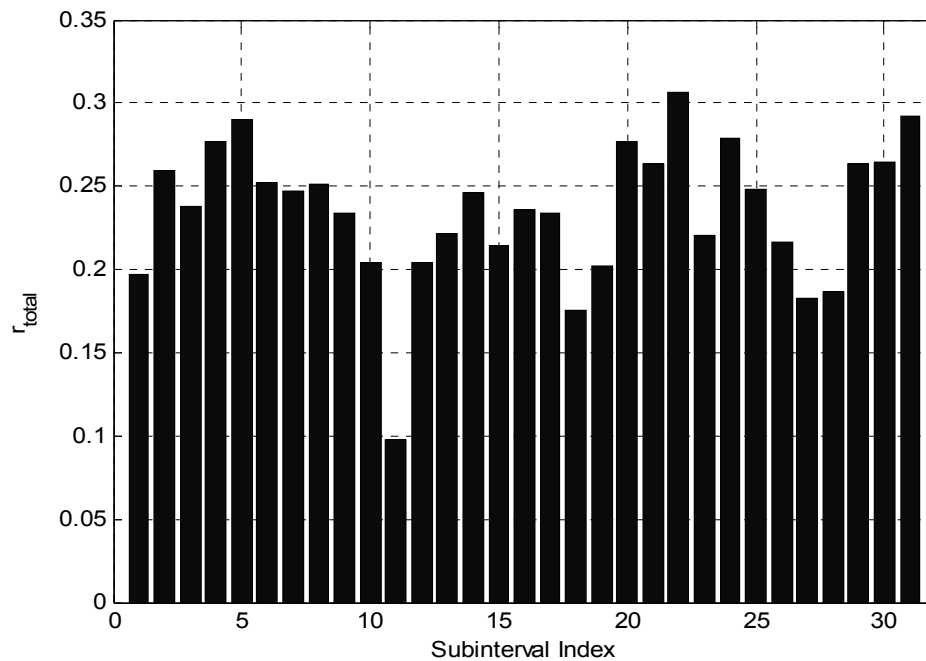
Figure 5.11   The r_{total} values computed for the classifier design of the thick dielectric rods in Section 5.2 for the frequency band (1-12 GHz).

From Figure 5.11, the optimal late-time interval is selected as index 22 (the interval from 4.26 to 4.58 nsec). The same optimal late-time interval is also determined for the (2-12 GHz) frequency band. For the (3-10 GHz) frequency band, the optimal late-time interval is found to be [3.78, 4.42] nsec. The FMSMs of the dielectric rods computed for the (1-12 GHz) band and the [4.26, 4.58] nsec optimal late-time interval are shown in Figure 5.12(a)-(d).

(a)

(b)

(c)

(d)
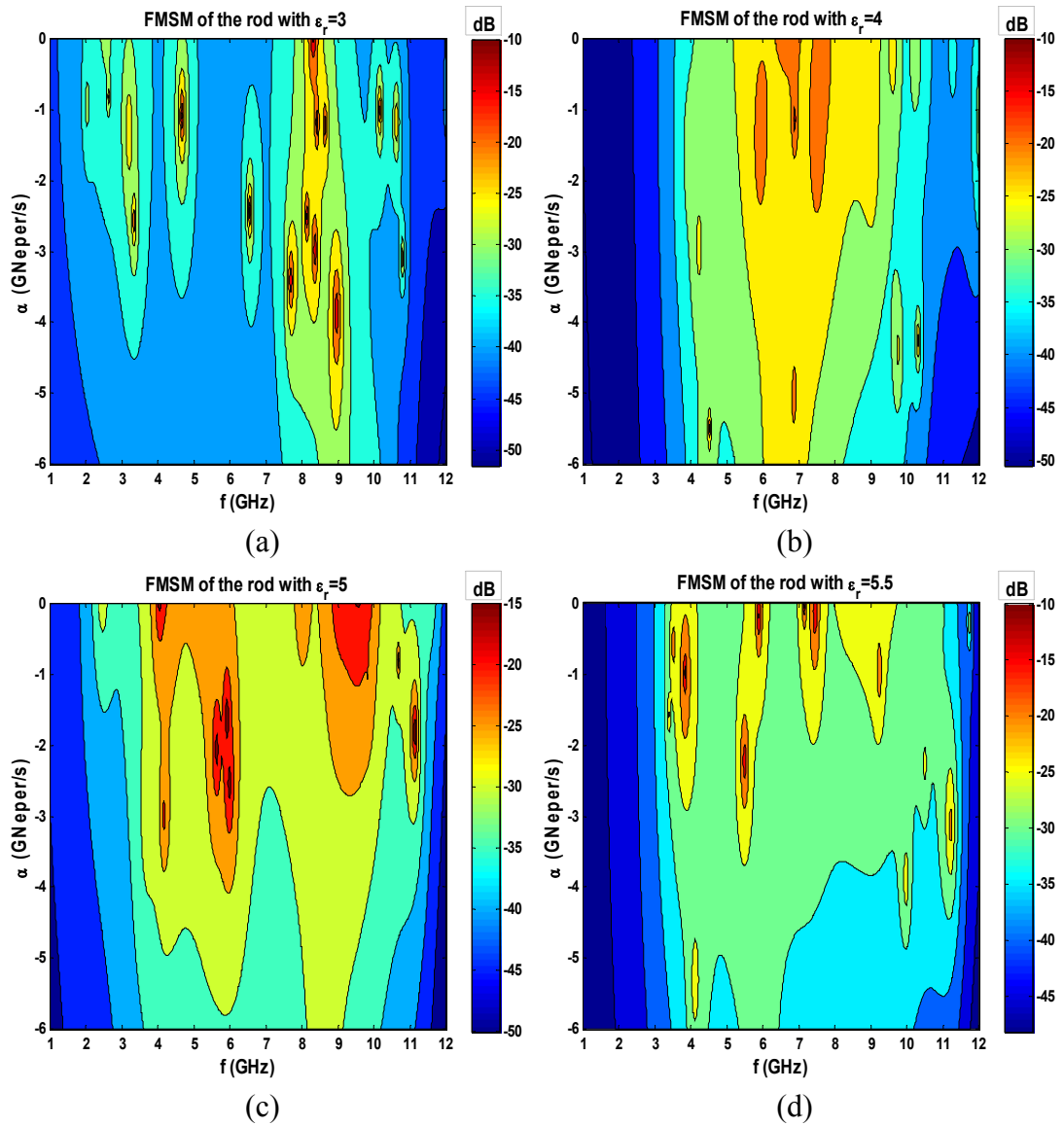
Figure 5.12   The FMSM features of the classifier design of the thick dielectric rods in Section 5.2 for the frequency band (1-12 GHz).

In the decision stage of this target classification simulation, a total of (4 targets) x (18 aspect angles)= 72 signals are used for testing purposes at the same SNR level. As an example, the testing MSM for the dielectric rod with ε_r= 5 at 100 degree aspect is computed over the (1-12 GHz) frequency band and shown in Figure 5.13. The matched correlation coefficient for this test target/aspect angle case is found as 0.4383 while the mismatched correlation coefficients are 0.0436, 0.3408 and 0.3849 for the dielectric rods with ε_r=3, 4 and 5.5, respectively.
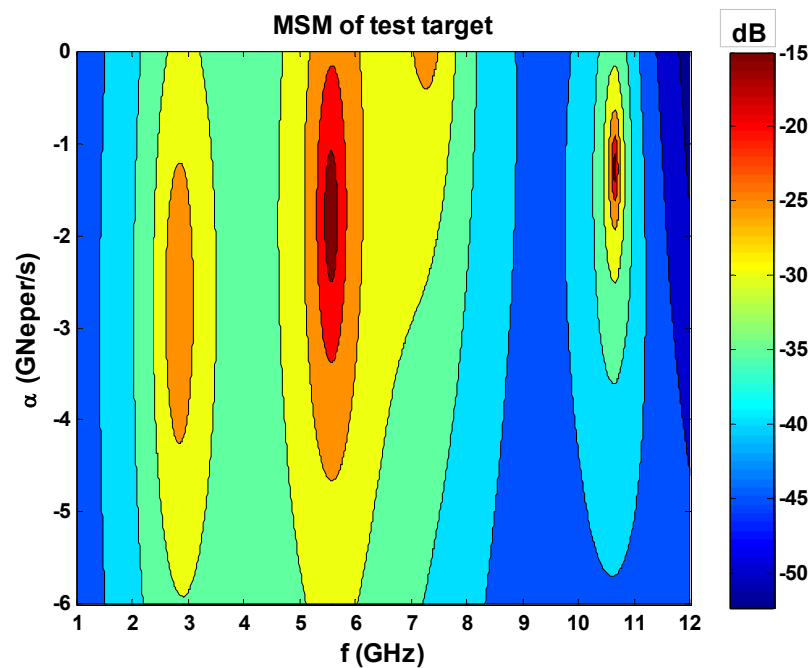
Figure 5.13   The MSM of the test target of the dielectric rod with ε_r= 5 at the aspect angle of 100 degree for 1-12 GHz frequency band.

According to correlation coefficient results, the overall correct classification rates of the dielectric rod classifiers designed over the (1-12 GHz), (2-12 GHz) and (3-10 GHz) frequency bands are found as 93, 93 and 89 percent for 0% margin criterion, respectively. The corresponding correct classification rates are found as 92, 90 and 86 percent based on 5% safety margin criterion. The confusion matrices for the

frequency bands (1-12 GHz), (2-12 GHz) and (3-10 GHz) are given in Table 5.3, Table 5.4 and Table 5.5, respectively. In these tables, the former values correspond to the decision numbers for 0% margin decision criterion; the latter values in parantheses are decisions numbers for the 5% safety margin case.

Table 5.3   The confusion matrix of the dielectric rod-classifier for the (1-12 GHz) frequency band (for the safety margins of 0% and 5% used in decisions).

Test Targets ⇓	Decision			
	The rod with ε_r=3	The rod with ε_r=4	The rod with ε_r=5	The rod with ε_r=5.5
The rod with ε_r=3	18 (17)	0 (1)	0 (0)	0 (0)
The rod with ε_r=4	0 (0)	17 (17)	1 (1)	0 (0)
The rod with ε_r=5	0 (0)	0 (0)	16 (16)	2 (2)
The rod with ε_r=5.5	0 (0)	0 (0)	2 (2)	16 (16)

Table 5.4   The confusion matrix of the dielectric rod-classifier for the (2-12 GHz) frequency band (for the safety margins of 0% and 5% used in decisions).

Test Targets ⇓	Decision			
	The rod with ε_r=3	The rod with ε_r=4	The rod with ε_r=5	The rod with ε_r=5.5
The rod with ε_r=3	18 (17)	0 (1)	0 (0)	0 (0)
The rod with ε_r=4	0 (1)	17 (16)	1 (1)	0 (0)
The rod with ε_r=5	0 (0)	1 (1)	16 (16)	1 (1)
The rod with ε_r=5.5	0 (0)	0 (0)	2 (2)	16 (16)

Table 5.5   The confusion matrix of the dielectric rod-classifier for the (3-10 GHz) frequency band (for the safety margins of 0% and 5% used in decisions).

Test Targets ⇓	Decision			
	The rod with ε_r=3	The rod with ε_r=4	The rod with ε_r=5	The rod with ε_r=5.5
The rod with ε_r=3	17 (17)	1 (1)	0 (0)	0 (0)
The rod with ε_r=4	1 (1)	16 (16)	1 (1)	0 (0)
The rod with ε_r=5	0 (0)	2 (2)	15 (14)	1 (2)
The rod with ε_r=5.5	0 (0)	0 (1)	2 (2)	16 (15)

Since the dominant poles of all dielectric targets are mostly confined to the frequency band (3-12 GHz) as concluded from the FMSMs plots given in Figure 5.12, the accuracy rates of the classifiers designed for the (1-12 GHz) and (2-12 GHz) frequency band are the same. However, the results begin to worsen for the classifier design over the (3-10 GHz) frequency band, as expected. However, the proposed method has still high accuracy rates for this dielectric rod classifier problem with measured frequency data having different degrees of incompleteness.

5.3. The Classifier Design for Small-Scale Aircraft Targets with Scattered Data Measured at METU MMW Laboratory

In the second classifier design of this chapter, the target library contains three conducting small-scale aircraft targets; Boeing 747, DC-10 and Boeing 767. As indicated in the introduction of this chapter, these aircraft targets are the small-scale models of the realistic aircraft targets that they are not modeled by thin wires like the library targets used in Section 4.3. The dimensions of the aircraft targets are scaled

by 1/500 for Boeing 747 and DC-10; but, by 1/600 for Boeing 767. In order to make a fair comparison, all targets need to be scaled by 1/500. Therefore, while the scattered fields of the targets are measured in the standard frequency band of the setup, which is the frequency band of (1-12 GHz), for Boeing 747 and DC-10. This frequency band of the measurement is set to (1.2-14.4 GHz) for Boeing 767 with a frequency scaling factor of 1.2. Thus, the resulting scattered signals of the present Boeing 767 model can be treated as the scattered data from a Boeing 767 model scaled by 1/500 with measurements conducted over the frequency band of (1-12 GHz). The photographic views of the measured aircraft targets are shown in Figure 5.14. The body, wing and tail lengths of each target are also given in Table 5.6; where the dimensions for the Boeing 767 are reported after proper scale adjustment so that all three aircraft can be considered to be scaled by the factor of 1/500.

Figure 5.14   The small-scale aircraft targets used in the classifer design of Section 5.3.

Table 5.6   The dimensions of the small-scale aircraft targets used in the classifier design of Section 5.3.

Substructure	Boeing 747	DC-10	Boeing 767
Body length (cm)	14.5	12.7	12.48
Wing length (cm)	12.7	11.4	12.54
Tail length (cm)	4.8	5.25	5

For the substructure dimensions listed in Table 5.6, the measurement frequencies over the band (1-12 GHz) fall in the resonance region. The VV-polarized frequency responses of targets are measured at the aspect angles of θ= 0 to 180 degrees with 10 degree steps, where at 0 degree the nose of aircraft target points +z axis. The incomplete frequency band of (1-12 GHz) is spanned by the stepping frequency of Δf = 13.75 MHz. Then, the scattered time domain signals for each target/aspect angle case are constructed with 5 psec time resolution. As an example, the scattered time domain signals corresponding to the small-scale aircraft targets (Boeing 747, DC-10 and Boeing 767) at the aspect angle of θ= 90 degrees over the frequency band (1-12 GHz) are given in Figure 5.15. Again, in order to observe the effect of frequency bandwidth on the classifier performance, the scattered responses are also obtained at the frequency bands of (2-12 GHz) and (3-10 GHz) with the same frequency resolution by truncating the frequency responses measured for the frequency band of (1-12 GHz). For this aircraft target set, the SNR values of the scattered signals are calculated only over the time interval [5.635, 10.152] nsec and they are found to be 12 dB on the average.
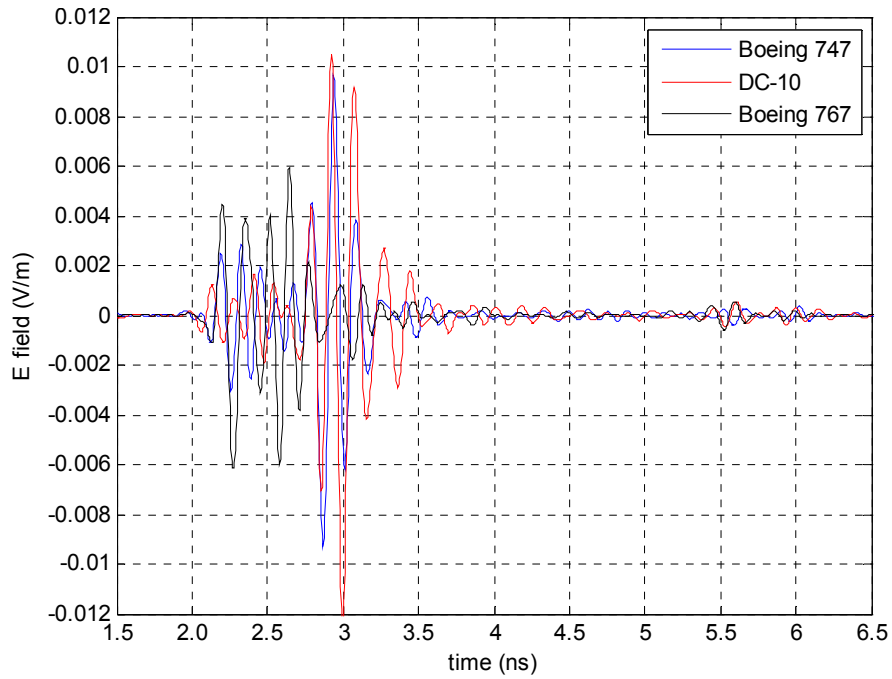
Figure 5.15   The scattered time signals of the small-scale aircraft targets Boeing 747, DC-10, Boeing 767 at the aspect angle of θ= 90 degree for the frequency band of (1-12 GHz).

Seven of the aspect angles, θ= 0, 30, 60, 90, 120, 150 and 180 degrees, out of nineteen aspect angles are chosen as reference aspect angles to construct the FMSM features of the classifier design for each frequency band. As the first step of the design procedure, the scattered time signal is divided into some overlapping subintervals starting from 2.5 nanoseconds with a total length of N= 128. For each subinterval and for every target/reference aspect, the parameters of normalized MUSIC spectrum matrices are chosen as $m = 64$, L= 32 with two different values of time resolution, $\Delta t = 2.5$ psec and $\Delta t = 5$ psec. The subinterval having the highest r_{total} value is again selected as the optimal late-time interval for each frequency band. As an example, r_{total} values of subintervals for 1-12 GHz band are given in Figure 5.16 where the definitions of the subintervals are the same as the preceding classifier design.

132
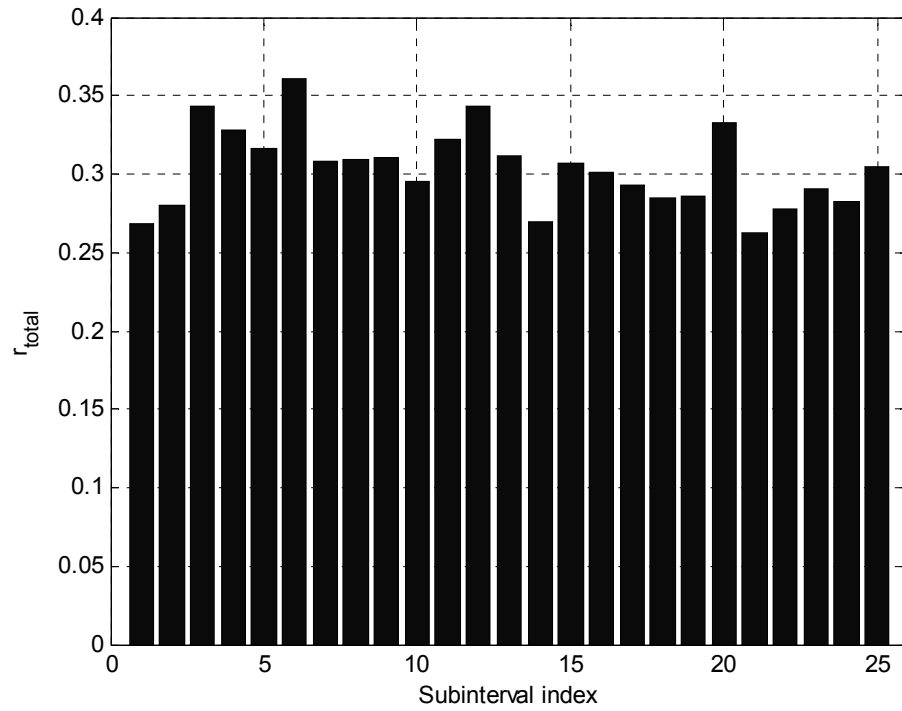
Figure 5.16   The r_{total} values computed for the classifier design of the small-scale aircraft targets in Section 5.3 for the frequency band 1-12 GHz.

The optimal late-time interval for this small-scale aircraft classifier is found as [4.1 nsec - 4.74 nsec] corresponding to the index 6 for the frequency measurements over the band (1-12 GHz). The same optimal late-time interval is also valid for the (2-12 GHz) and (3-10 GHz) frequency bands. Resulting FMSMs of the small-scale aircraft models for the frequency band of (1-12 GHz) and for the optimal late-time interval [4.1 nsec - 4.74 nsec] are shown in Figure 5.17(a)-(c).
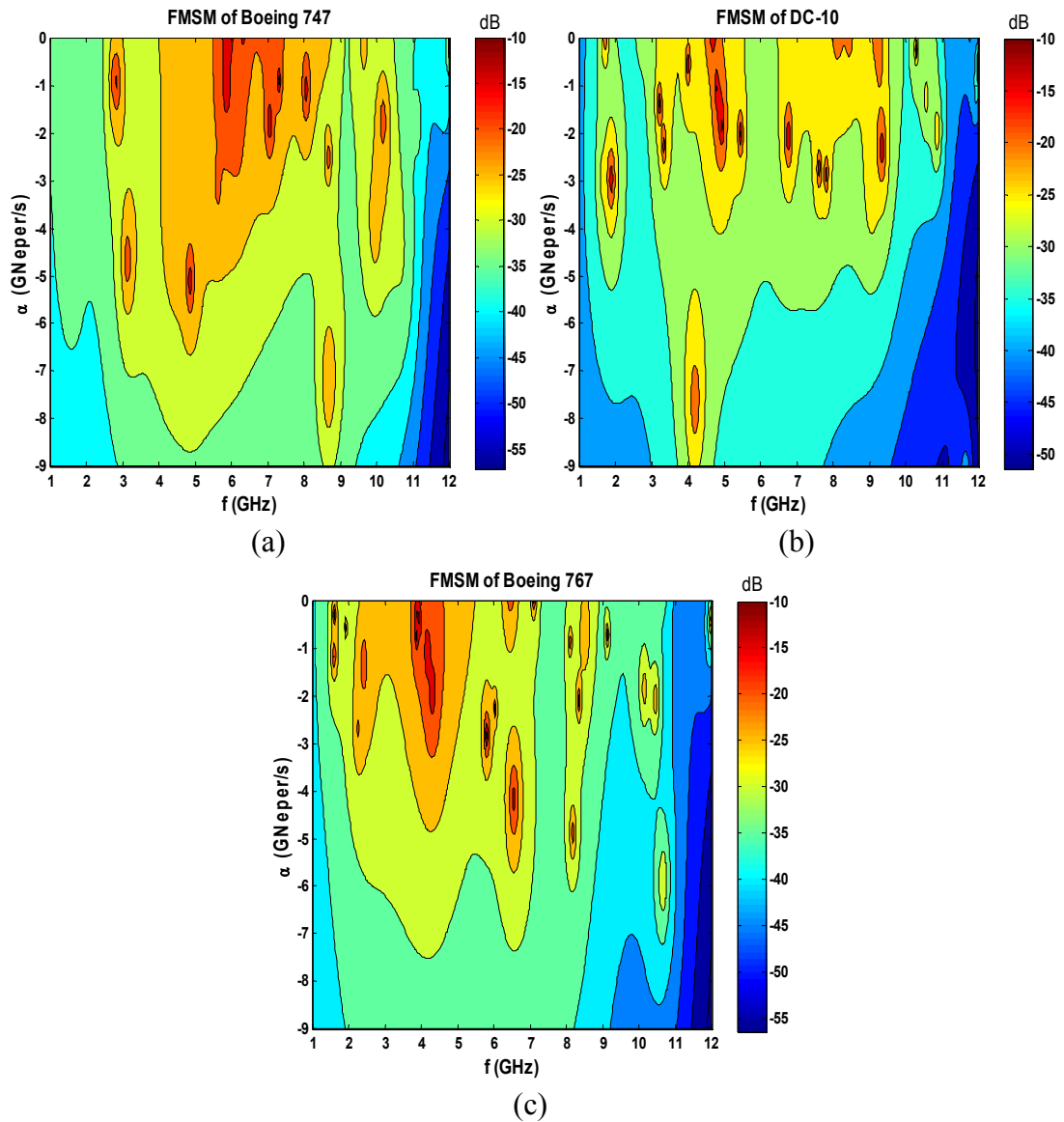
Figure 5.17   The FMSM features of the classifier design of the small-scale aircraft targets in Section 5.3 for the frequency band of (1-12 GHz).

Later, in decision stage, a total of (3 targets) x (19 aspect angles) = 57 signals are used for testing the classifiers over each frequency band. As an example, the correlation coefficients obtained for all test cases for the classifier designed over the frequency band of (1-12 GHz) is given Table 5.7. The incorrect decision cases are

indicated on this table by bold prints. The target Boeing 747 is misclassified as the target DC-10 for instance at 170 degree aspect angle. The same target is correctly classified at 70 degrees on the other hand using the 0% safety margin criterion while it cannot pass the 5% safety margin criterion.

Table 5.7   The correlation coefficients between the MSMs of test targets and FMSMs of the candidate targets for the classifier designed in Section 5.3 over the incomplete frequency band (1-12 GHz).

Test Target/Aspect Angle Case ⇓	Boeing 747	DC-10	Boeing 767
Boeing 747 at θ=0 degree	0.7517	0.3633	0.3428
Boeing 747 at θ=10 degree	0.4056	0.2085	0.1553
Boeing 747 at θ=20 degree	0.4498	0.1683	0.1092
Boeing 747 at θ=30 degree	0.5356	0.2134	0.1997
Boeing 747 at θ=40 degree	0.4416	0.2592	0.1899
Boeing 747 at θ=50 degree	0.5258	0.3067	0.1823
Boeing 747 at θ=60 degree	0.4063	0.0984	0.0528
Boeing 747 at θ=70 degree	**0.4268**	**0.4239**	**0.3097**
Boeing 747 at θ=80 degree	0.4092	0.3162	0.1465
Boeing 747 at θ=90 degree	0.4341	0.1153	0.0894
Boeing 747 at θ=100 degree	0.5178	0.2930	0.3551
Boeing 747 at θ=110 degree	0.5868	0.3415	0.2429
Boeing 747 at θ=120 degree	0.7368	0.2320	0.1843
Boeing 747 at θ=130 degree	0.6344	0.4507	0.3032
Boeing 747 at θ=140 degree	0.4619	0.2206	0.1630
Boeing 747 at θ=150 degree	0.5466	0.0866	0.0731
Boeing 747 at θ=160 degree	0.4239	0.2484	0.2083
Boeing 747 at θ=170 degree	**0.4797**	**0.4854**	**0.4831**
Boeing 747 at θ=180 degree	0.3690	0.0578	0.0385
DC-10 at θ=0 degree	0.1215	0.5278	0.1003
DC-10 at θ=10 degree	0.1699	0.3494	0.1456
DC-10 at θ=20 degree	0.4883	0.5789	0.3092
DC-10 at θ=30 degree	0.1591	0.4881	0.0952
DC-10 at θ=40 degree	0.3887	0.4270	0.2556
DC-10 at θ=50 degree	**0.2469**	**0.3424**	**0.3729**

Table 5.7 cont'd

DC-10 at θ=60 degree	0.1860	0.4415	0.1362
DC-10 at θ=70 degree	0.1001	0.3302	0.0768
DC-10 at θ=80 degree	0.3211	0.5458	0.3268
DC-10 at θ=90 degree	0.2247	0.6436	0.1547
DC-10 at θ=100 degree	0.3400	0.4725	0.2660
DC-10 at θ=110 degree	0.2661	0.3544	0.2272
DC-10 at θ=120 degree	0.1021	0.3816	0.1802
DC-10 at θ=130 degree	0.3766	0.5473	0.4344
DC-10 at θ=140 degree	0.3654	0.5307	0.3917
DC-10 at θ=150 degree	0.1443	0.4614	0.1601
DC-10 at θ=160 degree	0.3746	0.5214	0.2367
DC-10 at θ=170 degree	0.4223	0.4582	0.3962
DC-10 at θ=180 degree	0.0868	0.3753	0.0649
Boeing 767 at θ=0 degree	0.2002	0.1559	0.5416
Boeing 767 at θ=10 degree	0.4862	0.3849	0.6253
Boeing 767 at θ=20 degree	0.2307	0.3262	0.5031
Boeing 767 at θ=30 degree	0.0499	0.054	0.4259
Boeing 767 at θ=40 degree	**0.3822**	**0.3232**	**0.3379**
Boeing 767 at θ=50 degree	0.3982	0.3131	0.5398
Boeing 767 at θ=60 degree	0.0533	0.0684	0.4621
Boeing 767 at θ=70 degree	0.3758	0.2767	0.4755
Boeing 767 at θ=80 degree	0.4109	0.3705	0.4590
Boeing 767 at θ=90 degree	0.1611	0.1500	0.5147
Boeing 767 at θ=100 degree	0.2211	0.2074	0.3210
Boeing 767 at θ=110 degree	**0.3145**	**0.5162**	**0.4807**
Boeing 767 at θ=120 degree	0.2561	0.3875	0.6867
Boeing 767 at θ=130 degree	0.2613	0.2784	0.5201
Boeing 767 at θ=140 degree	0.3601	0.3516	0.5891
Boeing 767 at θ=150 degree	0.1231	0.0763	0.4847
Boeing 767 at θ=160 degree	0.3369	0.3452	0.5089
Boeing 767 at θ=170 degree	0.4361	0.2610	0.4816
Boeing 767 at θ=180 degree	0.0486	0.0315	0.3235

According to the correlation coefficient results given in Table 5.7, the overall correct classification rate of this small-scale aircraft target classifier is found as 93 percent for the 0% margin criterion and 91 percent for the 5% margin criterion, over the frequency band of (1-12 GHz). Similarly, the small-scale aircraft classifiers designed

over the frequency bands of (2-12 GHz) and (3-10 GHz) reach the accuracy rates of 91 percent and 88 percent, respectively, using the 0% margin criterion. These accuracy rates drop to 88 percent and 84 percent when the 5% safety margin criterion is applied. As it is seen from the FMSMs in Figure 5.17, there are some dominant pole contributions around 2 GHz especially for the targets Boeing 747 and DC-10. Therefore, narrowing the classifier's design bandwidth from (1-12 GHz) to (2-12 GHz) causes the accuracy rates to drop. The accuracy rates further decrease for the (3-10 GHz) design bandwidth for the same reason. However, the proposed target classifier method still gives successful results for this aircraft recognition problem even when the classifier is designed with the realistic measurement data of highly truncated frequency content.

5.4. The Classifier Design for Small-Scale Aircraft Targets with Scattered Data Measured at Ohio State University

In this classifier design, two small-scale aircraft targets, Boeing 747 and DC-10, are used in the classifier library. The number of targets in this classifier design is only two, however, the polarization invariance property of the suggested target recognition technique can be investigated in this simulation problem as the scattered signal database include measurements at various polarizations. The aircraft targets to be used in the classifier design are again small-scale models of the actual Boeing 747 and DC-10 aircraft targets with the scale factor of 3/500. The monostatic frequency response measurements of these aircraft targets were done at the ElectroScience Laboratory of the Ohio State University for different polarizations and aspect angles [125]. The list of measurement polarizatios and aspect angles for the library targets is given Table 5.8. In this table, VV, HH and X symbols refer to the vertical-vertical, horizontal-horizontal and cross polarizations respectively.

Table 5.8   The list of available scattered data for the model targets Boeing 747 and DC-10 measured at various polarizations and aspect angles (HH: horizontal-horizontal, VV: vertical-vertical, X: cross polarization).

Polarization	HH		VV		X	
Aircraft Target	Boeing 747	DC-10	Boeing 747	DC-10	Boeing 747	DC-10
Aspect Angle (degrees)	0, 30, 45, 60, 90, 120, 150, 180	0, 30, 45, 60, 70, 90, 120, 150, 180	0, 30, 45, 60, 90, 120, 150, 180	0, 30, 45, 70, 90, 120,150	30, 60, 90, 120, 135, 150	0, 30, 45, 60, 70, 90, 150, 180

The operating frequency band of the measurements is 1-12 GHz with 50 MHz frequency resolution (221 points) except the Boeing 747's HH polarization measurement data. The frequency band of measurements for these exceptional cases is (1.5-12 GHz) with the same frequency resolution. Due to these missing frequency data between 1 GHz and 1.5 GHz in Boeing 747 HH polarization measurements, it is decided to design two different classifiers for this aircraft target set.

In the first classifier design, HH polarization measurements of Boeing 747 are excluded from the total target/polarization/aspect angle cases of the classifier that the whole test target/polarization/aspect angle cases are given in Table 5.8 except HH polarization measurements of Boeing 747. Since HH polarization measurements of Boeing 747 are excluded, the operating frequency band of this classifier design is taken as 1-12 GHz. All measured incomplete frequency data are transformed into time domain by using bandpass Gaussian windowing, zero padding and IFFT to obtain scattered time signals with $\Delta t = 25$ psec resolution. The scattered time signals of both aircraft targets for VV polarization/90 degree case are given in Figure 5.18 as an example.
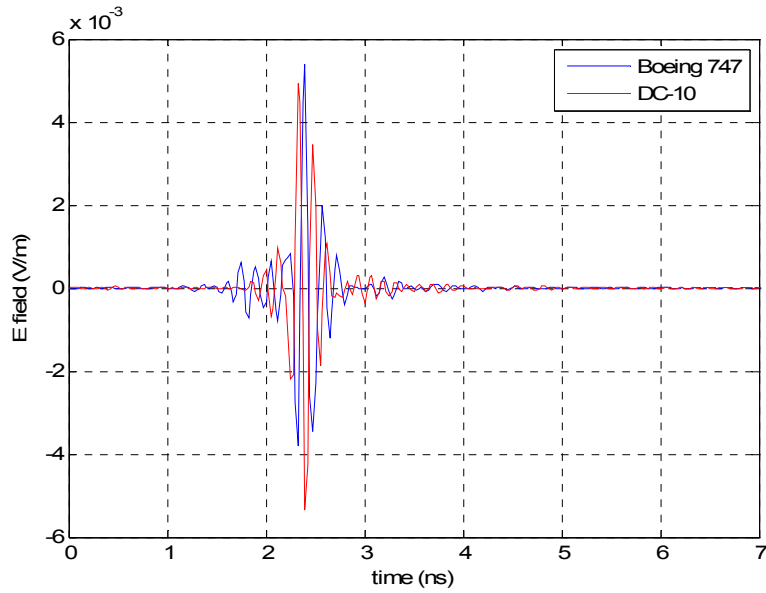
Figure 5.18   The scattered time signals of the small-scale aircraft targets in Section 5.4 for VV polarization/90 degree case and the frequency band of (1-12 GHz).

Six of the polarization/aspect angle cases, VV45, VV90, VV120, X30, X60 and X150, which are common cases for both aircraft targets, are chosen as reference combinations for each target to construct the FMSM database of the classifier. The construction of the fused feature database of the classifier design and the recognition are carried according to the following steps. For a given target/polarization/reference aspect angle case, the scattered signal is divided into some overlapping subintervals starting from 2 nanoseconds with a total length of N= 64. For each subinterval, the normalized MUSIC spectrum matrices are constructed with constant parameter values m = 32, L= 16 and two different values of Δt. Two alternative values of time step, Δt = 25 psed and Δt = 12.5 psec, are used in the analysis where time signals with 12.5 psec resolution are obtained by the linear interpolation of time signals with 25 psec resolution. Then, the steps of the proposed MUSIC-based method are applied to this design problem. The optimal late-time value is found according to highest

r_{total} value. The r_{total} values for different time intervals and $\varDelta t$ values corresponding to this target set are shown in Figure 5.19 where

- indices 1 to 8 along the horizontal axis refers to a total of 8 subintervals in time established with $m = 32$, $\varDelta t = 25$ psec, time duration= 64x25 psec= 1.6 nsec and shifting by 0.4 nsec (i.e. index 1 corresponds to 2 nsec-3.2 nsec interval; index 2 corresponds to 2.4 nsec-3.6 nsec interval, etc. and finally index 8 corresponds to 4.8 nsec-6.4 nsec interval).

- indices 9 to 25 along the horizontal axis refers to a total of 16 subintervals in time established with $m = 32$, $\varDelta t = 12.5$ psec, time duration= 64x12.5 psec= 0.8 nsec and shifting by 0.2 nsec (i.e. index 9 corresponds to 2 nsec-2.8 nsec interval; index 10 corresponds to 2.2 nsec-3 nsec interval, etc. and finally index 25 corresponds to 5.2 nsec-6 nsec interval).
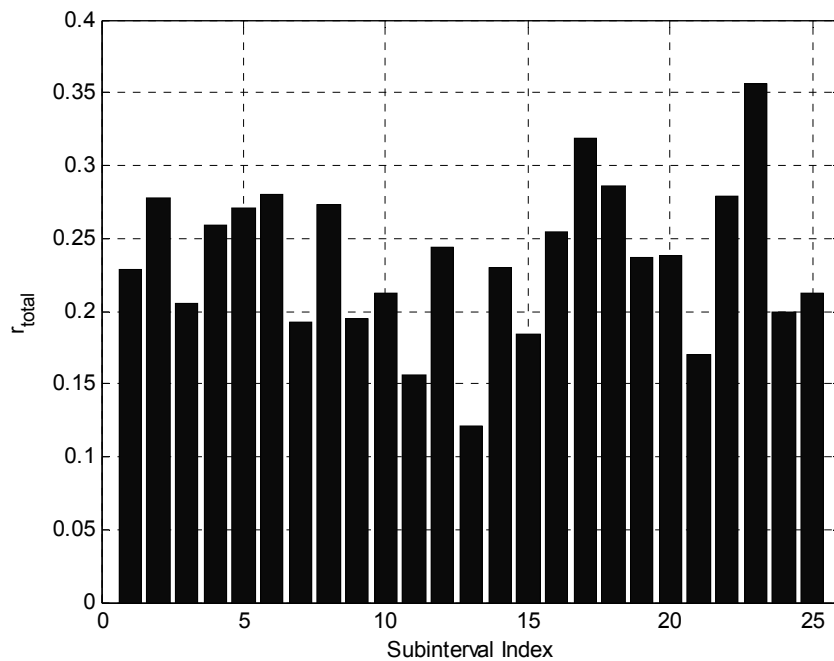
Figure 5.19   The r_{total} values computed for the classifier design of the small-scale aircraft targets in Section 5.4 for the frequency band of (1-12 GHz).

The optimal late-time interval for this small-scale aircraft classifier is found as the interval from 4.8 nsec to 5.6 nsec (index 23). The FMSMs of this aircraft target set are computed far this optimal late-time interval and they are plotted in Figure 5.20.

(a)

(b)
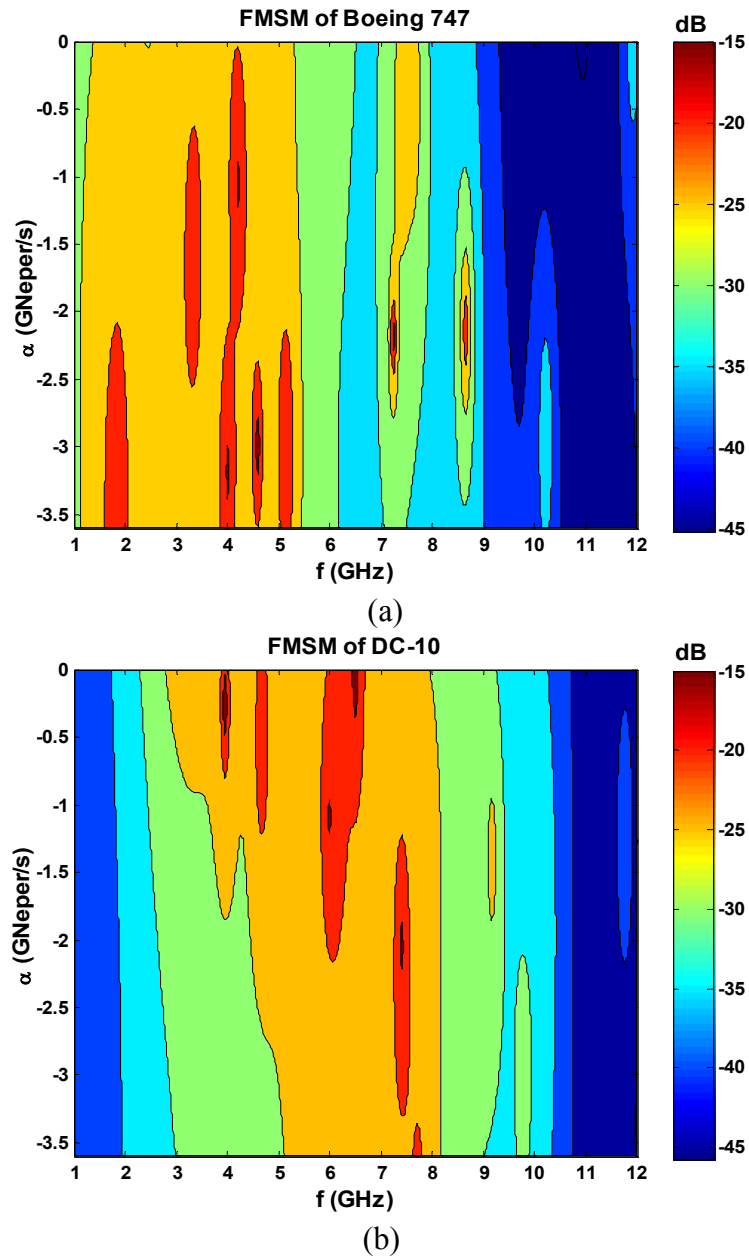
Figure 5.20   The FMSM features of the classifier design of the small-scale aircraft targets in Section 5.4 for the frequency band 1-12 GHz.

After the design work is completed, the classifier is tested at all polarization/aspect angle combinations shown in Table 5.8, expect the HH polarization measurements for the Boeing 747. 39 test signals are used for testing. The correlation coefficients computed between the MSMs of test signals and the FMSMs of the library targets are given in Table 5.9. Again, the correlation coefficient values leading to incorrect recognition are printed in bold in this table. Only 3 incorrect decisions and 1 decision violating 5% margin criterion are made out of 39 tests as shown.

Table 5.9   The correlation coefficients between the MSMs of test targets and FMSMs of the candidate targets for the classifier design in Section 5.4 with the frequency band of (1-12 GHz).

Test Target/Polarization/Aspect Angle Case ⇓	Boeing 747	DC-10
Boeing 747/VV/0 degree	0.5180	0.3254
Boeing 747/VV/30 degree	**0.6250**	**0.6765**
Boeing 747/VV/45 degree	0.6625	0.2940
Boeing 747/VV/60 degree	0.5562	0.2713
Boeing 747/VV/90 degree	0.5196	0.1869
Boeing 747/VV/120 degree	0.6737	0.2477
Boeing 747/VV/150 degree	0.4628	0.3798
Boeing 747/VV/180 degree	0.6914	0.6210
Boeing 747/X/30 degree	0.4300	0.1493
Boeing 747/X/45 degree	**0.3632**	**0.3533**
Boeing 747/X/60 degree	0.5826	0.1017
Boeing 747/X/90 degree	0.4567	0.3532
Boeing 747/X/120 degree	0.3794	0.2448
Boeing 747/X/135 degree	0.5296	0.3859
Boeing 747/X/150 degree	0.4427	0.2666
DC-10/HH/0 degree	0.2112	0.3354
DC-10/HH/30 degree	**0.6058**	**0.5805**
DC-10/HH/45 degree	0.4256	0.5472
DC-10/HH/60 degree	0.3667	0.5626
DC-10/HH/70 degree	0.2472	0.4224
DC-10/HH/90 degree	0.1749	0.4022

Table 5.9 cont'd

DC-10/HH/120 degree	0.1254	0.3177
DC-10/HH/150 degree	0.4854	0.6312
DC-10/HH/180 degree	0.4857	0.6796
DC-10/VV/0 degree	**0.4039**	**0.3707**
DC-10/VV/30 degree	0.3229	0.3744
DC-10/VV/45 degree	0.1715	0.4015
DC-10/VV/70 degree	0.3311	0.6167
DC-10/VV/90 degree	0.2434	0.5728
DC-10/VV/120 degree	0.1498	0.6503
DC-10/VV/150 degree	0.5034	0.7956
DC-10/X/0 degree	0.5410	0.6134
DC-10/X/30 degree	0.1000	0.5493
DC-10/X/45 degree	0.1896	0.5178
DC-10/X/60 degree	0.1099	0.6097
DC-10/X/70 degree	0.5029	0.6029
DC-10/X/90 degree	0.3904	0.6170
DC-10/X/150 degree	0.5576	0.7554
DC-10/X/180 degree	0.3247	0.4000

According to this correlation coefficient table, the accuracy rate of the classifier is found as 92 percent with 0% margin criterion and 90 percent with 5% margin criterion. In other words, the proposed target recognition method has given successful results for this classifier design also. Furthermore, these results show that the suggested method is invariant not only to aspect changes but also to polarization changes, as required. Moreover, as deduced from Table 5.9, the correct decision rate within the cross-polarized data (X polarization) is 100 percent (for 0% margin criterion, which is higher than accuracy rates within the co-polarized data (VV and HH polarizations) for 0% margin. This is due to the fact that the specular portion of the backscattered response from geometrically complicated targets is predominantly in the co-polarized return; hence, a very dominant specular return in the co-polarized data usually masks the resonance effects [126]. However, it can be safely concluded that only a weak entire function component exists in the cross-polarized return. As it is shown in this classifier design, this means better stability for the features extracted

from the cross-polarized returns. Thus, the results obtained from cross-polarized data are much more stable (with respect to aspect angle and polarization) than the results obtained from co-polarized data.

In the second classifier design, HH polarization measurements of Boeing 747 are included in the total target/polarization/aspect angle combinations of the classifier database. Accordingly, this alternative classifier design contains all cases shown in Table 5.8. However, to keep the operating frequency band the same for all measurements, the frequency band of the classifier is narrowed down to 1.5-12 GHz by preserving the frequency resolution of 50 MHz. All the measured incomplete frequency domain data are again transformed into time domain with bandpass Gaussian windowing, zero padding and IFFT to obtain scattered signals with $\Delta t = 25$ psec.

Seven of the polarization/aspect angle cases, HH0, HH30, HH120, VV45, VV90, X60, X150 are chosen for each target sets to construct reference FMSMs of the classifier. The procedure steps, the parameter values and the definition of subintervals are all the same as those used in the previous classifier design. The optimal late-time interval is found as [4 nsec to 5.6 nsec] (index 6). In the decision stage, all polarization/aspect angle cases in Table 5.8 (47 test signals) are used for testing purpose. The correlation coefficients computed between the MSMs of test signals and the FMSMs of the classifier's feature database are given in Table 5.10.

Table 5.10   The correlation coefficients between the MSMs of test targets and FMSMs of the candidate targets for the classifier design in Section 5.4 with the frequency band 1.5-12 GHz.

Test Target/Polarization/Aspect Angle Case ⇓	Boeing 747	DC-10
Boeing 747/HH/0 degree	0.7139	0.2205
Boeing 747/HH/30 degree	0.7432	0.2583
Boeing 747/HH/45 degree	0.4389	0.3668
Boeing 747/HH/60 degree	0.4376	0.3566
Boeing 747/HH/90 degree	0.4494	0.3135
Boeing 747/HH/120 degree	0.6285	0.4360
Boeing 747/HH/150 degree	**0.4755**	**0.5024**
Boeing 747/HH/180 degree	0.5565	0.4726
Boeing 747/VV/0 degree	0.4607	0.2600
Boeing 747/VV/30 degree	0.6316	0.4871
Boeing 747/VV/45 degree	0.5858	0.3304
Boeing 747/VV/60 degree	0.4361	0.2771
Boeing 747/VV/90 degree	0.5265	0.3138
Boeing 747/VV/120 degree	0.5183	0.3437
Boeing 747/VV/150 degree	0.5442	0.4894
Boeing 747/VV/180 degree	**0.3867**	**0.4768**
Boeing 747/X/30 degree	0.6092	0.4188
Boeing 747/X/45 degree	0.4705	0.2055
Boeing 747/X/60 degree	0.4129	0.1066
Boeing 747/X/90 degree	**0.4845**	**0.4642**
Boeing 747/X/120 degree	0.5541	0.3717
Boeing 747/X/135 degree	0.4350	0.3655
Boeing 747/X/150 degree	0.7402	0.3372
DC-10/HH/0 degree	0.4137	0.6766
DC-10/HH/30 degree	0.2075	0.6825
DC-10/HH/45 degree	0.2000	0.3716
DC-10/HH/60 degree	0.4194	0.5356
DC-10/HH/70 degree	0.3044	0.3760
DC-10/HH/90 degree	**0.4578**	**0.4251**
DC-10/HH/120 degree	0.2834	0.6013
DC-10/HH/150 degree	0.3452	0.4392
DC-10/HH/180 degree	0.3971	0.7452
DC-10/VV/0 degree	0.1708	0.3173

Table 5.10 cont'd

DC-10/VV/30 degree	0.2977	0.3872
DC-10/VV/45 degree	0.4137	0.6766
DC-10/VV/70 degree	0.3766	0.4803
DC-10/VV/90 degree	0.2075	0.6825
DC-10/VV/120 degree	**0.5464**	**0.5038**
DC-10/VV/150 degree	0.3293	0.5861
DC-10/X/0 degree	0.3037	0.4051
DC-10/X/30 degree	0.3511	0.4400
DC-10/X/45 degree	0.2006	0.3709
DC-10/X/60 degree	0.3241	0.7313
DC-10/X/70 degree	0.1693	0.4343
DC-10/X/90 degree	0.4847	0.5329
DC-10/X/150 degree	0.2583	0.4705
DC-10/X/180 degree	0.2520	0.3440

According to correlation coefficients table, the accuracy rate of this classifier is found as 91.5 percent for the 0% margin criterion and as 89.5 percent for 5% margin criterion. Therefore, the proposed method is again found successful against polarization and aspect angle changes in this classifier design, which includes a higher number of test cases at various target/polarization/aspect angle cases and a narrower frequency band with respect to the first classifier design. Besides, the cross-polarized data are found having higher accuracy rates with respect to co-polarized data again as also observed in the first classifier design example.

CHAPTER 6

THEORY AND APPLICATIONS OF THE MULTI-TARGET RECOGNITION METHOD USING THE MUSIC ALGORITHM AND TIME CORRELATION CURVES

This chapter presents, for the first time in literature, a natural resonance based electromagnetic target recognition method that is useful not only for single target classification but also for the classification of multiple targets. A simpler "single target classifier" version of this method has already been described in the former chapters of this dissertation and shown to be very successful in recognizing isolated (single) targets of various geometries and material compositions even in high-noise scenarios. The purpose of the research work to be presented in this chapter is to show the feasibility of multiple target detection by the modified and enhanced version of the already suggested method. In this pioneering work, efforts will be focused to design classifiers whose target library may contain single targets and double-target groups altogether. Applications of the method to the classification of target groups containing three or more targets at once is considered to be a future work.

It is well known that electromagnetic target recognition is a very complicated problem due to the dependency of scattered fields on the operating frequency band, polarization and aspect angle. In order to minimize the effects of aspect and polarization dependency in target recognition, different late-time target recognition

techniques, which are based on the singularity expansion method (SEM), have been suggested in literature as already discussed in Chapter 2 of this dissertation. However, all of those present techniques are useful only for single target scenarios where the radar is assumed to collect scattered signals coming from only one target while neglecting the higher order effects due to the presence of any other scattering objects. Although the late-time scattering from a single target can be conveniently explained by the SEM theory, the scattering mechanism for a multi-target (a composite target composed of at least two objects separated from each other in space but sensed by a radar simultaneously) is much more complicated due to higher order electromagnetic interactions between the targets [127]. In the scattered response of a multi-target group, the first order and higher order scattered fields overlap in general. The higher order fields can be neglected when the distances between the elements of a multi-target are sufficiently large. In this "multiple but isolated targets" case, the total scattered response received by the radar is approximately equal to the superposition of targets' individual scattered responses and hence the effective system poles of the multi-target are simply the collection of system poles due to each individual target. However, as the distances between the individual targets decrease, the electromagnetic interactions become stronger and additional system poles may appear. Therefore, the target recognition problem in the case of multiple targets is also highly sensitive to the separation distances between the targets. Target classification errors caused by this kind of sensitivity are highly reduced in the suggested multi-target recognition method by a novel feature fusion technique that will be described in detail in Section 6.1.

As already explained in the previous chapters, in the suggested target classification method each library target is represented by its own fused MUSIC Spectrum Matrix (FMSM), which is the main target feature. In the "single target classifier" design problem, the sensitivity of target features to aspect angle is reduced by superposing the aspect dependent MSM patterns. In the case of "multi-target classifier" design problem, on the other hand, the MSM patterns computed for multi-target groups are

sensitive to both aspect angle and to the element topology within given multi-target groups. Here, the term topology refers not only to target-to-target separation distances between the elements of a given multi-target group but also to the positions of elements with respect to each other and with respect to the transmitter and receiver antennas. Therefore, the FMSM feature for a multi-target group should be obtained by a 2-step feature fusion process: First, for a given reference topology, the aspect dependent MSM patterns should be extracted and superposed to obtain an aspect invariant FMSM pattern. Then, this process should be repeated for the other reference topologies for the same multi-target group. Finally, the resulting aspect invariant but topology dependent FMSM patterns should be superposed one more time to obtain a target feature which has also a reduced sensitivity to the topology of this multi-target group. Usefulness of this "fusion over topology" approach will be demonstrated by the simulation examples in Section 6.2.

Extracting "aspect and topology invariant" target features (i.e. FMSMs) for library targets (single and/or multi-targets) is the most critical step in the design of a multi-target classifier. However, even this important contribution becomes insufficient for a practically important scenario where the test target happens to be a multi-target group having identical but highly separated elements. In this case, the electromagnetic interaction between the elements of the test target is negligible and the testing MSM computed for this multi-target group becomes highly correlated with the FMSM feature of the single library target, which is the same as the identical elements of the target group. As an example, let us assume that the target library of a classifier contains two perfectly conducting spheres of different radii, sphere A and sphere B. In addition to these single targets A and B, the double-target combinations AA, BB and AB are the multi-target groups of this classifier library. In other words, the library can be considered to have five targets altogether; A, B, AA, BB and AB where the distances between the elements of double-target groups may take any arbitrary value. Applying the proper design procedure, the feature database of the classifier can be constructed to have five different FMSM features, one for each

target. However, if the AA double-target group, for instance, occurs as a test target with a large separation distance between each sphere A, then the MSM test pattern computed for this AA group will be highly correlated with the FMSM feature of the single target, sphere A. In other words, the classifier will incorrectly recognize the existence of two A-type spheres as a single A-type sphere. To rule out this special type of decision error, the first step in the real-time test phase must include the computation of a time correlation curve for the received scattered time-domain test signal. If the radar senses two identical but almost isolated spheres, the received time domain signal will be made of the superposition of individual target responses. One of these response contributions will be delayed with respect to the other due to the separation distance between the spheres. Therefore, the time correlation curve computed from this composite response will contain a signal pattern repeated twice with two major peaks, instead of just one. This novel diagnostic step suggested for the first time here, will greatly help to increase the accurate decision rate of the multi-target classifier.

6.1. Mathematical Steps for Multi-Target Classifier Design

In the proposed design procedure, it is assumed that there exist K_1 different single targets and K_2 different multi-target groups in the library of the classifier. In other words, the classifier library contains $K = K_1 + K_2$ targets altogether where the indices $i = 1,\ldots,K_1$ refer to single targets and the indices $i = K_1 + 1,\ldots,K$ refer to multi-target groups. For each multi-target group, K_3 different reference topologies are considered. For instance, if there is a double-target group in the library, the location/distance between two elements may take K_3 different combinations indexed by $h = 1,\ldots,K_3$ notation. Accordingly, there exist $(K_2 K_3)$ different multi-target/topology combinations regarding the multi-target groups of this classifier library. For each one of these combinations and also for K_1 single targets, the

classifier's training database must contain scattered signals at a number of reference aspects indexed as $j = 1,\dots,K_A$. Therefore, the training database of the classifier has $K_A(K_1 + K_2K_3)$ scattered signals to be used in classifier design. Furthermore, an optimal late-time interval must be determined to design the classifier. For this purpose, the total time span of database signals is divided into P overlapping subintervals (indexed as $p = 1,\dots,P$).

Step 1: Computation of MSM patterns:

The MSM patterns are initially computed for all library targets for all aspect/topology combinations over each one of these subintervals as described in Section 3.1.

Step 2: Computation of the FMSM features over a given late-time subinterval for single targets of the classifier library:

In this case, computation of the FMSM features are exactly the same as described in Section 3.2.

Step 3: Computation of the FMSM features over a given late-time subinterval for multi-target groups of the classifier library:

The FMSM for a multi-target group (over a given late-time subinterval) is computed in two steps:

   i. For a given preselected reference topology $h = 1,\dots,K_3$, the MSM patterns of multi-target group is computed at each reference aspect for $j = 1,\dots,K_A$. Then, these MSMs are superposed and the resulting topology dependent sub-FMSM is normalized.

ii. Then, the process in i) is repeated at each reference topology for the same multi-target group. Resulting topology dependent sub-FMSM matrices are superposed again. After normalizing the resultant matrix, the aspect and topology invariant (almost) FMSM feature of this multi-target group is obtained.

iii. The procedure outlined in ii) is repeated for each multi-target group of the classifier library.

Step 4: Design steps 2 and 3 are repeated for each late-time subintervals p where $p = 1,\ldots,P$

Step 5: Determination of the optimal late-time interval for the classifier design:

After the construction of the FMSMs of all single and multi-targets over all late-time subintervals, the optimal late-time interval is determined as follows:

$$Index[Optimal\ late-time\ interval] = p^{*} \quad if\ r_{total}(p^{*}) \ge r_{total}(p) \quad \forall\ p = 1,..,P$$

where

$$r_{total}(p) = \frac{1}{K_{1}K_{A} + K_{2}K_{3}} \sum_{i=1}^{K} r_{i,match}$$
$$- \frac{1}{K_{1}((K_{1}-1)K_{A} + K_{2}K_{3}) + K_{2}((K_{2}-1)K_{3} + K_{1}K_{A})} \sum_{i=1}^{K} r_{i,mismatch} \tag{6.1}$$

$$r_{i,match} = \sum_{j=1}^{K_{A}} \sum_{v=1}^{k_{2}} \sum_{u=1}^{k_{1}} FMSM_{i}(u,v)P_{i,j}(u,v) \quad for\ i = 1,\ldots,K_{1}$$
$$r_{i,match} = \sum_{h=1}^{K_{3}} \sum_{v=1}^{k_{2}} \sum_{u=1}^{k_{1}} FMSM_{i}(u,v)P_{i,h}(u,v) \quad for\ i = K_{1}+1,\ldots,K \tag{6.2}$$

$$r_{i,mismatch} = \sum_{\substack{k=1 \\ k \neq i}}^{K_1} \sum_{j=1}^{K_A} \sum_{v=1}^{k_2} \sum_{u=1}^{k_1} FMSM_i(u,v)P_{k,j}(u,v)$$

$$+ \sum_{k=K_1+1}^{K} \sum_{h=1}^{K_3} \sum_{v=1}^{k_2} \sum_{u=1}^{k_1} FMSM_i(u,v)P_{k,h}(u,v) \qquad for \ \ i=1,\ldots,K_1$$

$$(6.3)$$

$$r_{i,mismatch} = \sum_{k=1}^{K_1} \sum_{j=1}^{K_A} \sum_{v=1}^{k_2} \sum_{u=1}^{k_1} FMSM_i(u,v)P_{k,j}(u,v)$$

$$+ \sum_{\substack{k=K_1+1 \\ k \neq i}}^{K} \sum_{h=1}^{K_3} \sum_{v=1}^{k_2} \sum_{u=1}^{k_1} FMSM_i(u,v)P_{k,h}(u,v) \qquad for \ \ i=K_1+1,\ldots,K$$

where $i = 1,\ldots,K$ is the total target index for single and multi-targets; $j = 1,\ldots,K_A$ is the reference aspect angle index; $h = 1,\ldots,K_3$ is the topology index for multi-target groups, $u = 1,\ldots,k_1$ and $v = 1,\ldots,k_2$ are the row and column indices of the MUSIC spectrum matrices, respectively. Here, $FMSM_i$ refers to the FMSM of the ith target, $P_{i,j}$ refers to the MSM of target i at the aspect angle j for single targets $(i = 1,\ldots,K_1)$ and $P_{i,h}$ refers to the matrix of target i at topology combination h for multi-target groups $(i = K_1 + 1,\ldots,K)$ which can be defined as

$$P_{i,h}(u,v) = \frac{\sum_{j=1}^{K_A} P_{i,h,j}(u,v)}{\left\| \sum_{j=1}^{K_A} P_{i,h,j}(u,v) \right\|} \quad for \ \ i=K_1+1,\ldots,K \ and \ h=1,\ldots,K_3 \quad (6.4)$$

where $P_{i,h,j}(u,v)$ is the MSM of multi-target group i at the topology combination h and aspect angle j.

After the selection of an optimal late-time interval, the FMSM features belonging to the determined optimal late-time interval are collected altogether and saved to form the feature database of the designed classifier. At the real-time classification phase, the MSM computed over the selected late-time interval of the test scattered signal is compared to the FMSM of each candidate target (single, multi) in the classifier's feature database. Finally, the decision is made over the optimal late-time interval according to following algorithm:

$$Test\ target\ = target\ \ i^{*}\quad if\ \ r(\ i^{*}\ ) \geq r(\ i\ )\quad \forall\ i = 1,..,\ K$$

where

$$r(\ i\ ) = \sum_{v=1}^{k_2} \sum_{u=1}^{k_1} FMSM\ _i(\ u,v\ )P_{test}(\ u,v\ )\qquad(6.5)$$

with P_{test} being the MSM pattern of the received test signal.

6.2. Classifier Design Simulations for Target Sets Containing Single and Multi-Targets

In this section, applications of the modified method described in Section 6.1 to the design of classifier target sets containing single and multiple perfectly conducting spheres are demonstrated. In Section 6.2.1, the classifier library contains two single conducting spheres and one multi-target group of two conducting spheres with different (not identical) elements. In Section 6.2.2, the classifier library contains two single conducting spheres and one multi-target group of two conducting spheres with identical elements, which are also identical to the single conducting sphere target. During the test phase for both classifiers, the center-to-center separation distance

154

between two conducting spheres of the double target group may take arbitrary values. To account for the effects of such variations, several reference distances are selected during the classifier design. The reference separation distances in these simulations are chosen according to the following argument:

The scattered fields which contribute to the response of this two-sphere multi-target group fall into three categories: i) reflected fields arising from direct and multiple reflections, ii) creeping waves bound to a single sphere, iii) combinations of both, called the hybrid fields [127]. The combination of direct reflection and creeping waves of a single sphere forms the first-order field of this sphere, which results from the excitation of this sphere by the incident plane wave alone. The other contributions constitute the higher order fields, which arise from multiple scattering interactions [128], [129]. These higher order fields are important and should be taken into account while processing the total scattered response, especially when individual spheres are close to each other. In the scattered response of a two sphere system, the first order fields and higher order fields overlap, however, the higher order fields can be neglected when the separation between the spheres is sufficiently large. Besides, the individual first-order fields may also overlap depending on the distance between two spheres. The response of the farther sphere to the observation point is seen later in time domain response due to the time shift between the first-order responses of two spheres. If the separation distance is sufficiently high, these responses do not overlap. The first-order response of the farther sphere starts after the response of the closer sphere almost vanishes, which may be called as "isolated case". Thus, in this isolated case, the higher order fields can be neglected and the first-order fields can be separated. When the separation distance between the elements of a multi-target group decreases, the effect of higher order fields increases and the first-order fields begin to overlap. These effects further dominate for smaller separation distances. The critical separation distance between two conducting spheres, satisfying the conditions of the isolated case, can be taken as $d_{iso} = 3D_{l\,arg\,est}$ where $D_{l\,arg\,est}$ is the diameter of the largest sphere in the system since the time response of a single sphere is

sufficiently attenuated at about $t = 3D/c$ after the creeping wave is seen at $t \cong 2.57D/c$ [28]. Although there is no formal proof for it, the selection of $d_{iso} = 3D_{l\,arg\,est}$ turns out to be a large enough separation distance to neglect the higher order fields in simulations.

6.2.1. Classifier Design for a Target Library Containing Single and Double Conducting Spheres with Different Elements

In this section, performance of the proposed method given in Section 6.1 is demonstrated for a target library, which contains single conducting spheres with 24 and 30 mm radii and one multi-target group of two conducting spheres with 24 and 30 mm radii. For the multi-target group of two conducting spheres, four different reference values of separation distance, d= 80, 120, 160 and 200 mm, are chosen where 200 mm is higher than $d_{iso} = 3D_{l\,arg\,est}$ =180 mm and satisfies the condition for the isolated case. The target responses are numerically generated for a plane wave excitation which is linearly polarized in y-direction and propagates in −z direction, which is shown in Figure 6.1(a) and Figure 6.1(b) for the single target and for the multi-target group, respectively.

Figure 6.1(a)

156

$\bar{E}^{inc} = \hat{a}_y e^{jk_o z}$

$P_{observation}(R, \theta, 0)$

R=720 mm

(ε_o, μ_o)

$\sigma \to \infty$

$\sigma \to \infty$

d

r

r

r= 30 mm

r= 24 mm

(b)
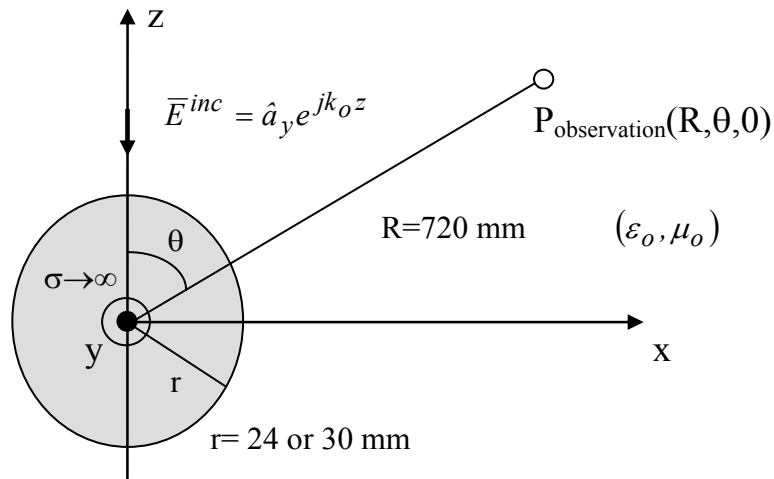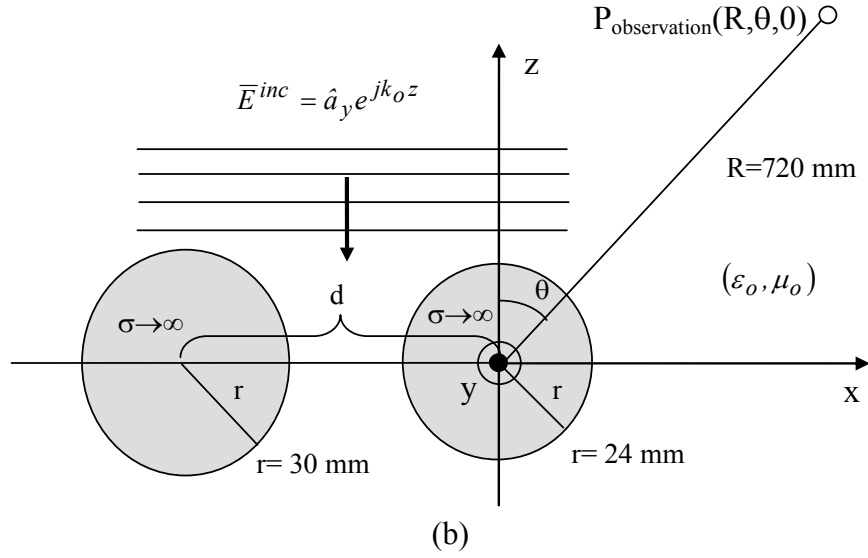
Figure 6.1   The schematic views of the configuration for (a) single target (b) multi-target group.

As it is seen from the figures, the center of the single conducting spheres is located on the origin, $(x,y,z)=(0,0,0)$ while computing their target responses. To compute the responses of multi-target groups, the center of the conducting sphere with 24 mm radius is kept at $(x,y,z)=(0,0,0)$ and the center of the conducting sphere with 30 mm radius is varied at positions $(x,y,z)=(-d,0,0)$. The position of the smaller sphere is deliberately kept at the origin in order to make the starting time instants of all single and multi-target responses the same. The far field bistatic scattered responses of all single targets and multi-target groups are computed over the operating frequency band 0-12 GHz with the frequency step of 13.75 MHz at $\phi= 0$ degree, with a radial observation distance of 720 mm from the origin (satisfying the far field assumption), for ten different aspect angles, $\theta= 0, 10, 20, 30, 40, 50, 60, 70,$ 80 and 90 degrees. The responses are numerically generated with CST (Computer Simulation Technology) Microwave Studio simulation program described in detail in Section 4.3. The simulation view of the configuration for the multi-target group is given in Figure 6.2.
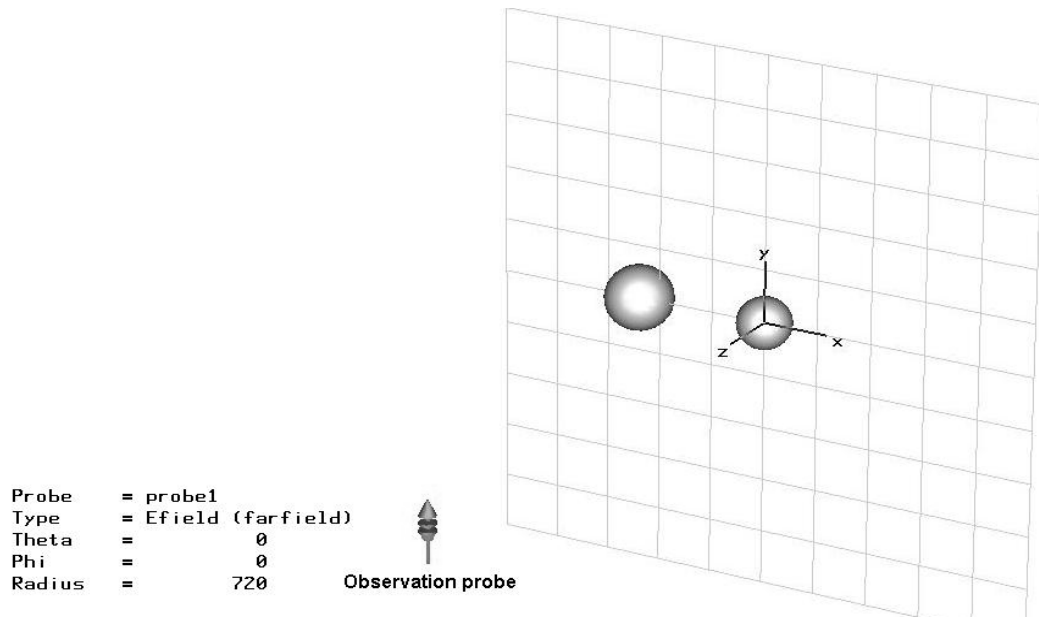
Figure 6.2　　CST Microwave Studio view of the setup for multi-target group.

In the simulation example, scattered fields are computed for the $\phi\phi$ polarization for all library targets. The time-domain scattered signals for the noise-free case at all aspect angles are obtained by using Gaussian windowing, IFFT and zero padding. The resulting time signals have 701 sample points with $\Delta t = 5$ psec time resolution. Out of ten different aspect angles, three aspect angles ($\theta = 0$, 40 and 90 degrees) are chosen as reference aspects to construct the feature database and to design the classifier. Time domain responses of the double-sphere target for different separation values are computed at reference aspect angles and the results are given in Figure 6.3. Here, the response belonging to the isolated case is clearly seen in black curve ($\theta = 90$ degree) of Figure 6.3(d) that the response of the bigger sphere nearly starts after that of the smaller one.

As the first step of the design procedure, for each given single target/reference aspect angle or multi-target/reference topology/aspect angle case, the scattered signal is divided into parts over the overlapping subintervals of time starting from 2.3 nsec

with a total length of N= 128. For each subinterval and for every target/reference aspect angle, the normalized MUSIC spectrum matrices are constructed with L= 32 $m = 64$ and two different values of time resolution, $\Delta t = 2.5$ psec and $\Delta t = 5$ psec.
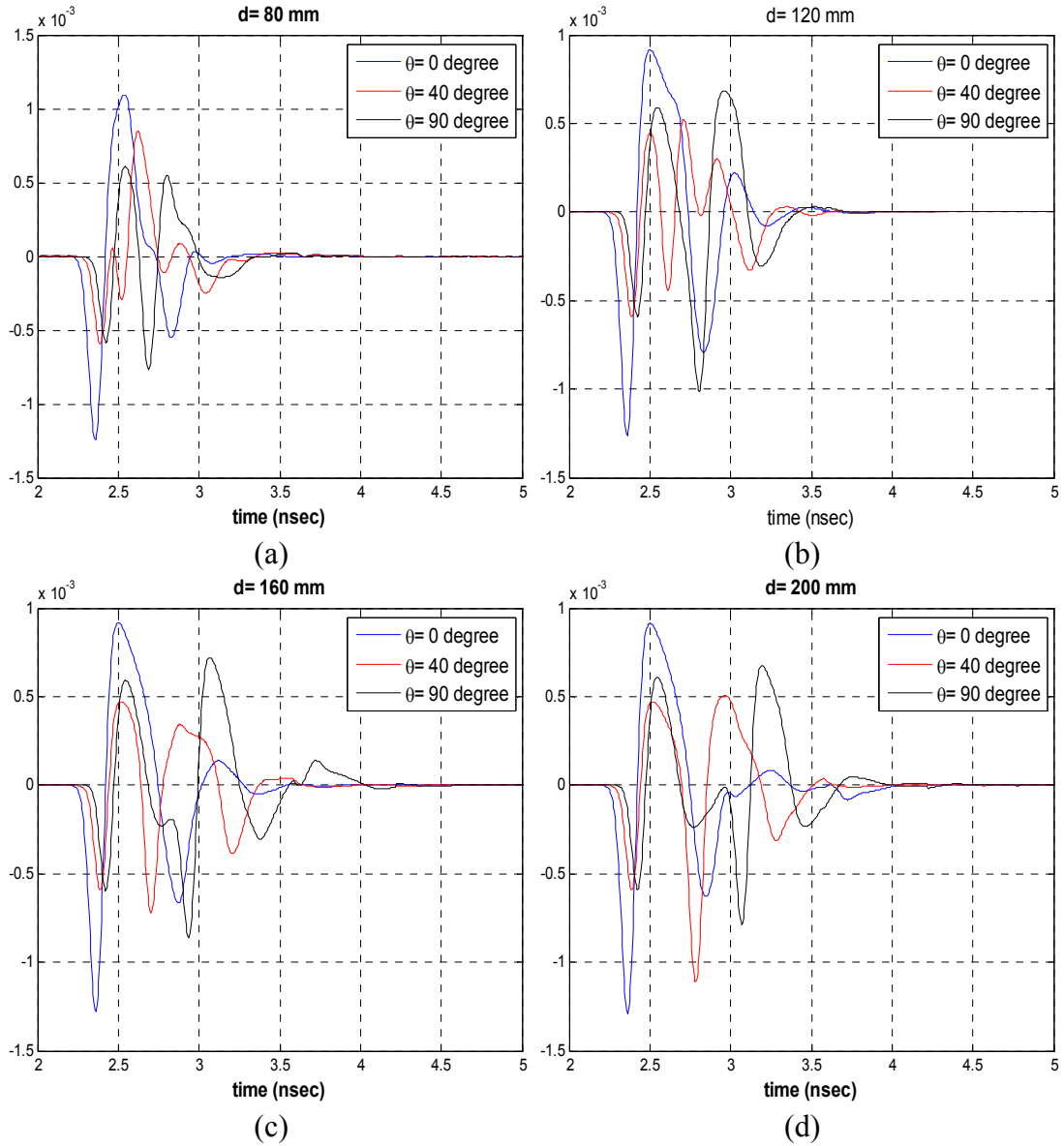
Figure 6.3   The noise-free time-domain signals scattered from a group of two perfectly conducting spheres with 24 and 30 mm radii at reference aspects angles θ= 0, 40 and 90 degrees when the separation between two spheres is (a) d= 80 mm (b) d= 120 mm (c) d= 160 mm (d) d= 200 mm.

The MUSIC spectrum matrices, $P_{i,j}(u,v)$, computed at each different reference aspect angle for single targets and matrices $P_{i,h}(u,v)$ (obtained previously as superpositions of $P_{i,h,j}(u,v)$ matrices) for the multi-target group are superposed for each given target over each subinterval to obtain the fused MUSIC spectrum matrices. After obtaining these FMSMs, r_{total} values are computed for each subinterval and the optimal late-time interval of the classifier is found as [3.58, 4.22] nsec. The normalized FMSMs of single conducting spheres and $P_{i,h}(u,v)$ matrices of the double sphere group for different separations are given in Figure 6.4. Here, the designation of $P_{i,h}(u,v)$ matrices for the double-target group instead of giving FMSM of multi-target is considered to be more informative in order to observe the effect of separation values on pole distribution of the multi-target group features.
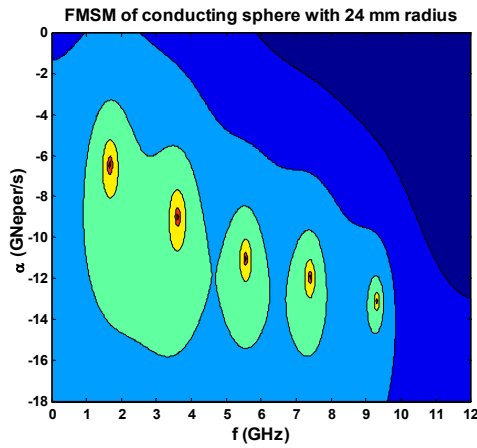
Figure 6.4(a)
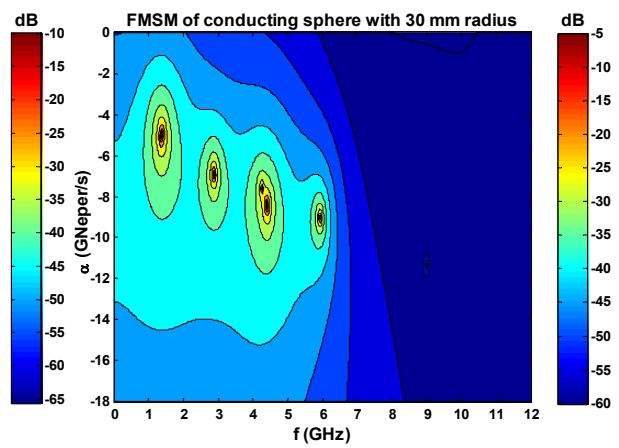
Figure 6.4(b)
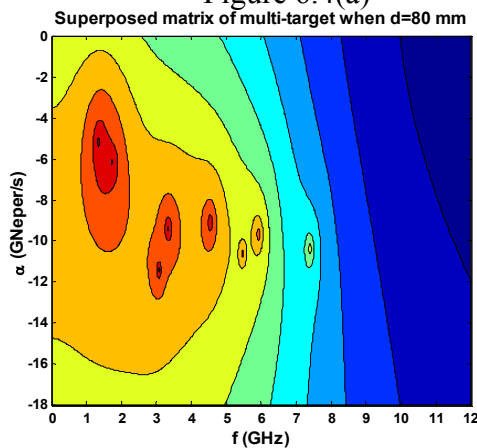
Figure 6.4(c)
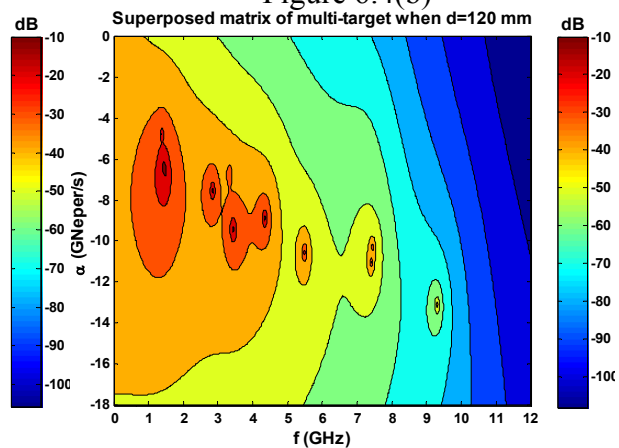
Figure 6.4(d)
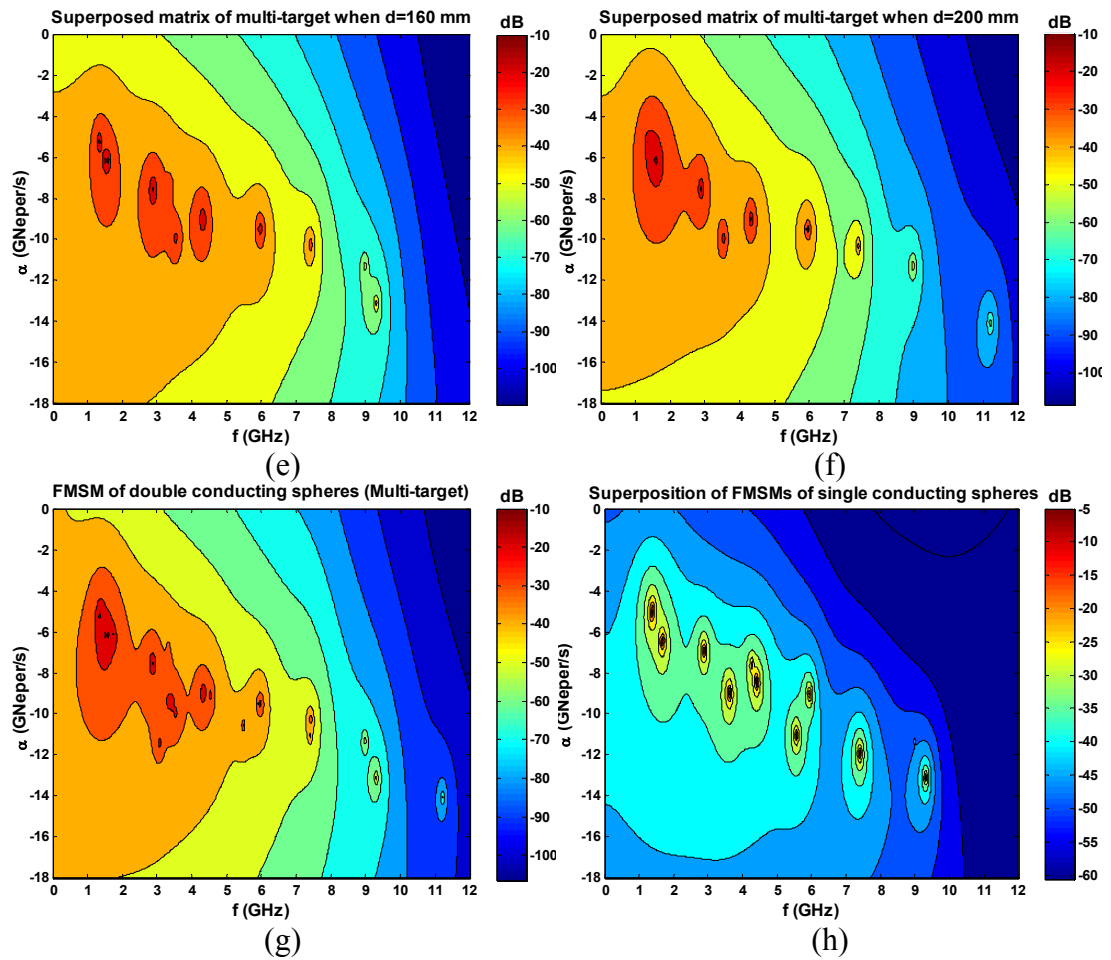
Figure 6.4   (a)-(b) The FMSM features of the conducting spheres with 24 and 30 mm radii (c)-(f) the superposed matrices of two conducting spheres with 24 and 30 mm radii for separation values d= 80, 120, 160 and 200 mm (g) the FMSM feature of double conducting spheres (h) the superposition of FMSMs of single conducting spheres.

It should be noticed that the matrices from Figure 6.4(c) to Figure 6.4(f) are obtained with the superposition of MSMs at different aspect angles of corresponding reference topology. The FMSM of the double conducting spheres, which is given in Figure 6.4(g), is constructed then by the superposition of the matrices in Figure 6.4(c) through Figure 6.4(f), as explained earlier.

161

From the FMSMs of single conducting spheres in Figure 6.4(a) and Figure 6.4(b) and the matrices of multi-target group from Figure 6.4(c) to Figure 6.4(f), it can be deduced that the power distribution maps of multi-target group having high separation values (d= 160 mm and 200 mm) contain the collection of individual spheres' poles; however; multi-target group with low separation values (d= 80 mm and 120 mm) contain some extra poles in addition to the poles of individual spheres. This result is consistent with the theory of scattering from multiple targets due to the following reason: As mentioned in Section 6.2, the scattered field from a multiple conducting sphere group consists of first order fields due to individual spheres and higher order fields due to interaction between spheres. Therefore, theoretically, the power distribution of multi-target group should contain the poles of individual spheres due to first order fields and some other poles, which may vary with respect to the separation distance between the spheres due to the higher order fields. These additional system poles can appear in the power distribution maps of multi-target group with low separation distance values as shown in the maps of Figure 6.4(c) and Figure 6.4(d); but they may not appear in the large separation distance maps since the first order fields are very dominant as compared to the higher order fields. In other words, the group of double conducting spheres with high separation values has power distributions (Figure 6.4(e) and (f)), which are highly similar to the power distribution belonging to the superposition of FMSMs of the individual spheres as given in Figure 6.4(h).

In the decision stage, the signals of all target type/topology/aspect angle cases, (2 single targets+1 multi-target x 4 situions) x (10 aspect angles)= 60 signals, are used for testing purpose. The correlation coefficients between the MSMs of test signals and the FMSMs of library targets are again calculated as described in Section 3.2 and the decisions are made based on the highest correlation coefficient value. The correlation coefficients computed for each one of 60 test signals are tabulated in Table 6.1.

Table 6.1   The correlation coefficients between the MSMs of test signals and FMSMs of the candidate targets for the classifier design in Section 6.2.1.

Target/Separation or Radius/ Aspect angle	Two conducting spheres (Multi-target)	Single conducting sphere with 24 mm radius	Single conducting sphere with 30 mm radius
Multi-target/80 mm/0 degree	0.2425	0.0349	0.0181
Multi-target/80 mm/10 degree	0.4231	0.0271	0.0274
Multi-target/80 mm/20 degree	0.4202	0.0310	0.0187
Multi-target/80 mm/30 degree	0.5695	0.0856	0.3635
Multi-target/80 mm/40 degree	0.6153	0.0756	0.3489
Multi-target/80 mm/50 degree	0.3038	0.0695	0.2295
Multi-target/80 mm/60 degree	0.3117	0.0265	0.0175
Multi-target/80 mm/70 degree	0.6642	0.0271	0.1667
Multi-target/80 mm/80 degree	0.6884	0.0833	0.1957
Multi-target/80 mm/90 degree	0.5654	0.0459	0.1031
Multi-target/120 mm/0 degree	0.5587	0.0375	0.0361
Multi-target/120 mm/10 degree	0.3714	0.0161	0.0219
Multi-target/120 mm/20 degree	0.4914	0.0245	0.0703
Multi-target/120 mm/30 degree	0.2797	0.1278	0.1496
Multi-target/120 mm/40 degree	0.2757	0.0243	0.1140
Multi-target/120 mm/50 degree	0.3128	0.0989	0.1854
Multi-target/120 mm/60 degree	0.3291	0.0092	0.0742
Multi-target/120 mm/70 degree	0.3279	0.0096	0.0636
Multi-target/120 mm/80 degree	0.3594	0.0084	0.1501
Multi-target/120 mm/90 degree	0.5192	0.0192	0.0458
Multi-target/160 mm/0 degree	0.3740	0.0126	0.0107
Multi-target/160 mm/10 degree	0.3458	0.0101	0.0092
Multi-target/160 mm/20 degree	0.3008	0.0163	0.0152
Multi-target/160 mm/30 degree	0.3637	0.0280	0.1871
Multi-target/160 mm/40 degree	0.4953	0.0351	0.0085
Multi-target/160 mm/50 degree	0.3799	0.0142	0.0125
Multi-target/160 mm/60 degree	0.3932	0.0071	0.0075
Multi-target/160 mm/70 degree	0.2370	0.0033	0.0745
Multi-target/160 mm/80 degree	0.5079	0.0080	0.1523
Multi-target/160 mm/90 degree	0.5252	0.0098	0.1861
Multi-target/200 mm/0 degree	0.4382	0.0044	0.0946

Table 6.1 cont'd

Multi-target/200 mm/10 degree	0.4847	0.0668	0.1081
Multi-target/200 mm/20 degree	0.3792	0.0599	0.1143
Multi-target/200 mm/30 degree	0.3520	0.0334	0.0170
Multi-target/200 mm/40 degree	0.5056	0.0384	0.0092
Multi-target/200 mm/50 degree	0.2811	0.0201	0.0111
Multi-target/200 mm/60 degree	0.3634	0.0044	0.0841
Multi-target/200 mm/70 degree	0.4133	0.0045	0.0959
Multi-target/200 mm/80 degree	0.4412	0.0044	0.0954
Multi-target/200 mm/90 degree	0.7151	0.0950	0.0935
Single target/24 mm/0 degree	0.0886	0.6721	0.0044
Single target/24 mm/10 degree	0.0016	0.5894	0.0006
Single target/24 mm/20 degree	0.0008	0.5636	0.0003
Single target/24 mm/30 degree	0.0390	0.7263	0.0024
Single target/24 mm/40 degree	0.0653	0.8265	0.0044
Single target/24 mm/50 degree	0.0409	0.7061	0.0025
Single target/24 mm/60 degree	0.0013	0.5383	0.0002
Single target/24 mm/70 degree	0.0315	0.4259	0.0010
Single target/24 mm/80 degree	0.0433	0.4824	0.0017
Single target/24 mm/90 degree	0.0018	0.6301	0.0007
Single target/30 mm/0 degree	0.1806	0.0034	0.7524
Single target/30 mm/10 degree	0.1582	0.0048	0.4400
Single target/30 mm/20 degree	0.1683	0.0051	0.4674
Single target/30 mm/30 degree	0.1559	0.0048	0.3831
Single target/30 mm/40 degree	0.0679	0.0024	0.5900
Single target/30 mm/50 degree	0.1427	0.0038	0.4070
Single target/30 mm/60 degree	0.1699	0.0051	0.4620
Single target/30 mm/70 degree	0.0355	0.0008	0.4742
Single target/30 mm/80 degree	0.0305	0.0007	0.4619
Single target/30 mm/90 degree	0.1222	0.0034	0.7060

According to the correlation coefficients table shown above, the accuracy rate of this classifier containing single and multiple conducting spheres for noise-free case is found as 100 percent for both 0% margin and 5% margin criteria.

6.2.2. The Classifier Design for a Target Library Containing Single Conducting Sphere and Multiple Conducting Spheres with Identical Elements

In this section, performance of the proposed method is investigated for a classifier library containing a single perfectly conducting sphere (B) with 30 mm radius and a multi-target group, which contains two identical conducting spheres (B-B) of 30 mm radius. In other words, elements of the double-target group are identical to the single conducting sphere in the classifier library. In this classifier design simulation, the single conducting sphere (A) with 24 mm radius is not included in the classifier library since the main purpose of this classifier design is to specifically investigate performance of the method in discriminating the single sphere B and the double-sphere group B-B when all the elements are identical.

The problem geometry used to compute the time responses of the single conducting sphere and double conducting sphere group is the same as described in Section 6.2.1 except that the conducting sphere with 24 mm radius in Figure 6.1(b) is replaced by the conducting sphere with 30 mm radius. The far field bistatic scattered responses of the single target and the double-target group are again obtained over the operating frequency band of (0-12 GHz) with the frequency step of 13.75 MHz at $\phi = 0$ degree and $\theta = 0, 20, 40, 60, 80$ and 90 degrees with CST Microwave Studio simulation program. The time-domain scattered signals having 701 sample points with $\Delta t = 5$ psec time resolution are obtained by using Gaussian windowing, IFFT and zero padding at all aspect angles for the noise-free case. The same three aspect angles ($\theta = 0, 40$ and 90 degrees) are chosen as reference to construct the feature database and to design the classifier.

In the step of searching for the optimal late-time interval, the MSMs are constructed by using the same candidate subintervals and the same MUSIC parameters as those used in the simulation problem of Section 6.2.1. The optimal late-time interval for

this classifier design is found as [3.58 nsec, 4.22 nsec], which is the same optimal interval found in the classifier simulation of Section 6.2.1. The normalized FMSM of the single sphere and the $P_{i,h}(u,v)$ matrices of the two- sphere group are given in Figure 6.5 for four different separation values.
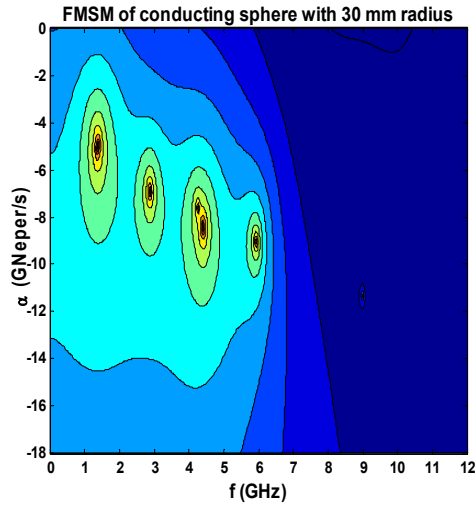
Figure 6.5(a)
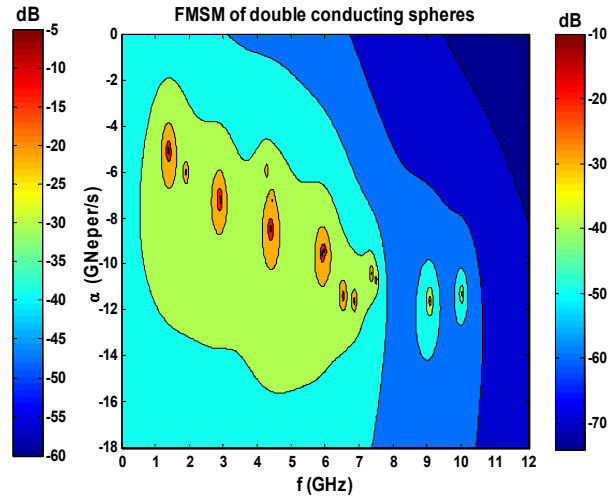
Figure 6.5(b)
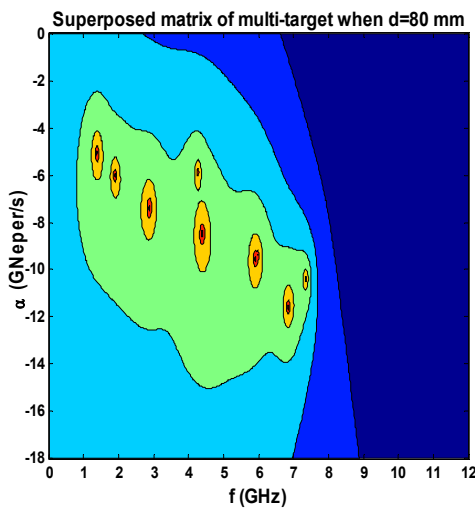
Figure 6.5(c)
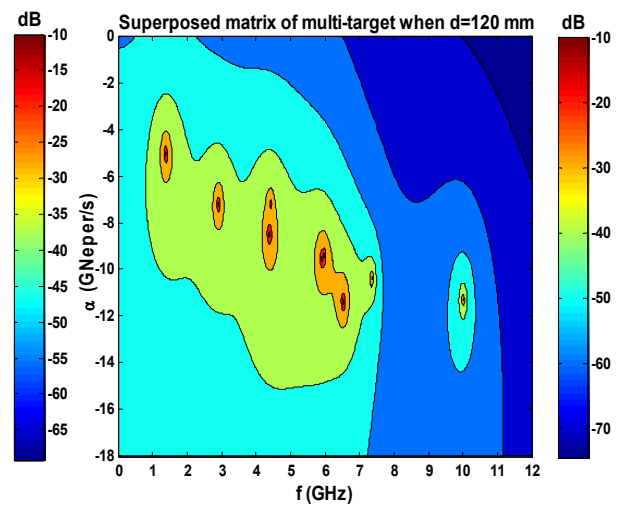
Figure 6.5(d)
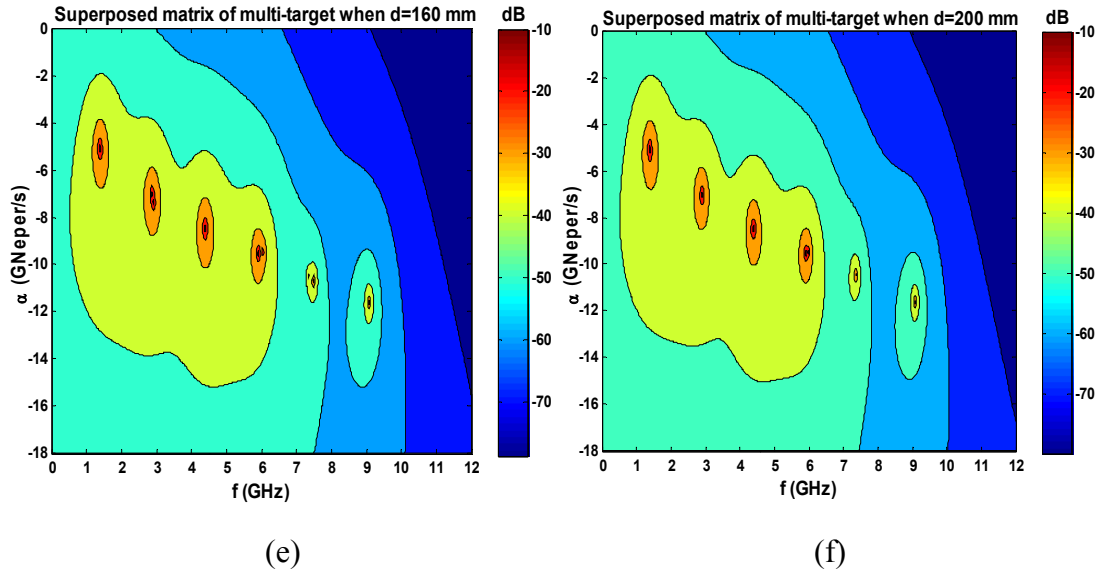
Figure 6.5   (a)-(b) The FMSM feature of the single conducting sphere with 30 mm radius and of the two conducting sphere group with 30 and 30 mm radii (c)-(f) the superposed matrices of two conducting spheres with 30 and 30 mm radii for separation values d= 80, 120, 160 and 200 mm.

It can be concluded based on the context of Figure 6.5 that the power distribution maps of the double-sphere group for high separation values (d= 160 mm in Figure 6.5(d) and d= 200 mm in Figure 6.5(e)) are very similar to the FMSM feature of the single sphere shown in Figure 6.5(a) especially in the frequency range up to 6 GHz. The power distribution maps shown in Figure 6.5(b) for d= 80 mm and in Figure 6.5(c) for d= 120 mm, on the other hand, show different resonance features interpreted as additional poles particularly in the frequency region up to 7 GHz. These results point to a serious drawback of the suggested multi-target recognition method that the designed classifier may not discriminate the single target from the multi-target group when all the elements of multi-target group is the same as that single target when the separation between the elements of multi-target is large.

After the target classifier is designed as explained above, it is tested by (1 single target+1 multi-target x 4 situions) x (6 aspect angles)= 30 test signals. The resulting correlation coefficients computed between the MSMs of test signals and FMSM features of the classifier in database are listed in Table 6.2.

Table 6.2   The correlation coefficients between the MSMs of test signals and FMSMs of the candidate targets for the classifier design in Section 6.2.2.

Target/Separation or Radius/ Aspect angle	Two conducting spheres (Multi-target)	Single conducting sphere with 30 mm radius
Multi-target/80 mm/0 degree	0.2276	0.0241
Multi-target/80 mm/20 degree	0.2861	0.1054
Multi-target/80 mm/40 degree	0.8245	0.6134
Multi-target/80 mm/60 degree	0.5916	0.3626
Multi-target/80 mm/80 degree	0.2397	0.0124
Multi-target/80 mm/90 degree	0.2495	0.0148
Multi-target/120 mm/0 degree	0.5040	0.4579
Multi-target/120 mm/20 degree	0.5490	0.3559
Multi-target/120 mm/40 degree	0.8118	0.5377
Multi-target/120 mm/60 degree	0.5893	0.4476
Multi-target/120 mm/80 degree	0.2910	0.0281
Multi-target/120 mm/90 degree	0.2769	0.0219
Multi-target/160 mm/0 degree	0.6357	0.4676
Multi-target/160 mm/20 degree	**0.5282**	**0.6435**
Multi-target/160 mm/40 degree	0.7997	0.4897
Multi-target/160 mm/60 degree	0.7751	0.4479
Multi-target/160 mm/80 degree	0.4296	0.1852
Multi-target/160 mm/90 degree	0.3817	0.1723
Multi-target/200 mm/0 degree	0.5302	0.2055
Multi-target/200 mm/20 degree	**0.5597**	**0.7054**
Multi-target/200 mm/40 degree	0.8038	0.5025
Multi-target/200 mm/60 degree	0.7684	0.4675
Multi-target/200 mm/80 degree	**0.4888**	**0.4711**
Multi-target/200 mm/90 degree	0.4956	0.2546

Table 6.2 cont'd

Single target/30 mm/0 degree	0.3971	0.7524
Single target/30 mm/20 degree	**0.4650**	**0.4674**
Single target/30 mm/40 degree	0.3567	0.5900
Single target/30 mm/60 degree	**0.4789**	**0.4620**
Single target/30 mm/80 degree	0.2671	0.4619
Single target/30 mm/90 degree	0.4220	0.7060

According to the correlation coefficients shown in Table 6.2, accuracy rate of this classifier is found as 90 percent (27/30) for 0% margin criterion and 83 percent (25/30) for 5% margin criterion for the noise free case. The incorrect decisions in Table 6.2 mostly correspond to the multi-target test group with high separation values, as expected. The resulting accuracy rates are not satisfactory enough considering that tests are conducted for the noise-free case. It is not hard to guess that classifier's performance would get even worse as it is tested against noisy data. Although the classifier design in Section 6.1 for multi-targets with different elements turned out to be successful, the classifier designed in this section for multi-target groups with identical elements show an unsatisfactory performance. As a result, we have come to the conclusion that a major additional improvement is needed in the present method for multi-target classification. The solution we suggested for this problem will be discussed in the next subsection.

6.3. Use of Time Correlation Curves as a Diagnostic Measure to Recognize Multi-Target Groups with Highly Separated Identical Elements

As explained throughout Section 6.2, the target recognition method outlined in Section 6.1 has difficulty in discriminating a single target and a multi-target group whose elements are the same as this single target. This problem may be solved if the

targets in classifier library can be separated into two main sets; a set of single targets and a set of multi-target groups and then the recognition is done within the properly selected set. In other words, initially a test target can be designated as being a single target or a multi-target and then the classifier design is applied to only single target set without interfering with multi-target groups if the test target is designated as a single target, vice versa.

It can be deduced from the time domain responses of two conducting spheres in Figure 6.3 that these responses almost repeat the same signal pattern due to the existence of specular fields received from two identical targets with a time lag especially for high separation distances. In other words, the responses of a multi-target group can be thought as being equal to the superposition of the single target response and a shifted version of this response when the elements of multi-target group are the same. Then, to benefit from this special composite signal form, time correlation curves of such scattered signals are computed using the following expression:

$$
r_{xx}(\tau) = E\left\{x(t+\tau)x^*(t)\right\} = \frac{\sum\limits_{n=1}^{701} x(n \times 5 \; p \; sec)x(n \times 5 \; p \; sec + \tau)}{\sum\limits_{n=1}^{701} \left[x(n \times 5 \; p \; sec)\right]^2}
\tag{6.6}
$$

where E is the expected value operator, $x(t)$ is a scattered time domain signal of a test target and τ is the delay parameter. The time correlation curves computed for all targets used in the simulation example of Section 6.2.2 at all possible combinations of reference aspect angles topologies are plotted in Figure 6.6.
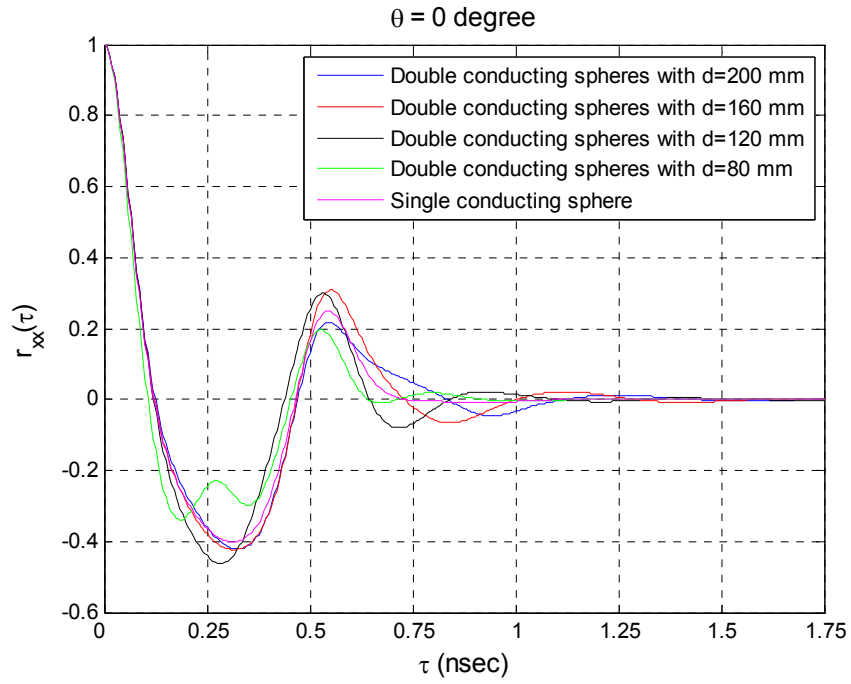
Figure 6.6(a)

Figure 6.6(b)

171

θ = 90 degree

(c)
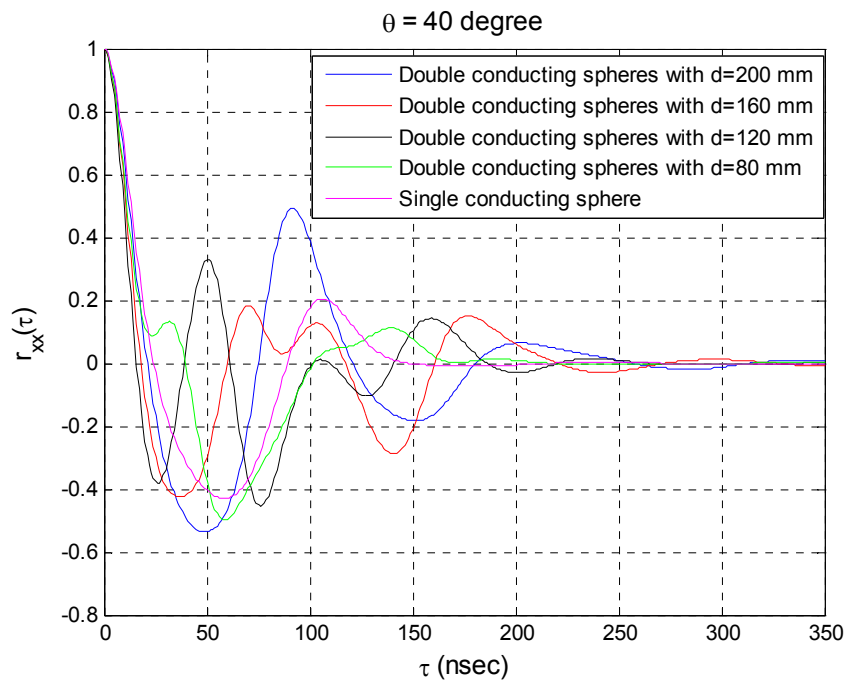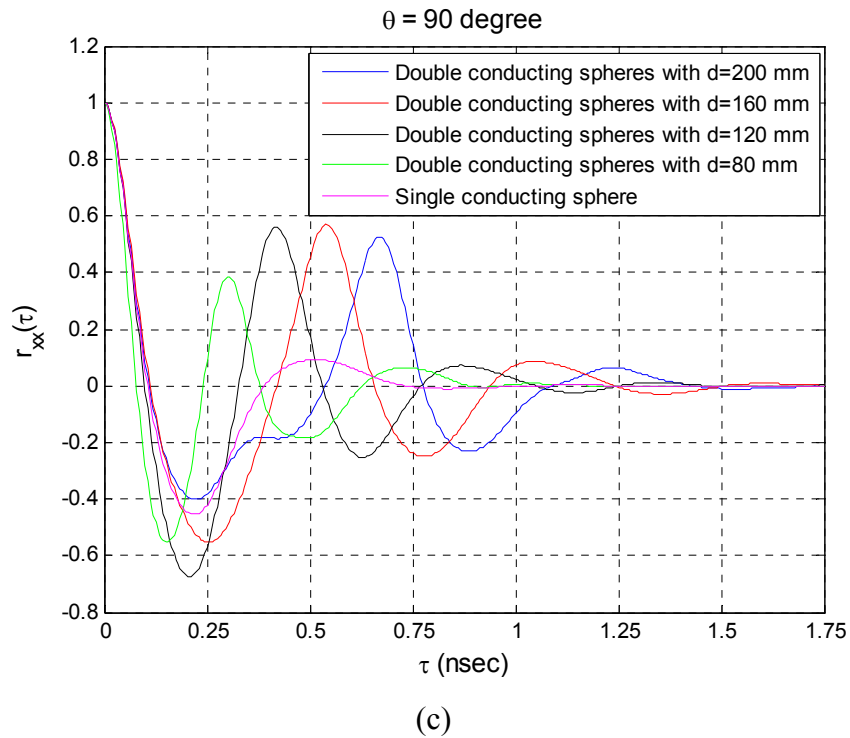
Figure 6.6   Time correlation coefficient curves computed for the tests signals of the target classifier simulation given in Section 6.2.2 at the reference aspect angles of θ= 0, 40 and 90 degrees.

It can be deduced from the curves plotted in Figure 6.6 that the time correlation curves belonging to multi-target groups attenuate down to very small levels for larger delay parameter (τ) values. The so called "cut-off τ" values, where correlation coefficient curves drop to the threshold of 0.01, are given in Table 6.3 for different target/topology cases at various aspect angles.

172

Table 6.3   The cut-off τ values in nsec, where the time correlation curve values drop to 0.01, for the classifier design in Section 6.2.2.

	θ= 0 degree	θ= 40 degree	θ= 90 degree
Single conducting sphere	0.705	0.710	0.780
Double spheres with d=80 mm	0.870	0.995	1.035
Double spheres with d=120 mm	1.035	1.220	1.385
Double spheres with d=160 mm	1.235	1.540	1.475
Double spheres with d=200 mm	1.315	1.520	1.610

As seen from Table 6.3, the cut-off τ values corresponding to the multi-target group, especially for high separation distances, are considerably larger than those of the single conducting sphere. Therefore, based on this observation, a multi-target can be easily separated from the single target by comparing the cut-off τ values of time correlation coefficient curves. This comparison can be done with a distance measure such as the Euclidean distance or the Mahalanobis distance. Classifier designs presented in this chapter both measures are used. Mathematically speaking, the Euclidean distance between a point, x, and a set is defined as $\dfrac{x-\mu}{\sigma}$ where μ and σ are the mean and standard deviation of the data set. The point having Euclidean distance of 3 or greater is classified as out of the data set. The Mahalanobis distance, on the other hand, is a measure introduced by P. C. Mahalanobis [130]. It is based on correlations between variables by which different patterns can be identified and analysed. It is a useful way of determining similarity or dissimilarity of an unknown sample set to a known one. It differs from Euclidean distance in that it takes into account the correlations of the data set, it is scale-invariant and more strict than the Euclidean distance. In theory, the samples that have a Mahalanobis distance of 3 or greater have a probability of 0.01 or less and can be classified as non-members of the group as in the case of Euclidean distance applications. Consequently, if

Mahalanobis or Euclidean distances between the τ value of test signal and τ value arrays of single targets are all bigger than 3, then the test target is classified as a multi-target group. For example, let the test target be two conducting sphere group with 80 mm separation distance observed at 0 degree aspect angle. Then, the Mahalanobis distance between the τ value of this test target (0.870 nsec) and τ value array of single conducting sphere ([0.705 0.710 0.780] nsec) is 10.88. For the same test problem, the Euclidean distance is found to be only 3.

Now, integrating all these ideas in the design procedure, the resulting modified classifier design method for the target sets containing single and multiple targets has the following steps:

- The aspect/topology invariant FMSM features are computed and stored in the classifier's feature database.

- The standard deviation (σ_i) and mean (μ_i) values of $r_{i,match}$ correlation coefficients belonging to each target are also computed and stored.

- For each reference scattered signal belonging to a given single target, the corresponding time correlation curve is computed. Then, the cut-off delay value $\tau_{i,j}$ is determined (for single target i, reference aspect angle j) for which the time correlation curve drops to a threshold value such as 0.01, for example.

- Assume a text signal x(t) is received from an unknown test target. Then, the following decision mechanism, described by the flow chart given in Figure 6.7, is used in the real-time testing phase:
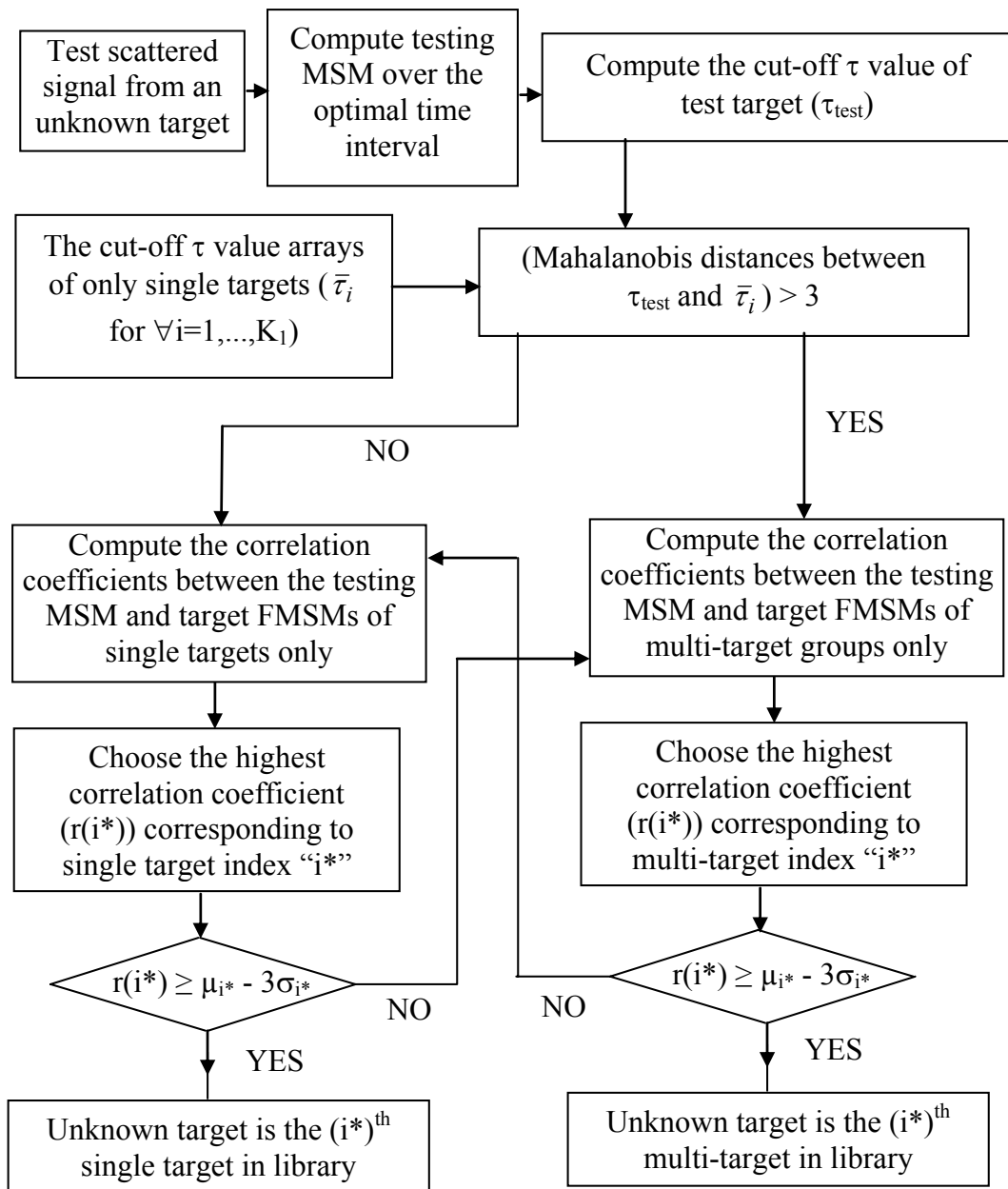
Figure 6.7 The flow chart of the decision algorithm for the suggested multi-target recognition method.

If a test target does not satisfy the criterion of $(\mu_{i^*} - 3\sigma_{i^*}) \leq r(i^*)$ for both single and multi-target sets, then the decision is made within the overall target library using the following criterion:

$$Test \ target \ = target \ i^* \quad if \ r(i^*) \geq r(i) \quad \forall \ i = 1,.., K$$

6.4. Classifier Design Simulations for a Target Library Containing Single and Multi-Targets Using the Modified Method Described in Section 6.3

As the first classifier design simulation of this section, the target classifier design problem of Section 6.2.2 is repeated here, now by using the modified multi-target recognition method described in Section 6.3. In other words, the targets of this classifier are the single conducting sphere of 30 mm radius and the double-sphere group whose elements are identical 30 mm radius spheres. The resulting accuracy rates are found as 100 percent for both 0% and 5% margin criteria when the Mahalanobis distance is used. 97 percent accuracy is obtained for both 0% and 5% margin criteria when Euclidean distance is used. Earlier, in Section 6.2.2, the corresponding accuracy rates were found as 90 percent (for 0% criterion) and 83 percent (for 0% criterion) without using the time correlation curve comparisons. Therefore, adding time correlation information improves the accuracy performance of the suggested multi-target recognition method considerably.

In the first subsection to follow, the novel multi-target classifier design method described in Section 6.3 is initially applied to a target set containing two single and three double perfectly conducting spheres whose responses are generated synthetically using CST Microwave Studio. Then, the method is demonstrated for a target set containing single and multiple small-scale aircraft targets whose responses

176

are obtained with the measurement setup in METU MMW Lab explained in Section 5.1 in detail. The aircraft targets are the small-scale models of realistic aircraft targets used in Section 5.3.

6.4.1. Classifier Design for a Classifier Library Containing Single Conducting Spheres and Double Conducting Sphere Groups

The modified and improved multi-target recognition method described in Section 6.3 is going to be demonstrated for a classifier library, which contains two single conducting spheres with 24 mm radius (target A) and 30 mm radius (target B) and three double-target groups consisting of two conducting spheres with 24 and 24 mm radii (target group AA), 24 and 30 mm radii (target group AB) and 30 and 30 mm radii (target group BB). As seen, two of these double-target groups have identical elements, which are also identical with one of the single conducting spheres in the library. For the double sphere groups, four different separation distances, d= 80, 120, 160 and 200 mm, are considered as reference values.

The problem geometry used to compute the time responses of single and double conducting spheres is the same as the configuration used in Figure 6.1(b). The far field bistatic scattered responses of all single and double-target groups are obtained over the operating frequency band of (0-12 GHz) with the frequency step of 13.75 MHz at the aspect angles of ϕ= 0 degree and θ= 0, 20, 40, 60, 80 and 90 degrees using the CST Microwave Studio simulation program. The time-domain scattered signals having 701 sample points with $\Delta t = 5$ psec time resolution are obtained by using Gaussian windowing, IFFT and zero padding at all aspect angles for the noise-free case. Three aspect angles (θ= 0, 40 and 90 degrees) are chosen as the reference angles to construct the feature database of this classifier.

In the step of searching for the optimal late-time interval, r_{total} values are computed for each subinterval by using the same MUSIC parameters and the same subintervals as in the previous classifier designs. The optimal late-time interval of the classifier is found to be [3.58 nsec, 4.22 nsec]. Then, in addition to the FMSMs, which are given in Figure 6.4(a) and Figure 6.4(b) for the single conducting spheres with 24 and 30 mm radii and in Figure 6.8 for the double conducting spheres, the standard deviation and mean values of $r_{i,match}$ correlation coefficient sequences of each target (for the noise-free case) are stored in the feature database. Furthermore, as mentioned in Section 6.3 the τ values, at which the time correlation curves drops to 0.01 threshold level, are recorded and stored as [0.720 0.725 0.745] nsec for the single conducting sphere with 24 mm radius and [0.705 0.710 0.780] nsec for the single conducting sphere with 30 mm radius, for all three reference aspect angles.

From the maps given in Figure 6.8, it can be observed that the FMSM of double conducting spheres with 24 and 30 mm radii (i.e. the group AB) covers higher number of pole effects since this multi-target group has two different elements resulting in the reception of two different first order field distributions in the response. On the other hand, each of the other double-sphere groups contains two identical elements, which causes the reception of only one type of first order field distribution. For that reason, less number of poles is observed in the FMSM features given in Figure 6.8(b) and 6.8(c).
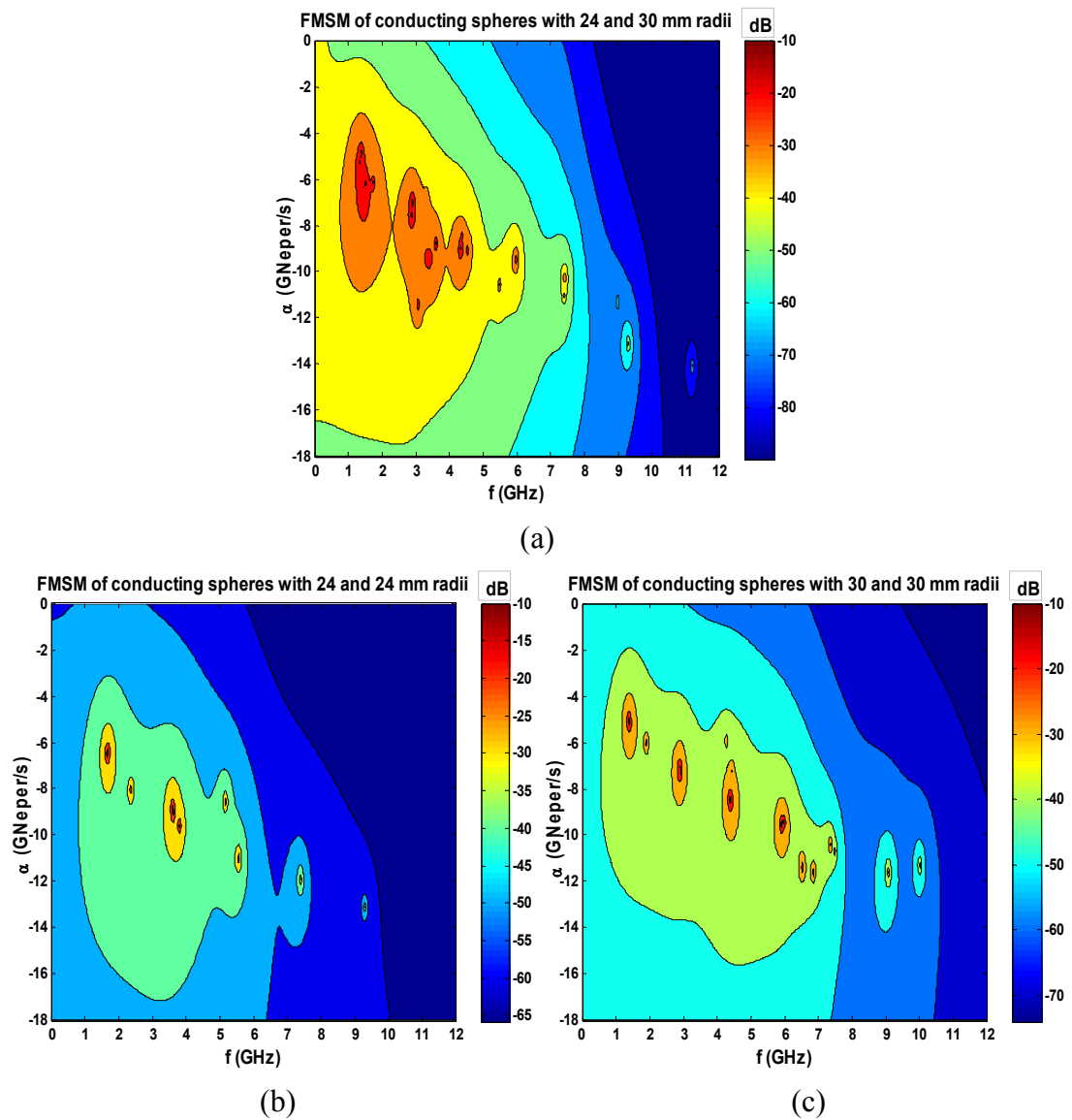
Figure 6.8 (a) The FMSM feature of multiple conducting spheres with 24 and 30 mm radii (b) the FMSM feature of multiple conducting spheres with 24 and 24 mm radii (c) the FMSM feature of multiple conducting spheres with 30 and 30 mm radii.

After the classifier design is completed, the classifier is tested by (2 single targets+3 multi-target groups x 4 situations) x (6 aspect angles)= 84 signals. The accuracy rate for this classifier design is found as 100 percent for both decision criteria when the

Mahalanobis distance is used. The accuracy becomes 98 and 97 percent for 0% margin criterion and 5% margin criterion, respectively by using the Euclidean distance.

After the noise-free case, the noise performance of this classifier design is investigated. For this purpose, the noisy time domain signals are synthesized at the SNR values of 20, 15, 10, 5 and 0 dB for testing. As in the classifier designs given in Section 4.1 and Section 4.4.1, the FMSM features of the targets are constructed using only noisy signals of 10 dB SNR level at the reference aspect angles. However, while determining the τ values, it is observed that these values for the threshold 0.01 are severely affected by the additive noise so that their values do not remain stationary and spread randomly with the increase in noise level. In Figure 6.9, at $\theta = 40$ degree aspect angle, the time correlation curves of the single conducting sphere with 30 mm radius and the double conducting spheres with 30 and 30 mm radii are given for SNR= 10 dB and 5 dB. The corresponding noise-free time correlation curves of these targets were already given in Figure 6.6(b). Examining these time correlation curves at different SNR levels, the threshold value was raised to 0.05 from 0.01 to obtain more stable τ values. Next, the τ values, where the time correlation curves drop to 0.05, are found as [0.55 0.56 0.59] nsec for the single conducting sphere with 24 mm radius and as [0.63 0.66 0.675] nsec for the single conducting sphere with 30 mm radius.
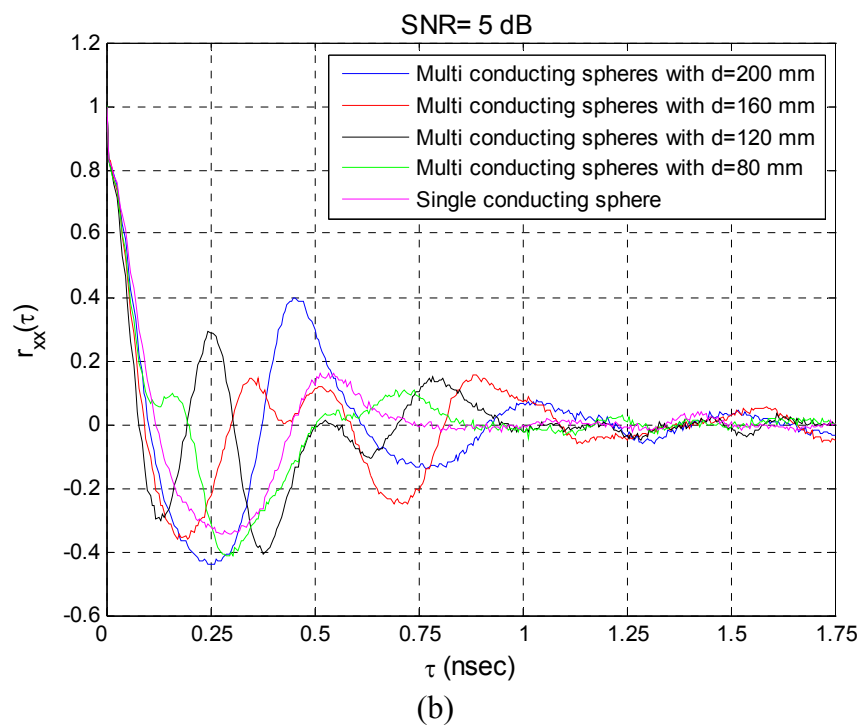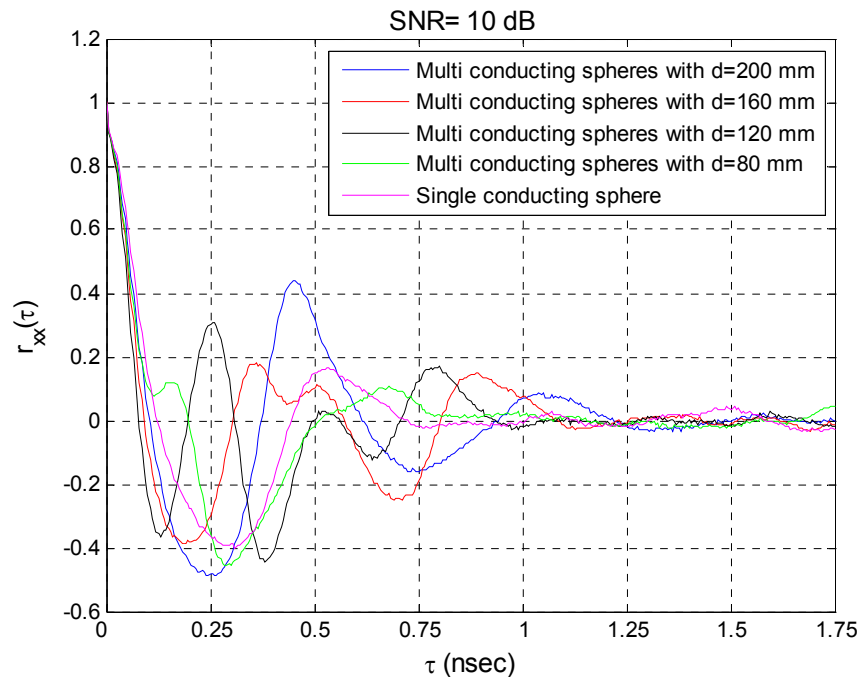
Figure 6.9   The time correlation curves of single conducting sphere with 30 mm radius and double conducting spheres with 30 and 30 mm radii at θ= 40 degrees for (a) SNR= 10 dB (b) SNR= 5 dB.

In classifier testing, again 84 signals per SNR level are used. The overall correct classification rates of the classifier is listed in Table 6.4 for several SNR values, using two different distance measures (Euclidean and Mahalanobis distances) and two different decision criteria (0% margin and 5% margin).

Table 6.4 The correct classification rates (in percentage) of the classifier designed in Section 6.4.1 (with 10 dB SNR data) containing single and double conducting spheres in its library.

SNR Levels	∞		20 dB		15 dB		10 dB		5 dB		0 dB	
Safety margin for decisions	0%	5%	0%	5%	0%	5%	0%	5%	0%	5%	0%	5%
Mahalanobis distance	100	100	100	100	99	98	97	95	89	86	82	80
Euclidean distance	98	97	98	96	95	93	91	90	84	82	78	75

It is seen from the results shown in Table 6.4 that at all SNR levels the accuracy rates of the classifier is higher when the Mahalanobis distance is used rather than the Euclidean distance. Therefore, Mahalanobis distance is found more suitable to be used in the proposed target recognition method and will be used in the following classifier design and test examples to follow. The classifier designed by using the Mahalanobis distance in the algorithm can be regarded as successful up to 10 dB SNR level. However, although the accuracy rates are satisfactory up to 10 SNR level, the rates for this classifier design significantly drop after this level. One of the main reasons of this drop is the association of the test target with the wrong target set in the initial separation phase of the algorithm. In this phase, the cut-off τ values may be determined incorrectly, while using the threshold value of 0.05, especially for low

aspect angles under excessive noise. Furthermore, the results show that, the incorrect decisions mostly involve the single target tests. This observation can be explained by the fact that a common optimal late-time interval is determined for both single and multi-target groups while designing the classifier. This common design interval is conveniently at the starting part of the late-time region for multi-target groups but it is far beyond the starting part of the late-time region for the single conducting spheres. The scattered signals of the single conducting spheres are already attenuated to very small values over this optimal late-time interval becoming too vulnerable to added noise. Thus, as the SNR level of the test data gets smaller, the late-time characterization of the single targets gets worse leading to incorrect recognition results.

6.4.2. Classifier Design for a Target Library Containing Single and Multiple Small-Scale Aircraft Targets

In this classifier design simulation, the target library includes two single small-scale aircraft targets, Boeing 767 and DC-10, and three double-aircraft groups containing (Boeing 767 and Boeing 767), (DC-10 and DC-10) and (Boeing 767 and DC-10). As in Section 5.3, these aircraft targets are the small-scale models of the realistic aircraft targets. The dimensions of the aircraft targets used in this classifier are all scaled by 1/600. The photographs of the aircraft targets are given in Figure 6.10.

Frequency domain responses of the targets are obtained with measurements described in Section 5.1. The responses for single aircraft targets are measured by using same setup in Figure 5.1. Two different reference values for the separation distances, d= 100 and 200 mm, are chosen for the double-aircraft target groups where d= 100 mm case corresponds to non-isolated case and d= 200 mm case almost satisfies the isolated case. The schematic view of the measurement setup, which is used to collect scattered data for the aircraft, is given Figure 6.11.
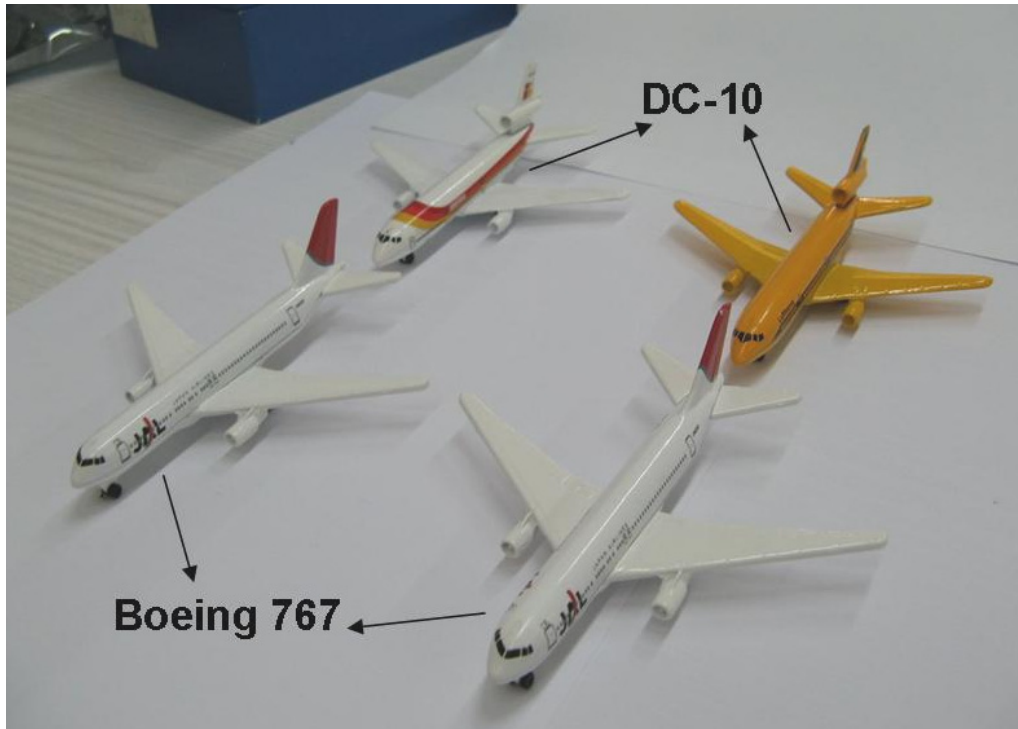
Figure 6.10   The small-scale aircraft targets used in the classifier design in Section 6.4.1.
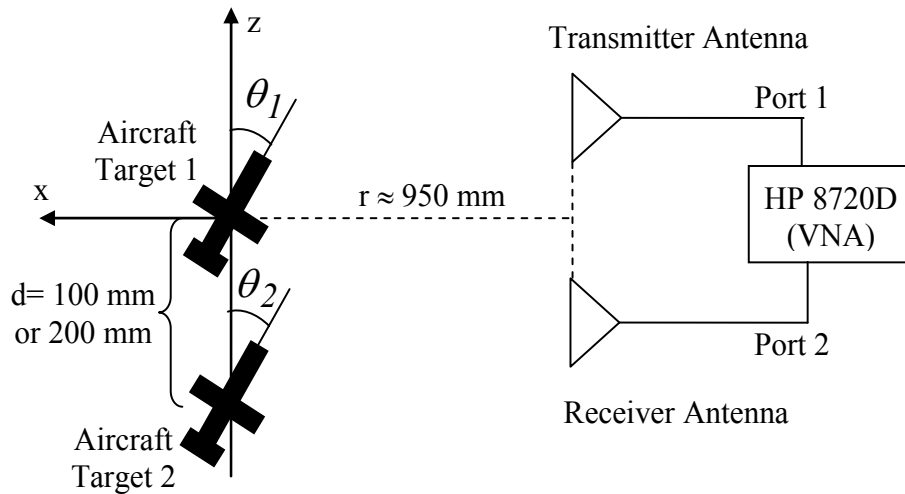
Figure 6.11   The schematic view of the measurement setup for multiple aircraft targets in Section 6.4.2.

The VV-polarized frequency responses of the targets are measured for the incomplete data bandwidth of 1-12 GHz with Δf = 13.75 MHz frequency steps. The measurements are performed at aspect angles from θ = 0 degrees to 90 degrees with 10 degree aspect angle steps for single targets; and from $\theta_1 = \theta_2 = 0$ to 90 degrees with 10 degree steps for multi-targets. Then, the scattered time domain signals with 5 psec time resolution are constructed. As an example, the scattered time domain signals corresponding to the single aircraft targets, Boeing 767 and DC-10, at the aspect angle of θ = 90 degree are plotted in Figure 6.12. Scattered time domain signals for double-aircraft target groups, (Boeing 767 and Boeing 767) and (DC-10 and DC-10) at the aspect angles of $\theta_1=\theta_2=90$ degree are also shown in same figure.
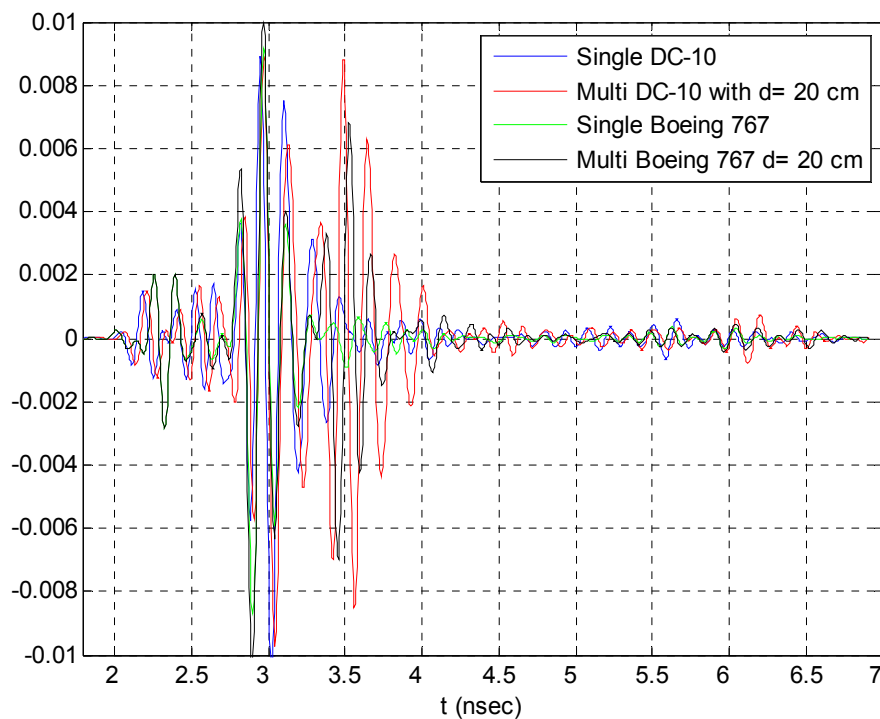
Figure 6.12   The scattered time domain signals of the single aircraft targets, Boeing 767 and DC-10, at the aspect angle of θ= 90 degrees and the double-aircraft targets, (Boeing 767 and Boeing 767) and (DC-10 and DC-10) at the aspect angles of $\theta_1=\theta_2$= 90 degrees.

Out of ten different aspect angles, four aspect angles ($\theta=\theta_1=\theta_2=0$, 30, 60 and 90 degrees) are chosen as reference to construct the feature database of this classifier. In the step of choosing the optimal late-time interval, the scattered signals are divided into some overlapping subintervals from 1.8 nanoseconds. The MSMs of targets at each subinterval are constructed with MUSIC parameters N= 128, $m = 64$, L= 32 and $\Delta t = 5$ psec or 2.5 psec. The optimal late-time interval of this classifier is found as [3.84 nsec-4.48 nsec]. As in the previous classifier design, the FMSMs of targets and matched correlation coefficients corresponding to this optimal interval in addition to the τ values where correlation coefficients drop to 0.05 are stored.

In the decision stage, (2 single aircraft targets+3 multiple aircraft targets x 2 situtions) x (10 aspect angles)= 80 measured test signals are used for performance testing. In order to compare the τ values of test signals and τ value sets of single aircraft targets, only the Mahalanobis distance is used. The accuracy rate of this classifier is found as 94 percent (75/80) for both 0% margin and 5% margin where incorrect decisions are indicated in Table 6.5.

Table 6.5   Incorrect decisions for the small-scale aircraft target classifier designed and tested in Section 6.4.2.

Test Target	Decision
DC-10 at θ= 10 degree	Multi-target: DC-10 and DC-10
Boeing 767 at θ= 40 degree	Multi-target: Boeing 767 and Boeing 767
DC-10 and DC-10 with d= 200 mm at $\theta_1=\theta_2$= 40 degree	Multi-target: Boeing 767 and DC-10
DC-10 and DC-10 with d= 100 mm at $\theta_1=\theta_2$= 10 degree	Single Target: DC-10
Boeing 767 and DC-10 with d= 100 mm at $\theta_1=\theta_2$= 20 degree	Single Target: DC-10

According to the incorrect decisions given in Table 6.5, it can be concluded that four of the total of five incorrect decisions result from the assignment of test target into a wrong target set (i.e. assignment of a single test target as a multi-target or a multiple test target as a test target). Since the SNR levels of the scattered signals are moderate (about 15 dB), the selection of optimal late-time interval in a too late time region should not constitute a considerable drawback for this classifier design.

This aircraft classifier design simulation is also repeated without using the time correlation information and the accuracy rates are found to drop considerably to 83 percent (66/80) for 0% margin and 81 percent (65/80) for 5% margin. In other words, use of valuable information provided by time correlation curves in the decision process leads to very high accuracy rates even in this challenging target classification example that involves totally realistic and complicated target geometries (small scale aircraft targets) with experimental scattered data used in both classifier design and test phases.

CHAPTER 7

CONCLUSIONS AND FUTURE WORK

This thesis presents a novel aspect and polarization invariant electromagnetic target recognition method in resonance region. A natural-resonance based classifier model is integrated with a MUSIC algorithm-based signal processing technique in the context of multi-aspect feature fusion approach. The "Fused MUSIC Spectrum Matrices (FMSMs)" generated for each target by superposing the individual MUSIC spectrum matrices at the optimal late-time interval are used as the main target feature in the suggested method. These FMSMs improve the performance of the method by including more pole effects and reducing both aspect and polarization dependency. The resulting, computationally simple technique is used to design highly efficient and successful classifier designs throughout this thesis.

It must be emphasized that the success of an electromagnetic target recognition technique can be easily judged on the objective and fair grounds simply by checking a standard set of performance/design criteria. It is shown in Chapter 4 and 5 that the proposed method satisfies the following performance/design criteria for single targets:

- Admissibility of arbitrary target geometries/material compositions: For the first time in literature, the proposed method is demonstrated to be applicable to all of highly challenging target classes of (a) very low-Q targets (perfectly conducting spheres), (b) dielectric targets with complicated internal

resonances (lossless dielectric spheres, thick dielectric rods), (c) moderately high-Q targets with complex geometries (small-scale aircraft targets modeled by conducting straight wires, small-scale aircraft targets as being the models of realistic aircraft targets). None of the target identification methods reported in the recent literature demonstrate their validity for all these extremely demanding target types. Some are demonstrated for the simplest case of high-Q straight, thin conducting wires [82], [83], [87], some are applied to moderately high-Q targets with complex geometries [81], [84]-[86]; while some other methods are demonstrated for low-Q conducting spheres and/or dielectric targets [23], [66], [91] but not tested for targets with complex geometries.

- <u>High accuracy rate (i.e. correct classification ratio)</u>: With the proposed technique, excellent classifiers are designed having (a) almost 100 percent accuracy for the aircraft classifier designed in Section 4.3 even under moderately noisy conditions with overall SNR levels as low as 10 dB (b) 97 percent accuracy for dielectric sphere classifier at 10 dB SNR (c) 98 percent accuracy (at 15 dB SNR) and 94 percent accuracy (at 10 dB SNR) for conducting sphere classifiers. Attaining accuracy rates close to 100 percent is demonstrated in some studies in literature for the noise-free case studies [91]. However, at SNR levels as low as 10 dB, the accuracy rates of the present techniques drop below 90 percent.

- <u>Invariance with respect to aspect and polarization:</u> All of the given classifier designs, especially the aircraft target classifier in Section 4.3, have been demonstrated as being highly aspect and polarization invariant. For the first time in literature, the proposed method is demonstrated to be polarization invariant in addition to being fully aspect (both in azimuth and elevation invariant) invariant based on intensive testing over a broad range of signal-to-noise ratio. None of the target identification methods in the

literature has given such a complete analysis for these mandatory invariance requirements. The best analyses are given in [23], [86], [91] which provided a detailed analysis for the aspect invariance (with respect to azimuth variations only in [86]). Most of the other techniques are either demonstrated at a single aspect angle [82]-[84], [87], or at a small number of aspect angles [21], [81], [85]. No polarization invariance has been demonstrated in any present study so far.

- Robustness with respect to noise: It is well accepted by researchers working on the electromagnetic target recognition area that being robust under noisy conditions is a mandatory requirement for a properly designed and practically useful target classifier. Being functional in noiseless or low-noise (roughly with SNR levels larger than 25-30 dB) conditions is definitely not enough for an acceptable classifier performance. Deterioration in classifier accuracy is of course inevitable but the amount of deterioration must remain within acceptable limits. Classifier designs given in this thesis are demonstrated to be highly accurate even at very low SNR levels. For instance, while the conducting and dielectric sphere classifier designs in Section 4.1 and 4.2 can attain accuracy rates of 85-86 percent at the 0 dB SNR level, the aircraft target classifier design in Section 4.3, a challenging design, still has 93 percent accuracy (with 0% margin criterion) rate at the very high noise case of 0 dB SNR which means the noise power is equal to the signal power. In the literature, no present study has reached similar accuracy rates for such low SNR levels.

- Classifier design with noisy data: For the first time in literature, the proposed technique is demonstrated to be useful for electromagnetic classifier design using substantially noisy reference scattered data. All the other methods demonstrated in literature use either noise-free numerical data or very low noise measurement data (recorded in controlled environments such as

compact ranges) in the classifier design phase. After the design, they test the performance of their classifiers with noisy data. With the method proposed in this thesis, successful classifiers are designed with already noisy data using reference signals having 5 dB SNR level (in Section 4.2); 10 dB SNR level (in Section 4.1 and 4.3). These classifiers are demonstrated to produce 97-100 percent accuracy rates when tested with signals having SNR values as low as 10 dB. Even at very low testing SNR values such as 0 dB or -5 dB the classifier designs still give completely acceptable accuracy rates.

- <u>Classifier design with only a few aspect angles and small memory storage:</u> The proposed method needs reference data at only a few aspect angles which requires a very small volume of data. This property is shared by only the E-pulse/K-pulse type methods as well as the methods reported in [23] and [91]. However, some methods, such as the one in [86] for instance, is at the other extreme of using too many reference aspect angles. The proposed method also uses only one matrix for each target in the feature database which considerable reduces the memory storage of the classifier designs.

- <u>Simplicity and repeatibility of the design method and difficulties encountered in choosing design parameters:</u> The proposed target recognition technique is a natural resonance-based technique processing the late-time scattered data in a very simple and repeatable way using the MUSIC algorithm only and without using any a priori target pole or other information. The method is inspired by the SEM of Baum, similar to the methods such as E-pulse/K-pulse methods. However, the suggested method in this thesis is very different from those methods in terms of the signal processing techniques needed for feature extraction procedure that the difficulties encountered in these former methods are not valid for the proposed technique. For instance, in E-pulse/K-pulse methods, in general, those E-pulse or K-pulse feature signals are (a) either synthesized from the known/extracted poles of the target, where a good

estimate for number of target poles is needed. Also, very low noise design data are needed for accurate pole extraction which may not be always possible, (b) or they are optimized (without using target pole information) via conventional or global optimization techniques. Optimization itself is a tricky signal processing approach; results may not be repeatable especially when there are many local optimal solutions. Reaching the globally optimal solution may not be possible in the case of complex target geometries or non-conducting material compositions. Therefore, the target classifier design technique suggested in this thesis is very simple and repeatable, which uses the MUSIC algorithm as the only signal processing tool for feature extraction.

- <u>The ability of discriminating an alien target from the target set:</u> For the first time in literature, the proposed method is demonstrated to discriminate an alien target from the targets in database. Besides, the correct decision rate of this operation is similar with the accuracy rates of the classification of candidate targets in the database. There is no such study in literature of target recognition area about discrimination of an alien target from a known target database.

To sum up, this thesis has not only shown the feasibility of a new electromagnetic target recognition technique with very high correct classification rates; but it has also provided extremely detailed analysis results to prove that the proposed technique is indeed (i) aspect and polarization invariant, (ii) very robust under noise and (iii) works out for even the most difficult target recognition problems involving very low-Q targets, dielectric targets and conducting targets with complex geometries. As an additional and very important asset, the proposed target recognition technique is also useful to design very effective target classifiers using noisy reference data. After comparing the contents of the target recognition methods in literature to the content of the proposed method, it can be confidently claimed that the technique introduced

in this thesis is the only one successfully satisfying all eight criteria listed above, which are objective and fair measures to test performance of any target classification method in electromagnetics.

From the results in Chapter 4 and 5, it is seen that the suggested target recognition technique is general enough to be applicable to any single target scenario. Application of this technique to the recognition of target sets containing multi-targets is a very challenging problem because of the complicated multiple scattering mechanisms. This problem is addressed in Chapter 6 and solved after introducing major modifications for multi-topology feature fusion and using time correlation curves as the diagnostic measure for identical and isolated multi-target groups. For the first time in literature, performance of the resulting design method is found fully satisfactory in classifying not only single but also multiple targets accurately within composite target libraries. The demonstrations are given for two classifier libraries; library of conducting spheres and library of small-scale model aircraft.

The future work for both single and multi-target classification can be summarized as follows:

- Performance of the proposed single/multiple target classification method needs to be investigated for lossy target applications.

- The proposed method may be applied to classification of targets made of metametarials.

- The classifier design realized for multi-targets in Section 6.4.2 may be repeated for different target topologies where different locations of the aircraft targets within the double-target groups can be used for training and/or testing.

193

- The invariance of the multi-target classification method may be tested with respect to polarization and elevation angle.

- In this thesis, the proposed method for multi-targets is only demonstrated for the classifier designs containing double-target groups. The number of elements in the multi-target groups can be increased to three or more to test the performance of the resulting classifiers.

- Applicability of the proposed method to the detection of single or multiple landmines using ground penetrating radar (GPR) data may be investigated. For this purpose, scattered fields from landmine structure should be obtained either by simulations (CST) or measurements (GPR).

- Applicability of the proposed method to discriminate a target from the clutter in the background may be investigated.

REFERENCES

[1] M. I. Skolnik, Introduction to Radar Systems, 2nd Ed., McGraw-Hill, New York, 2001.

[2] A. Farina, P. Lombardo, M. Marsella, "Joint tracking and identification algorithms for multisensor data," *IEE Proc.- Radar, Sonar and Navigation,* vol. 149, no. 6, pp. 271-280, Dec. 2002.

[3] N. Ukita, T. Matsuyama, "Real-time cooperative multi-target tracking by communicating active vision agents," *The 16th International Conference on Pattern Recognition,* vol. 2, pp. 758-763, July 2003.

[4] W. Bridge, "IFF System Concept Based on Time Synchronization," *IEEE Transactions on Communication,* vol. 28, no. 9, part 1, pp. 1630-1637, Sept. 1980.

[5] T. M. Schuck, B. Shoemaker, J. Willey, "Identification friend-or-foe (IFF) sensor uncertainties, ambiguities, deception and their application to the multi-source fusion process," *National Aerospace and Electronics Conference (NAECON),* pp. 85-94, Oct. 2000.

[6] N. Ikram, J. S. Shepherd, "A new approach towards secure IFF technique," *Military Communications Conference (MILCOM),* vol. 3, pp. 1013-1017, Oct. 1998.

[7] P. R. Foster, M. W. S. Grigson, C. W. R., "D band IFF for army air defense systems," *Radar 97 (Conf. Publ. No. 449),* pp. 705-709, Oct. 1997.

[8] A. A. Ksienski, Y. T. Lin, L. J. White, "Low-frequency approach to target identification," *Proc. IEEE,* vol. 63, no. 12, pp. 1651-1660, Dec. 1975.

[9] H. Lin, A. A. Ksienski, "Optimum frequencies for aircraft classification," *IEEE Trans. Aerospace Elect. Syst.,* vol. 17, no. 5, pp. 656-665, Sept. 1981.

[10]   C. W. Chuang, D. L. Moffatt, "Natural resonances of radar targets via Prony's method and target discrimination," *IEEE Trans. Aerospace Elect. Syst.*, vol. 12, no. 6, pp. 583-589, Nov. 1975.

[11]   C. E. Baum, Toward an engineering theory of electromagnetic scattering: the singularity and eigenmode expansion methods, in P. L. E. Uslenghi (Ed.), Electromagnetic Scattering, Academic Press, New York, 1978.

[12]   M. A. Morgan, "Singularity expansion representations of fields and currents in transient scattering," *IEEE Trans. Antennas and Propagation,* vol. 32, no. 5, pp. 466-473, May 1984.

[13]   H. Uberall, G. Gaunaurd, "Relation between the ringing of resonances and surface waves in radar scattering," *IEEE Trans. Antennas and Propagation,* vol. 32, no. 10, pp. 1071-1079, Oct. 1984.

[14]   M. L. Van Blaricum, R. Mittra, "A technique for extracting the poles and residues of a system directly from its transient response," *IEEE Trans. Antennas and Propagation,* vol. 23, no. 6, pp. 777-781, Nov. 1975.

[15]   Y. Hua, T. K. Sarkar, "Generalized Pencil-of-Function method for extracting poles of an EM system from its transient response," *IEEE Trans. Antennas and Propagation,* vol. 37, no. 2, pp. 229-234, Feb. 1989.

[16]   B. Drachman and E. Rothwell, "A continuation method for identification of the natural frequencies of an object using a measured response," *IEEE Trans. Antennas and Propagation*, vol. 33, no. 4, pp. 445-450, April 1985.

[17]   E. J. Rothwell, K.-M. Chen, D. P. Nyquist, "Extraction of the natural frequencies of a radar target from a measured response using E-pulse techniques," *IEEE Trans. Antennas and Propagation*, vol. 35, no. 6, pp. 715-720, June 1987.

[18]   H. T. Kim, N. Wang, D. L. Moffatt, "K-pulse for a thin circular loop," *IEEE Trans. Antennas and Propagation*, vol. 33, no. 12, pp. 1403-1407, Dec. 1985.

[19]   K. M. Chen, D. P. Nyquist, E. J. Rothwell, L. L. Webb, B. Drachman, "Radar target discrimination by convolution of radar returns with extinction-pulses

and single-mode extraction signals," *IEEE Trans. Antennas and Propagation,* vol. 34, no. 7, pp. 896-904, July 1986.

[20] G. Turhan-Sayan, K. Leblebicioglu, T. Ince, "Electromagnetic target classification using time-frequency analysis and neural networks," *Microwave Opt. Tech. Lett.,* vol. 21, no. 1, pp. 63-69, April 1999.

[21] J. E. Mooney, Z. Ding, L. S. Riggs, "Performance analysis of a GLRT automated target discrimination scheme," *IEEE Trans. Antennas and Propagation,* vol. 49, No. 12, pp. 1827-1835, Dec. 2001.

[22] W. Dangwei, M. Xinyi, S. Yi, "Radar target identification using a likelihood ratio test and matching pursuit technique," *IEE Proc.- Radar, Sonar and Navigation*, vol. 153, no. 6, pp. 509-515, Dec. 2006.

[23] G. Turhan-Sayan, "Natural resonance-based feature extraction with reduced aspect sensitivity for electromagnetic target classification," *Pattern Recognition*, vol. 36, no. 7, pp. 766-776, July 2003.

[24] Q. Li, P. Ilavarasan, J. E. Ross, E. J. Rothwell, K.-M. Chen, D. P. Nyquist, "Radar target identification using a combined early-time/late-time E-pulse technique," *IEEE Trans. Antennas and Propagation,* vol. 46, no. 9, pp. 1272-1277, Sept. 1998.

[25] W. Dangwei, S. Yi, M. Xinyi, W. Shaogang, "Natural resonance frequency extraction using an early-time and late-time responses combined technique," *Conference on Ultrawideband and Ultrashort Impulse Signals,* pp. 201-204, Sept. 2004.

[26] M. Secmen and G. Turhan-Sayan, "A novel electromagnetic target recognition method by MUSIC algorithm," *IEEE Antennas and Propagation Society International Symposium*, pp. 1299-1302, July 2006.

[27] E. M. Kennaugh, R. L. Corgiff, "The use of impulse response in electromagnetic scattering problems," *IRE National Convention Record*, part I, pp. 72-77, 1958.

[28] E. M. Kennaugh, D. L. Moffatt, "Transient and impulse response approximations," *Proc. IEEE,* vol. 53, no. 8, pp. 893-901, Aug. 1965.

[29]   D. L. Moffatt, R. K. Mains, "Detection and discrimination of radar target," *IEEE Trans. Antennas and Propagation,* vol. 23, no. 3, pp. 358-367, May 1975.

[30]   L. Marin, "Natural-mode representation of transient scattered fields," *IEEE Trans. Antennas and Propagation,* vol. 21, no. 6, pp. 809-818, Nov. 1973.

[31]   C. E. Baum, "Emerging technology for transient and broad-band analysis and synthesis of antennas and scatterers," *Proc. IEEE,* vol. 64, no. 11, pp. 1598-1616, Nov. 1976.

[32]   L. Marin, "Major results and unresolved issues in singularity expansion method," *Electromagnetics,* vol. 1, no. 4, pp. 361-373, 1981.

[33]   C. E. Baum, E. J. Rothwell, K.-M. Chen, D. P. Nyquist, "The singularity expansion method and its application to target identification," *Proc. IEEE,* vol. 79, no. 10, pp. 1481-1492, Oct. 1991.

[34]   C. E. Baum, The singularity expansion method, in L. B. Felsen (Ed.), Transient electromagnetic fields, Springer-Verlag, Berlin, 1976.

[35]   J. Bak, D. J. Newman, Complex Analysis, 2nd Ed., Springer-Verlag, New York, 1997.

[36]   L. B. Felsen, "Comments on early-time SEM," *IEEE Trans. Antennas and Propagation,* vol. 33, no. 1, pp. 118-119, Jan. 1985.

[37]   E. Heyman, L. B. Felsen, "A wavefront interpretation of the singularity expansion method," *IEEE Trans. Antennas and Propagation,* vol. 33, no. 7, pp. 706-718, July 1983.

[38]   E. J. Rothwell, K. M. Chen, D. P. Nyquist, P. Ilavarasan, J. E. Ross, R. Bebermeyer and Q. Li, "A general E-pulse scheme arising from the dual early-time/late-time behaviour of radar scatterers," *IEEE Trans. Antennas and Propagation,* vol. 42, no. 9, pp. 1336-1341, Sept. 1994.

[39]   F. M. Tesche, "On the analysis of scattering and antenna problems using the singularity expansion method," *IEEE Trans. Antennas and Propagation,* vol. 21, no. 1, pp. 53-62, Jan. 1973.

[40] J. Van Bladel, Electromagnetic Fields, 2nd Ed., John Wiley & Sons Inc., New Jersey, 2007.

[41] E. J. Rothwell, K. M. Chen, D. P. Nyquist, J. E. Ross and R. Bebermeyer, "A radar target discrimination scheme using discrete wavelet transform for reduced data storage," *IEEE Trans. Antennas and Propagation,* vol. 42, no. 7, pp. 1033-1037, July 1994.

[42] P. K. Bharadwaj, P. R. Runkle and L. Carin, "Target identification with wave-based matched pursuits and hidden markov models," *IEEE Trans. Antennas and Propagation,* vol. 47, no. 10, pp. 1543-1554, Oct. 1999.

[43] J.-H Lee, I.-S. Choi, H.-T. Kim, "Natural frequency-based neural network approach to radar target recognition," *IEEE Trans. on Signal Processing,* vol. 51, no. 12, pp. 3191-3197, Dec. 2003.

[44] S. L. Marple, Digital Spectral Analysis with Applications, Prentice-Hall Englewood Cliffs, New Jersey, 1987.

[45] A. J. Poggio, M. L. Van Blaricum, E. K. Miller and R. Mittra, "Evaluation of a processing technique for transient data," *IEEE Trans. Antennas and Propagation,* vol. 26, no. 1, pp. 165-173, Jan. 1978.

[46] C.-C. Chen, L. Peters, "Buried unexploded ordnance identification via complex natural resonances," *IEEE Trans. Antennas and Propagation,* vol. 45, no. 11, pp. 1645-1654, Nov. 1997.

[47] N. H. Younan, C.M. Shearin, T.F. Nash, "Natural frequencies extraction of a radar target from a measured response using the Prony method", *IEEE Antennas and Propagation Society International Symposium*, pp. 66-69, July 1993.

[48] M. L. VanBlaricum and R. Mittra, "Problems and solutions associated with Prony's method for processing transient data," *IEEE Trans. Antennas and Propagation,* vol. 26, no. 1, pp. 174-182, Jan. 1978.

[49] D. G. Dudley, "Parametric modeling of transient electromagnetic systems," *Radio Science,* vol. 14, no. 6, pp. 387-396, June 1979.

[50]   G. Majda, W. Strauss and M. Wei, "Computation of exponentials in transient data," *IEEE Trans. Antennas and Propagation*, vol. 37, no. 10, pp. 1284-1290, Oct. 1989.

[51]   A. G. Ramm, "Extraction of resonances from transient fields," *IEEE Trans. Antennas and Propagation*, vol. 33, no. 2, pp. 223-226, Feb.1985.

[52]   Y. Hua and T. K. Sarkar, "A discussion of E-pulse method and Prony's method for radar target resonance retrieval from scattered field," *IEEE Trans. Antennas and Propagation*, vol. 37, no. 7, pp. 944-946, July 1989.

[53]   Y. Hua and T. K. Sarkar, "A perturbation property of the TLS-LP method," *IEEE Trans. on Acoustics, Speech and Signal Processing*, vol. 38, no. 11, pp. 2004-2005, Nov. 1990.

[54]   Y. Hua and T. K. Sarkar, "On the total least squares linear prediction method for frequency estimation," *IEEE Trans. on Acoustics, Speech and Signal Processing*, vol. 38, no. 12, pp. 2186-2189, Dec. 1990.

[55]   Y. Hua and T. K. Sarkar, "Matrix pencil method for estimating parameters of exponentially damped/undamped sinusiods in noise," *IEEE Trans. on Acoustics, Speech and Signal Processing*, vol. 38, no. 5, pp. 814-824, May 1990.

[56]   T. K. Sarkar, O. Pereira, "Using the Matrix pencil method to estimate the parameters of a sum of complex exponentials," *IEEE Antennas and Propagation Magazine*, vol. 37, no. 1, pp. 48-55, Feb. 1995.

[57]   Y. Hua and T. K. Sarkar, "Matrix pencil method and its performance," *IEEE International Conference on Acoustics, Speech and Signal Processing*, vol. 4, pp. 2476-2479, April 1988.

[58]   V. K. Jain, T. K. Sarkar and D. D. Weiner, "Rational modeling by pencil-of-function methods," *IEEE Trans. on Acoustics, Speech and Signal Processing*, vol. 31, no. 6, pp. 564-573, June 1983.

[59]   A. J. Mackay and A. McCowen, "An improved pencil-of-function method and comparisons with traditional methods of pole extraction," *IEEE Trans. Antennas and Propagation*, vol. 35, no. 4, pp. 435-441, April 1987.

[60] E. K. Miller, Time-Domain Measurements in Electromagnetics, Van Nostrand-Reinhold, New York, 1986.

[61] S. Al Khouri-Ibrahim, R. Gomez Martin, F. J. Munoz-Delgado, V. Raminez-Gonzalez, "Extraction of the poles of noisy rational signals by the continuation method," *Proc. Inst. Elect. Eng.,* part F, pp. 57-62, Feb. 1989.

[62] L. C. Kaufman, "A variable projection method for solving separable nonlinear least squares problems," *BIT Numerical Mathematics*, vol. 15, no. 1, pp. 49-57, March 1975.

[63] D. A. Ksienski, "Pole and residue extraction from measured data in frequency domain using multiple data sets," *Radio Science,* vol. 20, no. 1, pp. 13-19, Jan. 1985.

[64] S.-W. Park, J. T. Cordaro, "Improved estimation of SEM parameters from multiple observations," *IEEE Trans. Aerospace Elect. Syst.*, vol. 30, no. 5, pp. 145-153, May 1988.

[65] C. E. Baum, "A priori application of results of electromagnetic theory to the analysis of electromagnetic interaction data," *Radio Science,* vol. 20, no. 12, pp. 1127-1136, Dec. 1985.

[66] G. Turhan-Sayan and M. Kuzuoglu, "Pole estimation for arbitrarily-shaped dielectric targets using genetic algorithm based resonance annihilation technique," *Electronics Lett.*, vol. 37, no. 6, pp. 380-381, March 2001.

[67] E. J. Rothwell, K.-M. Chen and D. P. Nyquist, "Extraction of the natural frequencies of a radar target from a measured response using E-pulse techniques," *IEEE Trans. Antennas and Propagation*, vol. 35, no. 6, pp. 715-720, June 1987.

[68] E. M. Kennaugh, "The K-pulse concept," *IEEE Trans. Antennas and Propagation*, vol. 29, no. 2, pp. 327-331, Mar. 1981.

[69] F. Y. S. Fok, D. L. Moffatt, N. Wang, "K-pulse estimation from the impulse response of a target," *IEEE Trans. Antennas and Propagation*, vol. 35, no. 8, pp. 926-933, Aug. 1987.

[70] G. Turhan-Sayan, D. L. Moffatt, "K-pulse estimation using Legendre polynomial expansions and target discrimination," *Journal of Electromagnetic Waves and Applications*, vol. 4, no. 2, pp. 113-128, 1990.

[71] F. Y. S. Fok, D. L. Moffatt, "The K-pulse and E-pulse," *IEEE Trans. Antennas and Propagation*, vol. 35, no. 11, pp. 1325-1326, Nov. 1987.

[72] K. M. Chen, D. P. Nyquist, D. Westmoreland, C. I. Chuang, B. Drachman "Radar waveform synthesis for single-mode scattering by a thin cylinder and application for target discrimination," *IEEE Trans. Antennas and Propagation*, vol. 30, no. 9, pp. 867-880, Sept. 1982.

[73] E. J. Rothwell, K. M. Chen, D. P. Nyquist, W. Sun, "Frequency domain E-pulse synthesis and target discrimination," *IEEE Trans. Antennas and Propagation*, vol. 35, no. 4, pp. 426-434, April 1987.

[74] E. J. Rothwell, D. P. Nyquist, K. M. Chen, B. Drachman, "Radar target discrimination using the extinction-pulse technique," *IEEE Trans. Antennas and Propagation*, vol. 33, no. 9, pp. 929-936, April 1985.

[75] K. M. Chen, "Radar waveform synthesis method- a new radar detection scheme," *IEEE Trans. Antennas and Propagation*, vol. 29, no. 4, pp. 553-565, July 1981.

[76] E. J. Rothwell, D. P. Nyquist, K. M. Chen, "Synthesis of kill-pulse to excite selected target modes," *IEEE Antennas and Propagation Society International Symposium*, pp. 15-18, June 1984.

[77] G. Turhan-Sayan, D. L. Moffatt, "K-pulse estimation and target identification of low-Q radar targets," *Wave Motion*, vol. 11, no. 5, pp. 453-461, Nov. 1989.

[78] P. Ilavarasan, J. E. Ross, E. J. Rothwell, K.-M. Chen, D. P. Nyquist, "Performance of an automated radar target discrimination scheme using E pulses and S pulses," *IEEE Trans. Antennas and Propagation*, vol. 41, no. 5, pp. 582-588, May 1993.

[79] G. Turhan-Sayan, K. Leblebicioglu, S. Inan "Input signal shaping for target identification," *Microwave and Optical Technology Letters*, vol. 17, no. 2, pp. 128-132, Feb. 1998.

[80] A. Gallego, M. C. Carrion, D.-P. Ruiz, J. A. Morente, "Improved S-pulse automated scheme using subsectional polynomial basis functions," *IEEE Trans. Antennas and Propagation*, vol. 44, no. 6, pp. 859-862, June 1996.

[81] J. E. Mooney, Z. Ding and L. S. Riggs, "Performance analysis of an automated E-pulse target discrimination scheme," *IEEE Trans. Antennas and Propagation*, vol. 48, no. 3, pp. 619-628, Mar. 2000.

[82] D. Blanco, D. P. Ruiz, E. A. Hernandez, M. C. Carrion, "An asymptotically unbiased E-pulse scheme for radar target discrimination," *IEEE Trans. Antennas and Propagation*, vol. 52, no. 5, pp. 1348-1350, May 2004.

[83] D. Blanco, D. P. Ruiz, E. A. Hernandez, M. C. Carrion, "Extinction pulses synthesis for radar target discrimination using β-splines, new E-pulse conditions," *IEEE Trans. Antennas and Propagation*, vol. 54, no. 5, pp. 1577-1585, May 2006.

[84] H. S. Lui and N. V. Z. Shuley, "Radar target identification using a "banded" E-pulse technique," *IEEE Trans. Antennas and Propagation*, vol. 54, no. 12, pp. 3874-3881, Dec. 2006.

[85] J. E. Mooney, Z. Ding and L. S. Riggs, "Robust target identification in white Gaussian noise for ultrawide-band radar systems," *IEEE Trans. Antennas and Propagation*, vol. 46, no. 12, pp. 1817-1823, Dec. 1998.

[86] K.-T. Kim, I.-S. Choi and H.-T. Kim, "Efficient radar target classification using adaptive joint time-frequency processing," *IEEE Trans. Antennas and Propagation*, vol. 48, no. 12, pp. 1789-1801, Dec. 2000.

[87] J. H. Lee and H.-T. Kim, "Radar target recognition based on late time representation: closed-form expression for criterion," *IEEE Trans. Antennas and Propagation*, vol. 54, no. 9, pp. 2455-2462, Sept. 2006.

[88] Y. Shi and X. D. Zhang, "A Gabor atom network for signal classification with application in radar target recognition," *IEEE Trans. on Signal Processing,* vol. 49, no.12, pp. 2994-3004, Dec. 2001.

[89]   M. R. Azimi-Sadjadi, De Yao, Q. Huang, G.J. Dobeck, "Underwater target classification using wavelet packets and neural networks," *IEEE Trans. on Neural Networks*, vol. 11 , no. 3, pp. 784-794, May 2000.

[90]   X. Miao, M. R. Azimi-Sadjadi, Bin Tan, A.C. Dubey, N. H. Witherspoon, "Detection of mines and minelike targets using principal component and neural-network methods," *IEEE Trans. on Neural Networks*, vol. 9, no. 3, pp. 454-463, May 1998.

[91]   G. Turhan-Sayan, "Real time electromagnetic target classification using a novel feature extraction technique with PCA-based fusion," *IEEE Trans. Antennas and Propagation*, vol. 53, no. 2, pp. 766-776, Feb. 2005.

[92]   L. Cohen, Time-Frequency Analysis, Prentice-Hall Englewood Cliffs, New Jersey, 1995.

[93]   M. Ayar, "Design of an electromagnetic classifier for spherical targets," M. Sc. Thesis, Middle East Technical University, April 2005.

[94]   M. O. Ersoy, "Application of a natural-resonance based feature extraction technique to small-scale aircraft modeled by conducting wires for electromagnetic target classification," M. Sc. Thesis, Middle East Technical University, Sept. 2004.

[95]   R. O. Schmidt, "Multiple emitter location and signal parameter estimation," *IEEE Trans. Antennas and Propag.*, vol. 34, no. 3, pp. 276-280, Mar. 1986.

[96]   G. Bienvenu, "Influence of spatial coherence of background noise on high resolution passive methods," *International Conference on Acoustic, Speech and Signal Processing*, pp. 306-309, 1979.

[97]   P. Stoica and K. C. Sharman, "Maximum likelihood methods for direction-of-arrival estimation," *IEEE Trans. on Acoustics, Speech and Signal Processing*, vol. 38, no. 7, pp. 1132-1143, July 1990.

[98]   T. T. Georgiou, "Signal estimation via selective harmonic amplification: MUSIC, Redux," *IEEE Trans. on Acoustics, Speech and Signal Processing*, vol. 48, no. 3, pp. 780-790, Mar. 2000.

[99]   M. C. Dogan, J. M. Mendel, "Single sensor detection and classification of multiple sources by higher-order spectra," *IEE Proceedings F, Radar and Signal Processing*, vol. 140, no. 6, pp. 350-355, Dec. 1993.

[100] R. O. Schmidt, "Multiple emitter location and signal parameter estimation," *Proc. RADC, Spectral Estimation Workshop*, pp. 243-258, 1979.

[101] P. Stoica, R. Moses, Introduction to Spectral Analysis, Prentice Hall, Englewood Cliffs, New Jersey, 1997.

[102] Y. Li, J. Razavilar and K. J. Ray Liu, "DMUSIC algorithm for 2D NMR Signals," *Engineering in Medicine and Biology Society, IEEE 17th Annual Conference*, pp. 477 – 478, Sept. 1995.

[103] F. Hlawatsch and G. F. Boudreaux-Bartels, "Linear and quadratic time-frequency signal representations," *IEEE Signal Processing Mag.*, vol. 9, no. 2, pp. 21-67, April 1992.

[104] K. M. Chen, D. P. Nyquist, E. J. Rothwell, and W. M. Sun, "New progress on E/S pulse techniques for noncooperative target recognition," *IEEE Trans. Antennas and Propagation*, vol. 40, no. 7, pp. 829-833, July 1992.

[105] A. Gallego, M. C. Carrion, J. Porti, D.-P. Ruiz, "SubSectional-polynomial E-pulse synthesis and application to radar target discrimination," *IEEE Trans. Antennas and Propagation*, vol. 41, no. 9, pp. 1204-1211, Sept. 1993.

[106] C. Chen, "Electromagnetic resonances of immersed dielectric spheres," *IEEE Trans. Antennas and Propagation*, vol. 46, no.7, pp. 1074-1083, July 1998.

[107] C. A. Balanis, Advanced Engineering Electromagnetics, John Wiley & Sons Inc., New York, 1989.

[108] M. Kerker, The Scattering of Light and Other Electromagnetic Radiation, Academic Press, New York, 1969.

[109] M. Seçmen and G. Turhan-Sayan, "A new electromagnetic target classification method with MUSIC algorithm," *14th IEEE Signal Processing and Communications Applications*, pp. 1-4, April 2006.

[110] FEKO User's Manual, EM Software & Systems-S. A. (Pty) Ltd, July 2003.

[111] M. O. Ersoy and G. Turhan-Sayan, "Electromagnetic target classification of small-scale aircraft modeled by conducting wire structures using a natural resonance based feature extraction technique," *IEEE Antennas and Propagation Society International Symposium*, pp. 468-471, July 2005.

[112] M. Secmen and G. Turhan-Sayan, "A novel method for electromagnetic target classification using the MUSIC algorithm: Applied to small-scale aircraft targets," *European Conference on Antennas and Propagation (EUCAP)*, pp. 523-528, November 2006.

[113] T. Weiland, "A discretization method for the solution of Maxwell's equations for six-component fields," *Electronics and Communication (AEU)*, pp. 116-120, 1977.

[114] CST Microwave Studio Getting Started & Tutorials, April 2005.

[115] D. Yao, M. R. Azimi-Sadjadi, A. A. Jamshidi and G. J. Dobeck, "A study of effects of sonar bandwidth for underwater target classification," *IEEE Journal of Oceanic Engineering*, vol. 27, no. 3, pp. 619-628, July 2002.

[116] K.-T. Kim, J.-H. Bae and H.-T. Kim, "Effect of AR model-based data extrapolation on target recognition performance," *IEEE Trans. Antennas and Propagation*, vol. 51, no. 4, pp. 912-914, April 2003.

[117] K.-T. Kim, D.-K. Seo, H.-T. Kim, "Efficient radar target recognition using the MUSIC algorithm and invariant features," *IEEE Trans. Antennas and Propagation*, vol. 50, No. 3, pp. 325-337, March 2002.

[118] R. Kohavi, F. Provost, "Glossary of terms," *Special Issue on Applications of Machine Learning and the Knowledge Discovery Process, Journal of Machine Learning,* vol. 30, no. 2, pp. 271-274, Feb. 1998.

[119] HP 8720D Network Analyzer User's Guide, Hewlett-Packard, Feb. 1999.

[120] Application note, "Applying error correction to network analyzer measurements," Agilent AN 1287-3, Agilent Technologies.

[121] A. V. Oppenheim, R. W. Schafer and J. R. Buck, Discrete-Time Signal Processing, 2nd Ed., Prentice-Hall Upper Saddle River, New Jersey, 2000.

[122] E. J. Rothwell, K. M. Chen, D. P. Nyquist, J. E. Ross, "Time-domain imaging of airborne targets using ultra-wideband or short-pulse radar," *IEEE Trans. Antennas and Propagation*, vol. 43, no. 3, pp. 327-329, March 1995.

[123] J. E. Ross, "Application of transient electromagnetic fields to radar target discrimination," Ph. D. Thesis, Michigan State University, 1992.

[124] Custom Materials Inc., http://www.custommaterials.com, November 2007.

[125] E. K. Walton and J. D. Young, "The Ohio State University compact radar cross-section measurement range," *IEEE Trans. Antennas and Propagation*, vol. 32, no. 11, pp. 1218-1223, Nov. 1984.

[126] D. L. Moffatt and C.-Y. Lai, "Complex natural resonance extraction from cross-polarized measured scattering data," *Wave Motion*, vol. 8, no. 3, pp. 259-265, March 1986.

[127] J. H. Bruning, Y. T. Lo, "Electromagnetic scattering by two spheres," *Proc. IEEE*, vol. 56, no. 1, pp. 119-120, Jan. 1968.

[128] J. H. Bruning, Y. T. Lo, "Multiple scattering of EM waves by spheres, Part I and Part II," *IEEE Trans. Antennas and Propagation*, vol. 19, no. 3, pp. 378-400, May 1971.

[129] A.-K. Hamid, I. R. Ciric, M. Hamid, "Iterative solution of the scattering by an arbitrary configuration of conducting or dielectric spheres," *IEE Proc.-H*, vol. 138, no. 6, pp. 565-572, Dec. 1991.

[130] P. C. Mahalanobis, "On the generalized distance in statistics," *Proceedings of the National Institute of Science of India*, vol. 12, pp. 49-55, 1936.

[131] C. A. Balanis, Antenna Theory: Analysis and Design, 2nd Ed., John Wiley & Sons Inc., New York, 1997.

[132] N. L. Ridenour, Radar System Engineering, MIT Radiation Laboratory Series, vol. 1, Mc-Graw Hill, New York, 1947.

[133] E. F. Knott, J. F. Shaeffer and M. T. Tuley, Radar Cross Section, 2nd Ed., MA: Artech House, Norwood, 1993.

[134] Lord Rayleigh, "On the scattering of light by small particles," *Phil. Mag.,* vol. 41, pp. 447-454, 1871.

[135] J. Rheinstein, "Scattering of short pulses of electromagnetic waves," *Proc. IEEE*, vol. 53, no. 8, 1069-1070, Aug. 1965.

[136] E. Heyman, L. B. Felsen, "Creeping waves and resonances in transient scattering by smooth convex objects," *IEEE Trans. Antennas and Propagation,* vol. 31, no. 5, pp. 426-437, May 1983.

[137] L. B. Felsen, Hybrid formulation of wave propagation problems, Martinus Nijhoff Publishers, Dordrecht, 1984.

[138] H. J. Li, S. H. Yang, "Using range profiles as feature vectors to identify aerospace targets," *IEEE Trans. Antennas and Propagation,* vol. 41, no. 3, pp. 261-268, May 1993.

[139] G. J. Linde, "Use of wideband waveforms for target recognition with surveillance radars," *Record of the IEEE 2000 International Radar Conf.*, pp. 128-133, May 2000.

[140] G. J. Linde, C. V. Platis, "Target recognition with surveillance radar," *NRL Review*, Naval Research Laboratory, pp. 118-120, 1995.

[141] H.-J. Li, Y.-D. Wang, L.-H. Wang, "Matching score properties between range profiles of high-resolution radar targets," *IEEE Trans. Antennas and Propagation,* vol. 44, no. 4, pp. 444-452, April 1996.

[142] H. J. Li, V. Chiou, "Aerospace target identification- Comparison between and the matching score approach and the neural network approach," *Journal of Electromagnetic Waves and Applicat.*, vol. 7, no. 6, pp. 873-893, June 1993.

[143] B. Pei, Z. Bao, M. Xing, "Radar target recognition by a logarithm bispectrum-based method," *CIE International Conference on Radar,* pp. 488-492, Oct. 2001.

[144] X. Zhang, Y. Shi, Z. Bao, "A new feature vector using selected bispectra for signal classification with application in radar target recognition," *IEEE Trans. on Signal Processing,* vol. 49, no. 9, pp. 1875-1885, Sept. 2001.

[145] M.-D. Xing, Z. Bao and B. Pei, "The properties of high-resolution range profiles," *SPIE Optical Engineering,* vol. 41, no. 2, pp. 493-504, Feb. 2002.

[146] L. Du, H. Liu, Z. Bao, M. Xing, "Radar HRRP target recognition based on higher order spectra," *IEEE Trans. on Signal Processing,* vol. 53, no. 7, pp. 2359-2368, July 2005.

[147] S. K. Wong, "Non-cooperative target recognition in the frequency domain," *IEE Proc.- Radar, Sonar and Navigation,* vol. 151, no. 2, pp. 77-84, April 2004.

[148] I. Jouny, F. D. Garber, S. C. Ahalt, "Classification of radar targets using synthetic neural networks," *IEEE Trans. Aerospace Elect. Syst.,* vol. 29, no. 2, pp. 336–343, April 1993.

[149] K.-T. Kim, H.-R. Jeong, "Identification of multiaspect radar signals based on the feature space trajectory concept," *IEEE Trans. Antennas and Propagation,* vol. 53, no. 11, pp. 3811-3821, Nov. 2005.

[150] R. Hu, et al., "Researches on radar target classification based on high resolution range profiles", *Proc. IEEE,* vol. 2, pp. 951-955, 1997.

[151] W. Caiyun, X. Xiaojian, "Some new results of radar target identification using high resolution range profiles," *IEEE Antennas and Propagation Society International Symposium,* vol. 4B, pp. 122-125, July 2005.

[152] A. Zyweck, R. E. Bogner, "Radar target classification of commercial aircraft," *IEEE Trans. Aerospace Elect. Syst.,* vol. 32, no. 2, pp. 598–606, April 1996.

[153] S. Hudson, D. Psaltis, "Correlation filters for aircraft identification from radar range profiles," *IEEE Trans. Aerospace Elect. Syst.,* vol. 29, no. 3, pp. 598-606, July 1993.

[154] J. B. Keller, "Geometrical theory of diffraction," *Journal of Optical Society Amer.,* pp. 116-130, Jan. 1962.

[155] L. C. Potter, D.-M. Chiang, R. Carriere, M. J. Gerry, "A GTD-based parametric model for radar scattering," *IEEE Trans. Antennas and Propagation,* vol. 43, no. 10, pp. 1058-1066, Oct. 1995.

[156] L. B. Felsen, M. Marcuvitz, Radiation and Scattering of Waves, IEEE Press, New York, 1994.

[157] J. Wang, "A parametric scattering centers model with frequency dependence for radar target recognition," *Radio Science Conference,* pp. 98-100, Aug. 2004.

[158] F. D. Garber, N. F. Chamberlain, O. Snorrason, "Time-domain and frequency-domain feature selection for reliable radar target identification," *Proc. IEEE 1988 Nat. Radar Conf.,* pp. 79-84, April 1988.

[159] M. P. Hurst and R. Mittra, "Scattering center analysis via Prony's method," *IEEE Trans. Antennas and Propagation,* vol. 35, no. 8, pp. 986-988, Aug. 1987.

[160] N. F. Chamberlain, E. K. Walton, F. D. Garber, "Radar target identification of aircraft using polarization diverse features," *IEEE Trans. Aerospace Elect. Syst.*, vol. 27, no. 1, pp. 58-67, Jan. 1991.

[161] Q. Li, E. J. Rothwell, K.-M. Chen, D. P. Nyquist, "Scattering center analysis of radar targets using fitting scheme and genetic algorithm," *IEEE Trans. Antennas and Propagation,* vol. 44, no. 2, pp. 198-207, Feb. 1996.

[162] S.-Y. Wang, S.-K. Jeng, "A deterministic method for generating a scattering-center model to construct the RCS pattern of complex radar targets," *IEEE Trans. on Electromagnetic Compatibility,* vol. 39, no. 4, pp. 315-323, Nov. 1997.

[163] L. C. Trintinalia, R. Bhalia, H. Ling, "Scattering center parameterization of wide-angle backscattered data using adaptive Gaussian representation," *IEEE Trans. Antennas and Propagation,* vol. 45, no. 11, pp. 1664-1668, Nov. 1997.

[164] K.-T. Kim, H.-T. Kim, "One-dimensional scattering centre extraction for efficient radar target classification," *IEE Proc.- Radar, Sonar and Navigation,* vol. 146, no. 3, pp. 147-158, June 1999.

[165] K.-T. Kim, D.-K. Seo, H.-T. Kim, "Radar target identification using one-dimensional scattering centres," *IEE Proc.- Radar, Sonar and Navigation,* vol. 148, no. 5, pp. 285-296, Oct. 2001.

[166] K.-T. Kim, H.-T. Kim, "Two-dimensional scattering center extraction based on multiple elastic modules network," *IEEE Trans. Antennas and Propagation,* vol. 51, no. 4, pp. 848-861, April 2003.

[167] J. Wang, "Radar targets identification based on perfect parametric modeling using artificial neural networks," *IEEE Conference on Computers, Communications, Control and Power Engineering (TENCON),* vol. 3, pp. 1302-1305, Oct. 2002.

[168] R. Bhalla, H. Ling, "Three-dimensional scattering center extraction using the shooting and bouncing ray technique," *IEEE Trans. Antennas and Propagation,* vol. 44, no. 11, pp. 1445-1453, Nov. 1996.

[169] R. Bhalla, J. Moore, H. Ling, "A global scattering center representation of complex targets using the shooting and bouncing ray technique," *IEEE Trans. Antennas and Propagation,* vol. 45, no. 12, pp. 1850-1856, Dec. 1997.

[170] M. I. Skolnik, Radar Handbook, McGraw-Hill, New York, 1990.

[171] C.-P. Yeang, C. Cho, J. H. Shapiro, "Toward target recognition from synthetic aperture radar imagery using electromagnetics-based signature," *SPIE Optical Engineering,* vol. 42, no. 7, pp. 2129-2149, July 2003.

[172] A. Filippidis, L. C. Jain, N. Martin, "Fusion of intelligent agents for the detection of aircraft in SAR images," *IEEE Trans. on Pattern Analysis and Machine Intelligence,* vol. 22, no. 2, pp. 378-384, April 2000.

[173] R. Schumacher, J. Schiller, "Non-cooperative target identification of battlefield targets- classification results based on SAR images," *IEEE International Radar Conference,* pp. 167-172, May 2005.

[174] D. N. Pedlar, D. J. Coe, "Target geolocation using SAR," *IEE Proc.- Radar, Sonar and Navigation,* vol. 152, no. 1, pp. 35-42, Feb. 2005.

[175] M. A. Richards, Fundamentals of Radar Signal Processing, McGraw-Hill, New York, 2005.

[176] K.-T. Kim, D.-K. Seo, H.-T. Kim, "Efficient classification of ISAR images," *IEEE Trans. Antennas and Propagation,* vol. 53, no. 5, pp. 1611-1621, May 2005.

[177] S. Musman, D. Kerr, C. Bachmann, "Automatic recognition of ISAR ship images," *IEEE Trans. Aerospace Elect. Syst.*, vol. 32, no. 4, pp. 1392-1404, Oct. 1996.

[178] G. Dural, D. L. Moffatt, "ISAR imaging to identify basic scattering mechanism," *IEEE Trans. Antennas and Propagation,* vol. 42, no. 1, pp. 99-110, Jan. 1994.

[179] A. Maki, K. Fukui, Y. Kawawada, M. Kiya, "Automatic ship identification in ISAR imagery: an on-line system using CMSM," *IEEE Radar Conference,* pp. 206-211, April 2002.

[180] A. B. del Campo, A. A. Lopez, B. P. D. Naranjo, J. G. Menoyo, D. R. Moran, C. C. Duarte, "Vehicle control classification and identification through ISAR imaging," *European Radar Conference (EURAD),* pp. 65-68, Oct. 2005.

[181] B. D. Steinberg, "Microwave imaging of aircraft," *Proc. IEEE,* vol. 76, no. 12, pp. 1578-1592, Dec. 1988.

[182] B. D. Steinberg, D. L. Carlson, W. Lee "Experimental localized radar cross sections of aircraft," *Proc. IEEE,* vol. 77, no. 5, pp. 663-669, May 1989.

[183] H. J. Li, R. Y. Lane, "Utilization of multiple polarization data for aerospace target identification," *IEEE Trans. Antennas and Propagation,* vol. 43, no. 12, pp. 1436-1440, Dec. 1995.

[184] D. A. Garren, A. C. Odom, M. K. Osborn, J. S. Goldstein, S. U. Pillai, J. R. Guerci, "Full-polarization matched-illumination for target detection and identification," *IEEE Trans. Aerospace Elect. Syst.*, vol. 38, no. 3, pp. 824-837, July 2002.

[185] D. H. Dai, X. F. Wu, Y. Z. Li, X. S. Wang, S. P. Xiao, "Polarization target detection algorithm based on instantaneous Stokes sub-vector," *IEEE International Symposium on Microwave, Antenna, Propagation and EMC Technologies for Wireless Communication,* vol. 1, pp. 310-313, Aug. 2005.

[186] M. Robinson, M. R. Azimi-Sadjadi, J. Salazar, "Multi-aspect target discrimination using hidden Markov models and neural networks," *IEEE Trans. on Neural Networks,* vol. 16, no. 2, pp. 447-459, March 2005.

[187] I. Jouny, "On SVM for classification of real and synthetic radar signatures," *IEEE Antennas and Propagation Society International Symposium,* vol. 1B, pp. 2-5, July 2005.

[188] P. D. Gader, M. Mystkowski, Y. Zhao, "Landmine detection with ground penetrating radar using hidden Markov models," *IEEE Trans. on Geoscience and Remote Sensing*, vol. 39, no. 6, pp. 1231-1243, June 2001.

[189] W. Mei, G.-L. Shan, X. R. Li, "An efficient Bayesian algorithm for joint tracking and classification," *International Conference on Signal Processing (ICSP),* vol. 3, pp. 2090-2098, Aug. 2004.

APPENDIX A

SCATTERING REGIONS AND THE OPTICAL REGION METHODS FOR TARGET RECOGNITION

The radar cross section (RCS) of a target can be basically defined in Equation (A.1) as [131]

$$\sigma = \lim_{R \to \infty} \left[4\pi R^2 \frac{\left| E^s \right|^2}{\left| E^i \right|^2} \right] \qquad (A.1)$$

where R is the range from the receiver point to target, E^s is the scattered electric field strength at the receiver and E^i is the electric field strength incident on the target.

Scattered target response, in general, and the radar cross section of a target depend on the ratios of characteristic dimensions of the target to the operating wavelength "λ". For example, the normalized monostatic radar cross section of a perfectly conducting sphere is shown in Figure A.1 as a function of ka, where a is the radius of the sphere and $k = \dfrac{2\pi}{\lambda}$ is the wavenumber.
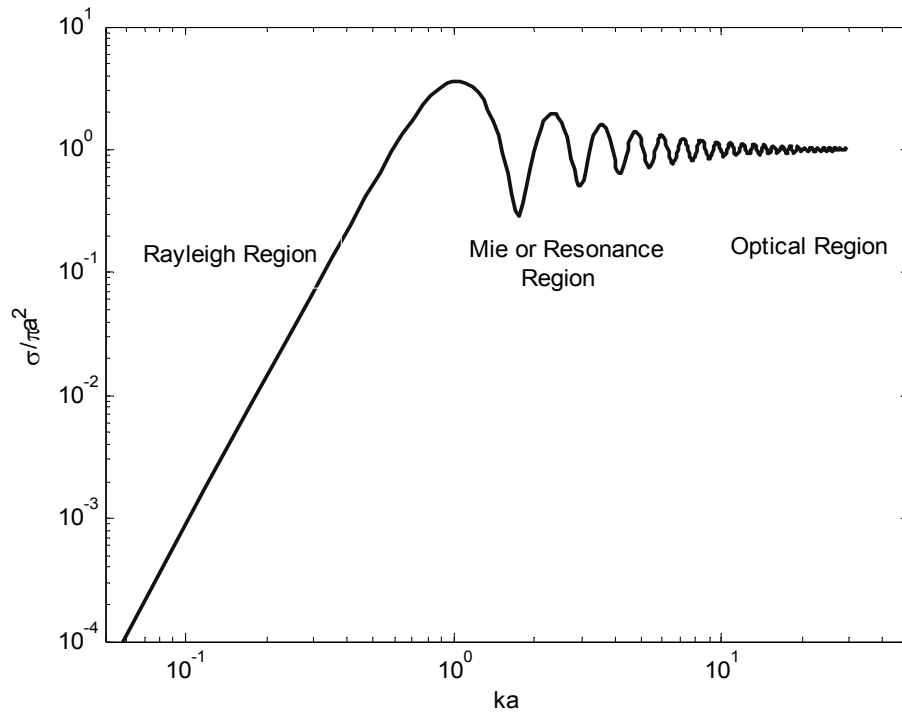
Figure A.1   Normalized monostatic radar cross section of a perfectly conducting sphere as a function of ka (a = radius; k = wavelength).

The scattered signal of a target show distinct characteristics as frequency changes. There are basically three different scattering regions which are also described in Figure A.1. The region where $ka \gg 1$ is the optical region and in this region the radar cross section approaches the physical area of the target. For example, conventional narrowband radars aiming to detect aircraft targets or ships at microwave frequencies generally operate in the optical region. Although it is seemed that the change in RCS with respect to operating frequency is not so significant, the radar cross sections of the targets in this region are extremely dependent on the aspect angle. In Figure A.2, the variation of the backscattered RCS (in dB scale) from a propeller-driven aircraft, a two-engine B-26 medium bomber, at the operating frequency of 3 GHz with respect to azimuth angle [132]-[133] is plotted. Changes in the radar cross section by as much as 15 dB can occur for a change in the aspect angle of only 1/3 degree.

215
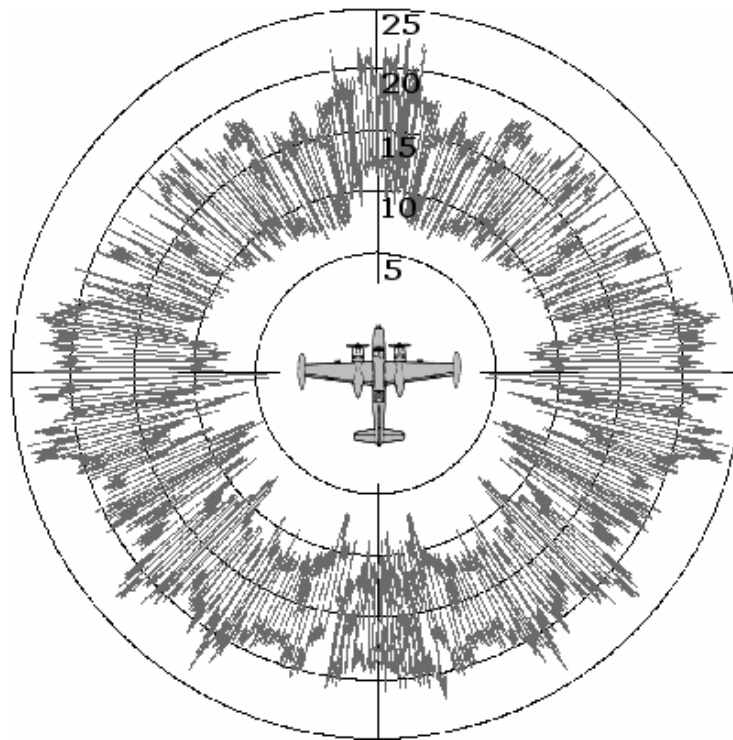
Figure A.2   Backscattering from a full-scale two-engine B-26 medium bomber aircraft at 3 GHz with respect to azimuth angle [132], [133].

The region where $ka \ll 1$ in Figure A.1 is called as Rayleigh region [134]. In this region, the radar cross section is proportional to the fourth power of the operating frequency and is determined more by the volume of the target than by its shape. For example, the backscattering from rain is described by Rayleigh scattering at radar frequencies.

The region between the Rayleigh and the optical region, which is also the region for the target recognition method introduced in this thesis, is Mie or the resonance region. In this region, where the wavelength is comparable to the targets' dimensions, the changes in radar cross section of the targets with respect to the frequency are significant since there are two main waves that can interfere inphase or

out of phase. While the first wave is the direct reflections from the front faces of the target and multiple internal reflections for the penetrable targets, the other one is the creeping wave which circumnavigates around back sides of the target, returns and interferes with the reflections of the target [135]-[137]. As the operating frequency increases, the electrical path around the circumference of the target increases; therefore, greater loss in creeping waves occurs. Since the creeping waves attenuate more as frequency increases, their contributions to the total RCS or the scattered field of the target get smaller in the optical region while their contributions are significant in the resonance region. This is the reason why the magnitude of the fluctuation in RCS with respect to operating frequency is low at optical region. In the resonance region, where radar cross section can be larger than the other two regions, the targets' scattered responses do not change much within a few degrees of aspect angles as it happens in the optical region. Significant changes in target responses can be seen with 10-15 degrees of aspect angle change in this region for smooth objects.

In the following part of this appendix the optical region methods such as high range resolution profile (HRRP), scattering center, synthetic aperture radar (SAR), inverse synthetic aperture radar (ISAR) and polarization response method will be described briefly.

- **High Range Resolution Profile (HRRP) Method**

A radar with sufficiently high range resolution can resolve the individual scattering centers of a target and provide the range profile (the one-dimensional image) of the target [138]. In these methods, the range profiles are used as feature vectors to identify the targets. As an example, the range profile of a Boeing 737 aircraft viewed from broadside and obtained with an L band (1.2 GHz-1.4 GHz) radar having 1 m range resolution is given in Figure A.3 [139], [140].
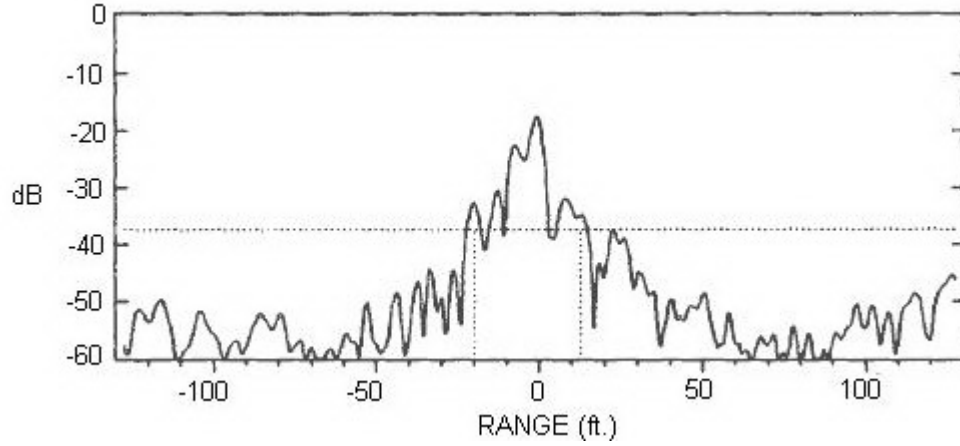
Figure A.3   The range profile of a Boeing 737 aircraft from broadside with a radar having 1 m range resolution and frequency band 1.2 GHz-1.4 GHz [139], [140].

The basic intuitive decision rule is to compare the similarity between the feature vectors of the unknown target with those stored in the database. The matching score is a parameter for measuring this similarity, which is explicitly given in [141], and [142]. The correlation coefficient between the normalized range profiles of test target and candidate target in database with a range shift Δr is defined as

$$c(\Delta r) = \left| \int \hat{R}_{test}(r) \cdot \hat{R}^*_{candidate}(r + \Delta r) dr \right| \qquad (A.2)$$

where $\hat{R}_{test}(r)$ and $\hat{R}^*_{candidate}(r + \Delta r)$ are the normalized range profiles of test and candidate targets, respectively. The maximum of the quantity $c(\Delta r)$ is referred to as matching score of these two range profile and is equal to one, if and only if $\hat{R}_{test}(r) = C\hat{R}^*_{candidate}(r)$. The matching score is defined as coherent or incoherent depending on whether the complex range profiles or the magnitudes of the range profiles are used.

The range profile has often been worked as a potential method for the target recognition in many studies in literature [143]-[152]. However, the true physical target length might not be determined accurately with this method. Even if the length could be measured with accuracy, a serious problem exists that the details of range profile can change with only a small change in aspect angle. Therefore, when creating a library of range profiles to be used to match an unknown profile, each target in database has to be characterized by many reference range profiles corresponding to different aspect angles. Therefore, a huge number of reference range profiles must be stored in database for each target increasing the need for memory storage space and decreasing the real time recognition speed. These factors make the use of high resolution range profiles for target recognition not so practical in realistic target recognition scenarios [152], [153].

- **Scattering Center Method**

The target recognition methods based on scattering center determination are similar to high resolution range profile methods, as the crucial points in range profiles, which are called as scattering centers, are used for target characterization instead of full range profiles. It has been discussed in literature [154] that at sufficiently high frequencies, the scattering response of a target can be well approximated by a sum of responses from individual scatterers or scattering centers located at the target as seen in Figure A.4.
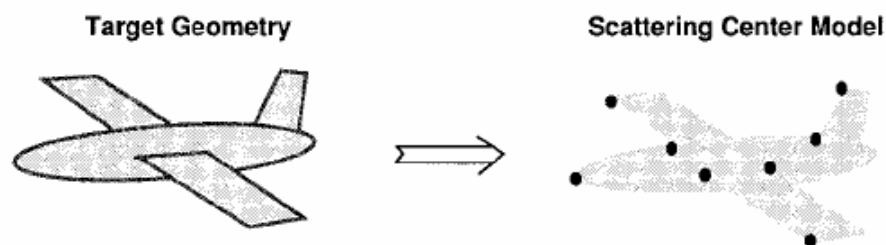
Figure A.4   The scattering center representation of a target.

Therefore, the high-frequency scattered field, y_i, at the frequency f_i can be represented using undamped exponentials as

$$y_i = \sum_{k=1}^{L} a_k \, exp(-j\frac{4\pi f_i}{c} r_k), \qquad i = 1,2,....,N \qquad (A.3)$$

where r_k is the location of the kth scattering center, a_k is the associated amplitude, L is the number of scattering centers on the target and N is the number of frequency samples. A modified parametric approach to this scattering center method is reported in literature [155]-[157] where the diffraction coefficients of the scatterers are also taken into account. The scattering center distribution provides an insight into the geometrical and physical characteristics of the target and can be used in target recognition [158]-[160]. Target recognition methods based on scattering center extraction have been investigated by several researchers [161]-[163]. Target features in terms of one-dimensional, two-dimensional and three-dimensional scattering centers [164]-[169] have been used to identify targets. However, scattering center extraction algorithms are not robust to noise, which restricts target recognition performance of such algorithms. Besides, the scattering center extraction is highly aspect dependent which leads to a significant storage retrieval problem.

- **Synthetic Aperture Radar (SAR) and Inverse Synthetic Aperture Radar (ISAR)**

The two-dimensional image of a target (in range and cross-range) can be obtained by use of an imaging radar such as synthetic aperture radar (SAR) and inverse synthetic aperture radar (ISAR).

Synthetic aperture radar (SAR) is a form of radar in which sophisticated post-processing of radar data is used to produce a very narrow effective beam. SAR produces a high-resolution image of a scene of the target's surface in both range and cross-range [170]. It can produce images of scenes at long range which are not possible with infrared and optical sensors. It is restricted to be used only by moving instruments over recognition of stationary targets, but it is widely used in remote sensing, mapping, target recognition, military and space applications [171]-[174]. In the basic operation of a SAR application, a single radar antenna is attached to the side of an aircraft or a space shuttle. Therefore, rather than constructing a large physical phased array antenna to meet the requirements of high-resolution imaging, a single array element of the antenna is implemented on a moving and then utilized from the antenna platform to obtain a complete array performance. During the motion of the antenna, at each element position, a pulse is transmitted and the resulting fast-time data collected. When the antenna element has traversed the length of the complete array, the data from each position is coherently combined through signal processing to create the effect of a large phased array. Thus, the system synthesizes a large phased array antenna aperture by operating a single element from multiple locations in space. The fundamental limitation of SAR is that the theoretical cross-range resolution is D/2, where D is the the dimension of SAR's real antenna aperture [175]. A typical example to a SAR image, an X-band SAR image of Venus, is shown in Figure A.5.

Figure A.5   The surface of Venus imaged by the Magellan probe using SAR.

Inverse Synthetic Aperture Radar (ISAR) is a technique to identify the scattering centers of the target with high spatial resolution. A fine two-dimensional scattering map of the target is generated by using a large bandwidth transmitted signal in order to achieve high range resolution; and by coherently processing the echoes received from different aspect angles of the target, to achieve fine cross-range resolution. ISAR can be considered as a radar in which the cross-range resolution is obtained by means of high resolution in the doppler frequency domain. Each part of a moving target can have a different velocity with respect to radar. Resolution in doppler frequency allows the parts of moving target to be resolved in the cross range. The cross-range resolution is $\lambda/(2\Delta\theta)$, where $\Delta\theta$ is the change in aspect angle during the observation time and λ is the operating wavelength. Resolution in range is obtained with either a short pulse or pulse compression so that a two-dimensional image is obtained. Unlike SAR, ISAR takes the advantage of target's motion to provide a two-dimensional image. The availability of this two-dimensional high resolution image permits the radar to better identify the target and it can also be useful for the purpose of target recognition [176]-[180]. As an example, the resulting ISAR image

of an L-1011 commercial aircraft with a X-band radar made up by superimposing three independent images is shown in Figure A.6 along with a plan view drawing of the L-1011 for comparison [181], [182].

(a)   (b)
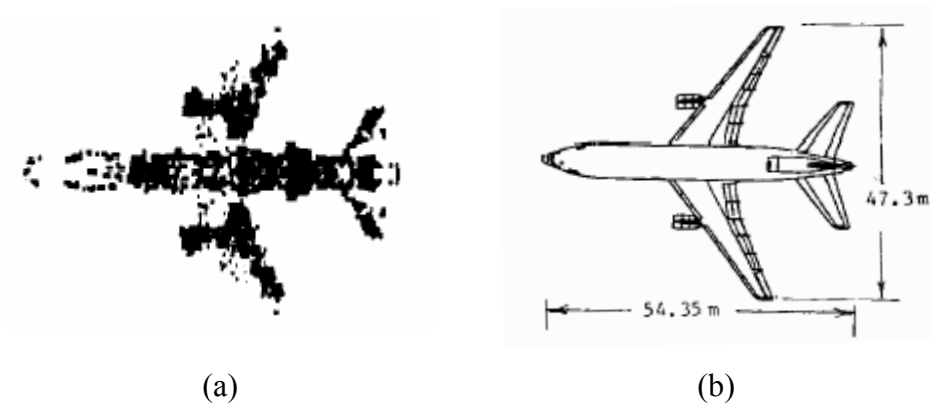
Figure A.6   (a) ISAR image of an L-1011 aircraft (b) Outline drawing of the same aircraft [181], [182].

- **Other methods**

As mentioned before, the scattered signal from a target is highly dependent on the polarization of the incident and reflected fields. The target recognition methods based on this polarization diversity generally requires the data of what is called the polarization matrix. This is obtained from the scattered signals received on both horizontal and vertical polarizations. The polarization matrix is a *2×2* complex scattering operator which characterizes a target's scattering properties where HH and VV are both co-polar components and HV and VH are both cross-polar components. There have been many attempts to use the polarization matrix of the target's scattered signal and other polarization features for target recognition [183]-[185]; however, there has not been the desired success in applying these methods for practical target recognition [1].

In addition to optical region methods explained so far, there exist some other methods in literature such as genetic algorithm methods (neural network (NN) methods, support vector machine (SVM) methods) [186], [187] or probabilistic methods such as hidden-Markov model (HMM) and the Bayesian algorithm [188], [189].

APPENDIX B

DERIVATION OF SINGULARITY EXPANSION METHOD

In this appendix, important steps of the derivation of singularity expansion method are given since the complete derivation is over 40 pages [11]. It is well-known in literature [34] that the Electric Field Integral Equation (EFIE) and Magnetic Field Integral Equation (MFIE) for the scattering problem involving a perfect conducting target in Laplace domain are given in Equation (B.1) and Equation (B.2), respectively, as

$$\vec{E}_{inc}(\vec{r},s) = s\mu_o \int_S \vec{J}_S(\vec{r}',s)G(\vec{r},\vec{r}',s)dS'$$
$$+ \frac{1}{s\varepsilon_o} \int_S \nabla'.\vec{J}_S(\vec{r}',s)\nabla'G(\vec{r},\vec{r}',s)dS' \tag{B.1}$$

$$\hat{n} \times \vec{H}_{inc}(\vec{r},s) = \frac{1}{2}\vec{J}_S(\vec{r},s) - \hat{n} \times \int_S \nabla G(\vec{r},\vec{r}',s) \times \vec{J}_S(\vec{r}',s)dS' \tag{B.2}$$

where S is the surface of conducting target, $\vec{J}_S$ is the induced current density on the exterior side of S and $G(\vec{r},\vec{r}',s) = \dfrac{1}{4\pi|\vec{r}-\vec{r}'|}e^{-\frac{s}{c}|\vec{r}-\vec{r}'|}$ is the free space Green's function. The integral equations for dielectric targets also exist; but, the derivation is given here for perfectly conducting objects which have exterior target poles only. However, the derivation can be easily repeated for other targets with interior poles with the same approach. For the rest of the derivation, it is convenient to use a notation given in Equation (B.3) due to simplicity.

$$\left\langle \vec{\Gamma}(\vec{r},\vec{r}',s)\bullet\vec{J}_S(\vec{r}',s)\right\rangle = \int_S \vec{\Gamma}(\vec{r},\vec{r}',s)\bullet\vec{J}_S(\vec{r}',s)dS' = \vec{F}(\vec{r},s) \tag{B.3}$$

where $\vec{F}(\vec{r},s)$ is the forcing function such as normalized temporal delta function incident electric or magnetic field and $\vec{\Gamma}(\vec{r},\vec{r}',s)$ is the dyadic kernel of the integral equations [34]. It can be shown that these kernels are bounded operators analytic in the entire s plane. Besides, the square of them are Hilbert-Schmidt operators. These give a solution for current which is an analytic function of s except poles in the finite s plane [30].

If the target is complicated (geometry or material composition) then using method of moments (MoM) these integral equations can be converted into a matrix equation in the form

$$\left(\Gamma_{n,m}(s)\cdot j_m(s)\right) = F_n(s) \qquad n,m = 1,2,...,N \tag{B.4}$$

The elements of $\Gamma_{n,m}(s)$ are related to the Green's functions which are analytic functions of s except s=0. So, they are entire functions except for finite order poles at s=0. Besides, the elements of forcing vectors $F_n(s)$ are entire functions

corresponding to delta function excitation in time domain. The solution of Equation (B.4) can be given as

$$j_m(s) = ((\Gamma_{n,m}(s))^{-1} \cdot F_n(s)) = \frac{(adj(\Gamma_{n,m}(s)) \cdot F_n(s))}{det(\Gamma_{n,m}(s))} \qquad (B.5)$$

In the finite s plane $(adj(\Gamma_{n,m}(s)) \bullet F_n(s))$ and $[det(\Gamma_{n,m}(s))]^{-1}$ have only pole singularities, therefore, $j_m(s)$ has also only pole singularities. The natural frequencies and natural modes of the integral equations in (B.2) for the delta function response can be found with the non-trivial solution of Equation (B.3) that

$$\left\langle \vec{\Gamma}(\vec{r},\vec{r}',s_\alpha) \bullet \vec{v}_\alpha(\vec{r}') \right\rangle = \vec{0} \qquad (B.6)$$

where $\vec{v}_\alpha(\vec{r}')$ is the natural mode belonging to the non-trivial solution of the equations without a forcing function at s_α. The MoM version of this equation is

$$\left\langle \Gamma_{n,m}(s_\alpha) \cdot (\vec{v}_m)_\alpha \right\rangle = 0_n \qquad (B.7)$$

which gives an equation for the natural frequencies as $[det(\Gamma_{n,m}(s_\alpha))] = 0$. It is crucial that the elements of $\Gamma_{n,m}(s)$ depends on target's material properties and geometry and not on the forcing function or spatial coordinates (aspect angle of incident wave). Thus, s_α values depend only on the shape, size and material properties of a target. Then, the Laplace transformed surface currents induced by delta function excitation on finite-size perfectly conducting targets are

$$\vec{J}_S(\vec{r},s) = \left\langle (\vec{\Gamma}(\vec{r},\vec{r}',s))^{-1} \bullet \vec{F}(\vec{r}',s) \right\rangle = \sum_{\alpha=1}^{\infty} \frac{\eta_\alpha(s)\vec{v}_\alpha(\vec{r})}{(s-s_\alpha)} + \vec{W}(\vec{r},s) \quad (B.8)$$

where $\eta_\alpha(s)$ can be called as the coupling coefficient which is the strength of the natural oscillation depending on the target and forcing function parameters such as polarization and propagation direction of the incident wave. $\vec{W}(\vec{r},s)$ is an entire function representing the trivial solution of integral equations due to forcing response. Besides, according to Mittag-Leffler theorem, each pole term in the infinite series requires an entire function to guarantee convergence of the series, which also explains the necessity of this entire function. These additional entire functions, which depend on the target parameters, position on the target and incident wave parameters, have not been shown explicitly due to the simplicity of the proof. In this equation, it is also assumed to be only first-order pole as the singularities by excluding both essential singularities and branch point singularities with their associated branch cuts [11].

In order to find the coupling coefficients, first it should be needed to find the coupling vectors belonging to s_α from

$$\left\langle \vec{\mu}_\alpha(\vec{r}) \bullet \vec{\Gamma}(\vec{r},\vec{r}',s_\alpha) \right\rangle = 0 \tag{B.9}$$

Then, the kernel of the integral equation and forcing function can be expanded in a power series around s_α as

$$\vec{\Gamma}(\vec{r},\vec{r}',s) = \sum_{l=0}^{\infty} \frac{(s-s_\alpha)^l}{l!} \left(\frac{\partial^l}{\partial s^l} \vec{\Gamma}(\vec{r},\vec{r}',s) \right)_{s=s_\alpha}$$
$$\vec{F}(\vec{r},s) = \sum_{l=0}^{\infty} \frac{(s-s_\alpha)^l}{l!} \left(\frac{\partial^l}{\partial s^l} \vec{F}(\vec{r},s) \right)_{s=s_\alpha} \tag{B.10}$$

By equating the coefficient of the $(s-s_\alpha)$ term gives respectively at s_α

$$\left\langle \vec{\Gamma}(\vec{r},\vec{r}',s_\alpha) \bullet \vec{W}(\vec{r}',s) \right\rangle$$

$$+ \left\langle ((\frac{\partial}{\partial s}\vec{\Gamma}(\vec{r},\vec{r}',s))_{s=s_\alpha}) \bullet \eta_\alpha(s_\alpha)\vec{v}_\alpha(\vec{r}') \right\rangle = \vec{F}(\vec{r},s_\alpha) \tag{B.11}$$

By operating on the left by $\vec{\mu}_\alpha(\vec{r})$ and using (B.9) to the first term in (B.11) is thereby made to be zero. So, the equation is solved for the coupling coefficient as

$$\eta_\alpha(s_\alpha) = \frac{\left\langle \vec{\mu}_\alpha(\vec{r}) \bullet \vec{F}(\vec{r},s_\alpha) \right\rangle}{\left\langle \vec{\mu}_\alpha(\vec{r}) \bullet \left\langle \vec{\Gamma}(\vec{r},\vec{r}',s_\alpha) \bullet \vec{v}_\alpha(\vec{r}') \right\rangle \right\rangle} \tag{B.12}$$

As seen from Equation (B.12), the coupling coefficient depends on the parameters of forcing function (incident wave) such as polarization and target geometry. This coupling coefficient can also be thought as the residue belonging to s_α.

For finite size objects, the electric and magnetic fields have properties similar to that associated with complex natural frequencies, natural modes and possible entire functions for the surface currents. Once the surface current is found, by using classical radiation expression the scattered electric and magnetic fields at point (r_o,θ,ϕ) can be written as

$$\vec{E}^r(\vec{r}_o,s) = -s\mu_o \int\limits_S \vec{J}_S(\vec{r}',s)G(\vec{r}_o,\vec{r}',s)dS'$$

$$+ \frac{1}{s\varepsilon_o}\int\limits_S \nabla'.\vec{J}_S(\vec{r}',s)\nabla G(\vec{r}_o,\vec{r}',s)dS' \tag{B.13}$$

$$\vec{H}^r(\vec{r}_o,s) = \int\limits_S \nabla G(\vec{r}_o,\vec{r}',s) \times \vec{J}_S(\vec{r}',s)dS'$$

From Equation (B.13), the field expressions are again related to the Green's functions. So, these Green's functions do not add a new pole (possibly add a pole at s=0) to the poles of surface current, then the poles of fields and surface current are identical which are crucially dependent only on the shape, size and material properties of a target and independent from propagation direction (aspect angle) of incident wave, position (aspect angle) of the receiving point and polarization of the incident and reflected waves. The entire function in the surface current also exists in the field expressions in different form which correspond to the specular fields contributing to early-time response. This entire function is highly dependent on the incident wave and target parameters. The residues corresponding to the poles of the field expressions are also highly dependent on the receiving position (aspect angle) since Green's functions in (B.13) containing $\vec{r}_o$ in their argument and polarization of the incident and reflected fields. Finally, the total reflected electric field can be expressed formally in the Laplace domain by an expansion over the poles of the meromorphic function plus an entire function as

$$\vec{E}(\vec{r}_o,s) = \vec{W}_E(\vec{F},\vec{r}_o,s) + \sum_{\alpha=1}^{\infty} \frac{\vec{R}_\alpha(\vec{F},\vec{r}_o,s)}{(s-s_\alpha)} \qquad (B.14)$$

where a similar expression can also be written for magnetic field.

APPENDIX C

SCATTERED FIELD EXPRESSIONS FOR PERFECTLY CONDUCTING AND DIELECTRIC SPHERES

Let a dielectric sphere of given isotropic characteristics $(\varepsilon_r \varepsilon_o, \mu_o)$ be immersed in an x polarized electric field of a plane wave as shown in Figure C.1.
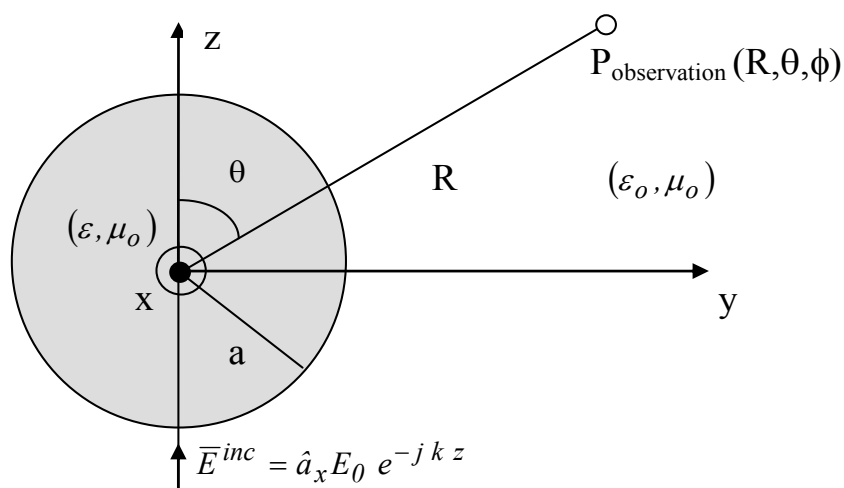
Figure C.1   The geometry for scattered electromagnetic fields from the spherical targets.

This incident and scattered electric and magnetic fields can be expressed in terms of Hertz and Debye potentials as [108]

$$\vec{E} = \nabla \times \nabla \times (vR\hat{a}_R) - j\omega\mu_o \nabla \times (wR\hat{a}_R) = \nabla \times \nabla \times \vec{\pi}_e - j\omega\mu_o \nabla \times \vec{\pi}_m$$

$$\vec{H} = \underbrace{j\omega\varepsilon_o \nabla \times (vR\hat{a}_R)}_{TM} - \underbrace{\nabla \times \nabla \times (wR\hat{a}_R)}_{TE} = \underbrace{j\omega\varepsilon_o \nabla \times \vec{\pi}_e}_{TM} - \underbrace{\nabla \times \nabla \times \vec{\pi}_m}_{TE} \qquad (C.1)$$

where electric Hertz potential, $\vec{\pi}_e$, called the electric wave or transverse magnetic wave (TM) and magnetic Hertz potential, $\vec{\pi}_m$, called the magnetic wave or transverse electric wave (TE) satisfy the following forms of the general vector wave equations:

$$\nabla^2 \vec{\pi}_e - \sigma\mu \frac{\partial \vec{\pi}_e}{\partial t} - \varepsilon\mu \frac{\partial^2 \vec{\pi}_e}{\partial t^2} = -\frac{\vec{P}}{\varepsilon}$$

$$\nabla^2 \vec{\pi}_m - \sigma\mu \frac{\partial \vec{\pi}_m}{\partial t} - \varepsilon\mu \frac{\partial^2 \vec{\pi}_m}{\partial t^2} = -\vec{M} \qquad (C.2)$$

where $\vec{P}$ and $\vec{M}$ are the electric and magnetic polarizations arise from the electric and magnetic dipoles. In terms of Debye potentials, the component of the scattered electric field vectors in spherical coordinates in vacuum are given by

$$E_r = \frac{\partial^2 (vR)}{\partial R^2} + \omega^2 \mu_o \varepsilon_o (vR), \ E_\theta = \frac{1}{R} \frac{\partial^2 (vR)}{\partial R \partial \theta} + \frac{j\omega\mu_o}{R \sin\theta} \frac{\partial (wR)}{\partial \phi},$$

$$E_\phi = \frac{1}{R \sin\theta} \frac{\partial^2 (vR)}{\partial R \partial \phi} - \frac{j\omega\mu_o}{R} \frac{\partial (wR)}{\partial \theta} \qquad (C.3)$$

The Hertz-Debye potentials are also solutions of the scalar wave equation which can be solved by the method of separation of the variables. In spherical coordinates, the wave equation becomes

$$\frac{1}{R}\frac{\partial^2(vR)}{\partial R^2} + \frac{1}{R^2\sin\theta}\left(\sin\theta\frac{\partial v}{\partial\theta}\right) + \frac{1}{R^2\sin^2\theta}\frac{\partial^2 v}{\partial\phi^2} + k^2 v = 0 \qquad (C.4)$$

The general solution of Equation (C.4) is given in Equation (C.5) that the details and extraction of this solution can be found in many books [40], [107], [108].

$$\begin{Bmatrix} v \\ w \end{Bmatrix} = R(r)\Theta(\theta)\Phi(\phi) = \sum_{n=0}^{\infty}\left(c_n j_n(kR) + d_n n_n(kR)\right)P_n^{(1)}(\cos\theta)\begin{Bmatrix} \cos\phi \\ \sin\phi \end{Bmatrix}$$
$$= \sum_{n=0}^{\infty}a_n h_n^{(2)}(kR)P_n^{(1)}(\cos\theta)\begin{Bmatrix} \cos\phi \\ \sin\phi \end{Bmatrix} \qquad (C.5)$$

where $P_n^{(1)}(\cos\theta)$ are the associated first kind Legendre polynomials. The functions of $j_n(kR)$, $n_n(kR)$ and $h_n^{(2)}(kR)$ are spherical Bessel, Neumann and Hankel functions where $h_n^{(2)}(kR)$ has the property of vanishing when kR becomes infinite and is useful for this reason.

The incident field can be written in Equation (C.7) by utilizing from expressions in Equation (C.6) after a long mathematical computation.

$$e^{-jk_o R\cos\theta} = \sum_{n=1}^{\infty}(-j)^n(2n+1)P_n(\cos\theta)j_n(k_o R),$$
$$\frac{d}{d\theta}\left(e^{-jk_o R\cos\theta}\right) = jk_o R\sin\theta e^{-jk_o R\cos\theta} \qquad (C.6)$$
$$= \sum_{n=1}^{\infty}(-j)^n(2n+1)P_n^{(1)}(\cos\theta)j_n(k_o R)$$

$$\vec{E}^{inc} = \hat{a}_x e^{-jk_oR\cos\theta} = \sum_{n=1}^{\infty}(-j)^n \frac{2n+1}{n(n+1)}\left\{\frac{jn(n+1)}{k_oR}j_n(k_oR)P_n^{(1)}(\cos\theta)\cos\phi\,\hat{a}_R\right.$$

$$+\left[\frac{j_n(k_oR)P_n^{(1)}(\cos\theta)}{\sin\theta} + \frac{j}{k_oR}\frac{d}{dR}[Rj_n(k_oR)]\frac{dP_n^{(1)}(\cos\theta)}{d\theta}\right]\cos\phi\,\hat{a}_\theta \qquad (C.7)$$

$$-\left[j_n(k_oR)\frac{dP_n^{(1)}(\cos\theta)}{d\theta} + \frac{j}{k_oR\sin\theta}\frac{d}{dR}[Rj_n(k_oR)]P_n^{(1)}(\cos\theta)\right]\sin\phi\,\hat{a}_\phi$$

By using Equation (C.1) and (C.7), the Debye potentials for the incident field can be written as

$$v^{inc} = \frac{j}{k_o}\sum_{n=1}^{\infty}\frac{(-j)^n}{n(n+1)}\frac{2n+1}{n(n+1)}j_n(k_oR)P_n^{(1)}(\cos\theta)\cos\phi,$$

$$w^{inc} = \frac{j}{\omega\mu_o}\sum_{n=1}^{\infty}\frac{(-j)^n}{n(n+1)}\frac{2n+1}{n(n+1)}j_n(k_oR)P_n^{(1)}(\cos\theta)\sin\phi, \qquad (C.8)$$

The functions $n_n(k_oR)$ have been dropped from these expressions since they are infinite at the origin through which the incident wave must pass. The expressions of Debye potentials for scattered field and the field inside sphere are given as

$$v^{scat} = -\frac{j}{k_o}\sum_{n=1}^{\infty}\frac{(-j)^n}{n(n+1)}\frac{2n+1}{n(n+1)}a_n h_n^{(2)}(k_oR)P_n^{(1)}(\cos\theta)\cos\phi,$$

$$w^{scat} = -\frac{j}{\omega\mu_o}\sum_{n=1}^{\infty}\frac{(-j)^n}{n(n+1)}\frac{2n+1}{n(n+1)}b_n h_n^{(2)}(k_oR)P_n^{(1)}(\cos\theta)\sin\phi,$$

$$v^{in} = \frac{j}{\sqrt{\varepsilon_r}k_o}\sum_{n=1}^{\infty}\frac{(-j)^n}{n(n+1)}\frac{2n+1}{n(n+1)}c_n j_n\left(\sqrt{\varepsilon_r}k_oR\right)P_n^{(1)}(\cos\theta)\cos\phi, \qquad (C.9)$$

$$w^{in} = \frac{j}{\omega\mu_o}\sum_{n=1}^{\infty}\frac{(-j)^n}{n(n+1)}\frac{2n+1}{n(n+1)}d_n j_n\left(\sqrt{\varepsilon_r}k_oR\right)P_n^{(1)}(\cos\theta)\sin\phi,$$

Again, only the function $n_n\left(\sqrt{\varepsilon_r}k_oR\right)$ may be used in the expression for the potential inside the sphere since $n_n\left(\sqrt{\varepsilon_r}k_oR\right)$ becomes infinite at the origin. On the other hand, the scattered wave must vanish at infinity and $h_n^{(2)}(k_oR)$ function imparts precisely this property. The constants a_n, b_n, c_n and d_n can be determined by requiring the tangential components of electric and magnetic fields to be continuous at the surface of the sphere (i.e., at R=a). In terms of Debye potentials, these conditions take the form

$$\frac{d}{dR}\left(R\frac{dv^{in}}{d\theta}\right) = \frac{d}{dR}\left(R\frac{d\left(v^{inc}+v^{scat}\right)}{d\theta}\right), \quad \frac{dw^{in}}{d\theta} = \frac{d\left(w^{inc}+w^{scat}\right)}{d\theta},$$

$$\frac{d}{dR}\left(R\frac{dw^{in}}{d\theta}\right) = \frac{d}{dR}\left(R\frac{d\left(w^{inc}+w^{scat}\right)}{d\theta}\right), \quad \varepsilon_r\frac{dv^{in}}{d\theta} = \frac{d\left(v^{inc}+v^{scat}\right)}{d\theta} \tag{C.10}$$

By inserting series expressions in Equation (C.8) and (C.9) into (C.10) gives

$$a_n = \frac{\varepsilon_r j_n\left(\sqrt{\varepsilon_r}k_oa\right)\left[\dfrac{d\left(xj_n(x)\right)}{dx}\right]_{k_oa} - j_n(k_oa)\left[\dfrac{d\left(xj_n(x)\right)}{dx}\right]_{\sqrt{\varepsilon_r}k_oa}}{\varepsilon_r j_n\left(\sqrt{\varepsilon_r}k_oa\right)\left[\dfrac{d\left(xh_n^{(2)}(x)\right)}{dx}\right]_{k_oa} - h_n^{(2)}(k_oa)\left[\dfrac{d\left(xj_n(x)\right)}{dx}\right]_{\sqrt{\varepsilon_r}k_oa}}$$

$$b_n = \frac{j_n\left(\sqrt{\varepsilon_r}k_oa\right)\left[\dfrac{d\left(xj_n(x)\right)}{dx}\right]_{k_oa} - j_n(k_oa)\left[\dfrac{d\left(xj_n(x)\right)}{dx}\right]_{\sqrt{\varepsilon_r}k_oa}}{j_n\left(\sqrt{\varepsilon_r}k_oa\right)\left[\dfrac{d\left(xh_n^{(2)}(x)\right)}{dx}\right]_{k_oa} - h_n^{(2)}(k_oa)\left[\dfrac{d\left(xj_n(x)\right)}{dx}\right]_{\sqrt{\varepsilon_r}k_oa}} \tag{C.11}$$

These coefficients are important that the complex natural resonance frequencies (pole values) can be found from these a_n and b_n coefficients where resonances occur when denominators in Equation (C.11) vanish. The root values for the

denominators of a_n and b_n give TM and TE mode poles for spheres, respectively. It is particularly interesting to evaluate the scattered fields in the radiation region. This can be done by introducing the asymptotic values of Hankel functions as follows:

$$\lim_{R \to \infty} h_n^{(2)}(k_o R) = j^{n+1} \frac{e^{-jk_o R}}{k_o R}, \ \lim_{R \to \infty} \frac{d}{dR}\left[R h_n^{(2)}(k_o R)\right] = j^n e^{-jk_o R} \quad (C.12)$$

Besides, the radial component E_r falls off as R^2 so that they can be neglected in the far-field zone. The fields can be obtained by inserting Equation (C.9) into (C.1)

$$E_\phi^{scat} = -\frac{je^{-jk_o R}}{k_o R} \sin\phi \sum_{n=1}^{\infty} \frac{2n+1}{n(n+1)}\left\{ a_n \frac{P_n^{(1)}(\cos\theta)}{\sin\theta} + b_n \frac{dP_n^{(1)}(\cos\theta)}{d\theta}\right\}$$

$$E_\theta^{scat} = \frac{je^{-jk_o R}}{k_o R} \cos\phi \sum_{n=1}^{\infty} \frac{2n+1}{n(n+1)}\left\{ a_n \frac{dP_n^{(1)}(\cos\theta)}{d\theta} + b_n \frac{P_n^{(1)}(\cos\theta)}{\sin\theta}\right\}$$

$$(C.13)$$

The field expressions in Equation (C.13) are general for all spheres (dielectric, perfectly conducting); however, the coefficients of a_n and b_n simplifies to Equation (C.14) for perfectly conducting sphere by taking $\lim_{\varepsilon_r \to \infty}$ of expressions in Equation (C.11) and using information of $\lim_{\varepsilon_r \to \infty} \varepsilon_r j_n(\sqrt{\varepsilon_r} k_o R) = \infty, \ \lim_{\varepsilon_r \to \infty} j_n(\sqrt{\varepsilon_r} k_o R) = 0$

$$a_n = \frac{\left[d(x j_n(x))/dx\right]_{k_o a}}{\left[d(x h_n^{(2)}(x))/dx\right]_{k_o a}}, \ b_n = \frac{j_n(k_o a)}{h_n^{(2)}(k_o a)} \quad (C.14)$$

The n=1 TM mode, for example, has a resonance at $k_o a = \pm 0.866 + j0.5$ by equating a_1 in Equation (C.14) to zero.

APPENDIX D

A SAMPLE PROGRAM CODE WRITTEN IN MATLAB FOR AIRCRAFT TARGET SET

In this Appendix Section, the program codes of the proposed target recognition method in MATLAB after the generation of time domain responses of scattered fields are given.

```
warning('off','MATLAB:dispatcher:InexactMatch')
clear all
close all
load ucak1_60_5_1024time.mat    %loading all time domain responses
…
load ucak5_60_82_1024time.mat
%%%%%%%%%
xnorm1=ucak1_60_5_1024time(1:end).';  %choosing reference aspect angles
xnorm1(2,1:end)=ucak1_60_15_1024time(1:end).';
xnorm1(3,1:end)=ucak1_60_30_1024time(1:end).';
xnorm1(4,1:end)=ucak1_60_45_1024time(1:end).';
xnorm1(5,1:end)=ucak1_60_75_1024time(1:end).';
…
xnorm1(25,1:end)=ucak5_60_75_1024time(1:end).';
%%%%%%%%%
for uo=1:25
noise=noisecg(length(xnorm1(uo,:)));  realnoise=real(noise);
realnoise=realnoise-mean(realnoise);
SNRref=10;        % SNR in dB in construction of FMSMs
y1=sigmerge(xnorm1(uo,:)',realnoise,SNRref);
xnorm(uo,:)=mean(y1,2); xnorm2(uo,:)=interp1(xnorm(uo,:),1:0.5:512,'linear');
end
%%%%%%%%%%%
```

```
N=128; m=N/2; n=32; temp=0;
for you=1:2
      if you==1
         for ii=1:8
          T=0;GG=0;
           for kk=1:25
            y=real(xnorm(kk,1+(ii-1)*32:128+(ii-1)*32));
            y=y(:);
            N=length(y);                % data length
            % compute the sample covariance matrix
            R=zeros(m,m);
               for i = m : N,
               R=R+y(i:-1:i-m+1)*y(i:-1:i-m+1)'/N;
               end
            % get the eigendecomposition of R; use svd because it sorts eigenvalues
            [U,D,V]=svd(R); G=U(:,n+1:m);
            GG = G*G'; % find the coefficients of the polynomial
               for u=1:151
                  for v=1:257
                  alpha(u)=-(u-1)*0.0006; w(v)=(v-1)*0.00390625*pi;
                  s(u,v)=-alpha(u)+j*w(v);a=exp(s(u,v)*(0:m-1));
                  a=a./norm(a); T(u,v,kk)=abs(1./(a*GG*a'));
                  end
               end
         end
         for kk=1:25
           T(:,:,kk)=T(:,:,kk)./norm(T(:,:,kk),'fro');
         end
         T_totalucak1(:,:,ii)=T(:,:,1)+T(:,:,2)+T(:,:,3)+T(:,:,4)+ T(:,:,5);
         …
         T_totalucak5(:,:,ii)=T(:,:,21)+T(:,:,22)+T(:,:,23)+T(:,:,24)+ T(:,:,25);
         T_totalucak1(:,:,ii)=T_totalucak1(:,:,ii)./norm(T_totalucak1(:,:,ii),'fro');
         …
         T_totalucak5(:,:,ii)=T_totalucak5(:,:,ii)./norm(T_totalucak5(:,:,ii),'fro');
         %%%%%%%%
         corrcoef1(1,1)=sum(sum(T(:,:,1).*T_totalucak1(:,:,ii)));
         corrcoef1(2,1)=sum(sum(T(:,:,2).*T_totalucak1(:,:,ii)));
         …
         corrcoef1(25,1)=sum(sum(T(:,:,25).*T_totalucak5(:,:,ii)));
         corrcoef2(1,1)=sum(sum(T(:,:,1).*T_totalucak2(:,:,ii)));
         corrcoef2(2,1)=sum(sum(T(:,:,2).*T_totalucak2(:,:,ii)));
         …
         corrcoef2(100,1)=sum(sum(T(:,:,25).*T_totalucak4(:,:,ii)));

         CCF(ii)=(sum(corrcoef1)/25-sum(corrcoef2)/100)
```

```matlab
       if CCF(ii)>temp
          temp=CCF(ii); qstar=ii;
       end
    end
 else
    for ii=1:16
    T=0;GG=0;
      for kk=1:25
       y=real(xnorm2(kk,1+(ii-1)*32:128+(ii-1)*32));
       y=y(:);
       N=length(y);              % data length
       % compute the sample covariance matrix
       R=zeros(m,m);
          for i = m : N,
          R=R+y(i:-1:i-m+1)*y(i:-1:i-m+1)'/N;
          end
       [U,D,V]=svd(R);G=U(:,n+1:m);GG = G*G';
          for u=1:151
             for v=1:257
             alpha(u)=-(u-1)*0.0006; w(v)=(v-1)*0.00390625*pi/2;
             s(u,v)=-alpha(u)+j*w(v);a=exp(s(u,v)*(0:m-1));
             a=a./norm(a); T(u,v,kk)=abs(1./(a*GG*a'));
             end
          end
    end

    for kk=1:25
     T(:,:,kk)=T(:,:,kk)./norm(T(:,:,kk),'fro');
    end
    T_totalucak1(:,:,8+ii)=T(:,:,1)+T(:,:,2)+T(:,:,3)+T(:,:,4)+ T(:,:,5);
    …
    T_totalucak5(:,:,8+ii)=T(:,:,21)+T(:,:,22)+T(:,:,23)+T(:,:24)+ T(:,:,25);
T_totalucak1(:,:,8+ii)=T_totalucak1(:,:,8+ii)./norm(T_totalucak1(:,:,8+ii),'fro');
…
T_totalucak5(:,:,8+ii)=T_totalucak5(:,:,8+ii)./norm(T_totalucak5(:,:,8+ii),'fro');
%%%%%%%%%
    corrcoef1(1,1)=sum(sum(T(:,:,1).*T_totalucak1(:,:,8+ii)));
    corrcoef1(2,1)=sum(sum(T(:,:,2).*T_totalucak1(:,:,8+ii)));
    …
    corrcoef1(25,1)=sum(sum(T(:,:,25).*T_totalucak5(:,:,8+ii)));
    corrcoef2(1,1)=sum(sum(T(:,:,1).*T_totalucak2(:,:,8+ii)));
    corrcoef2(2,1)=sum(sum(T(:,:,2).*T_totalucak2(:,:,8+ii)));
    …
    corrcoef2(100,1)=sum(sum(T(:,:,25).*T_totalucak4(:,:,8+ii)));
```

```
        CCF((8+ii)=(sum(corrcoef1)/25-sum(corrcoef2)/100)
           if CCF(8+ii)>temp
              temp=CCF(8+ii); qstar=8+ii;
           end
         end
    end
end

xnorm1(21,1:end)=ucak1_60_10_1024time;  %loading other signals
…
xnorm1(60,1:end)=ucak5_60_82_1024time;

for uo=1:60
noise=noisecg(length(xnorm1(uo,:))); realnoise=real(noise);
realnoise=realnoise-mean(realnoise); SNRtest=5   %SNR in dB of test signals
y1(:,iter)=sigmerge(xnorm1(uo,:)',realnoise,5);
xnorm(uo,:)=mean(y1,2); xnorm2(uo,:)=interp1(xnorm(uo,:),1:0.5:512,'linear');
end

T=0;GG=0;
%%%%%%%%%%%
if qstar<9
  for kk=1:60
     y=real(xnorm(kk,(qstar-1)*32:128+(qstar-1)*32));
    y=y(:); N=length(y); R=zeros(m,m);
      for i = m : N,
      R=R+y(i:-1:i-m+1)*y(i:-1:i-m+1)'/N;
      end
    [U,D,V]=svd(R); G=U(:,n+1:m); GG = G*G';
    for u=1:151
       for v=1:257
       alpha(u)=-(u-1)*0.0006; w(v)=(v-1)*0.00390625*pi;
       s(u,v)=-alpha(u)+j*w(v); a=exp(s(u,v)*(0:m-1));
       a=a./norm(a); T(u,v,kk)=abs(1./(a*GG*a'));
       end
    end
  end
    for kk=1:60
    T(:,:,kk)=T(:,:,kk)./norm(T(:,:,kk),'fro'); %construct MSMs of test signal
    end
%correlation coefficients between FMSMs and MSMs
  corrcoef3(1,1)=sum(sum(T(:,:,1).*T_totalucak1(:,:,qstar)));
  …
  corrcoef3(60,1)=sum(sum(T(:,:,60).*T_totalucak1(:,:,qstar)));
  corrcoef3(1,2)=sum(sum(T(:,:,1).*T_totalucak2(:,:,qstar)));
```

```
      …
      corrcoef3(60,2)=sum(sum(T(:,:,60).*T_totalucak2(:,:,qstar)));
      …
      corrcoef3(60,5)=sum(sum(T(:,:,60).*T_totalucak5(:,:,qstar)))
else
   for kk=1:60
      y=real(xnorm(kk,(qstar-9)*32:128+(qstar-9)*32));
     y=y(:); N=length(y); R=zeros(m,m);
       for i = m : N,
       R=R+y(i:-1:i-m+1)*y(i:-1:i-m+1)'/N;
       end
     [U,D,V]=svd(R); G=U(:,n+1:m); GG = G*G';
     for u=1:151
        for v=1:257
        alpha(u)=-(u-1)*0.0006; w(v)=(v-1)*0.00390625*pi/2;
        s(u,v)=-alpha(u)+j*w(v); a=exp(s(u,v)*(0:m-1));
        a=a./norm(a); T(u,v,kk)=abs(1./(a*GG*a'));
        end
     end
   end
     for kk=1:60
       T(:,:,kk)=T(:,:,kk)./norm(T(:,:,kk),'fro'); %construct MSMs of test signal
     end
%correlation coefficients between FMSMs and MSMs
   corrcoef3(1,1)=sum(sum(T(:,:,1).*T_totalucak1(:,:,qstar)));
   …
   corrcoef3(60,1)=sum(sum(T(:,:,60).*T_totalucak1(:,:,qstar)));
   corrcoef3(1,2)=sum(sum(T(:,:,1).*T_totalucak2(:,:,qstar)));
   …
   corrcoef3(60,2)=sum(sum(T(:,:,60).*T_totalucak2(:,:,qstar)));
   …
   corrcoef3(60,5)=sum(sum(T(:,:,60).*T_totalucak5(:,:,qstar)))
end
% Find the accuracy rates in percentage for 0% and 5% margin
for kkk=1:12
     if corrcoef3(kkk,1)>max([corrcoef3(kkk,2),…,corrcoef3(kkk,5)])
        number=number+1;
     end
     if 0.95*corrcoef3(kkk,1)>max([corrcoef3(kkk,2),…,corrcoef3(kkk,5)])
        number1=number1+1;
     end
   if corrcoef3(kkk+12,2)>max([corrcoef3(kkk+12,1),…,corrcoef3(kkk+12,5)])
        number=number+1;
   end
   if 0.95*corrcoef3(kkk+12,2)>max([corrcoef3(kkk+12,1),…,corrcoef3(kkk+12,5)])
```

```
            number1=number1+1;
        end
     if corrcoef3(kkk+24,3)>max([corrcoef3(kkk+24,1),…,corrcoef3(kkk+24,5)])
            number=number+1;
        end
    if 0.95*corrcoef3(kkk+24,3)>max([corrcoef3(kkk+24,1),…,corrcoef3(kkk+24,5)])
            number1=number1+1;
        end
     if corrcoef3(kkk+36,4)>max([corrcoef3(kkk+36,1),…,corrcoef3(kkk+36,5)])
            number=number+1;
        end
    if 0.95*corrcoef3(kkk+36,4)>max([corrcoef3(kkk+36,1),…,corrcoef3(kkk+36,5)])
            number1=number1+1;
        end
     if corrcoef3(kkk+48,5)>max([corrcoef3(kkk+48,1),…,corrcoef3(kkk+48,4)])
            number=number+1;
        end
    if 0.95*corrcoef3(kkk+48,5)>max([corrcoef3(kkk+48,1),…,corrcoef3(kkk+48,4)])
            number1=number1+1;
        end
 end

perc_0=number*100/60;  %the percentage for 0% margin
perc_5=number1*100/60;  %the percentage for 5% margin
```

CURRICULUM VITAE

PERSONAL INFORMATION

Surname, Name: Seçmen, Mustafa

Nationality: Turkish (TC)

Date and Place of Birth: 8 May 1980, İzmir

Marital Status: Single

Phone: +90 312 210 45 26

Fax: +90 312 210 23 04

email: msecmen@metu.edu.tr

EDUCATION

Degree	Institution	Year of Graduation
B.Sc.	METU Electrical and Electronics Engineering	2002
High School	Bornova Anatolian High School, İzmir	1998

WORK EXPERIENCE

Year	Place	Enrollment
2002-2008	METU Electrical and Electronics Engineering	Teaching Assistant
2001 June	Tübitak-BİLTEN	Summer Practice
2000 July	TEKPAN A.Ş.	Summer Practice

FOREIGN LANGUAGES

Advanced English

INTERNATIONAL JOURNAL PUBLICATIONS

[1]   M. Secmen, G. Turhan-Sayan, "A novel electromagnetic target classification method using MUSIC algorithm-based fused power patterns," *submitted for Pattern Recognition.*

[2]   M. Secmen, S. Demir, A. Hizal, "Dual-polarised T/R antenna system suitable for FMCW altimeter radar applications," *IEE Proceedings - Microwaves, Antennas and Propagation,* vol. 153, no. 5, pp. 407-412, October 2006.

[3]   O. Koysuren, S. Yesil, G. Bayram, M. Secmen, O. A. Civi, "Effect of Carbon Black Surface Treatment on Microwave Properties of PET/Carbon Black Composites," *accepted for Journal of Applied Polymer Science.*

INTERNATIONAL CONFERENCE PUBLICATIONS

[1]   M. Secmen, G. Turhan-Sayan, A. Hizal, "A radar target recognition method with MUSIC algorithm: Application to aircraft targets with measured scattered data," *accepted for IEEE Radar Conference 2008*, Rome, Italy, May 2008.

[2]   M. Secmen, S. Demir, A. Hizal and O. A. Civi, "An elliptically polarized axial-mode helical antenna with a conformal polarizer," *presented in European Conference on Antennas and Propagation (EUCAP) 2007*, Edinburg, Scotland, November 2007.

[3]   S. Demir, M. Secmen, A. Hizal, "Accuracy of the equivalent noise model of clutter in radar equation," *International Radar Symposium (IRS) 2007*, Cologne, Germany, September 2007.

[4]   M. Secmen, G. Turhan-Sayan, "The MUSIC algorithm-based electromagnetic target classification for isolated targets from incomplete frequency domain data," *Antennas and Propagation Symposium (APS) 2007*, pp. 4601-4604, Honolulu, Hawai, USA, June 2007.

[5]   M. Secmen, S. Demir, A. Hizal and T. Eker, "Frequency diverse array antenna with periodic time modulated pattern in range and angle," *IEEE Radar Conference 2007*, pp. 427-430, Boston, USA, April 2007.

[6]   M. Secmen, G. Turhan-Sayan, "A novel method for electromagnetic target classification using the MUSIC algorithm: Applied to small-scale aircraft targets," *European Conference on Antennas and Propagation (EUCAP) 2006*, pp. 523-528, Nice, France, November 2006.

[7]   M. Secmen, S. Demir, L. Alatan, O. A. Civi and A. Hizal, "A compact corporate probe fed antenna array," *European Conference on Antennas and Propagation (EUCAP) 2006*, pp. 484-487, Nice, France, November 2006.

[8]   M. Secmen, G. Turhan-Sayan, "A novel electromagnetic target recognition method by MUSIC algorithm," *Antennas and Propagation Symposium (APS) 2006*, pp. 1299-1302, Albuquerque, New Mexico, USA, July 2006.

[9]   M. Secmen, S. Demir, A. Hizal and N. Candan "Accuracy of the equivalent noise model of clutter in radar equation," *International Radar Symposium (IRS) 2006*, pp. 291-294, Krakow, Poland, May 2006.

NATIONAL CONFERENCE PUBLICATIONS

[1]   M. Seçmen, E. Ekmekçi, G. Turhan-Sayan, "Kaynaştırılmış MUSIC tayf matrisleri ile elektromanyetik hedef tanıma yönteminin eksik frekans verilerine uygulanması ve performans analizi," *Sinyal İşleme ve Uygulamaları Kurultayı (SIU) 2007,* pp. 1-4, Eskişehir, Haziran 2007.

[2]   M. Seçmen, G. Turhan-Sayan, "MUSIC algoritması ve öznitelik kaynaştırma teknikleri kullanılarak açı değişimleri ve gürültüye duyarlılığı azaltılmış yeni bir elektromanyetik hedef sınıflandırıcı," *URSI Ulusal Konferansı 2006,* pp. 583-585, Ankara, Eylül 2006.

[3]   M. Seçmen, Ş. Demir, A. Hızal, K. Çağlar, E. Töngel, "E-düzlem sektörel boynuz anten güç bölücü," *URSI Ulusal Konferansı 2006,* pp. 122-124, Ankara, Eylül 2006.

[4]   M. Seçmen, G. Turhan-Sayan, "MUSIC algoritması ile yeni bir elektromanyetik hedef sınıflandırma yöntemi," *Sinyal İşleme ve Uygulamaları Kurultayı (SIU) 2006,* pp. 1-4, Antalya, Nisan 2006.

[5]   M. Seçmen, K. Topallı, M. Ünlü, E. Erdil, Ö. A. Çivi, A. Hızal "Doğrusal FMCW radar uygulamaları için ikili geniş bantlı anten analizi," *Sinyal İşleme ve Uygulamaları Kurultayı (SIU) 2006,* pp. 1-4, Antalya, Nisan 2006.

[6]   M. Seçmen, G. Turhan-Sayan, A. Hızal, "Hedef tanıma amacı ile Page dağılımı kullanarak elektromanyetik saçılım sinyallerinden kutup çıkarımı," *Sinyal İşleme ve Uygulamaları Kurultayı (SIU) 2005,* pp. 499-502, Kayseri, Mayıs 2005.

[7]   M. Seçmen, G. Turhan-Sayan, A. Hızal "Hedef tanıma için sinyal işleme yöntemleri ile bantgeçirici elektromanyetik geri yansıma ölçüm analizi," *URSI Ulusal Konferansı 2004,* pp. 303-305, Ankara, Eylül 2004.

[8]   Ş. Demir, M. Seçmen, A. Hızal "FMCW Altimetre Radar Sistemlerinde Sirkülatör Kullanımına Alternatifler," *URSI Ulusal Konferansı 2004,* pp. 152-154, Ankara, Eylül 2004.